

GRADUATE AERONAUTICAL LABORATORIES CALIFORNIA INSTITUTE OF TECHNOLOGY

Shock wave interaction in hypervelocity flow

Simon R. Sanderson

1995

1995
10-12

OTIC QUALITY IMPROVED &

Approved for public release
Distribution Unlimited

1995
10-12

Firestone Flight Sciences Laboratory

Guggenheim Aeronautical Laboratory

Karman Laboratory of Fluid Mechanics and Jet Propulsion


19960408 135

Pasadena

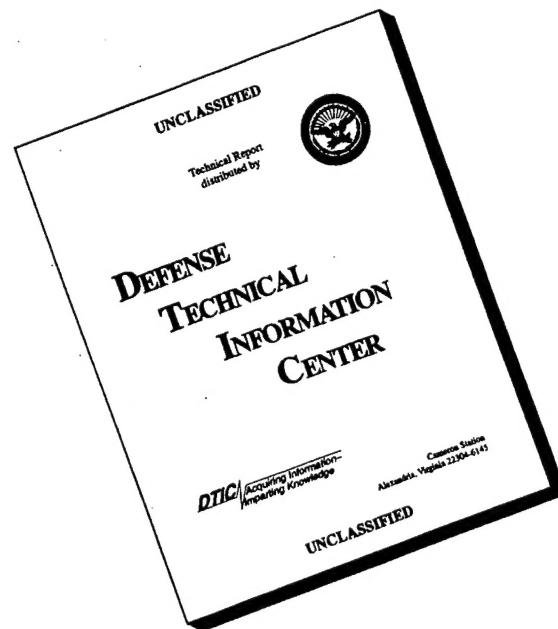
REPORT DOCUMENTATION PAGE

Form Approved
OMB No. 0704-0188

Public reporting burden for this collection of information is estimated to average 1 hour per response, including the time for reviewing instructions, searching existing data sources, gathering and maintaining the data needed, and completing and reviewing the collection of information. Send comments regarding this burden estimate or any other aspect of this collection of information, including suggestions for reducing this burden, to Washington Headquarters Services, Directorate for Information Operations and Reports, 1215 Jefferson Davis Highway, Suite 1204, Arlington, VA 22202-4302, and to the Office of Management and Budget, Paperwork Reduction Project (0704-0188), Washington, DC 20503.

1. AGENCY USE ONLY (Leave blank)		2. REPORT DATE 2 February 1996		3. REPORT TYPE AND DATES COVERED Final Technical Rept. 11/15/91-8/31/95	
4. TITLE AND SUBTITLE (S) Research in Hypervelocity Gasdynamics				5. FUNDING NUMBERS PE - PR - SA - G - F49610-92-J-0110	
6. AUTHOR(S) H, G. Hornung and B. Sturtevant Appendix C					
7. PERFORMING ORGANIZATION NAME(S) AND ADDRESS(ES) Graduate Aeronautical Laboratories California Institute of Technology 1201 E. California Blvd. Pasadena, CA 91125				AFOSR-TR-96 0143	
9. SPONSORING/MONITORING AGENCY NAME(S) AND ADDRESS(ES) AFOSR/NA 110 Duncan Avenue, Suite B115 Bolling AFB DC 20332-0001 Dr. Len Sakell				10. SPONSORING/MONITORING AGENCY REPORT NUMBER NA 	
11. SUPPLEMENTARY NOTES					
12a. DISTRIBUTION/AVAILABILITY STATEMENT Approved for public release; distribution is unlimited				12b. DISTRIBUTION CODE	
13. ABSTRACT (Maximum 200 words) The following important results were obtained from investigations of chemically reacting blunt-body flows and of shock wave interactions in hypervelocity flow: <ul style="list-style-type: none"> • A new view of the binary scaling concept resulted from experimental and theoretical work on flow over spheres, in terms of two dimensionless parameters. • The evolution of the vorticity generated by a curved shock wave could be visualized with resonant enhancement of streak lines. • The effect of recombination in flow along a streamline after a curved shock was explained. • Previous predictions of greatly enhanced heat flux by real-gas effects in shock-on-shock interactions were not borne out. • The study provided extensive corroboration of the computed free-stream conditions in the free-piston shock tunnel T5. • A number of improvements of shock tunnel technology were made, especially regarding diaphragm manufacture, nozzle throat material, and computation of the processes during operation. • Improved diagnostic techniques were generated, including low-noise coaxial thermocouple gauges and inexpensive high-quality holographic interferometry. 					
14. SUBJECT TERMS hypervelocity flow, shock wave, shock interaction, heat transfer, vorticity, dissociation				15. NUMBER OF PAGES 485	
				16. PRICE CODE	
17. SECURITY CLASSIFICATION OF REPORT Unclassified	18. SECURITY CLASSIFICATION OF THIS PAGE Unclassified	19. SECURITY CLASSIFICATION OF ABSTRACT Unclassified	20. LIMITATION OF ABSTRACT UL		

DISCLAIMER NOTICE



THIS DOCUMENT IS BEST QUALITY AVAILABLE. THE COPY FURNISHED TO DTIC CONTAINED A SIGNIFICANT NUMBER OF PAGES WHICH DO NOT REPRODUCE LEGIBLY.

Shock wave interaction in hypervelocity flow

Thesis by
Simon R. Sanderson

In Partial Fulfillment of the Requirements
for the Degree of
Doctor of Philosophy

California Institute of Technology
Pasadena, California

1995
(Submitted May 5, 1995)

© 1995

Simon R. Sanderson

All Rights Reserved

Acknowledgements

GALCIT is an institution that has prospered over the past 60 years because of the collective dedication of the diverse group of people that comprise it. The author wishes to express his gratitude to this community for the role it has played in the completion of this work. Through their insight, encouragement and wise direction, Professors Brad Sturtevant and Hans Hornung have contributed immeasurably to this endeavour. Equally appreciated are the efforts of Jacques Belanger, Eric Cummings, Patrick Germain, Bahram Valiferdowsi and Chih-yung Wen who helped to build T5 and formed part of the much larger group whose cooperation made involvement with this laboratory rewarding and enjoyable.

Personal thanks are due to the author's family who fostered his penchant for science from an early age. Their support has been unfailing ever since. Christina has been a kindhearted encourager and the truest friend one could wish for.

None of this would have been possible without the beneficence of contributors to the Institute. The author is grateful for assistance received from the Darryl G. Greenamyer Fellowship and C.L. Powell Fellowship funds. This work was supported by AFOSR Grant Nos. F49620-92-J-0110 and F49620-93-1-0338.

Abstract

The interaction of a weak oblique shock with the strong bow shock ahead of a blunt body in supersonic flow produces extreme heat transfer rates and surface pressures. Although the problem has been studied extensively in low enthalpy flows, the influences of high enthalpy real gas effects are poorly understood. Existing perfect gas models predict greatly increased heating with increasing Mach number and decreasing ratio of specific heats.

Experiments are conducted in a free piston shock tunnel to determine the effects of thermochemistry on the problem at high enthalpy. The flow topology is simplified by studying the nominally two-dimensional flow about a cylinder with a coplanar impinging shock wave. High resolution holographic interferometry is used to investigate changes in the flow structure as the location of the impinging shock wave is varied. Fast response heat transfer gauges provide time resolved measurements of the model surface temperature. The data that are obtained do not support the existing predictions of greatly increased heat transfer at high enthalpy.

A model is developed to study the thermochemical processes occurring in the interaction region. The phenomenon arises because the stagnation streamline is forced to pass through a system of oblique shock waves that produce less entropy than the undisturbed bow shock. Peak heating is shown to result from a balancing of the strengths of the oblique shock waves. This condition is demonstrated to simultaneously minimize the influence of thermochemistry on the flow. Real gas effects are shown to become important at lower Mach numbers (< 7.5) and for shock angles weaker or stronger than that which produces maximum heating. The model accurately reproduces the experimental observations.

A nonequilibrium approximation is introduced that applies when the oblique waves are weak with respect to the undisturbed bow shock. Within the scope of the approximation, non-monotonic behavior with the reaction rate is predicted. The reaction rate is not varied as an independent parameter in the current experiments.

Contents

Acknowledgements	iii
Abstract	iv
1 Introduction	1
1.1 Motivation	1
1.2 Description of the phenomenon	1
1.3 Real gas effects	8
1.4 Literature review	10
1.5 Scope of the current study	12
2 Experimental program	13
2.1 Description of the T5 hypervelocity shock tunnel	13
2.2 Test conditions	13
2.3 Description of experiment	16
2.3.1 Abstraction of the problem	16
2.3.2 Discussion of the flow topology	17
2.3.3 Critical points in the streamline patterns	17
2.3.4 Application of holographic interferometry	20
2.3.5 Summary	20
2.4 Apparatus	20
2.4.1 Test section arrangement	20
2.4.2 Alignment accuracy	21
2.4.3 Description of model	21
2.4.4 Instrumentation	22
2.4.5 Flow visualization and interferometry	23
2.4.6 Shock generator	23
3 Experimental results	25
3.1 Introduction	25
3.2 Description of the flow fields	25
3.2.1 Flows without shock impingement	26
3.2.2 Type I flows	26

3.2.3	Type II flows	26
3.2.4	Type III flows	27
3.2.5	Displacement of the stagnation point	27
3.2.6	Entrainment of the stagnation streamline	28
3.2.7	Turning of the shear layer at the surface	28
3.2.8	Transition to type IV	29
3.2.9	Type IV flows	30
3.2.10	Curvature of the supersonic jet	32
3.2.11	Detachment of the supersonic jet	32
3.2.12	Type V and VI flows	33
3.3	Summary of the heat transfer data	33
3.4	Comparison with existing data	34
3.5	Temporal characteristics of the data	36
3.5.1	Introduction	36
3.5.2	Flows without shock impingement	37
3.5.3	Unsteadiness of the type IV flow	39
3.5.4	Comparison with existing data.	40
3.6	Supplementary experiments	40
3.7	Summary of the experimental results	44
4	Models of the influence of real gas effects	45
4.1	Overview	45
4.2	Normal shock for an ideal dissociating gas	46
4.2.1	Frozen shock solutions	48
4.2.2	Equilibrium shock solution	48
4.2.3	Nonequilibrium solution	52
4.2.4	Reaction rate parameter	52
4.2.5	Physical constants for the IDG model	54
4.3	Extension to oblique shock waves	55
4.3.1	Normal components of the free stream parameters	55
4.3.2	Variation of parameters across an oblique shock wave	55
4.3.3	Features of IDG oblique shock waves	56
4.4	IDG oblique shock loci in the p - δ plane	56
4.4.1	Features of oblique shock loci	56
4.4.2	Mapping of the frozen sonic line	58
4.4.3	Shock wave interaction problems in the p - δ plane	58

4.5	λ -shock configuration for an ideal dissociating gas	61
4.5.1	Introduction	61
4.5.2	Formulation of the problem	61
4.5.3	Discussion of the solution	63
4.5.4	Representation of the nonequilibrium approximation in the p - δ plane.	63
4.6	Type IV inverted λ -shock for an ideal dissociating gas	67
4.7	Heat transfer model	70
4.7.1	Introduction	70
4.7.2	Fay & Riddell stagnation point heat transfer solution	70
4.7.3	Outer flow solutions	71
4.7.4	Stagnation point recombination rate parameter	72
4.7.5	Normalization of the stagnation point heat flux	74
4.8	Type IV jet heat transfer solution	76
4.8.1	Introduction	76
4.8.2	Heat transfer intensification due to jet impingement	77
4.8.3	Numerical solutions	78
4.8.4	Discussion	82
4.8.5	Interpretation of the mechanisms	83
4.9	Comparison with existing models	84
4.10	Comparison with experimental data	84
4.10.1	Heat flux data	86
4.10.2	Density data	86
4.11	Dissociation and recombination rate parameters for the type IV jet.	87
4.12	Summary	88
5	Conclusions	91
	Bibliography	93
A	Review of shock impingement flow field models	A-1
A.1	Introduction	A-1
A.2	Shock loci methods for a perfect gas	A-1
A.3	The type I-VI classification	A-4
A.3.1	Type I	A-4
A.3.2	Type II	A-4
A.3.3	Type III	A-4
A.3.4	Type IV	A-7

A.3.5	Type V	A-8
A.3.6	Type VI	A-8
B	Test section conditions	B-1
B.1	Summary	B-1
B.2	Prediction of the test section conditions	B-1
B.3	Variation of the free-stream conditions across the test section	B-3
B.4	Experimental verification of the flow density	B-5
B.4.1	Interferometric measurements for a finite aspect ratio cylinder	B-5
B.4.2	Abel transform interferometric measurements for a blunted cylinder	B-6
B.4.3	Density variation across the incident shock wave	B-7
B.5	Experimental verification of the shock standoff distance	B-9
B.6	Stagnation point heat transfer rate	B-10
C	Holographic interferograms and heat transfer data	C-1
D	Holographic interferometer	D-1
D.1	Description of optical apparatus	D-1
D.2	Modes of operation	D-2
D.3	Principles of operation	D-3
E	Surface junction thermocouple sensors	E-1
E.1	Introduction	E-1
E.2	Analysis of heat conduction in gauge substrate	E-2
E.3	Description of new gauge design	E-3
E.4	Deducing the surface heat transfer rate	E-5
E.5	Accuracy of measurements	E-7
F	Technical data	F-1

List of Figures

1.1	Schlieren visualization of the flow field about a model of the X-15-2 vehicle with interference from a scram-jet mounted on the vertical stabilizer (Burcham & Nugent [2]).	2
1.2	Damage to X-15 vertical stabilizer caused by impingement of scram-jet inlet shock wave (Edney [8]).	2
1.3	Schematic representation of the impingement of an oblique shock wave on the leading edge of a blunt body.	3
1.4	Holographic shadowgraph of the impingement of an oblique shock wave near the geometrical stagnation point of a cylinder in hypersonic flow. Following Edney [8] , this flow is categorized as type IV.	4
1.5	Schematic of the type IV shock interference flow field.	5
1.6	Representation of the type IV shock interference flow field in the p - δ plane.	6
1.7	Ratio of jet impingement pressure to undisturbed stagnation point pressure as a function of incident shock flow deflection angle, δ_1	7
1.8	Real gas effects at a λ -shock intersection point.	10
2.1	Schematic representation of the T5 free piston driver shock tunnel.	14
2.2	Abstracted model geometries for the shock impingement problem.	16
2.3	Surface streamlines for shear layer/jet attachment in the flow over a spherical body.	18
2.4	Streamlines in the symmetry plane showing the formation of a spiral vortex as a consequence of shear layer/jet attachment.	19
2.5	Streamline pattern for a cylindrically symmetric swept fin.	19
2.6	Layout of apparatus in the test section of T5.	21
2.7	Arrangement of the optical apparatus with respect to the test section.	22
2.8	Perspective view of shock generator and cylindrical model.	24
3.1	Type II interaction for a $\phi 50$ mm spherical model at condition A.	27
3.2	Interpretive sketch of the entrainment of the stagnation streamline.	29
3.3	Interpretive sketch of detachment of the compression wave.	30
3.4	Interpretive sketch of jet formation.	31
3.5	Emergence of the stagnation streamline from the supersonic jet.	33
3.6	Envelope of maximum heat transfer rates around the model at condition A.	34

3.7	Envelope of maximum heat transfer rates around the model at condition B.	35
3.8	Envelope of maximum heat transfer rates around the model at condition C.	35
3.9	Envelope of maximum heat transfer rates about a spherical model (Edney [8]); $M_\infty = 7$, $\delta_1 = 5^\circ$	36
3.10	Temporal characteristics of the flow without shock impingement at condition A; Shot T5-855.	38
3.11	Temporal characteristics of the flow without shock impingement at condition B; Shot T5-856.	38
3.12	Temporal characteristics of the flow without shock impingement at condition C; Shot T5-824.	39
3.13	Temporal variation of the surface heat flux for type IV flow at condition A; Shot T5-846.	41
3.14	Temporal variation of the surface heat flux for type IV flow at condition B; Shot T5-853.	41
3.15	Temporal variation of the surface heat flux for type IV flow at condition C; Shot T5-839.	42
3.16	Frequency spectra of nozzle reservoir pressure and surface heat flux (gauge #18) for type IV flow at condition A; Shot T5-846.	42
3.17	Frequency spectra of nozzle reservoir pressure and surface heat flux (gauge #18) for type IV flow at condition B; Shot T5-853.	43
3.18	Frequency spectra of nozzle reservoir pressure and surface heat flux (gauge #18) for type IV flow at condition C; Shot T5-839.	43
4.1	Strong shock solutions, $P \rightarrow 0$, of the conservation equations downstream of a normal shock wave in an ideal dissociating gas.	49
4.2	Relaxation of a nonequilibrium upstream state behind a normal shock wave in an ideal dissociating gas.	50
4.3	Equilibrium shock solution in the \hat{p} - α_2 plane.	51
4.4	Nonequilibrium solution for the relaxation downstream of a translational discontinuity in an ideal dissociating gas.	53
4.5	Behavior of the solution for an oblique shock wave in an ideal dissociating gas.	57
4.6	Behavior of the solution for an oblique shock wave in an ideal dissociating gas.	57
4.7	p - δ plane representation of an oblique shock wave for an ideal dissociating gas.	59
4.8	Extent of validity of p - δ plane representation for the interaction of oblique shock waves in an ideal dissociating gas.	59
4.9	p - δ plane representation of the interaction of oblique shock waves in an ideal dissociating gas.	60
4.10	Schematic of flow field and shock wave notation for the type IV interaction in the vicinity of the impingement point.	61

4.11 Density variations, dissociation levels, shock wave angles, streamline deflection, and reaction rates as functions of stagnation enthalpy, $H_{0\infty}$, at a λ -shock point in an ideal dissociating gas.	64
4.12 Representation of the IDG λ -shock configuration in the p - δ plane.	66
4.13 Schematic representation of the effects of finite rate dissociation on the λ -shock configuration.	66
4.14 Effect of finite rate dissociation on the shock wave angles and flow deflection downstream of a λ -shock configuration.	67
4.15 Density variations, dissociation levels, shock wave angles, streamline deflection, and reaction rates as functions of stagnation enthalpy, $H_{0\infty}$, at a type IV inverted λ -shock point in an ideal dissociating gas.	69
4.16 Contour plot of the recombination rate parameter, $\Sigma \frac{\zeta_2 \ell_d}{D}$, as a function of dimensionless stagnation enthalpy, H_0 , and equilibrium density ratio, $\hat{\rho}_d$	73
4.17 Adaption of the Fay & Riddell stagnation point solution to the jet impingement problem.	76
4.18 Influence of dimensionless stagnation enthalpy, Mach number and reaction rate on type IV heat transfer intensification.	79
4.19 Influence of impinging shock wave angle, β_1 , and reaction rate on type IV heat transfer intensification at very high Mach number; $P_\infty = 0.002$	80
4.20 Influence of impinging shock wave angle, β_1 , and reaction rate on type IV heat transfer intensification at high Mach number; $P_\infty = 0.010$	80
4.21 Influence of impinging shock wave angle, β_1 , and reaction rate on type IV heat transfer intensification at moderate Mach number; $P_\infty = 0.025$	81
4.22 Influence of impinging shock wave angle, β_1 , and reaction rate on type IV heat transfer intensification at low supersonic Mach number; $P_\infty = 0.050$	81
4.23 Variation of type IV jet shock strengths with impinging shock angle, β_1	83
4.24 Reaction rate parameters for the type IV jet stagnation point.	89
A.1 Interference types I–III for supersonic flow about a hemisphere; $M_\infty = 4.6$ (Edney [8])). Sequence of interactions is left–right, top–bottom.	A-2
A.2 Interference types IV–VI for supersonic flow about a hemisphere; $M_\infty = 4.6$ (Edney [8])). Sequence of interactions is left–right, top–bottom.	A-3
A.3 Schematic of type I interference flow and its representation in the p - δ plane.	A-5
A.4 Schematic of type II interference flow and its representation in the p - δ plane.	A-6
A.5 Schematic of type III interference flow and its representation in the p - δ plane.	A-7
A.6 Schematic of type V interference flow.	A-8
A.7 Schematic of type VI interference flow and its representation in the p - δ plane.	A-9

B.1	Flow nonuniformity in the nozzle exit plane for test condition A.	B-4
B.2	Flow nonuniformity in the nozzle exit plane for test condition B.	B-4
B.3	Flow nonuniformity in the nozzle exit plane for test condition C.	B-5
B.4	Abel transformation of density field for flow over the blunt faced cylinder at test condition A; Shot T5-819.	B-7
B.5	Abel transformation of density field for flow over the blunt faced cylinder at test condition C; Shot T5-820.	B-8
C.1	Shot T5-855; condition A, $g/D = 2.168$	C-3
C.2	Shot T5-844; condition A, $g/D = 2.128$	C-4
C.3	Shot T5-845; condition A, $g/D = 2.254$	C-5
C.4	Shot T5-849; condition A, $g/D = 2.339$	C-6
C.5	Magnified view of holographic interferogram; Shot T5-849	C-7
C.6	Shot T5-854 (holographic shadowgraph); condition A, $g/D = 2.368$	C-8
C.7	Magnified view of holographic shadowgraph; Shot T5-854	C-9
C.8	Shot T5-846; condition A, $g/D = 2.371$	C-10
C.9	Magnified view of holographic interferogram; Shot T5-846	C-11
C.10	Shot T5-850; condition A, $g/D = 2.396$	C-12
C.11	Magnified view of holographic interferogram; Shot T5-850	C-13
C.12	Shot T5-847; condition A, $g/D = 2.450$	C-14
C.13	Shot T5-848; condition A, $g/D = 2.565$	C-15
C.14	Shot T5-856; condition B, $g/D = 2.185$	C-16
C.15	Shot T5-853; condition B, $g/D = 2.163$	C-17
C.16	Magnified view of holographic interferogram; Shot T5-853	C-18
C.17	Shot T5-852; condition B, $g/D = 2.197$	C-19
C.18	Magnified view of holographic interferogram; Shot T5-852	C-20
C.19	Shot T5-851; condition B, $g/D = 2.281$	C-21
C.20	Shot T5-824; condition C, $g/D = 2.081$	C-22
C.21	Shot T5-840; condition C, $g/D = 1.361$	C-23
C.22	Shot T5-834; condition C, $g/D = 1.485$	C-24
C.23	Shot T5-833; condition C, $g/D = 1.622$	C-25
C.24	Shot T5-825; condition C, $g/D = 1.926$	C-26
C.25	Shot T5-826; condition C, $g/D = 2.036$	C-27
C.26	Shot T5-838; condition C, $g/D = 2.113$	C-28
C.27	Magnified view of holographic interferogram; Shot T5-838	C-29
C.28	Shot T5-831; condition C, $g/D = 2.149$	C-30

C.29 Magnified view of holographic interferogram; Shot T5-831	C-31
C.30 Shot T5-836; condition C, $g/D = 2.162$	C-32
C.31 Shot T5-827; condition C, $g/D = 2.179$	C-33
C.32 Shot T5-837; condition C, $g/D = 2.189$	C-34
C.33 Magnified view of holographic interferogram; Shot T5-837	C-35
C.34 Shot T5-830; condition C, $g/D = 2.198$	C-36
C.35 Magnified view of holographic interferogram; Shot T5-830	C-37
C.36 Shot T5-839; condition C, $g/D = 2.211$	C-38
C.37 Magnified view of holographic interferogram; Shot T5-839	C-39
C.38 Shot T5-829; condition C, $g/D = 2.246$	C-40
C.39 Magnified view of holographic interferogram; Shot T5-829	C-41
C.40 Shot T5-828; condition C, $g/D = 2.274$	C-42
C.41 Magnified view of holographic interferogram; Shot T5-828	C-43
C.42 Shot T5-832; condition C, $g/D = 2.307$	C-44
C.43 Shot T5-835; condition C, $g/D = 2.481$	C-45
C.44 Shot T5-841; condition C, $g/D = 2.620$	C-46
C.45 Shot T5-842; condition C, $g/D = 2.764$	C-47
C.46 Shot T5-843; condition C, $g/D = 3.074$	C-48
C.47 Flow over a $\phi 50\text{mm}$ blunt cylinder without shock impingement. Shot T5-819; condition A.	C-49
C.48 Flow over a $\phi 50\text{mm}$ blunt cylinder with type IV shock impingement. Condition A.	C-50
C.49 Flow over a $\phi 50\text{mm}$ blunt cylinder without shock impingement. Shot T5-820; condition C.	C-51
C.50 Flow over a $\phi 50\text{mm}$ blunt cylinder with type IV shock impingement. Condition C.	C-52
D.1 Optical and mechanical layout of the holographic interferometer.	D-3
D.2 Geometry of hologram reconstruction and conjugate image separation.	D-6
E.1 Asymptotic behavior of a surface temperature sensor.	E-3
E.2 Layout of new surface junction thermocouple sensor.	E-4
E.3 Effective thickness of thermocouple junction.	E-4
E.4 Schematic of amplifier circuit.	E-5
E.5 Stagnation point heat transfer measurement for sphere in hypervelocity flow using dummy Constantan - Constantan thermocouple at condition C.	E-7
F.1 Layout of thermocouple sensors.	F-2
F.2 Arrangement drawing of model support.	F-3

F.3 Shock generator technical details.	F-4
--	-----

List of Tables

2.1	Summary of the free-stream conditions.	15
3.1	Stagnation point fringe shift for type IV flows with cylindrical model.	31
3.2	Comparison of measured heating rates from previous studies.	37
4.1	Constants for IDG model.	54
4.2	Predicted recombination rate parameters for test conditions A, B & C.	74
4.3	Model predictions for condition A.	85
4.4	Model predictions for condition B.	85
4.5	Model predictions for condition C.	86
4.6	Comparison of measured and predicted heat transfer intensification for type IV flows with cylindrical model.	87
4.7	Comparison of measured fringe shift and predicted stagnation density intensification for type IV flows with cylindrical model.	87
B.1	Summary of the free-stream conditions.	B-2
B.2	Verification of ESTC/SURF computations by comparison with simplified IDG/NENZF model.	B-3
B.3	Interferometric verification of the stagnation density.	B-6
B.4	Interferometric verification of the stagnation density using Abel transform methods.	B-7
B.5	Density rise across the impinging shock wave.	B-8
B.6	Experimental verification of the shock standoff distance.	B-9
B.7	Predicted stagnation point Stanton numbers.	B-10
C.1	Physical constants for holographic interferograms.	C-1

Chapter 1 Introduction

1.1 Motivation

The impingement of a weak oblique shock wave on the bow shock ahead of a blunt body in steady supersonic flow is known to cause extremely high local heat transfer rates and surface pressures. This phenomenon represents a severe constraint on the design of hypervelocity vehicles. Korkegi [26] has conducted an extensive review of the literature and discusses the available data from flight test vehicles. A well documented example of the problem occurred during the X-15 flight research program. Damage to the vehicle resulted from the impingement of an oblique shock wave on the leading edge of the lower vertical stabilizer fin (Burcham & Nugent [2]). Shock interactions that occurred in the flow about a model of the X-15 vehicle are illustrated in figure 1.1. The damage sustained by the full scale vehicle (Figure 1.2) demonstrates the need for an improved understanding of the problem. The phenomenon is also observed in vehicles with a delta planform where the bow shock intersects the swept leading edge of the wing. Complex interaction flow fields also arise between vehicles and externally mounted tanks or boosters.

1.2 Description of the phenomenon

The most complete description of the shock impingement phenomenon is that due to Edney [8] [9]. Edney investigated the impingement problem for a variety of model geometries in a blowdown tunnel at Sweden's Flygtekniska Försöksanstalten (FFA). The FFA tunnel provided Mach 4.6 and 7.0 flows of air with maximum stagnation conditions of 625 K and 1.7 MPa through a 200 mm diameter test section. This wind tunnel was equipped with a model injection system that allowed the model to be removed from the test section during the startup process. Edney's investigation arose out of the need to calibrate thin film heat transfer gauges. Anomalous, elevated heat transfer rates were observed as the calibration model was traversed through a spurious shock wave generated at the tunnel wall. Subsequent high quality schlieren cinematography of the controlled injection of models through shocks of known strength, combined with novel heat transfer and surface pressure measurement techniques, allowed Edney to effectively classify the spectrum of interaction regimes.

Consider the impingement of a shock wave on the leading edge of a blunt body as illustrated schematically in figure 1.3. For the compressible flow of a perfect gas a sufficient set of dimensionless

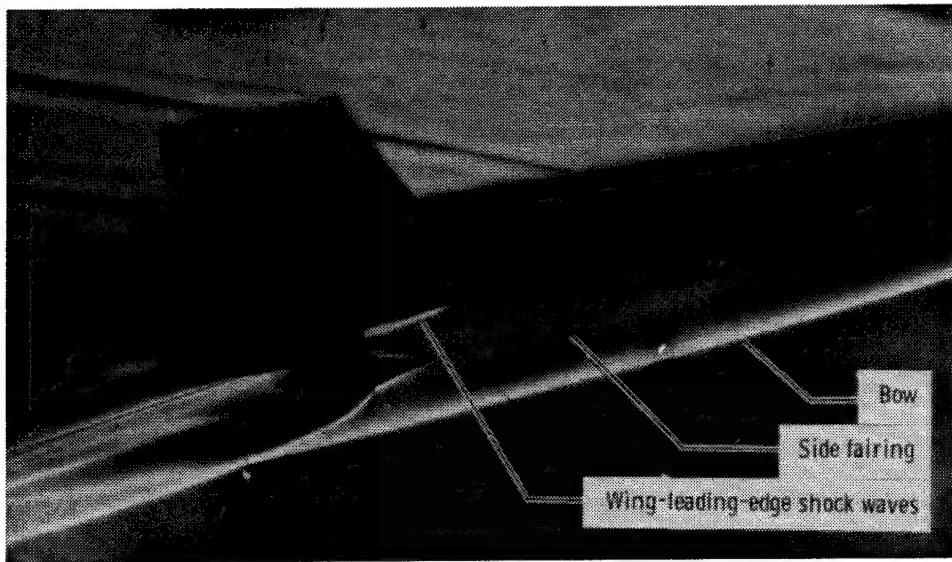


Figure 1.1: Schlieren visualization of the flow field about a model of the X-15-2 vehicle with interference from a scram-jet mounted on the vertical stabilizer (Burcham & Nugent [2]).

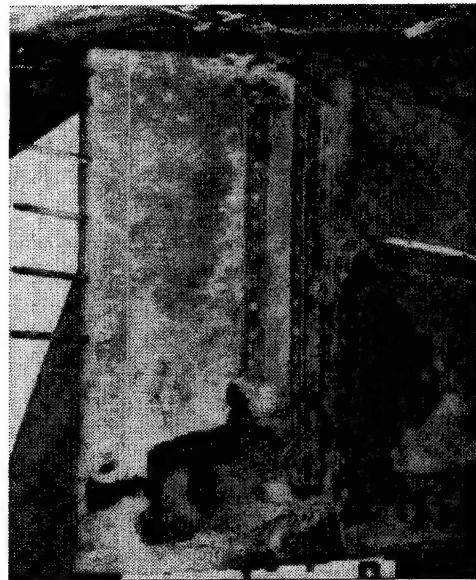


Figure 1.2: Damage to X-15 vertical stabilizer caused by impingement of scram-jet inlet shock wave (Edney [8]).

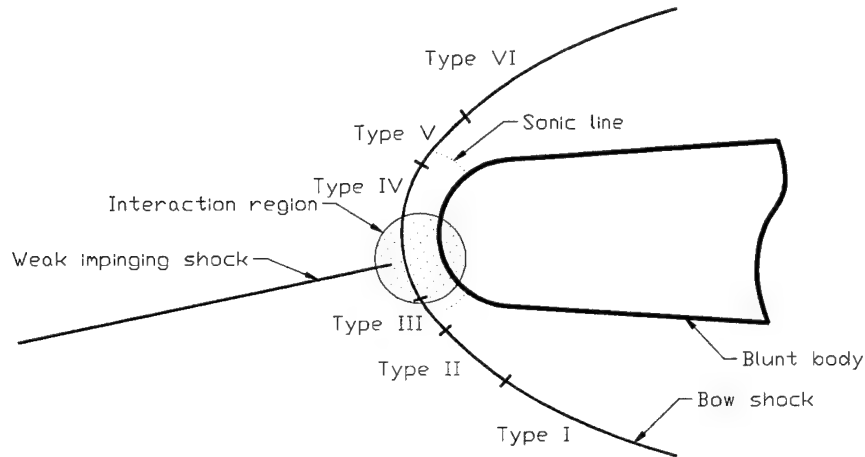


Figure 1.3: Schematic representation of the impingement of an oblique shock wave on the leading edge of a blunt body.

parameters to describe any quantity, ϕ , in the inviscid flow away from the vehicle surface is,

$$\phi = \phi[M_\infty, \gamma, \beta_1, g, \Gamma],$$

where M_∞ is the free-stream Mach number, γ is the ratio of specific heats, β_1 is the angle of the impinging shock wave, g describes the position of the impinging shock wave with respect to the body and Γ is a set of parameters defining the body geometry. Although viscous effects are important at the surface of the body where the heating occurs, the fundamental mechanisms that control the flow will be seen to be of an inviscid nature. In the case of fixed free-stream conditions, impinging shock strength and body geometry the only remaining dependence is the location of the impingement point relative to the body; i.e. $\phi = \phi[g]$. As the incident shock wave is translated relative to the body it potentially intersects with all possible shock strengths of both positive and negative slope. On the basis of an experiment such as this, with spherical and other axisymmetric blunt bodies, Edney [8] [9] observed and categorized six distinct interaction regimes. The interactions, that are known as types I–VI, occur for different locations of the impinging shock wave with respect to the body as indicated in figure 1.3. A review of this method of classification is contained in appendix A.

Severe heating occurs when the incident shock wave impinges in the vicinity of the geometrical stagnation point and a type IV flow results (Figures 1.4 & 1.5). Our discussion will concentrate initially on the type IV flow since the heating rates for the remaining regimes are less intense. A three shock λ -pattern is observed at the point where the impinging shock wave interacts with the bow shock. The interaction produces a strong vortex sheet that separates the upper region of subsonic flow from the lower region of supersonic flow. A second inverted λ -pattern is observed to appear where the strong bow shock continues below the interaction region. Embedding of the supersonic region between the two λ -shocks in the surrounding subsonic shock layer causes the formation of a

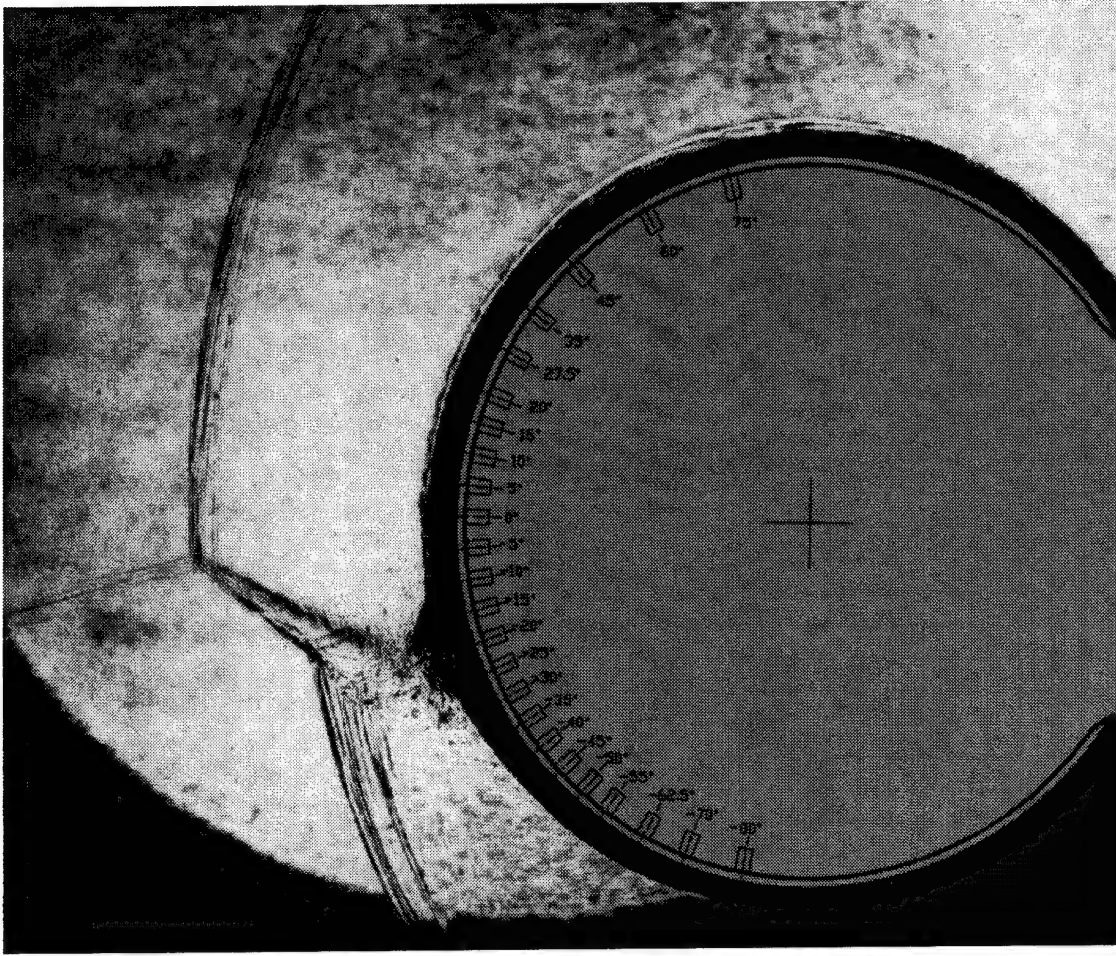


Figure 1.4: Holographic shadowgraph of the impingement of an oblique shock wave near the geometrical stagnation point of a cylinder in hypersonic flow. Following Edney [8], this flow is categorized as type IV.

supersonic jet. Greatly elevated heat transfer rates and surface pressures are observed where the jet impinges on the body.

Figure 1.5 shows the model of the type IV flow field that was originally proposed by Edney [8]. Whilst the global flow field is quite complex, some insight may be obtained by mapping the flow field in the vicinity of the shock wave intersection points into the pressure-flow deflection angle (p - δ) plane (Figure 1.6). In this method the shock interaction solution is represented graphically in the p - δ plane by the intersection of the loci of possible downstream states for each of the interacting waves. Further details of the technique may be found in appendix A. Here it is sufficient to recognize that given only the free stream conditions and the incident shock angle, the intersection of the loci representing states 2 and 3 in figure 1.6 completely determines the wave angles and flow properties at the shock impingement point. Since this fixes the strength of the wave that connects the two λ -points, the solution for states 4 and 5 at the second inverted λ -point is also determined. Note that

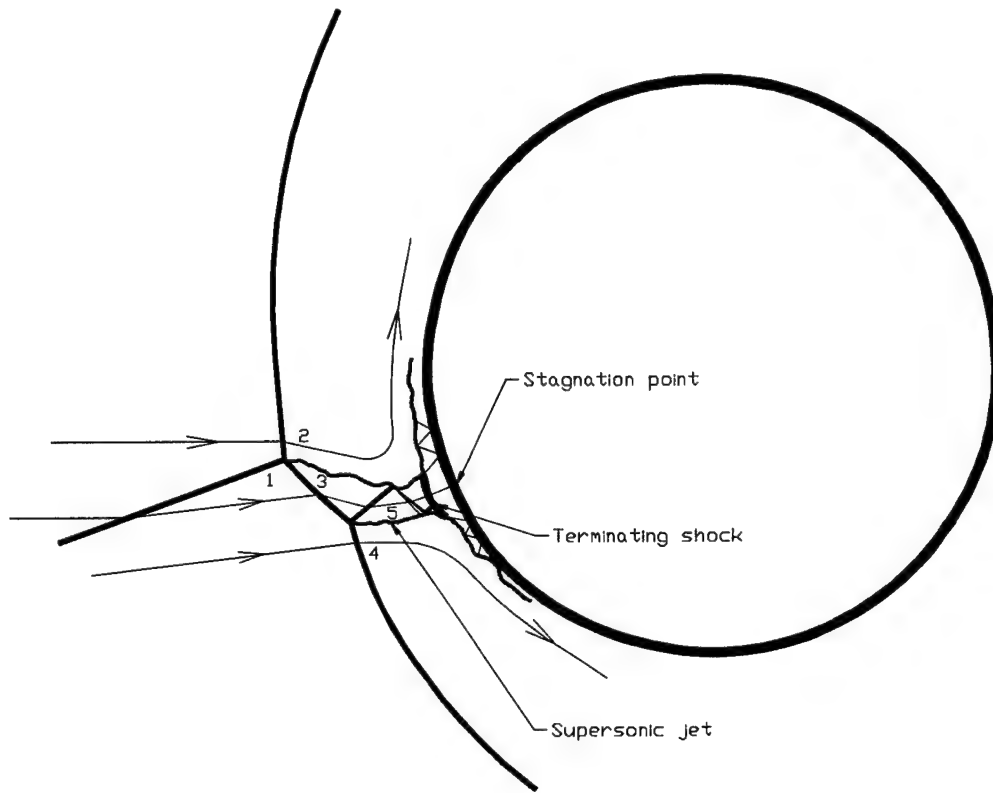


Figure 1.5: Schematic of the type IV shock interference flow field.

the formation of the jet and the state of the gas in it are therefore independent of the interaction of the flow with the body. This represents the fundamental inviscid mechanism that controls the shock impingement heating phenomenon.

Consider next the problem of estimating the pressure loads and heat fluxes at the jet impingement point. In order to estimate these quantities a local model is formulated under the assumption that the oblique waves in the supersonic jet remain straight. This is justified on dimensional grounds. The Mach number of the jet is high so that the inertia of the supersonic flow dominates the pressure forces of the subsonic shock layer. Similarly, the pressures in the subsonic shock layer above and below the supersonic jet are assumed to remain constant. Propagation of the oblique wave, 5, along the supersonic jet proceeds by multiple reflections from the shear layers that are treated as free streamline boundaries. The oblique wave, 5, is initially reflected from the shear layer as an expansion fan so that the constant pressure boundary condition is satisfied. This expansion fan, and all subsequent reflected waves, are assumed to be isentropic in order to compute the state upstream of the terminating strong shock. Specification of the pressure and entropy completely defines this state however the limitations of local modeling prevent exact determination of the pressure. Since the solution for the type IV flow is based on local models that apply only in the vicinity of the shock interactions, the scale of the impingement flow field, the location of the terminating shock

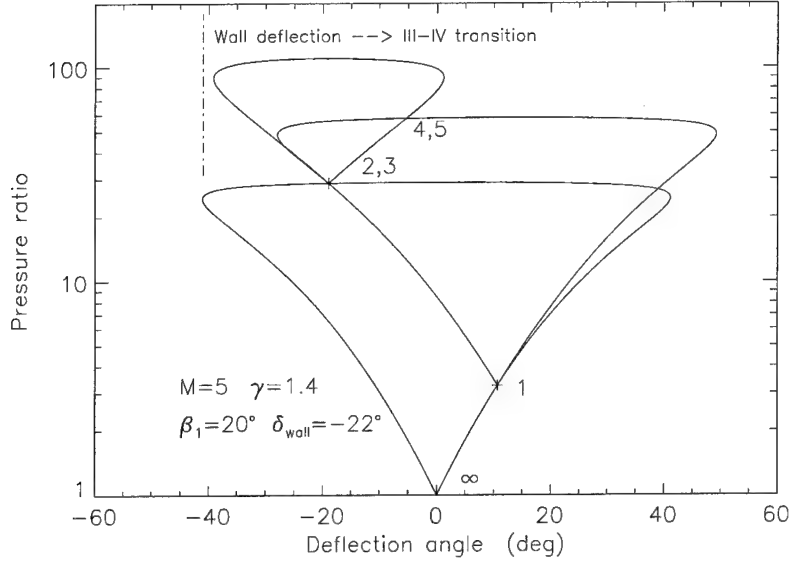


Figure 1.6: Representation of the type IV shock interference flow field in the p - δ plane.

and hence the exact state of the gas upstream of it remain indeterminate. The unknown length scales are determined by the interaction of the jet with the body. Without further knowledge of the number of oblique wave reflections in the supersonic jet, it is only possible to bound the pressure upstream of the terminating shock by the pressures in the subsonic regions above and below the jet. For simplicity, the pressure corresponding to state 5 is assumed for all calculations in the current study.

A portion of the supersonic jet passes both above and below the cylinder and so the stagnation streamline must pass through the supersonic jet (Figure 1.5). Computation of the pressure at the jet impingement point is based on the further assumption that the terminating shock is normal to the distorted stagnation streamline. Whilst stagnation enthalpy is conserved along all streamlines in steady flow, the stagnation density is higher for streamlines that pass through the weak jet shock system than for streamlines that experience a larger entropy rise across the adjacent strong bow shock. The elevated density and the strong velocity gradients produced by the impingement of the supersonic jet provide the mechanism for locally increased heat transfer. Edney [8] used the stagnation point boundary layer solution of Cohen & Reshotko [5] to correlate the heat transfer rate at the impingement point with the peak pressure and body diameter to jet width ratio, $D/\Delta x$;

$$\left(\frac{\dot{q}}{\dot{q}_0}\right)_{peak} \sim \sqrt{\left(\frac{p}{p_0}\right)_{peak} \frac{D}{\Delta x}}. \quad (1.1)$$

Here the peak heat transfer rate and pressure are normalized with respect to the undisturbed stag-

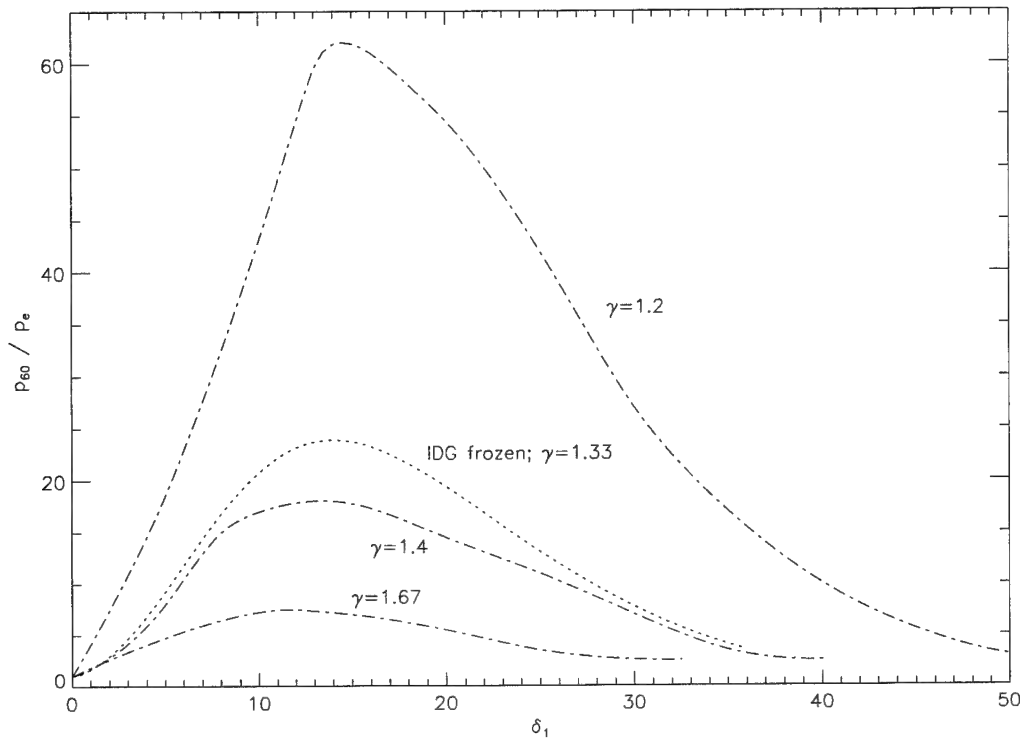


Figure 1.7: RATIO OF JET IMPINGEMENT PRESSURE TO UNDISTURBED STAGNATION POINT PRESSURE AS A FUNCTION OF INCIDENT SHOCK FLOW DEFLECTION ANGLE, δ_1 . — · — curves are for the perfect gas model with $M_\infty = 10$ (after Edney [8]; Figure 7-9). · · · curve is for the IDG model in the frozen limit with $P_\infty = 0.0075$ and $\alpha_\infty = 0$.

nation point values. The pressures that appear in equation 1.1 are determined from the local type IV solution in the p - δ plane.

Curvature of the supersonic jet is observed in experimental investigations of the type IV flow. We have noted that the strength of the oblique wave, 5, is determined entirely by the free stream conditions and the strength of the incident shock. The strength of this wave controls the pressure difference that exists between the subsonic regions above and below the interaction. It follows that the pressure gradient across the jet, and hence its curvature, vary inversely with the width of the jet.

The preceding discussion summarizes the mechanisms that control the shock impingement heating phenomenon. The key conclusion is that a non-linear interaction of the shock waves at the impingement point leads to the formation of a supersonic jet that is embedded in the surrounding subsonic shock layer. This inviscid jet formation process is local in nature and is independent of the interaction of the jet with the body. Elevated pressure loads and heat transfer rates are produced by the impingement of the low entropy jet fluid on the surface of the body.

1.3 Real gas effects

Dimensional analysis of the inviscid reacting flow away from the surface of a hypervelocity vehicle leads to three parameters involving the velocity;

$$M = \frac{u_\infty}{a_f} \quad K = \frac{mu_\infty^2}{k\theta_d} \quad \Delta = \frac{\frac{d\alpha}{dt}D}{u_\infty}, \quad (1.2)$$

where u_∞ is the velocity of the vehicle, a_f is the frozen speed of sound, k is Boltzmann's constant, θ_d is a temperature characterizing the energy of the dissociation reaction, $\frac{d\alpha}{dt}$ characterizes the reaction rate and D is some characteristic dimension of the vehicle. For the case of a vehicle traveling at near orbital speeds the Mach number, M , is large and strong shock waves will be dominant features of the flow. Oxygen and nitrogen dissociation occur at specific kinetic energies of approximately 17 MJ/kg and 34 MJ/kg respectively and so strong dissociation will occur in the flow about the vehicle. This influence on the equilibrium equation of state is expressed by the dimensionless specific kinetic energy, K . The dissociation rate parameter, Δ , which is equivalent to the Damköhler number in related chemical kinetics problems, expresses the finite length over which the reactions occur relative to the size of the vehicle. The reaction rate parameter will increase from zero for a vehicle in orbit to very large values at low altitudes. Since the rates of dissociation reactions scale with the density of the flow, finite rate chemical reactions become coupled with the gas dynamics at some intermediate condition where $\Delta \sim 1$.

By mapping the type IV flow field into the p - δ plane, as discussed in section 1.2, Edney [8] was able to compute the variation of the pressure at the jet impingement point for various free-stream conditions. Figure 1.7 shows the ratio of jet impingement pressure to undisturbed stagnation point pressure as a function of the flow deflection angle across the incident shock, δ_1 , and the ratio of specific heats, γ . The peak pressure initially increases with impinging wave strength before reaching a maximum for moderate strength waves. Significant real gas effects are suggested by the increase in the peak pressure with decreasing ratio of specific heats. Edney [8] showed that the peak pressure also increases strongly with increasing free-stream Mach number.

Although the variable γ model provides only a crude estimate of the influence of equilibrium real gas effects, figure 1.7 provides strong motivation for further study of the problem in high enthalpy test facilities. The primary effect of dissociation reactions on blunt body flows at large values of the flow specific kinetic energy, K , is to increase the density of the gas in the shock layer. Since shock standoff distances vary inversely with the shock layer density, equilibrium real gas effects must be expected to influence the length scales of the type IV interaction flow field.

In the nonequilibrium regime, where $\Delta \sim 1$, a thermochemical length scale is introduced into the problem. Nonequilibrium phenomena are most pronounced in regions of a flow field where discontin-

uous changes in the thermodynamic variables produce large deviations from chemical equilibrium. A familiar example is the relaxation that occurs downstream of the bow shock ahead of a blunt body (Hornung [19]). The disparate shock strengths produced at the two mutually inverted λ -shocks in the type IV flow must therefore be expected to produce strong nonequilibrium effects. Figure 1.8 indicates the possible real gas influences on a λ -shock intersection point. The three shock waves produce widely differing dissociation levels and reaction lengths. Variations in the relative magnitudes of the thermochemical and fluid mechanical length scales introduce effects that are not encompassed by existing models.

Figure 1.8 illustrates an additional effect on the shear layers that are generated at the λ -points. Energy that is released by mixing of the dissociated low speed fluid with the lower temperature supersonic fluid influences the density of the shear layer mixture. Although this effect is not addressed by the current study, turbulent diffusion must become significant when the jet width is small relative to the shock standoff distance.

Despite the inviscid nature of the mechanisms that control the flow, real gas effects also influence the viscous flow in the boundary layer that forms at the jet impingement point. Recombination occurs in the boundary layer because the wall temperature is low and, in the immediate vicinity of the jet impingement point, the behavior parallels that of the classical blunt body problem. Fay & Riddell [11] showed that when the recombination rate in the boundary layer is large,

$$\dot{q} \sim \sqrt{\rho_e \mu_e \left. \frac{du_e}{dx} \right|_0} h_0.$$

Here \dot{q} is the heat transfer per unit area and time, ρ_e , μ_e and $\left. \frac{du_e}{dx} \right|_0$ are the density, viscosity and transverse velocity gradient respectively at the outer edge of the boundary layer. Jet impingement does not influence the total enthalpy at the stagnation point, h_0 , since stagnation enthalpy is conserved at all points in steady flow. This also implies a limited influence on the viscosity, μ_e , since for diatomic gases $\mu_e \sim T_e^{0.7} \sim h_0^{0.7}$. The most important real gas influences on the stagnation point flow are therefore the increased density of the outer flow, ρ_e , and the coupled effect on the velocity gradient. Continuity implicitly couples the density and velocity gradient at the edge of the boundary layer. Finally, note that shock impingement greatly increases the recombination rates in the boundary layer since these scale with the square of the density intensification at the jet impingement point.

We conclude that both equilibrium and finite rate real gas effects may be expected to exert a significant influence on the type IV interaction flow field. Shock impingement was shown to produce elevated pressures, and hence densities, at the jet impingement point. A broad range of possible influences arise as a consequence of the strong interdependence of real gas effects and density.

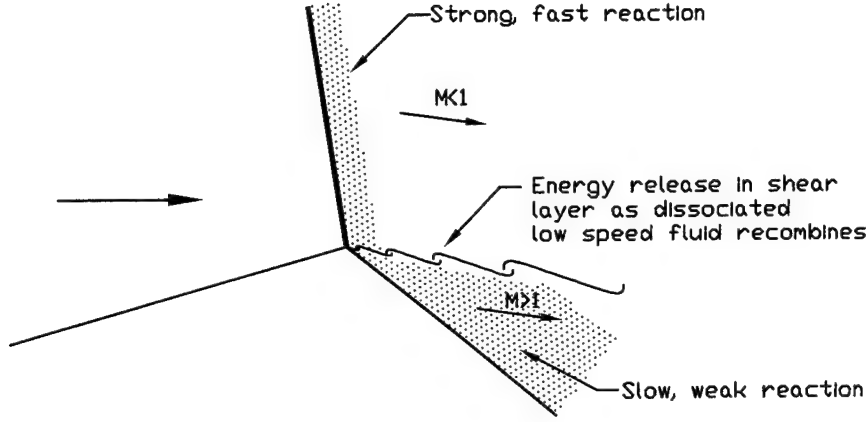


Figure 1.8: Real gas effects at a λ -shock intersection point.

1.4 Literature review

Before proceeding we wish to note additional important contributions to the literature. The need for an improved understanding of the shock impingement phenomenon motivated some of the earliest investigations that were summarized by Keyes & Hains [24]. Early investigations provided flow visualization and surface measurements for a variety of configurations, however these works failed to elucidate the fundamental mechanisms of the problem. The utility of the data that were obtained was limited by the large number of parameters involved and restricted spatial and temporal resolution of the sensors. Edney [8] discussed early attempts at modeling such as the acoustic disturbance model of Fontenot [12], the vorticity model of Francis [13] and the boundary layer model due to Hiers & Loubsky [18]. These were based on limited observations and the physical models that were utilized now appear to be inadequate. Keyes & Hains [24] reported experiments that further advanced the work of Edney [8] and conducted a parametric study of the heat transfer rates predicted by Edney's models.

Hiers & Loubsky [18] conducted experiments in a shock tunnel at enthalpies sufficient to produce vibrational excitation and limited oxygen dissociation in air however the results did not demonstrate any conclusive trends with enthalpy. Wieting & Holden [48] have conducted a recent experimental study and obtained data on the influence of Reynolds number, Mach number and shock strength variations at modest enthalpies. Kortz [27] and Kortz, McIntyre & Eitelberg [28] report on a recent experimental investigation conducted at enthalpies sufficient to cause significant nitrogen dissociation in the DLR HEG free piston shock tunnel. This work included the first quantitative interferometric visualization of shock impingement flows. Elevated heat transfer rates were not observed for the

range of parameters that were investigated and this appears to have resulted from a relatively coarse variation of the shock impingement location.

Progress in the development of monotonicity preserving shock capturing algorithms is evident in recently reported numerical studies of the shock impingement problem. Shock interference flow fields are simulated by the provision of an inflow boundary condition ahead of the blunt body that accounts for the discontinuity across the impinging shock. Tannehill & Holst [43] produced one of the earliest attempts at such a simulation however the results exhibited excessive numerical diffusivity. Recent applications of monotonicity preserving algorithms such as those of Klopfer & Yee [25] succeeded in capturing the gross features of the mean flow field. The unstructured adaptive meshing techniques employed by Vemaganti [44] provided remarkable resolution of the internal structure of the impinging jet for the type IV flow field. Vemaganti [44] used turbulence models to simulate the effect of the shear layers generated at the shock intersection points on the surface heat flux. The effect of finite rate chemical reactions was considered by Hannemann et al. [16] who simulated the experimental results reported by Kortz et al. [27] [28]. These computations indicated the persistence of the type IV behavior for shock impingement locations intermediate to those discussed by Kortz et al. . Kinetic theory based simulations of the shock impingement problem that were reported by Carlson & Wilmoth [3] represent an unusual application of DSMC methods. Results were presented for the variation of species concentrations across the shock layer and the impinging jet for a non-catalytic wall. An additional recent contribution is that of Yeung & Hall [49] who discussed differences in the computed flow fields about spherical and cylindrical models.

Numerical simulations of the mean flow fail to reproduce the unsteady flow features that are observed in the experimental data (Figure 1.4). The potential instabilities include those of the shear layers generated at shock intersection points and oscillations of the jet structure itself. Edney [8] noted oscillations that were observed in the jet impingement study of Henderson [17] but did not observe any analogous fluctuations of the type IV jet. Jet oscillations appeared in the computations of Prabhu et al. [36] and Gaitonde [15] where limit cycle oscillations were observed in the computational residual as the mesh was adaptively refined. Gaitonde [15] addressed the issue of time accuracy of the algorithms that were used and concluded that the oscillations were attributable to the physics of the problem. Similar conclusions may be drawn from the results of Zhong [50] who also obtained time accurate solutions for the jet fluctuations using essential non-oscillatory (ENO) schemes. The possibility of coherent fluctuations of the impinging jet restricts the gains attainable by adaptive meshing if extremely high resolution is required since the regions of grid refinement become dynamic. Despite these difficulties the numerical solutions are of great pragmatic value since they appear capable of providing the mean flow data necessary for the application of correlations for the sub-grid behavior.

The paucity of the existing data in the hypervelocity regime and the importance of the phe-

nomenon provide strong motivation for further study of the problem.

1.5 Scope of the current study

The objective of the present work is to determine the quantitative effects of thermochemistry on the shock impingement phenomenon. Models that were advanced by Edney [8] suggest that increases of the Mach number and reductions in the ratio of specific heats should produce strong increases in the peak heat transfer rates. Systematic experimental or parametric numerical studies to investigate these predictions have yet to appear. The current work consists primarily of an experimental investigation of the shock interaction problem that utilizes the capabilities the GALCIT T5 hypervelocity shock tunnel.

The variable γ model used by Edney [8] represents only a crude estimate of the influence of flow thermochemistry. The foregoing survey identifies a number of potentially significant mechanisms by which equilibrium and finite rate real gas effects may influence the shock interaction phenomenon. This work aims to develop models of these mechanisms and provide quantitative predictions of the influences of the controlling parameters.

In that the work of Edney [8] was made possible by effective instrumentation, a significant preliminary goal of the current study was to develop effective diagnostic techniques for use in the extreme conditions that occur in high enthalpy test facilities. This included the development of surface heat transfer gauges, differential and holographic interferometry, high speed data acquisition electronics and novel flow models. These topics are discussed further in the appendices.

Chapter 2 Experimental program

2.1 Description of the T5 hypervelocity shock tunnel

The experimental program was based upon the capabilities of the T5 free piston driver shock tunnel that has recently been constructed at GALCIT. Dimensional analysis of the inviscid flow away from the surface of a hypervelocity vehicle leads to three parameters (Equation 1.2) involving the velocity;

$$M = \frac{u_\infty}{a_f} \quad K = \frac{mu_\infty^2}{k\theta_d} \quad \Delta = \frac{\frac{d\alpha}{dt}D}{u_\infty}. \quad (2.1)$$

These dimensionless parameters express the requirements for similitude in a ground testing facility. With the same test gas the velocities of the full-scale and sub-scale flows must be matched in order to achieve the correct scaling, K , of the flow specific kinetic energy with respect to the dissociation energy. This requirement for high velocities implies that the facility stagnation temperature must be large; typically 10000 K to achieve enthalpies equivalent to low earth orbital velocities. High densities are required for similarity of the reaction rate parameter, Δ , with sub-scale models since the rates of dissociation reactions are proportional to the density. For typical vehicle flight trajectories this implies a nozzle reservoir pressure approaching 100 MPa.

The development of free piston driver shock tunnels, by Stalker [41] and coworkers, has enabled the simulation of these dimensionless parameters in the laboratory. Shock tunnels of this type are unique in their ability to produce the high densities necessary for simulation of both the kinetic energy, K , and the reaction rate parameter, Δ . The T5 facility is illustrated schematically in figure 2.1. High enthalpy and high pressure stagnation conditions are achieved in the nozzle reservoir by shock heating the test gas as in a conventional reflected mode shock tunnel. In order to achieve a sufficiently high shock speed at high pressures, the speed of sound of the driver gas is raised by adiabatically compressing helium to 100 MPa and 3000 K with a single stroke of a reusable compressed air driven piston. Further details of the performance and construction of this complex facility are given by Hornung, Sturtevant, Belanger, Sanderson, Brouillette & Jenkins [23].

2.2 Test conditions

Three different test conditions were used and these are summarized in table 2.1. The first case, A, represents a low enthalpy control condition where the only real gas effects were a partial excitation of the vibrational modes in the stagnation regions of the flow. Case C represents a high enthalpy

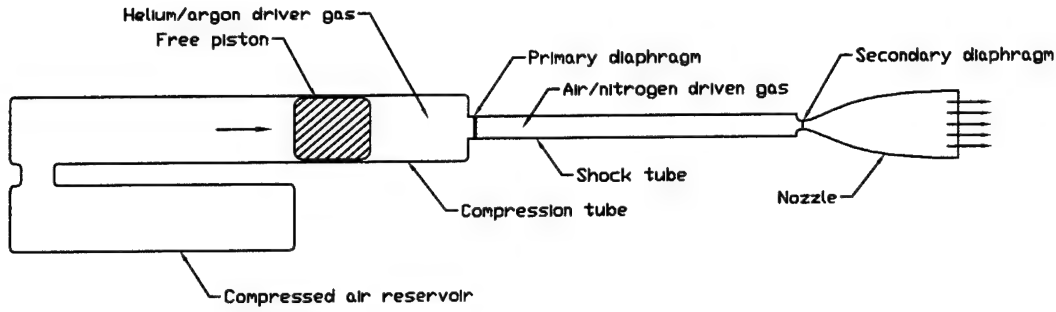


Figure 2.1: Schematic representation of the T5 free piston driver shock tunnel.

condition that was chosen to highlight the influence of nonequilibrium thermochemistry on the problem. Case B is an intermediate enthalpy condition that was designed to aid interpretation of the differences in the flow mechanisms for cases A and C. Nitrogen test gas was used for all experiments. Air was considered too aggressive for prolonged model life with shock impingement.

Appendix B contains an assessment of the flow quality and the accuracy of the test condition predictions. This assessment comprises two-dimensional nonequilibrium nozzle flow computations, interferometric stagnation density measurements using Abel transform methods to eliminate end effect errors, reacting flow shock standoff distance correlations, stagnation point heat flux measurements and frozen oblique shock density comparisons. The conclusion of these comparisons was that the Mach number is over-predicted for test condition A. This was attributed to nozzle flow nonuniformity at low enthalpy off design conditions. Condition B was very accurately confirmed by all the experimental measurements. Condition C produced blunt body shock layer densities that were somewhat less than the predictions. Contamination of the test gas with the helium-argon driver gas mixture is known to become limiting in shock tunnels at high enthalpy conditions. It was not possible to measure this contamination directly with the apparatus used in the present experiments. Although indirect measurements that are discussed in appendix B demonstrate some anomalies, the data reported here remained temporally constant and self consistent early during the test time. These data agree tolerably well with established theories. Flow contamination that was detectable with the current instrumentation did not become apparent until times beyond the period of test flow that was used to obtain the data.

Differing helium-argon driver gas mixtures were used at the three enthalpies to achieve tailored interface operation. In this condition the nozzle reservoir pressure and stagnation point heat flux remained temporally constant to within $\pm 10\%$ during the test time. Uniform conditions were maintained for 1.25 ms at condition C and in excess of 5 ms at condition A.

Test condition		A	B	C
Shock tube conditions	Fill pressure (kPa ± 0.5 kPa)	75	32.5	20
	Fill temperature (K ± 4 K)	297	297	297
	Shock speed (m/s)	1890 ± 100	3500 ± 245	4360 ± 255
Nozzle reservoir conditions	Pressure (MPa)	14.6 ± 0.7	22.3 ± 1.3	28.3 ± 1.9
	Temperature (K)	3210	7550	8960
	Enthalpy (MJ/kg)	3.88	12.0	19.1
Test section conditions	Velocity (m/s)	2540	4450	5350
	Density (kg/m ³)	0.0218	0.0155	0.0157
	Pressure (kPa)	1.03	5.48	11.4
	<i>N</i> concentration (mole/kg)	9.9×10^{-5}	6.9×10^{-1}	3.65×10^0
Test section dimensionless parameters	IDG P_∞	7.32×10^{-3}	1.79×10^{-2}	2.54×10^{-2}
	IDG $H_{0\infty}$	0.102	0.346	0.560
	IDG α_∞	1.4×10^{-6}	9.7×10^{-3}	0.051
	IDG $\hat{\rho}_d$	6.0×10^6	8.4×10^6	8.3×10^6
	IDG Δ per mm	$4. \times 10^{-13}$	3.4×10^{-2}	0.525
	Re per mm	5540	1630	1350

Table 2.1: SUMMARY OF THE FREE-STREAM CONDITIONS. Test conditions were computed on the basis of measurements of the initial shock tube fill pressure and temperature, incident shock speed prior to reflection, and nozzle reservoir pressure after shock reflection. The dimensionless parameters for the ideal dissociating gas (IDG) model are defined in section 4.2. Error estimates given for the fill conditions represent the accuracy of the pressure gauge and the variation of the ambient temperature. Error estimates for the measured shock speed and reservoir pressure are the standard deviation of the quantities sampled over the entire sequence of shots. The error in the computed quantities may be inferred from these estimates.

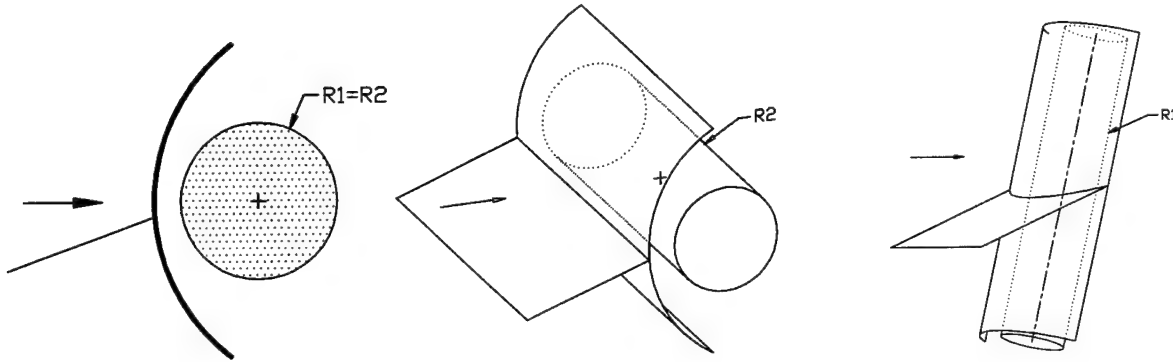


Figure 2.2: Abstracted model geometries for the shock impingement problem.

2.3 Description of experiment

2.3.1 Abstraction of the problem

If a blunt body is characterized by two principal radii of curvature at the stagnation point, R_1 and R_2 , then it is reasonable to consider the following simplified cases (Figure 2.2) as abstractions of the complex shock impingement flows that occur about flight vehicles;

1. Spherical body with $R_1 = R_2$.
2. Cylindrical body, with $R_1 \rightarrow \infty$, oriented normal to the free-stream flow direction and parallel to the plane of the incident shock wave. This is a two-dimensional flow field.
3. Swept cylindrical fin, with $R_2 \rightarrow \infty$, lying in the plane defined by the free-stream flow direction and the normal to the incident shock surface.

Each of these cases exhibits a single geometrical degree of freedom in the location of the impinging shock wave. In cases 1 and 2 this is the vertical displacement of the incident wave with respect to the model. If the fin of case 3 is so long that the flow is cylindrically symmetric far away from the ends, the sole geometric dependence of the flow is the sweep angle of the fin.

The experiments described in this report were intended to test models of the influence of thermochemistry on the local behavior near the impingement point and the manner in which this influences the global flow about the body. The local models are rigorous in nature whereas the global flow models represent interpretations of the flow structure. Whilst these topological considerations are qualitative in nature, the streamline patterns that are used to describe the shock interaction flow fields must be kinematically admissible. This aspect has been somewhat neglected in previous studies of the phenomenon.

2.3.2 Discussion of the flow topology

Consider the model of the type III flow field that is shown in figure A.5. On the basis of an analogy with the flow over a backward facing step, heating was presumed to occur at the point where the shear layer attaches to the body (Edney [8]). The two flows are topologically equivalent only in the extraordinary case where the stagnation streamline coincides with the shear layer. For all other cases the analogy violates the continuity equation in the absence of the upstream separation event that occurs in the flow over a step. A large mass flux enters the shock layer across the bow wave whereas the mass contained in the recirculation region downstream of a backward facing step is constant.

Similar difficulties arise in the interpretation of the type IV model as the incident shock wave moves upward. This causes the width of the supersonic jet to decrease and its curvature to increase. Impingement of the type IV jet requires that the stagnation streamline pass through it. Since the width of the jet is small, this can occur for only a limited range of locations of the impinging shock wave. Again, continuity prohibits the impingement of the jet if a stagnation point is presumed to exist at some other point on the body.

Despite the different characteristics of the type III and IV flows, the topological concerns are identical in both cases. We conclude that attachment of the disturbance generated by shock impingement is possible only in the seemingly extraordinary case when the type III shear layer coincides with the stagnation streamline and for the limited cases when the stagnation streamline passes through the type IV jet.

2.3.3 Critical points in the streamline patterns

The anomalies that are noted above appear to arise from a two-dimensional interpretation of line of sight integrated images of a three-dimensional flow field. From these images the shear layer or type IV jet away from the axis of symmetry appears to meet the surface at a finite angle as it passes around the three-dimensional model. There exist alternate three-dimensional surface flow patterns that can reconcile the difficulty.

All three abstracted configurations that are considered here exhibit a plane of symmetry. Streamlines are necessarily contained in this plane in which the out-of-plane velocity is zero. Streamlines are also locally contained in the plane tangential to surface at any given point on the body. In the vicinity of a critical point, where the in-plane velocities vanish and the streamline direction is indeterminate, the kinematical problem in planes that contain streamlines reduces to a pair of coupled autonomous ordinary differential equations;

$$u_i = \frac{dx_i}{dt} = B_{ij}x_j + O(x_j^2) \quad i = 1, 2 \quad j = 1, 2. \quad (2.2)$$

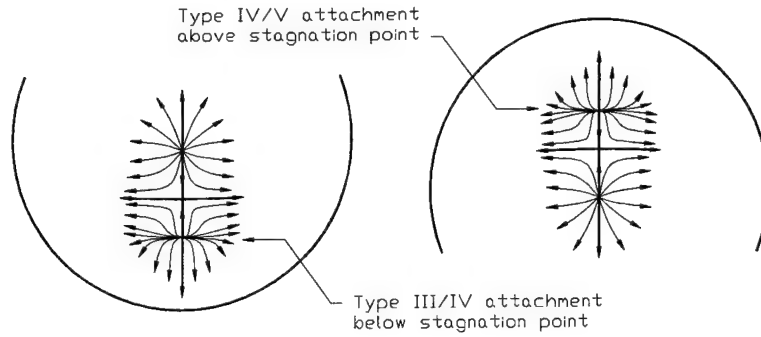


Figure 2.3: Surface streamlines for shear layer/jet attachment in the flow over a spherical body.

The coefficients, B_{ij} , are determined by substituting the expansion into the equations of motion. Here we consider only inviscid streamline patterns so that higher order terms of the expansion may be neglected. For the purposes of the immediate discussion it is sufficient to recognize that all possible critical points in the streamline patterns are described by the node, saddle, focus and center type solutions of equation 2.2. The form of each critical point is determined by the eigenvalues of B_{ij} . The terminology that is used in this description is based on the approach of Perry & Chong [35].

Consider first the impingement of an oblique shock wave onto a spherical model. The apparent contradiction of continuity is resolved if a saddle point is assumed to form in the surface streamline pattern between the nodes at the stagnation point and shear layer / jet attachment point (Figure 2.3). This interpretation is consistent with the surface oil flow visualization of Keyes & Hains [24] and the computations of Yeung & Hall [49] who observed that the velocity vanished at three points along the centerline for a spherical body. In the plane of symmetry, the stagnation point and shear layer / jet attachment point appear as saddle points (Figure 2.4). The intermediate critical point may be either a reattachment node or a separation saddle. The local buildup of oil observed near the middle critical point in the results of Keyes & Hains [24] supports the separation hypothesis. In this case a focus must be inserted away from the surface of the body to match the flow entering the shock layer (Figure 2.4). Streamlines away from the plane of symmetry spiral around the streamline that emerges out of the plane from the center of the focus. When inverted, the streamline pattern shown in figure 2.4 also describes the impingement of the type IV jet above the stagnation point. We conclude that the coexistence of a stagnation point and an impingement point on a three-dimensional blunt body leads directly to the formation of a saddle point in the surface streamline pattern and a spiral vortex that wraps around the body.

Symmetry prohibits the formation of a saddle in the surface streamline pattern in the two-dimensional shock impingement problem and so only a single critical point can exist on the forebody. The important conclusion is that either the stagnation point and the type III shear layer attachment / type IV jet impingement point must coincide exactly, or that attachment / impingement

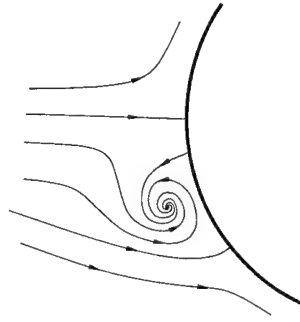


Figure 2.4: Streamlines in the symmetry plane showing the formation of a spiral vortex as a consequence of shear layer/jet attachment.

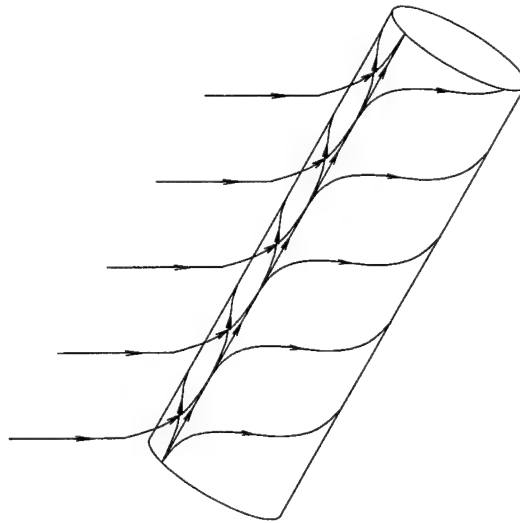


Figure 2.5: Streamline pattern for a cylindrically symmetric swept fin.

does not occur. If the type III shear layer or type IV jet disturbance does not coincide with the stagnation streamline then it must convect past the surface and remain at a finite distance from it far downstream. This is in direct contrast to the surface streamline pattern for the undisturbed cylindrically symmetric flow over a swept fin that is shown in figure 2.5. The pattern follows from the addition of a constant transverse velocity component to the two-dimensional flow field about a cylinder. Observe that all streamlines in the symmetry plane reach the surface where they arrive and depart tangentially from the bifurcation line that runs the length of the cylinder. The conclusion is that disturbances asymptote to the surface for a wide range of impingement locations and sweep angles. Although shock impingement disturbs these symmetries, the trends provide some insight. Finite length cylinders with an impinging wave are strictly topologically equivalent to the spherical case.

2.3.4 Application of holographic interferometry

Holographic interferometry provides a tool for directly measuring the location of the stagnation point and any separation regions in planar flow. Abel transform techniques are not applicable in the presence of shock impingement since the flow about an axisymmetric body becomes fully three-dimensional. Maxima in the fringe shift of the interferogram correspond to the saddle point and center type features that are admissible for two-dimensional flow. This interpretation remains approximately valid in the presence of shock induced vorticity if the velocity gradient near a critical point in the velocity field remains large with respect to the entropy gradient (appropriately normalized). Species concentration gradients also affect this interpretation in reacting flows. The technique remains valid when the maxima of density and dissociation level coincide since the refractivity of nitrogen atoms is larger than that for the molecules. Since density measurements are sensitive to real gas effects, holographic interferometry provides quantitative data that are valuable for discriminating investigations of the problem.

2.3.5 Summary

For the reasons outlined above, the majority of the experiments that are described in this report have concentrated on the nominally two-dimensional mean flow associated with the impingement of an oblique shock wave on the leading edge of a coplanar cylinder. This enabled investigation of the simplest possible flow topology under conditions where it was possible to directly observe the behavior.

2.4 Apparatus

2.4.1 Test section arrangement

The experimental arrangement is shown in figure 2.6. High temperature and pressure gas was generated in the nozzle reservoir by the T5 hypervelocity free piston shock tunnel. The gas was expanded into the test section using a contoured axisymmetric nozzle with an area ratio of 109 and an exit diameter of 315 mm. The model was positioned in the free jet test section through which the test gas exhausted into an evacuated dump tank. A large shock generator was partially inserted into the uniform nozzle core flow that extends upstream of the nozzle exit plane. Variations in the shock impingement flow field were investigated by vertically translating the model with respect to the exit of the shock generator. Care was taken to ensure that the nozzle exit expansion fan and separated shock generator boundary layer did not corrupt the flow about the model. A holographic interferometer was used to visualize the shock waves and figure 2.7 shows the vertical arrangement of the U-shaped interferometer enclosure about the test section. Optical access was available through

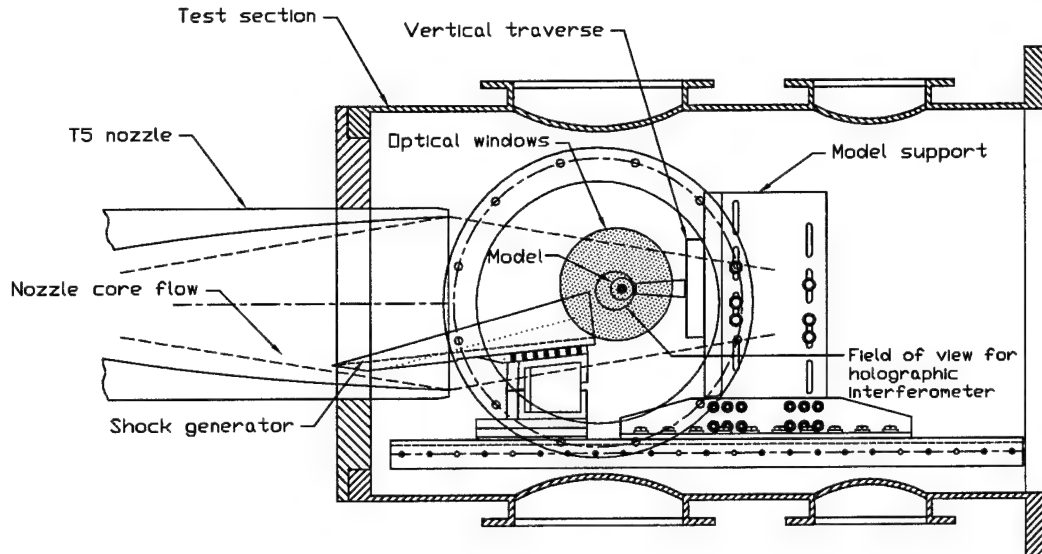


Figure 2.6: Layout of apparatus in the test section of T5.

two $\phi 200 \text{ mm} \times 40 \text{ mm}$ BK7 glass windows that were mounted to flanges on the sides of the test section. Figure 2.6 is an accurate scale drawing of the arrangement. All apparatus was mounted symmetrically with respect to the centerline in the third dimension that is not shown.

2.4.2 Alignment accuracy

The model, shock generator and holographic interferometer were aligned with respect to the nozzle exit within $\pm 1 \text{ mrad}$ about all three axes. Beam divergence of approximately 2 mrad for the NdYAG laser light source obviated the need for greater alignment accuracy. Optical alignment was performed by reflecting the interferometer beam from a mirror attached to a flat reference surface on the end of the cylindrical model. Care was necessary here to ensure that flow features close to the wall of the cylinder could be accurately resolved. The positional accuracy of the test section apparatus was estimated to be $\pm 5 \text{ mm}$ in all three coordinate directions. The vertical position of the model, which controlled the shock impingement location, was repeatable with a relative accuracy of $\pm 0.04 \text{ mm}$.

2.4.3 Description of model

Large diameter models were desirable in order to resolve the fine flow structure and to achieve conditions of thermochemical nonequilibrium at moderate pressures. Low pressure operation produces excellent flow quality in the T5 shock tunnel if the tube and test section are cleaned adequately between shots. A cylinder with aspect ratio 4.5 provided the largest possible model that adequately approximated a two-dimensional flow (Sykes [42]). Optimization of the arrangement within the geometrical constraints imposed by the nozzle diameter, nozzle exit expansion fan, shock generator and

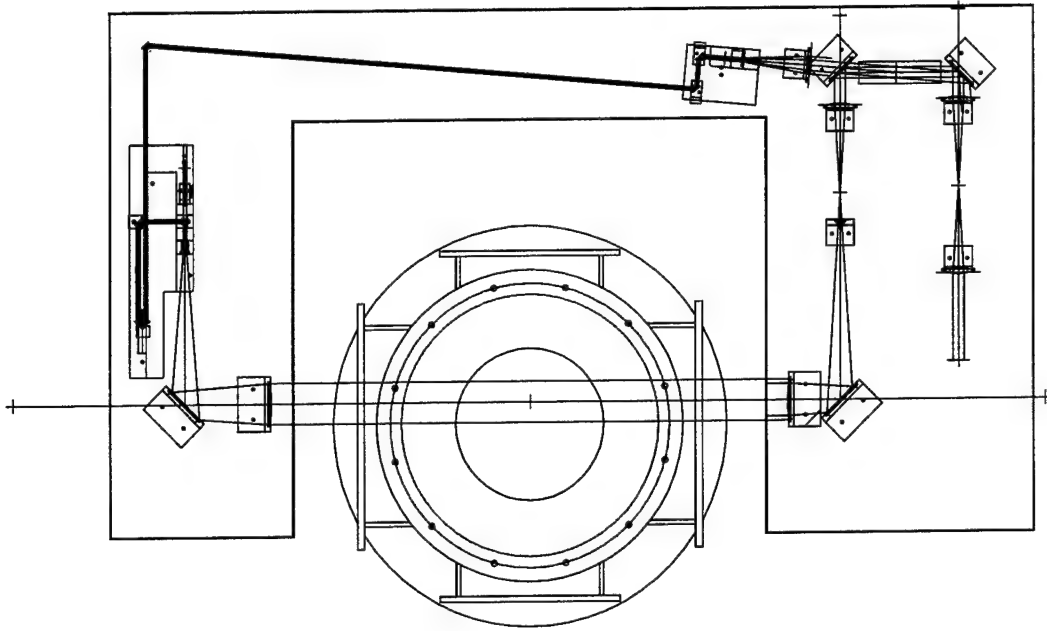


Figure 2.7: Arrangement of the optical apparatus with respect to the test section.

optical access led to the design indicated in figure 2.6 and a model diameter of 40 mm (Figure F.1). The model support shown in figure F.2 allowed precise vertical translation of the model to study the effect of different shock impingement locations. A cavity, internal to the model support, contained preamplifiers for the model instrumentation. This cavity and all components of the model were sealed from the external flow with O-rings and vented to the atmosphere through pressure tubing attached to the rear of the model support. This unusual feature contributed to signal quality by isolating the instrumentation from the test section gases. Glands allowed the pressure tubing, which also served as an instrumentation wiring conduit, to pass through the wall of the test section.

2.4.4 Instrumentation

Sensors were available to monitor all of the operating parameters of the T5 facility and determine the free-stream conditions in the test section. Piezo ceramic pressure transducers installed along the length of the shock tube were used to monitor the speed of the incident and reflected shock waves and the pressure in the nozzle reservoir.

Thermocouple gauges were used to record the surface temperature at 24 circumferential locations around the model forebody. The gauges were staggered in three planes arranged symmetrically with respect to the centerline to achieve maximum resolution (Figure F.1). Additional thermocouple ports were provided at the rear of the body however these were not used for the experiments described here. The sensitive area of the gauges subtended an angle of 2° at the center of the cylinder and were spaced at 5° intervals in the most densely instrumented portion.

Differential thermocouple preamplifiers (Figure E.4) were housed inside the test section to provide noise levels of $-35 \rightarrow -55$ dB depending on the signal level and gain setting. The lower figure reflects the need to provide headroom for the anticipated intense heat transfer rates. Mean square optimal spectral deconvolution techniques were used to infer time resolved heat transfer rates from the surface temperature data. Details are given in appendix E along with a description of the novel gauge design that was used to ensure adequate high frequency response. The signals were digitized with ± 11 bit resolution and recorded at a sampling frequency of 200 kHz. Aliasing was prevented by the bandwidth of the analog electronic circuitry and principally by the finite sensor size which limited the scale of the resolvable unsteady flow structures.

2.4.5 Flow visualization and interferometry

Laser interferometry was used to visualize the flow field and to provide quantitative measurements of the density field. Preliminary experiments utilized a $\phi 200$ mm field of view differential interferometer with a conventional folded Z mirror arrangement. Continuously variable differential shear was provided by the photoelastic birefringence of a polycarbonate prismatic beam.

The final experiments utilized a $\phi 75$ mm field of view high resolution holographic interferometer. Double pulse holography was used to sequentially record the test section wavefront before and during the flow. When the two beams were simultaneously reconstructed an interferogram was produced that was equivalent to an infinite fringe Mach-Zehnder interferogram. Note that this procedure, as it was applied to the experiments described here, produces no three-dimensional information. The device that is described in appendix D incorporated a multi-element lens imaging arrangement for the control of optical aberrations, Fourier plane conjugate image separation, white light reconstruction and Gaussian apodizing filters for non-oscillatory imaging of shock fronts.

2.4.6 Shock generator

A significant difficulty in this work was the generation of the impinging shock wave. At moderate Mach numbers the oblique shock wave produced by a wedge already lies quite close to the surface. The separation of the wedge surface and the shock wave determines the permissible model diameter. The shock generator that is illustrated in figure 2.8 represents a response to this difficulty and the concept is analogous to a wave-rider in hypersonic vehicle design (Nonweiler [33]). Its shape is generated by inclining a cylindrical tube at some arbitrary flow deflection angle and sectioning the tube at the corresponding oblique shock angle. This defines an internal surface that satisfies the inviscid boundary condition for the uniform flow behind a planar oblique shock wave attached to the elliptical planform leading edge. The argument holds for non-circular cylindrical sections such as the familiar example of a flat plate with side fins. Since the tube has finite thickness the rear

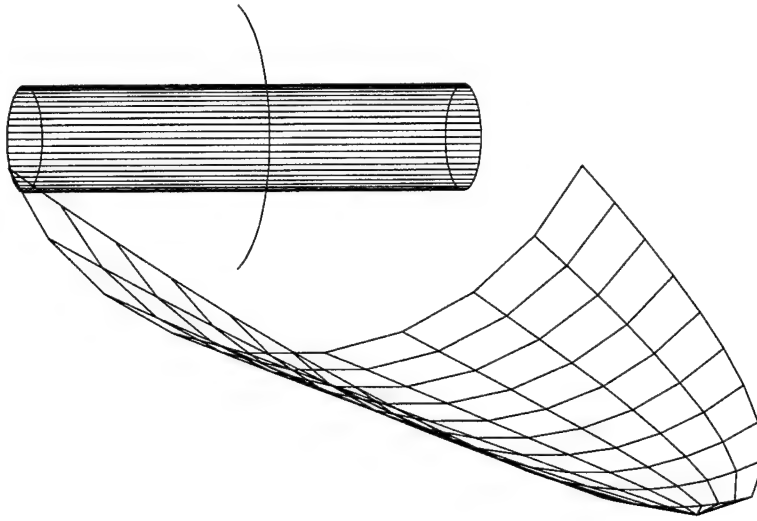


Figure 2.8: PERSPECTIVE VIEW OF SHOCK GENERATOR AND CYLINDRICAL MODEL. View point is from upstream, slightly offset to one side.

surface must be relieved at a fine angle to ensure that the shock on the exterior surface remains attached to the leading edge.

Optimal utilization of the test section volume is achieved when none of the nozzle flow spills underneath the shock generator. For modest flow deflection angles a circular cylinder with diameter equal to the nozzle exit diameter is a good approximation to the ideal elliptic cross-section. In practice a slightly smaller diameter is required to allow for the boundary layer inside the nozzle and the finite thickness of the generator (Figure 2.6). This arrangement allows the size of the model to be nearly doubled in comparison with a conventional wedge shock generator. Edge effects are absent so that the region of uniformly compressed flow spans the entire width of the shock generator.

The shock generator used for the current experiments produced a flow deflection angle of 6° and exact geometrical details are given in figure F.3. Since the flow in the nozzle exhibited some flow angularity and Mach number nonuniformity (Appendix B) the actual shock angles lay slightly further from the surface of the wedge than indicated by an inviscid calculation with allowance for the boundary layer thickness. The measured shock angles that form the best basis for any computations are listed in table B.5.

Chapter 3 Experimental results

3.1 Introduction

Holographic interferograms and heat transfer data were obtained for three different test conditions and a range of shock impingement locations. The data are contained in Appendix C along with an explanation of the format of presentation. This chapter begins with a description of the changes in the flow structure that were observed as the location of the impinging shock wave was varied. Following this, the peak heat transfer rates for the type IV flow field are examined for the three test conditions. The investigation shows that increases in the severity of the phenomenon at high enthalpy, owing to the effects of dissociation, are less significant than previously expected. Time resolved heat transfer measurements at the base of the type IV jet are then discussed in greater detail. The measurements reveal coherent fluctuations of the impinging jet. The oscillations are characterized by Strouhal numbers that are determined from the spectra of the heat transfer data. Supplementary experiments for a blunt faced cylindrical model are used to reinforce the conclusions of the main study. Finally, the experimental program is summarized and the results are used to motivate the development of improved models of real gas effects in the following chapter.

3.2 Description of the flow fields

In the conduct of the experiments, and in the description of them, deliberate emphasis was placed on the type IV jet configuration. This necessarily occurred at the expense of other interesting thermochemical aspects that were peripheral to the main objective. As a minimum requirement it was desirable that data for condition C should span the entire range of shock impingement locations. The data for conditions A and B concentrated almost exclusively on the type IV configuration.

Twenty shots were conducted at the high enthalpy condition C. The remaining data comprised nine shots at the low enthalpy control condition A, and four shots at the intermediate condition B to aid interpretation of the results. Vertical translation of the model provided a range of shock impingement locations at each condition. The shock generator was inclined at an angle of 6° with respect to the tunnel centerline for all conditions. These 33 sequential shots (T5-824-856) comprise the core holographic and heat flux data that are contained in appendix C.

Several series of preliminary experiments were conducted during the development of the instrumentation for this project. Initial experiments were conducted using differential interferometry to investigate the flow over a two-dimensional cylindrical model. Subtle differences were apparent

that could not be reconciled with the original data of Edney [8]. Confirmatory experiments with a spherical model at low enthalpy successfully reproduced Edney's observations. The differences were therefore ascribed to three-dimensional effects. Brief references to these additional data are made when appropriate.

3.2.1 Flows without shock impingement

The flow about the cylinder without shock wave impingement is shown for each of the three test conditions in figures C.1, C.14 and C.20 respectively. Appendix B contains a quantitative assessment of these results. In all three cases the models and data agree tolerably well. Closed fringes visible in the interferograms near the surface of the body generally indicate the location of the stagnation point. In these cases of undisturbed flow they naturally lie on the centerline.

3.2.2 Type I flows

Figure C.21 demonstrates a type I flow. The bow shock shape and heat transfer distribution remain undisturbed since the interaction occurs downstream of the sonic line. Preliminary experiments using differential interferometry indicated no significant variations with stagnation enthalpy or for a spherical model at low enthalpy. Real gas effects are known to influence the process of Mach reflection in a relaxing gas (Hornung et al. [21]). Investigation of these subtle effects on the type I-II transition process requires finer variation of the shock impingement location than was appropriate for the goals of the experiments described here.

3.2.3 Type II flows

As the impingement point was raised the transition to type II flow was observed. In figure C.22 a Mach stem connects the λ -pattern at the impingement point to the bow shock of the cylinder. At the intersection point a strong vortex sheet is observed separating the upper region of subsonic flow from the lower region of supersonic flow. No transmitted wave is resolvable at the upper end of the Mach stem which exhibits a point of inflection where it joins with the bow shock wave. The upper portions of the fringe pattern and heat transfer distribution remain symmetrical. A saddle point is observed in the interferometric fringe pattern above the impingement point. This corresponds to the increased density of the gas downstream of the Mach stem.

Differential interferometry with a cylindrical model at low enthalpy also failed to resolve a transmitted wave at the upper end of the Mach stem. This generic feature is expected for type II flows (Figure A.4). Figure 3.1 illustrates the single instance in which this wave was observed for low enthalpy flow over a sphere. This reproduces the result of Edney [8] that is indicated in frame 2 of figure A.1. Curvature of the bow shock wave out of the plane of symmetry appears to fix the

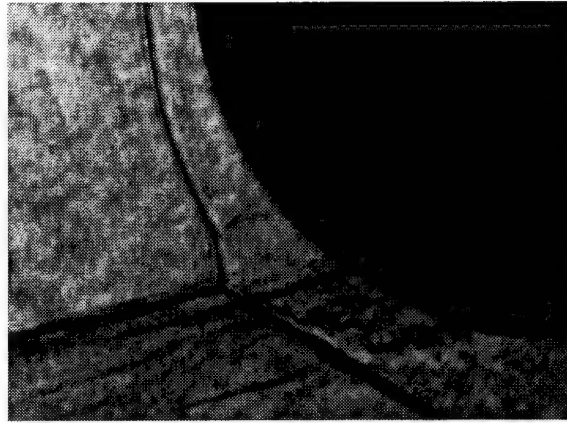


Figure 3.1: Type II interaction for a $\phi 50\text{mm}$ spherical model at condition A.

location of the Mach stem downstream of the sonic line.

3.2.4 Type III flows

Raising the impingement point caused the Mach stem to merge with the bow shock. In figure C.23 the bow shock above the impingement point exhibits little curvature and remains nearly normal below the centerline of the cylinder. A closed fringe slightly below the centerline indicates the location of the stagnation point. The saddle point in the fringe pattern above the impingement point leads to a secondary maximum in density away from the surface of the model. A sonic line must exist in the flow between the model and the shear layer. The density decreases downstream of the saddle as the flow accelerates through the sonic line. The shock standoff distance has increased only slightly from its value without shock impingement. Heat flux measurements shown in figure C.23 indicate a slightly asymmetric fullness below the centerline. Although the Mach stem and bow shock have merged, this flow does not exhibit the obvious asymmetries of the shock layer that are observed at higher impingement points (Figure C.24). This effect is possibly due to the behavior of the sonic line that is discussed in section 4.4.2.

3.2.5 Displacement of the stagnation point

In the current experiments Mach numbers of 3.0 and 0.3 were typical for the supersonic and subsonic streams of the shear layer. On dimensional grounds the inertia of the high Mach number stream dominates the pressure forces of the subsonic stream. Consequently the shear layer does not deflect as it approaches the surface of the cylinder (Figure C.25). This approach further reduces the size of the sonic throat that must exist between the shear layer and the body. The fringe pattern that is observed in figure C.25 supports this conclusion. The fringe shift remains nearly constant through the subsonic region of the shock layer and then decreases beyond the point of closest approach. The

mass flux that exits the shock layer through this throat must decrease as the shear layer approaches the body. The remaining mass flux that enters across the bow shock must pass above the cylinder and so the stagnation point is forced downward. This is evidenced by the maximum fringe shift in figure C.25 that occurs 30° below the centerline of the model. Similarly, the λ -shock intersection point stands away from the surface of the body. Heat transfer rates downstream of the sonic throat remain steady and increase in magnitude. Temporal fluctuations of the heat transfer rate would be indicated by a large deviation about the mean measurement. Equivalent flow features are observed in figure C.2 at low enthalpy. In this case spurious heat transfer fluctuations resulted from inversion of the surface temperature records at low signal levels.

3.2.6 Entrainment of the stagnation streamline

Raising the position of the impinging shock wave slightly causes the stagnation streamline to become entrained with the shear layer. Evidence for this statement at low and high enthalpy is obtained from the holographic interferograms in figures C.3 and C.30. Figure 3.2 is an interpretation of the flow field in the vicinity of the stagnation point. We observe closely spaced fringes lying parallel to the wall above the point where the shear layer meets the body. This region of high density gradient is presumably caused by a portion of the shear layer fluid being turned upward along the wall of the model. The stagnation point must necessarily lie below these stream lines. There exists only one local maximum in density along the surface of the body in each case. Enlargements of the interferograms allow the fringe order at the maxima to be determined. The orders are 30 ± 1 and 11 ± 1 in the low and high enthalpy cases respectively. Both values exceed the corresponding undisturbed stagnation point fringe shifts of 13 ± 1 and 9 ± 1 respectively. This can only occur for streamlines that have been entrained into the shear layer and mixed with the lower entropy fluid from the supersonic stream. Peak heating occurs at the same angular position as the maximum fringe shift. The relative heat transfer and density differences at low and high enthalpy cannot be compared directly since they are strong functions of the shock impingement location. Noticeably larger variance in the heat transfer data near the stagnation point is indicative of mixing that occurs in the shear layers. Short exposure times of approximately 30 ns freeze the motion of the vortical structures that are visible in the interferograms. These structures develop over lengths that are shorter than the shock standoff distance for all three test conditions.

3.2.7 Turning of the shear layer at the surface

The portion of the shear layer that is turned at the stagnation point and passes below the cylinder generates a compression wave that coalesces in the supersonic flow below the shear layer. At some distance from the wall this wave overtakes and steepens the third wave that originated at the

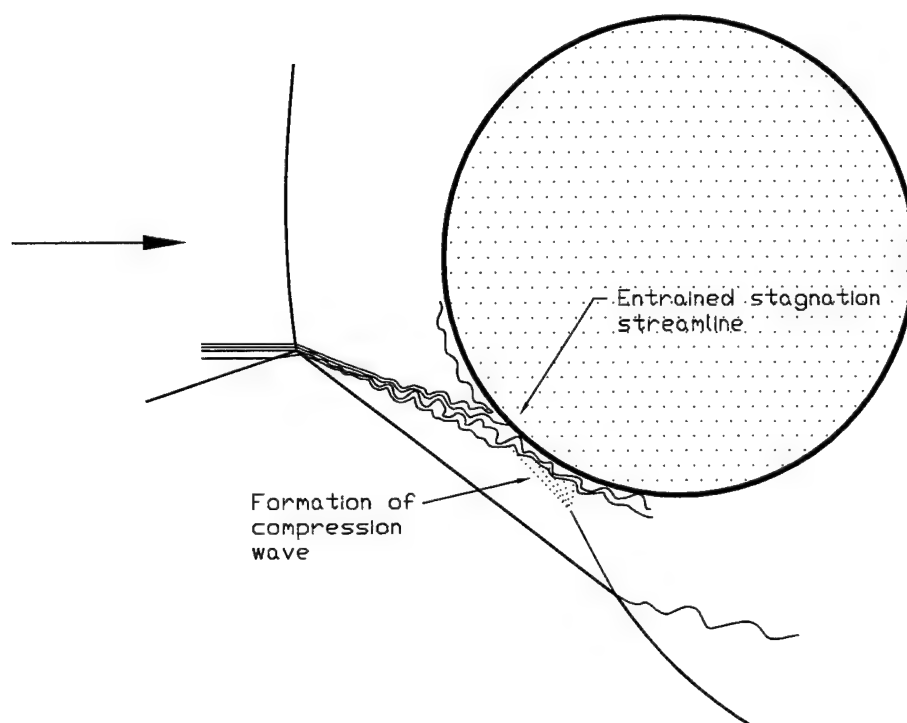


Figure 3.2: Interpretive sketch of the entrainment of the stagnation streamline.

impingement point. The compression wave is observable in figures C.3 and C.30 as a series of closely spaced fringes. The closed fringe that marks the local maximum of density along the wall forms a large balloon shape in each interferogram. The balloon shape envelops a fringe saddle that forms adjacent to the wall and the absolute density maximum that occurs behind the compression wave. This saddle-maximum combination is a manifestation of the density gradient across the shear layer that passes below the cylinder. The density maximum occurs only in the supersonic flow beyond the edge of the shear layer. Continuing this progression we see in figure C.31 that the saddle-maximum feature moves closer to the wall as less of the shear layer passes below the cylinder.

3.2.8 Transition to type IV

Edney [8] hypothesized that transition to type IV would occur when the angle between the shear layer and the wall exceeded the maximum deflection angle for the compression wave. The flows shown in figures C.3 and C.30 already approach the maximum deflection condition. Spreading of the shear layer near the impingement point makes more precise measurements difficult. In figures C.4 & C.5 at low enthalpy and figures C.26 & C.27 at high enthalpy we see that the saddle-maximum feature collapses into the surface of the body and the heat transfer rates increase rapidly. On the basis of continual increases in the peak fringe shift (20 ± 1 in figure C.27) we conclude that the

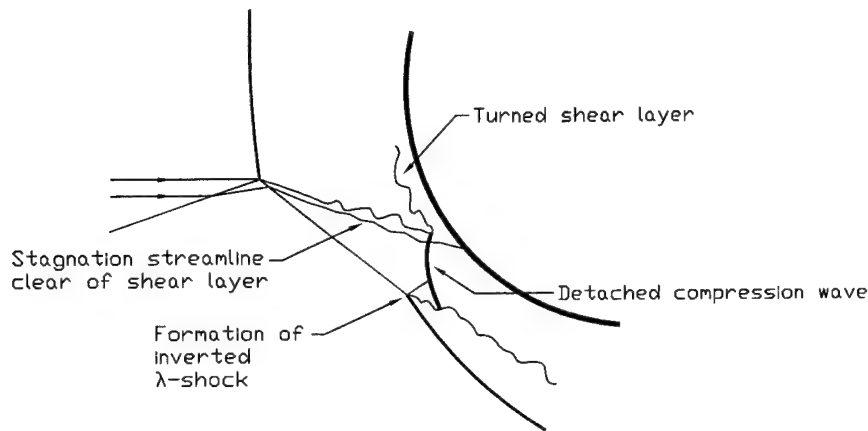


Figure 3.3: Interpretive sketch of detachment of the compression wave.

stagnation streamline moves closer to the high speed side of the shear layer. This interpretation is complicated by the large entropy gradient across shear layer whereby the maximum fringe shift no longer coincides exactly with the stagnation point. The large variance of the heat transfer traces indicates unsteadiness of the flow in the vicinity of the stagnation point. The compression wave adopts a confused, three-dimensional appearance in the interferograms and appears to detach and curve around the stagnation point (Figure 3.3). The wall pressure behind this wave is finally sufficient to overcome the inertia of the supersonic stream, which controls the location of the stagnation point, and turn the shear layer substantially above the cylinder. At several locations across the span of the image in figure C.5 we begin to see the appearance of an upward propagating oblique wave. This shows that the overtaking intersection of the compression wave and the bow wave has failed and a second λ -shock appears. We note by analogy with the type VI transition process that the appearance of this feature must occur before, and is independent of, the detachment of the compression wave from the wall. The inverted λ -shock feature becomes more prominent in figures C.28 and C.29 where the maximum fringe shift increases to 24 ± 1 .

3.2.9 Type IV flows

Once the compression wave detaches from the surface, the standoff distances must be controlled by a balance of the mass flux entering the shock layer. These influences are observed in figures C.8 & C.9, C.15 & C.16 and C.34 & C.35 at low, medium, and high enthalpy respectively. All of these flows lie in the regime that is classified as type IV. As the impingement point moves upward the second λ -point must stand away from the wall to accommodate the increased mass flux that must pass below the body. Simultaneously, the mass flux passing above the body reduces and the first λ -point moves closer to the body. As the second λ -point moves away from the body the type IV

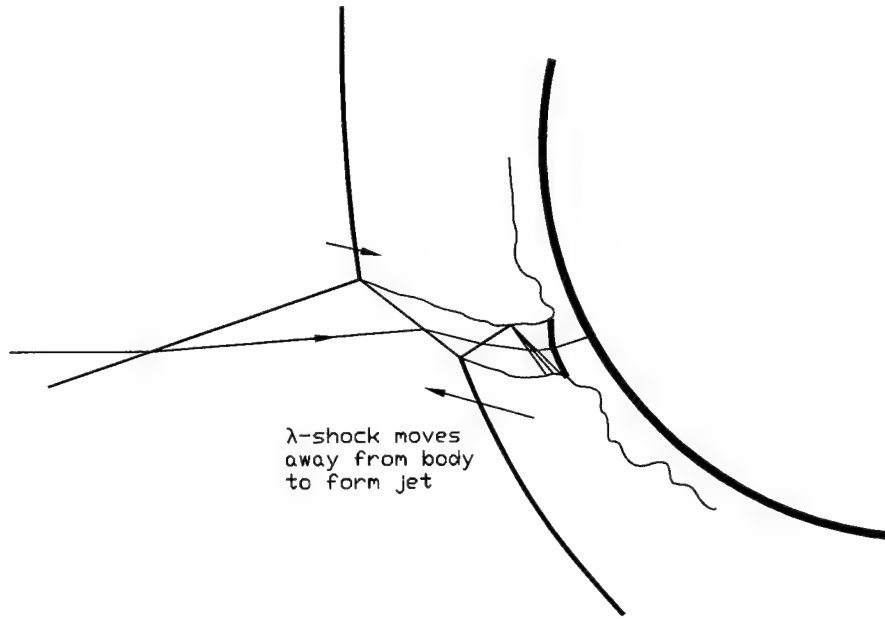


Figure 3.4: Interpretive sketch of jet formation.

Test condition	A	B	C
Undisturbed fringe shift	13 ± 1	10.5 ± 1	9 ± 1
Interferogram	Figure C.8	Figure C.15	Figure C.34
Type IV fringe shift	55 ± 2	29.5 ± 1	27 ± 1
Ratio	4.2 ± 0.5	2.81 ± 0.4	3.0 ± 0.4

Table 3.1: Stagnation point fringe shift for type IV flows with cylindrical model.

jet forms with a third oblique wave crossing the path of the stagnation streamline (Figure 3.4). A strong terminating shock, that originated as the detached compression wave, lies close to the stagnation point. The stagnation point fringe shift may be measured and compared with the value without shock impingement (Table 3.1). These measurements indicate a trend towards reduced density intensification at high enthalpy. Care must be taken in comparison of these highly localized measurements that are sensitive to variations across the span of the model. Spanwise nonuniformity is most pronounced in figures C.32, C.33, C.36 & C.37 where multiple images of shock fronts are observed along the line of sight. The nonuniformity is ascribed to the slight out-of-plane curvature of the incident shock wave.

Comparison of the type IV thermocouple data shown in figures C.8, C.15 and C.34 indicates a similar trend of reduced heat transfer intensification at the higher enthalpy conditions. In all cases the maxima of density and heat transfer occur at the same angular location.

We see that throughout this progression of impingement locations the stagnation streamline crosses a successively increasing number of weaker waves. In the undisturbed configuration, the

streamline crosses a single strong wave. As the stagnation streamline traverses the shear layer it mixes with lower entropy fluid that has crossed two weaker oblique shock waves. Raising the impingement point further causes the stagnation streamline to pass through two oblique waves and the strong detached compression wave before it meets the wall. As the standoff distances equalize the flow passes through a third oblique wave which results in an additional decrease in the stagnation entropy. The holographic shadowgraph shown in figures C.6 and C.7 demonstrates propagation of this third wave along the supersonic jet by multiple reflections from the bounding shear layers. These additional reflections alternate isentropically between the constant pressures of the subsonic flows above and below the jet. The behavior of the stagnation point that is observable in the sequence of holographic interferograms reinforces the discussion of the streamline patterns in section 2.3.3.

3.2.10 Curvature of the supersonic jet

The strength of the oblique wave that propagates along the supersonic jet is determined completely by the free-stream conditions and the incident shock wave angle. Consequently, the pressure gradient across the jet is inversely proportional to its width. This is consistent with the increased jet curvature observed in figures C.10, C.11, C.17, C.18, C.38 and C.39 at low, medium and high enthalpy respectively. The corresponding maximum fringe shift ratios are $13 \pm 1 \rightarrow 50 \pm 2$, $10.5 \pm 1 \rightarrow 24 \pm 1$ and $9 \pm 1 \rightarrow 24 \pm 1$ respectively. These values, and the corresponding heat transfer rates, have decreased slightly as the jet narrows. The stagnation point appears to form at the lower edge of the jet in all three cases. Again, this interpretation is sensitive to the entropy gradient across the lower shear layer that must entrain the stagnation streamline as the jet curls upward. Figures C.10, C.11, C.40 and C.41 illustrate the manner in which the low entropy jet fluid energizes the boundary layer on the body above and below the impingement point. Interactions of the jet shock waves with the shear layers produce large vortical structures that are observed to convect downstream in the interferograms.

3.2.11 Detachment of the supersonic jet

Figures C.13, C.19 and C.42 demonstrate that only slight changes in the shock impingement location produced curvature of the jet sufficient for it to pass entirely above the body. Figure 3.5 illustrates this process by which the stagnation streamline emerges from the supersonic jet. Note the extremely rapid decrease in the heat transfer rates as the disturbance detaches from the surface. This underscores the observation that the behavior of the stagnation streamline is controlled entirely by the inertia of the supersonic stream. The stagnation point fringe shift ratios are $13 \pm 1 \rightarrow 35 \pm 2$, $10.5 \pm 1 \rightarrow 24 \pm 1$ and $9 \pm 1 \rightarrow 20 \pm 1$ respectively for the three interferograms. Since these values are only slightly less than for the corresponding type IV flows, we conclude that the type IV fringe

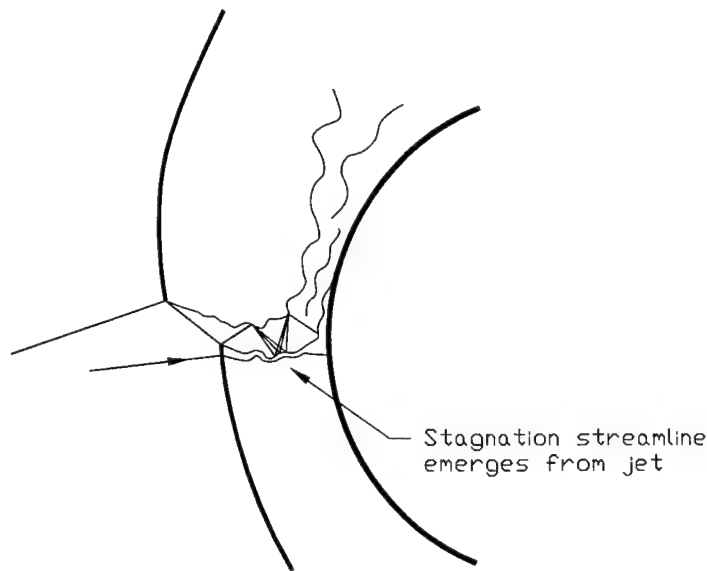


Figure 3.5: Emergence of the stagnation streamline from the supersonic jet.

shifts were influenced by inevitable variations of the peak density location across the span of the cylinder.

3.2.12 Type V and VI flows

Translating the shock impingement point towards the upper sonic line caused the jet width to decrease beyond the resolution of the interferometer (Figures C.43, C.44 & C.45). A point of inflection is apparent on the bow shock below the impingement point in these images. The characteristic type V shock wave was not observed for the range of parameters studied here and this is consistent with the absence of the type II wave that was discussed in section 3.2.3. Raising the shock impingement point beyond the upper sonic line produced the conventional type VI interaction shown in figure C.46.

3.3 Summary of the heat transfer data

Figures 3.6, 3.7 and 3.8 summarize the heat transfer data at the low, medium and high enthalpy test conditions respectively. Each plot represents a compilation of the heat transfer data for the entire sequence of shots at each test condition. Two sets of points are shown. The first set, +, is the maximum instantaneous heat flux recorded at each circumferential location on the model. The maximum value was determined by scanning all shots over an interval $0.5 \rightarrow 4.0$ ms after initiation of the flow. This scanning interval excludes flow starting transients and extends over the period of

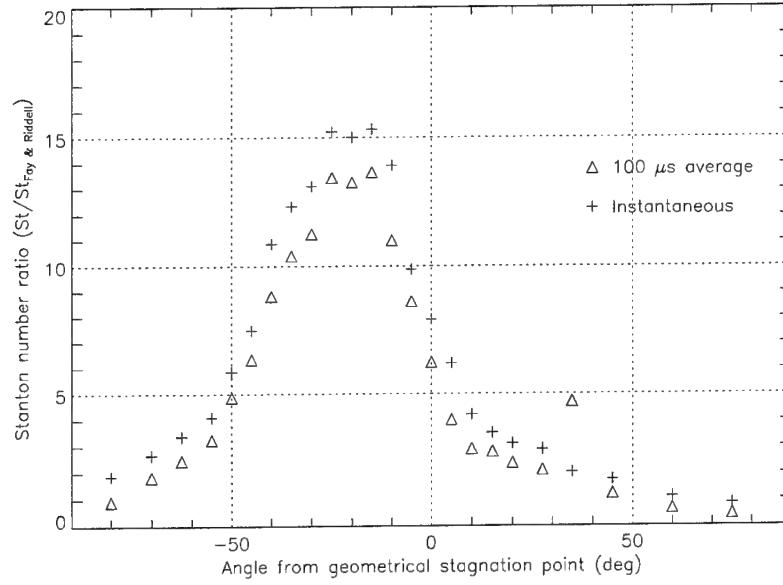


Figure 3.6: ENVELOPE OF MAXIMUM HEAT TRANSFER RATES AROUND THE MODEL AT CONDITION A. The anomalous point at $\theta = 35^\circ$ arises from contributions to the average beyond the ends of the sampling period.

useful test time. The second set of points, Δ , results from the same maximization procedure however the data were first averaged over an interval of $100\mu\text{s}$. We conclude from these statistics that the peak heat transfer intensification decreased by a factor of two as the tunnel stagnation enthalpy was increased from 4MJ/kg at condition A to 19MJ/kg at condition C.

3.4 Comparison with existing data

Precise comparison of the data with existing results is complicated by the large number of parameters involved. The data of Edney [8] that are shown in figure 3.9 may be compared with the results for the low enthalpy condition A (Figure 3.6). Despite the differences in the free-stream conditions and model geometries, the comparison validates the current measurements and peak heating was observed at identical circumferential locations. Table 3.2 lists the peak heating rates observed by other workers. Differing spatial and temporal resolution of the instrumentation that was used by the various authors limits the utility of this comparison. The use of time averaged values from the current study represented the best compromise. Interpolation between the results of Edney [8] and Wieting & Holden [48] gives good agreement with the low enthalpy data shown in figure 3.6.

The Mach number of the flow in T5 decreased as the stagnation enthalpy was increased (Table B.1) and this complicates interpretation of the current results. Coupling of these two parameters in the data with a single nozzle area ratio was unavoidable. In order to decouple the two effects,

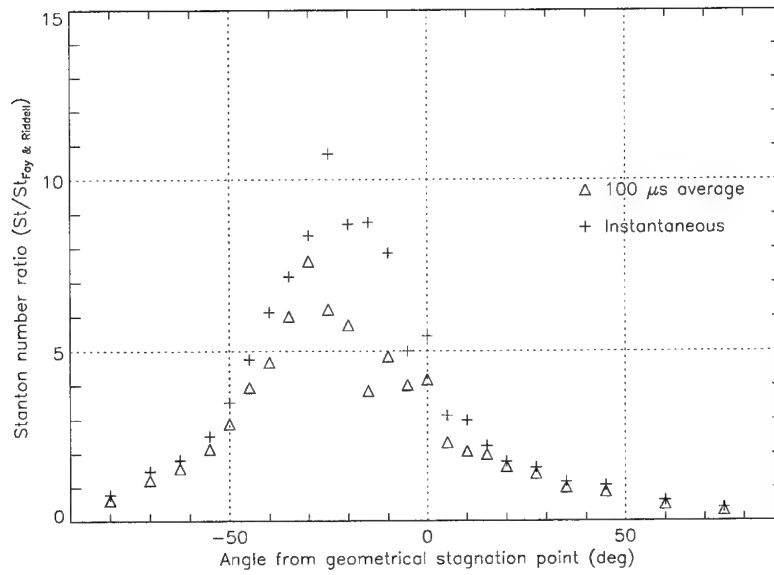


Figure 3.7: Envelope of maximum heat transfer rates around the model at condition B.

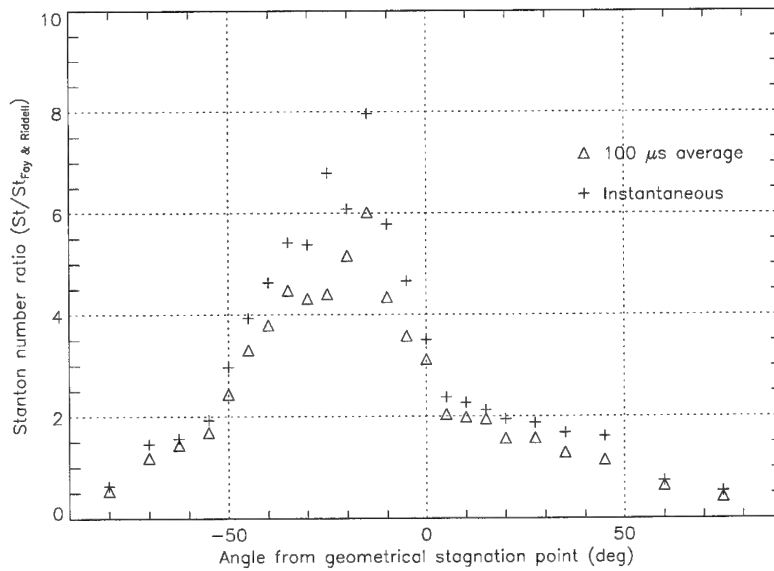


Figure 3.8: Envelope of maximum heat transfer rates around the model at condition C.

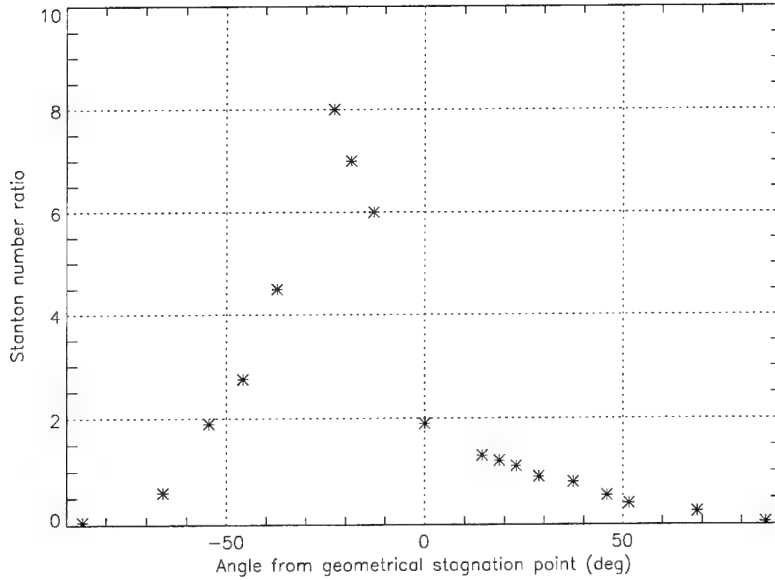


Figure 3.9: Envelope of maximum heat transfer rates about a spherical model (Edney [8]); $M_\infty = 7$, $\delta_1 = 5^\circ$.

consider the experiments of Edney [8] at low enthalpy with $M_\infty = 4.6$ and $\delta_1 = 5^\circ$ that produced a heat transfer intensification of 6.5 (Table 3.2). The current high enthalpy experiments at condition C with $M_\infty = 5.3$ and $\delta_1 = 6^\circ$ produced a surprisingly similar heat transfer intensification of 6.0 (Table 3.2). Despite the different model geometries for the two studies, we see that the prediction of dramatic real gas effects is not supported by the current data.

Table 3.2 also shows that the high enthalpy data reported by Kortz [27] lie below the heat transfer rates measured in the current experiments at the same enthalpy and also below those of Wieting & Holden [48] at the same Mach number and wedge angle.

3.5 Temporal characteristics of the data

3.5.1 Introduction

The instrumentation and signal processing techniques that are described in appendix E provided unusually high bandwidth measurements of the heat transfer intensification caused by shock impingement. These measurements reveal temporal fluctuations of the type IV jet flow that have not previously been reported. Edney [8] noted the possibility of jet oscillations that were observed in the jet impingement study of Henderson [17] but did not observe them. Recent numerical simulations of the type IV flow field also indicate the existence of jet fluctuations. Several authors (Prahbu et al. [36], Klopfer & Yee [25]) have reported difficulty in obtaining converged steady state solutions

Reference	M_∞	δ_1	Enthalpy	Geometry	\dot{q}
Edney [8]	4.6	5.°	Low	Sphere	6.5
	4.6	10.°	Low	Sphere	7.5
	4.6	15.°	Low	Sphere	10.
	7.0	5.°	Low	Sphere	8.
Wieting et al. [48]	8.0	10.°	Low	Cylinder	13.
	8.0	12.5°	Low	Cylinder	18.
	8.0	15.°	Low	Cylinder	25.
Kortz [27]	9.9	10.°	20. MJ/kg	Cylinder	4. [†]
Figure 3.6	9.9	6.°	3.9 MJ/kg	Cylinder	13.5
Figure 3.7	6.3	6.°	12. MJ/kg	Cylinder	7.5 [†]
Figure 3.8	5.3	6.°	19. MJ/kg	Cylinder	6.

Table 3.2: Comparison of measured heating rates from previous studies. [†] These measurements were based on a limited number of data points and may not resolve the maximum heat transfer rate.

for type IV interactions. Gaitonde [15] and Zhong [50] addressed the issue of time accuracy of the algorithms that were used and independently concluded that the oscillations are attributable to the physics of the problem. Evidence for unsteadiness is also observed in many of the interferograms that are contained in appendix C. Unsteady structures appear to be generated at the jet impingement point and convect along the surface of the body (e.g. Figures C.8 & C.10). Here we begin by establishing the capability of the current experiment to resolve the temporal fluctuations. This is achieved by studying the background signal levels for flows without shock impingement. Typical examples of type IV flows are then selected from the data in appendix C and the time histories of the heat transfer rates in the vicinity of the jet impingement point are examined. Frequency spectra are computed and the behavior is characterized by a dimensionless Strouhal number.

3.5.2 Flows without shock impingement

Figures 3.10–3.12 demonstrate the constancy of the test conditions during the period of time over which the results were obtained. Figure 3.11 reveals some undertailoring at condition B. This condition was used for only 4 shots to obtain a confirmatory data point and was not optimized. The holographic interferograms were exposed at $t = 2.125$ ms, 1.625 ms and 1.275 ms for conditions A, B and C respectively. The heat flux traces demonstrate some digitiser quantisation jitter and noise that were amplified by the deconvolution procedure. Signal levels for $t < 0$ indicate the magnitude of this effect that was exacerbated by the requirements of wide dynamic range and high bandwidth. Any signals above this background level are real and indicate flow fluctuations that arose during operation of T5.

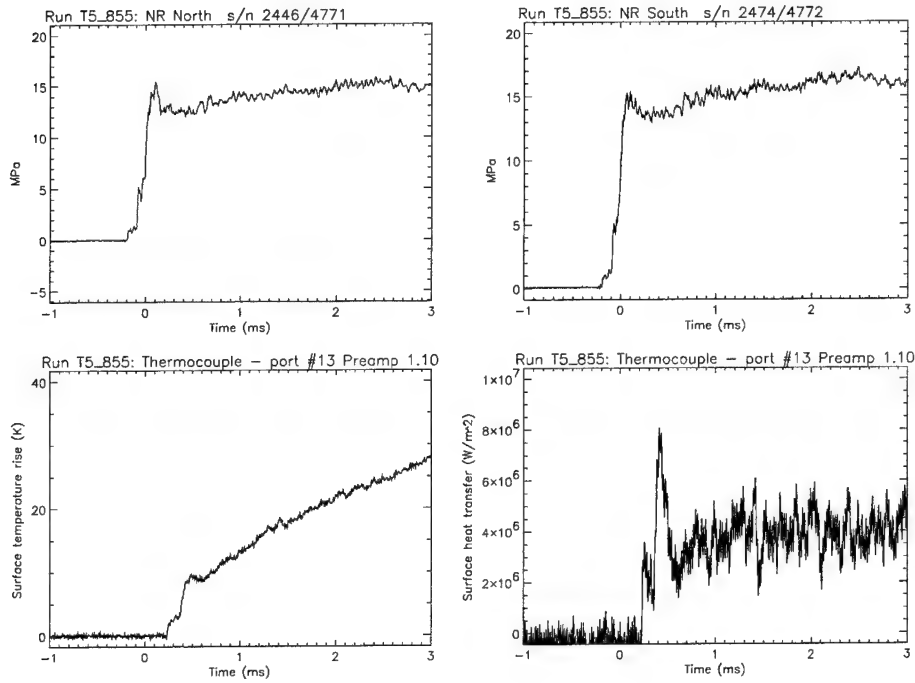


Figure 3.10: TEMPORAL CHARACTERISTICS OF THE FLOW WITHOUT SHOCK IMPINGEMENT AT CONDITION A; SHOT T5-855. Top row plots are the nozzle reservoir pressure. Bottom row plots are the stagnation point surface temperature and the heat flux inferred from it.

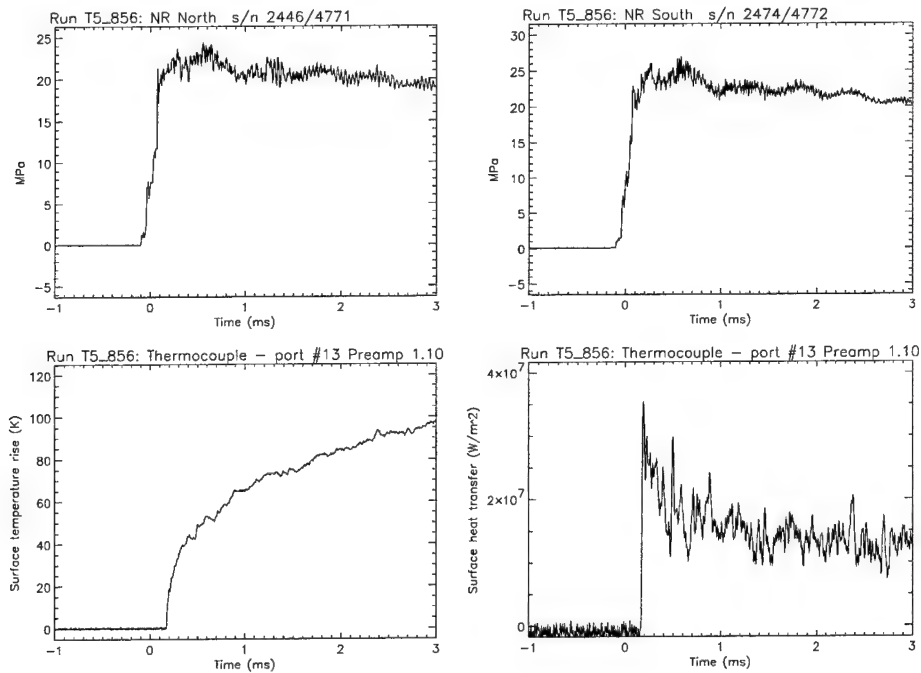


Figure 3.11: TEMPORAL CHARACTERISTICS OF THE FLOW WITHOUT SHOCK IMPINGEMENT AT CONDITION B; SHOT T5-856. Top row plots are the nozzle reservoir pressure. Bottom row plots are the stagnation point surface temperature and the heat flux inferred from it.

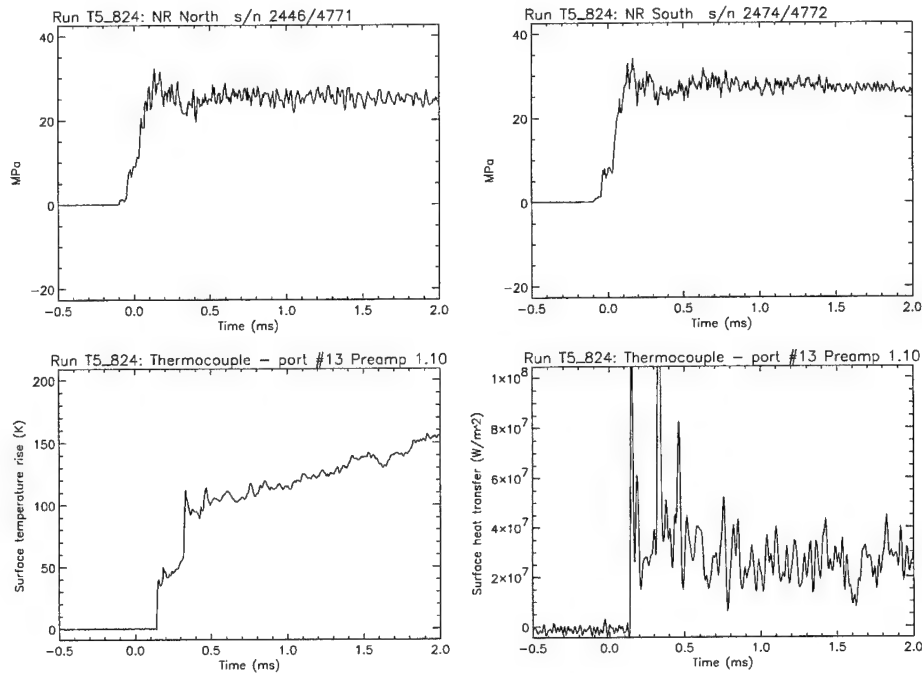


Figure 3.12: TEMPORAL CHARACTERISTICS OF THE FLOW WITHOUT SHOCK IMPINGEMENT AT CONDITION C; SHOT T5-824. Top row plots are the nozzle reservoir pressure. Bottom row plots are the stagnation point surface temperature and the heat flux inferred from it.

3.5.3 Unsteadiness of the type IV flow

Figures 3.13–3.15 demonstrate the time history of the surface heat flux in the vicinity of the impingement point for three representative cases at low, medium and high enthalpy respectively. Corresponding frequency spectra for the thermocouple gauge located at $\theta = -25^\circ$ and the nozzle reservoir pressure are indicated in figures 3.16–3.18. The spectra were obtained from a window of width 1.0 ms disposed symmetrically about the laser firing time. Sharp peaks in the spectra at high frequencies are a manifestation of digitizer jitter and the sensitivity of the results to the deconvolution filter parameters was negligible.

The low enthalpy results shown in figures 3.13 and 3.16 demonstrate an oscillatory behaviour that has its peak power density at a frequency of 6.5 kHz. Noise levels in the deconvoluted signals appear at least an order of magnitude below these peaks. Each fluctuation cycle is observable as a sawtooth shaped perturbation of the surface temperature record. This shape reflects equation E.7 which describes the response of the gauge substrate to an impulsively applied thermal load. Additional realizations of this flow that are shown in figures C.6 and C.19 produced somewhat broader peaks that extended from 5–15 kHz. Computer graphical θ - t color plots of the heat flux, that are not reproduced here, demonstrated that the fluctuations of the individual gauges are spatially correlated. Further evidence of the coherent nature of these fluctuations is provided by the repeatability of the peak

heat flux for each cycle. Although the power spectral density of the heat flux signal exceeds that of the nozzle reservoir gauge by at least two orders of magnitude over the range of frequencies at which oscillations were observed (Figure 3.16), data from a transducer placed immediately upstream of the model would be required to conclusively demonstrate the independence of the fluctuations from free-stream perturbations.

Figures 3.14 and 3.15 demonstrate that the peak heating was fortunately achieved for only a short period of time at the higher enthalpy test conditions. This occurred because the shock generator was long with respect to the diameter of the model. Small variations in the shock angle during the test time produced a large effect on the position of the impinging wave. The flow structure is extremely sensitive to this location. A sequence of interactions was produced during each run as the shock wave moved downward with respect to the model. For this reason the type III interaction in figure C.25 also indicates the peak heat transfer profile for a type IV interaction that occurred earlier during the run. Similarly, figure C.42 represents a type IV flow at later times. The observed invariance of the peak heating rate at different test times provides further confidence in the flow quality.

Frequency spectra of the surface heat flux at conditions B and C are shown in figures 3.17 and 3.18. The quality of the spectra was severely limited by the small number of cycles that were observed.

3.5.4 Comparison with existing data.

Using the free-stream data from table B.1, the frequency of oscillation for condition A may be expressed as a Strouhal number, $Sh = fD/u_\infty \approx 0.16 \pm 0.08$. Best estimates of the Strouhal number are $0.11 \pm 100\%$ at condition B and $0.06 \pm 100\%$ at condition C. Caution should be exercised in the interpretation of this trend since stagnation enthalpy was not the sole parameter. Oscillations were observed in the recent time resolved computations of Gaitonde [15] and Zhong [50] who simulated the experimental results of Wieting & Holden [48]. Both computations independently predicted the result, $Sh \approx 1.3$. It should be noted that convergence of the oscillation cycle was not achieved. Grid refinement produced continually increasing modulation of the fluctuation cycle and this was much less than that shown in figure 3.13. Contour plots of the results demonstrated features that are remarkably similar to those observed in the holographic interferograms. Gaitonde [15] cites additional experiments by Holden that indicated a Strouhal number in the range, $Sh = 0.13 \rightarrow 0.45$. This agrees tolerably well with the current data at condition A.

3.6 Supplementary experiments

Holographic interferometry yields an image that is integrated across the width of the test section. Whilst the use of a cylindrical model simplified quantitative analysis of the data, the inevitable three-dimensional variations blurred the fine details of the images. To overcome this difficulty additional

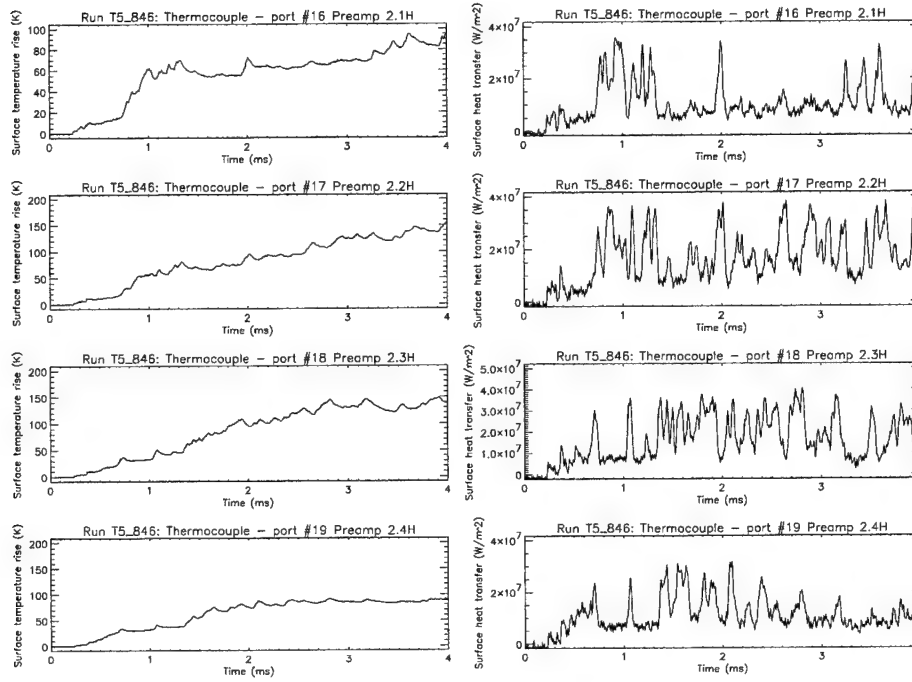


Figure 3.13: TEMPORAL VARIATION OF THE SURFACE HEAT FLUX FOR TYPE IV FLOW AT CONDITION A; SHOT T5-846. Top-bottom: $\theta = -15^\circ, -20^\circ, -25^\circ, -30^\circ$.

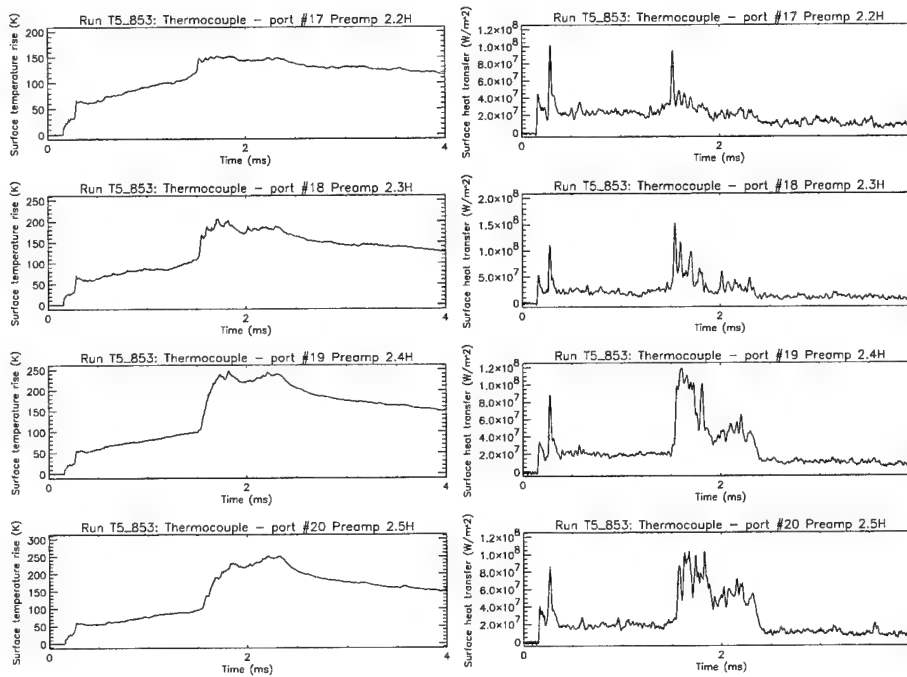


Figure 3.14: TEMPORAL VARIATION OF THE SURFACE HEAT FLUX FOR TYPE IV FLOW AT CONDITION B; SHOT T5-853. Top-bottom: $\theta = -20^\circ, -25^\circ, -30^\circ, -35^\circ$.

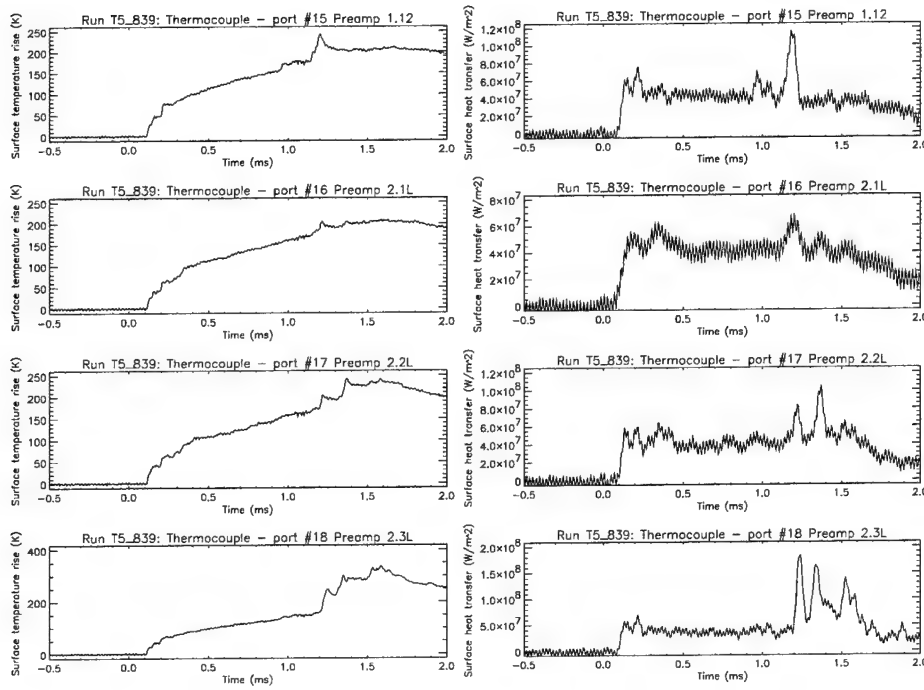


Figure 3.15: TEMPORAL VARIATION OF THE SURFACE HEAT FLUX FOR TYPE IV FLOW AT CONDITION C; SHOT T5-839. Top-bottom: $\theta = -10^\circ, -15^\circ, -20^\circ, -25^\circ$.

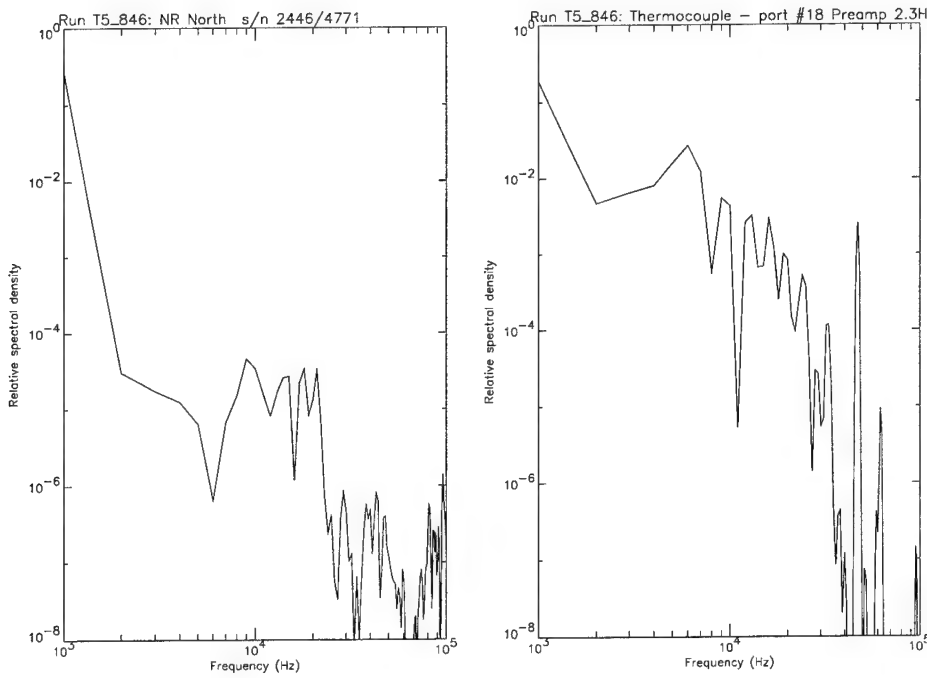


Figure 3.16: Frequency spectra of nozzle reservoir pressure and surface heat flux (gauge #18) for type IV flow at condition A; Shot T5-846.

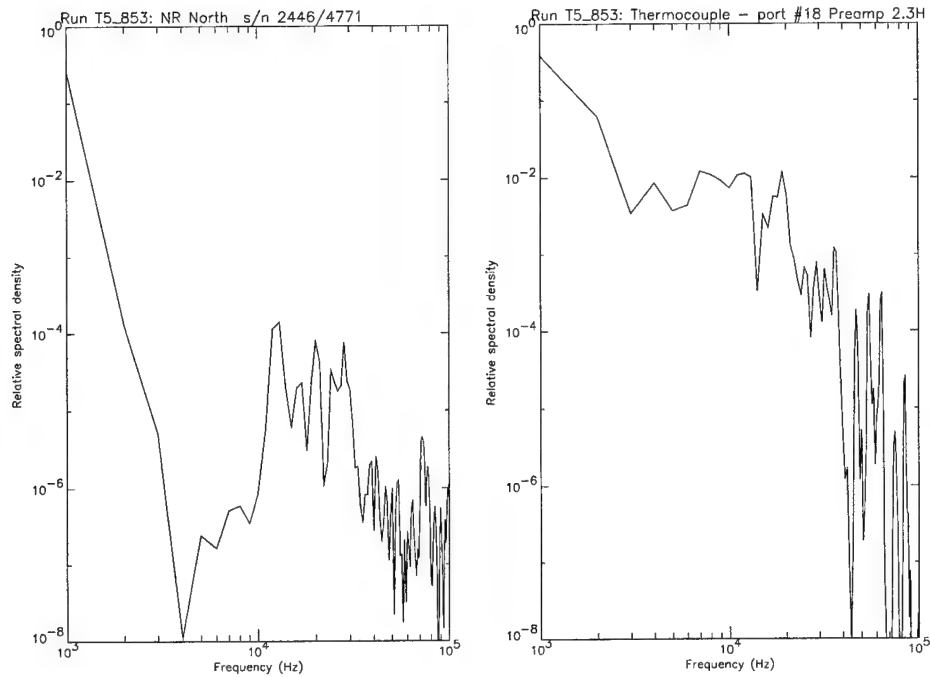


Figure 3.17: Frequency spectra of nozzle reservoir pressure and surface heat flux (gauge #18) for type IV flow at condition B; Shot T5-853.

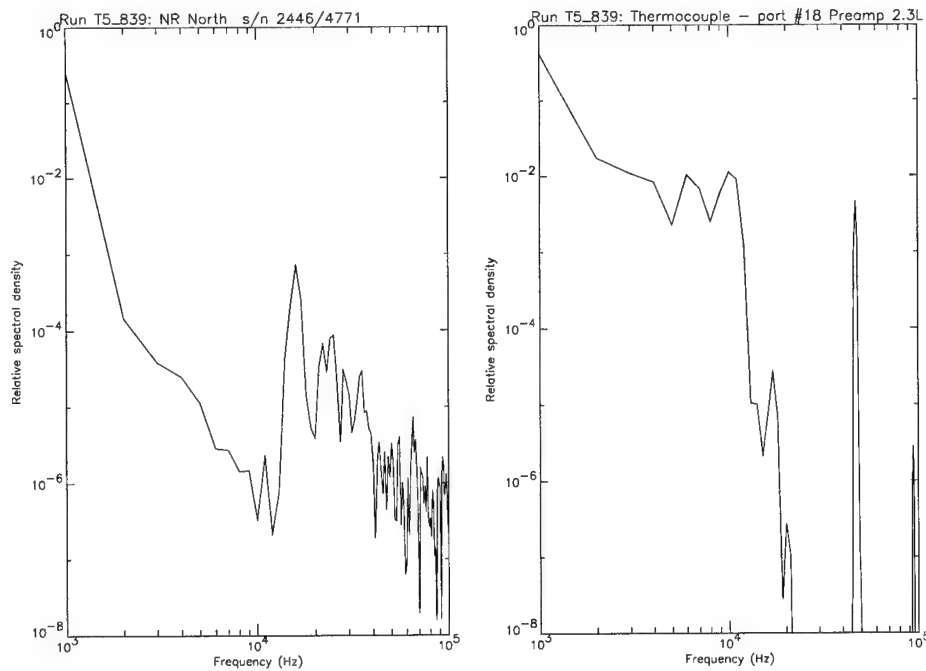


Figure 3.18: Frequency spectra of nozzle reservoir pressure and surface heat flux (gauge #18) for type IV flow at condition C; Shot T5-839.

tests were conducted with a $\phi 50$ mm blunt cylinder model. The flat face of the cylinder was oriented directly towards the free-stream flow. This configuration reduced the bow shock curvature so that the interaction region was enlarged and the short path length across the blunt face of the model provided high spatial resolution and acceptable sensitivity. Figures C.47–C.50 successfully resolve the oblique wave structure of the jet, the terminating normal shock and the region of elevated density behind it. They provide further confirmation of the decrease in stagnation density intensification with increasing tunnel stagnation enthalpy.

3.7 Summary of the experimental results

The experimental data indicated a clear trend towards reduced stagnation density and heat transfer intensification as the tunnel stagnation enthalpy was increased. Critical assessment of the flow conditions confirmed the validity of these measurements. Comparison with existing data allowed a crude decoupling of the effects of Mach number and stagnation enthalpy. It was concluded that the observations do not support the existing predictions (Figure 1.7) of greatly increased heat transfer intensification at high enthalpy. Care must be taken in interpreting this conclusion since the data have been reduced to Stanton number form, $St = \dot{q}/\rho_\infty u_\infty h_{0_\infty}$. The dimensional heat transfer rate therefore increases considerably with stagnation enthalpy.

Holographic interferometry demonstrated the controlling influence of the inertia of the supersonic stream on the flow topology. Quantitative interpretation of the fringe shift at the base of the type IV jet was complicated by three-dimensional averaging along the line of sight. Additional interferograms successfully resolved the internal structure of the type IV jet for the flow over a blunt faced cylinder.

Time resolved heat flux measurements demonstrated the existence of coherent fluctuations of the type IV jet and allowed the estimation of Strouhal numbers for the phenomenon.

Chapter 4 Models of the influence of real gas effects

4.1 Overview

The experimental investigation indicates that further increases in shock impingement heat transfer rates due to real gas effects are less significant than indicated by the existing variable γ model (Section 1.2). The model that is described here follows the pattern of the existing analysis but incorporates refined models of the influence of real gas effects. Development of the model proceeds in four stages;

1. Normal shock solutions are obtained using the ideal dissociating gas (IDG) model due to Lighthill [29].
2. Extension of solutions to oblique shock waves.
3. Mapping of oblique shock waves into the p - δ plane to obtain solutions for the λ -shock interaction points that control the formation of the type IV jet.
4. Modeling of the impingement heating using the equilibrium reacting flow similarity solution of Fay & Riddell [11].

Sections 4.2 and 4.3 are devoted to the preliminary steps 1 and 2. Careful nondimensionalization of the problem leads to a tractable formulation and facilitates identification of the important parameters in the subsequent steps.

Three different solutions of the above model are obtained in order to study the influence of nonequilibrium thermochemistry;

1. A frozen solution that applies when $\Delta \ll 1$.
2. An equilibrium solution that applies when $\Delta \gg 1$.
3. A nonequilibrium approximation that applies when $\Delta \sim 1$.

The dissociation rate parameter, Δ , is defined as the initial rate of the dissociation reaction downstream of a normal shock normalized with respect to the rate of flow over the body (Equation 4.25). The frozen and equilibrium solutions are obtained by using appropriate thermodynamic models for the shock jump calculations. The nonequilibrium solution arises from the observation that the shock waves produced at the λ -points differ greatly in strength (Figure 1.8). It is assumed that the weak type IV jet waves remain frozen (Shocks 1, 3 & 5 in figure 4.10) whilst the bow wave and the

terminating jet shock relax to equilibrium (Shocks 2, 4 & 6 in figure 4.10). The validity of the approximation is assessed by computing the reaction rates (Freeman [14]) immediately downstream of the translational discontinuities. All three solutions are computed for a range of parameters and the results are used to demonstrate generic influences of real gas effects on shock interaction problems.

Specific predictions of the model are presented for the test conditions used in the experimental investigation. The most appropriate choice between the three solutions discussed above is determined by the dissociation rate parameter, Δ , for each free stream condition. The predictions are then compared with the experimental data.

4.2 Normal shock for an ideal dissociating gas

We begin by deriving the jump conditions for a normal shock wave in a relaxing gas. The problem is known in the literature (Vincenti & Kruger [45]) however the compact dimensionless form presented here encompasses a nonequilibrium upstream state and is particularly convenient for the solution of multiple wave interaction problems. Consider the relaxation to equilibrium of the system,

$$N_2 + M \rightleftharpoons N + N + M \quad (4.1)$$

where here Nitrogen is the prototypical gas and M represents a non-reacting third body. The translational and rotational shock thickness is neglected and we consider only the relaxation of the internal modes over a length scale comparable to that of the fluid motion. The mass, momentum and energy conservation equations that apply across the one-dimensional translational discontinuity and throughout the downstream relaxation zone are,

$$\rho_2 u_2 = \rho_1 u_1 \quad (4.2)$$

$$p_2 + \rho u_2^2 = p_1 + \rho u_1^2 \quad (4.3)$$

$$h_2 + \frac{1}{2} u_2^2 = h_1 + \frac{1}{2} u_1^2 \quad (4.4)$$

where ρ is the density of the gas, u is the velocity normal to the shock, p is the pressure and h is the enthalpy per unit mass. The subscripts, 1 and 2, refer here to the upstream and downstream states respectively. In dimensionless form equations 4.2 and 4.3 become,

$$\hat{\rho} \hat{u} = 1 \quad (4.5)$$

$$\hat{p} = 1 + \frac{1}{P} \frac{\hat{p} - 1}{\hat{\rho}} \quad (4.6)$$

where the variables are normalized with respect to their upstream values and generally the notation $\hat{\phi} = \phi_2/\phi_1$ applies. The dimensionless parameter, P , arises and it behaves as $P \sim 1/M_\infty^2$ for a perfect gas;

$$P = p_1/\rho_1 u_1^2. \quad (4.7)$$

We use Lighthill's model [29] for the thermodynamics of the system 4.1,

$$p = \frac{k}{2m}(1 + \alpha)\rho T \quad (4.8)$$

$$h = \frac{k}{2m}[(4 + \alpha)T + \alpha\theta_d] \quad (4.9)$$

where k is Boltzmann's constant, m is the mass of one atom of the gas, T is the temperature, θ_d is a temperature characterizing the dissociation energy and α is the dissociated mass fraction determined from the number densities, $\alpha = \frac{n_N}{n_N + 2n_{N_2}}$. Using the caloric equation of state 4.9 and the dimensionless continuity equation 4.5 the dimensionless energy conservation equation becomes,

$$(4 + \alpha_2)\frac{\hat{T}}{\Theta} + \alpha_2 + \frac{K}{\hat{\rho}^2} = H_0 \quad (4.10)$$

where the dimensionless parameters are defined as;

$$\Theta = \frac{\theta_d}{T_1}, \quad (4.11)$$

$$K = \frac{mu_1^2}{k\theta_d}, \quad (4.12)$$

$$H_0 = \frac{2mh_0}{k\theta_d}. \quad (4.13)$$

The conserved stagnation enthalpy, H_0 , is normalized with respect to the dissociation energy of the gas and K is the normalized specific kinetic energy of the upstream flow.

Importantly, for a nonequilibrium binary mixture of thermally perfect components, three parameters are sufficient to define the state of the upstream gas. Here we specify P , H_0 and α_1 . The remaining parameters, Θ and K , are then given by the following identities, obtained from h_0 written in terms of the conditions upstream of the discontinuity;

$$\Theta = \frac{4 + \alpha_1}{H_0 - K - \alpha_1}, \quad (4.14)$$

$$K = \frac{H_0 - \alpha_1}{1 + 2P\frac{4 + \alpha_1}{1 + \alpha_1}}. \quad (4.15)$$

From equation 4.8 the dimensionless form of the thermal equation of state becomes;

$$\hat{T} = \frac{\hat{p}(1 + \alpha_1)}{\hat{\rho}(1 + \alpha_2)}. \quad (4.16)$$

Eliminating \hat{T} and Θ from equation 4.10 with the pressure given by 4.6 leads to the following quadratic equation for the density,

$$(H_0 - \alpha_2)\hat{\rho}^2 - 2K(1 + P)\frac{4 + \alpha_2}{1 + \alpha_2}\hat{\rho} + K\frac{7 + \alpha_2}{1 + \alpha_2} = 0. \quad (4.17)$$

One solution describes the variation of density throughout the relaxation region downstream of the translational shock. The remaining solution describes relaxation of the possibly nonequilibrium upstream state without any discontinuity. Both solutions are parameterized in terms of the dissociation mass fraction, α_2 , whose rate of reaction remains indeterminate. Note that this formulation encompasses the case of a recombination shock wave where $\alpha_1 > 0$ and $\alpha_2 < \alpha_1$ although this does not arise in the current problem. The solutions are illustrated for typical values of the parameters in figures 4.1 and 4.2.

4.2.1 Frozen shock solutions

Consider the frozen solutions that apply directly downstream of the translational discontinuity. Here $\alpha_2 = \alpha_1$ and the solutions of the quadratic expression 4.17 are,

$$\hat{\rho}_f = \begin{cases} 1 \\ \frac{7 + \alpha_1}{(1 + \alpha_1) + 2P(4 + \alpha_1)} \end{cases}. \quad (4.18)$$

In the strong shock limit, $P \rightarrow 0$, this simplifies to,

$$\hat{\rho}_f = \begin{cases} \begin{cases} 1 \\ 7 \\ 1 \end{cases}, & \alpha_1 = 0, \\ \begin{cases} 1 \\ 4 \end{cases}, & \alpha_1 = 1. \end{cases}$$

These solutions are consistent with the limiting cases of a partially vibrationally excited diatomic gas and a monatomic gas respectively. Note also the value $P_{max} = \frac{3}{4 + \alpha_1}$ which produces $\hat{\rho}_f = 1$ and corresponds to sonic flow upstream of the shock wave.

4.2.2 Equilibrium shock solution

Equation 4.17 may be combined with an equilibrium expression to obtain the asymptotic state far downstream from the translational shock. This determines the endpoints for the trajectories shown

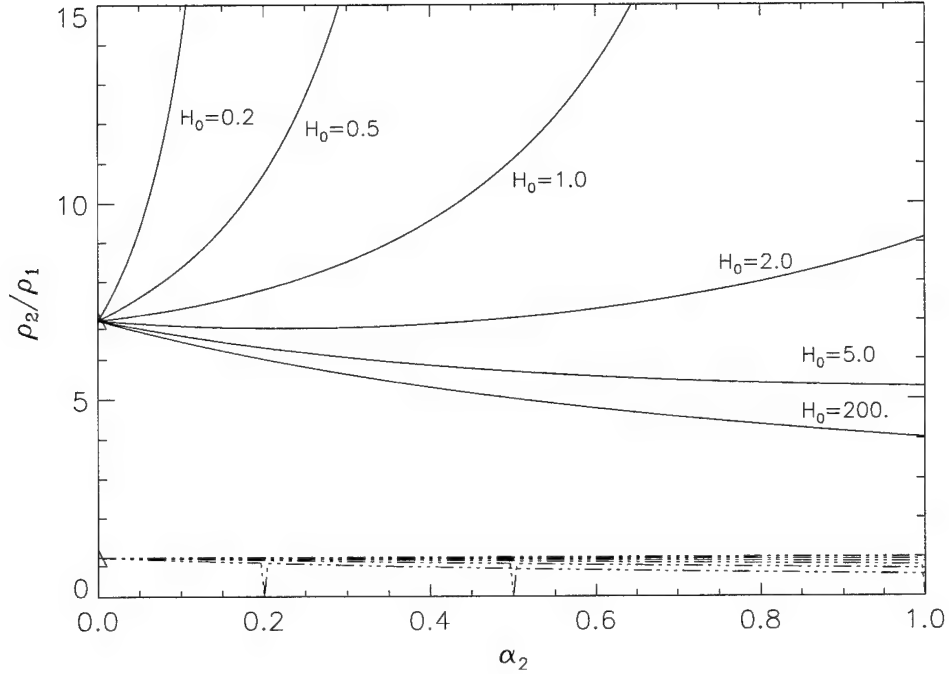


Figure 4.1: STRONG SHOCK SOLUTIONS, $P \rightarrow 0$, OF THE CONSERVATION EQUATIONS DOWNSTREAM OF A NORMAL SHOCK WAVE IN AN IDEAL DISSOCIATING GAS. The upstream conditions are taken as $P = 0$, $\alpha_1 = 0$ and solutions are plotted for differing values of H_0 . The two frozen solutions (Δ) are marked on the vertical axis. The solid curves represent the relaxation of the density downstream of the translational discontinuity. For moderate values of H_0 the density increases monotonically as the flow relaxes. For $H_0 > (\frac{7}{6})^2$ the density initially decreases. As $H_0 \rightarrow \infty$ the solution asymptotes to $\hat{\rho} = 4$ which is the strong shock limit for a monatomic gas. At these enthalpies the model is inaccurate since it does not model the electronic excitation that would occur. Each of the solutions exhibits a singularity at $H_0 - \alpha_2 = 0$. Beyond this singularity the specific kinetic energy downstream of the relaxation zone becomes negative as may be observed from equation 4.15. The second set of solutions shown by the $-\cdots-$ curves represent the relaxation of the upstream state without a translational discontinuity. This effect becomes larger at high enthalpies as the upstream state $\alpha_1 = 0$ deviates further from equilibrium.

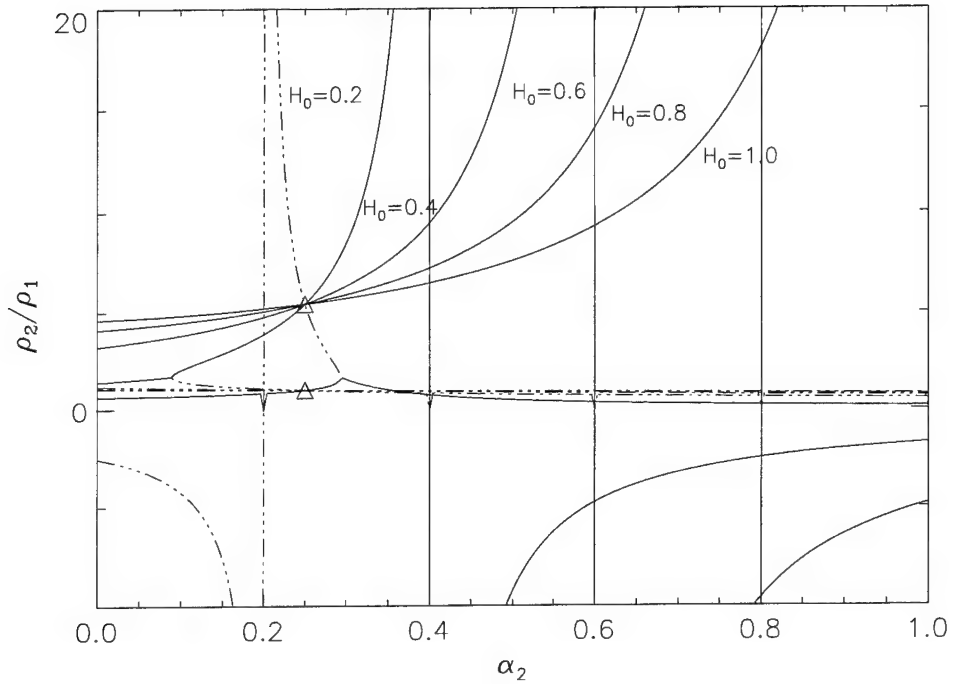


Figure 4.2: RELAXATION OF A NONEQUILIBRIUM UPSTREAM STATE BEHIND A NORMAL SHOCK WAVE IN AN IDEAL DISSOCIATING GAS. The upstream state is taken as $P = 0.01$, $\alpha_1 = 0.25$ and $H_0 = 0.2 \rightarrow 1.0$. We see that the frozen solutions (Δ) are displaced from the vertical axis as a result of the upstream dissociation level. The interpretation of the two sets of solutions that are indicated by the solid and dot-dash curves is qualitatively similar to figure 4.1 for the cases $H_0 = 0.6, 0.8, 1.0$. The case $H_0 = 0.4$ corresponds to a recombination shock where the exothermic relaxation process causes the density to decrease downstream of the shock. The case $H_0 = 0.2$ is physically unrealistic since for values of $H_0 < \alpha_1$ the specific kinetic energy of the flow is negative.

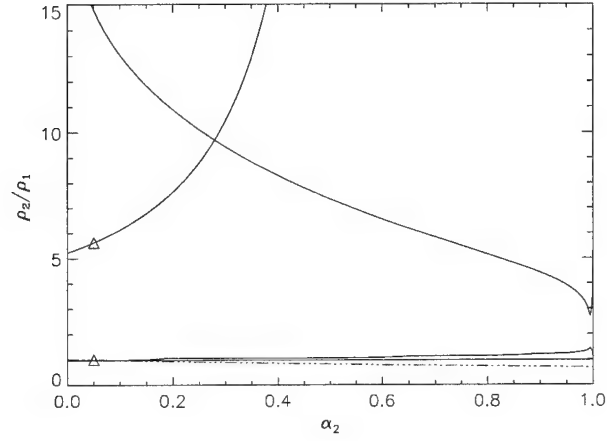


Figure 4.3: EQUILIBRIUM SHOCK SOLUTION IN THE $\hat{\rho}$ - α_2 PLANE. The free-stream conditions are $P = 0.025$, $H_0 = 0.55$, $\hat{\rho}_d = 1 \times 10^7$, $\alpha_1 = 0.05$.

in figures 4.1 and 4.2. For the equilibrium ideal dissociating gas (Lighthill [29]),

$$\frac{\alpha_{2eq}^2}{1 - \alpha_{2eq}} = \frac{\rho_d}{\rho_{eq}} e^{-\theta_d/T}.$$

Writing this in dimensionless form, using the identity 4.14 and expressing the temperature ratio in terms of the density ratio leads to a second transcendental equation relating α_2 and $\hat{\rho}$;

$$\frac{\alpha_{2eq}^2}{1 - \alpha_{2eq}} = \frac{\hat{\rho}_d}{\hat{\rho}_{eq}} e^{\frac{(1+\alpha_{2eq})\hat{\rho}_{eq}^2}{2K(1-\hat{\rho}_{eq}(1+P))}}. \quad (4.19)$$

An additional dimensionless equilibrium constant is introduced,

$$\hat{\rho}_d = \rho_d/\rho_1. \quad (4.20)$$

Numerically solving equation 4.17 with $\alpha_2 = \alpha_{2eq}$ given by 4.19 gives the equilibrium shock solution for specified upstream conditions P , H_0 and α_1 . This solution is represented graphically in figure 4.3 by the intersection of the two curves in the ρ - α plane defined by equations 4.17 and 4.19. When solving these equations numerically the solution is bracketed in the intervals $\hat{\rho}_{2eq} \in [\hat{\rho}_f, \infty)$ and $\alpha_{2eq} \in [\alpha_1, 1]$. This enables the development of a robust solver with known convergence properties in the troublesome weak shock limit. For the routine construction of p - δ loci this is a significant concern.

4.2.3 Nonequilibrium solution

The rate at which the dissociation reaction proceeds for the IDG model is given by Freeman [14],

$$\frac{d\alpha_2}{dx} = \frac{d\alpha_2}{dt} \frac{dt}{dx} = \frac{C\rho T^\eta}{u} \left[(1 - \alpha_2)e^{\frac{-\Theta}{T}} - \frac{\rho}{\rho_d} \alpha_2^2 \right]; \quad (4.21)$$

where C is the reaction rate constant and η represents its temperature dependence. Defining the characteristic reaction length,

$$\ell_d = \frac{u_1}{C\rho_1\theta_d^\eta}, \quad (4.22)$$

and applying the previous dimensionless notation this becomes;

$$\frac{d\alpha_2}{d\hat{x}} = \ell_d \frac{d\alpha_2}{dx} = \hat{\rho}^2 \hat{T}^\eta \Theta^{-\eta} \left[(1 - \alpha_2)e^{\frac{-\Theta}{\hat{T}}} - \frac{\hat{\rho}}{\hat{\rho}_d} \alpha_2^2 \right]. \quad (4.23)$$

Eliminating the temperature dependence using equations 4.16, 4.6 and 4.14 we obtain,

$$\frac{\Theta}{\hat{T}} = \frac{\hat{\rho}^2(1 + \alpha_2)}{2K(\hat{\rho}(P + 1) - 1)}. \quad (4.24)$$

Equations 4.23 and 4.24 represent a third expression in terms of α_2 and $\hat{\rho}$ that, when combined with equation 4.17, determines the relaxation of the density between the frozen state given by equation 4.18 and the equilibrium solution given by equations 4.17 and 4.19 simultaneously. Integrating this ordinary differential equation in the downstream direction produces the relaxation profiles that are shown in figure 4.4.

4.2.4 Reaction rate parameter

The reaction rate immediately downstream of the translational discontinuity, when normalized with respect to the rate of flow over a blunt body, represents a useful indication of the departure of the flow field from equilibrium. This leads to definition of the dissociation rate parameter,

$$\Delta = \frac{d\alpha_2}{dt} \bigg|_f \frac{D}{u_1} = \frac{d\alpha_2}{dx} \bigg|_f \frac{u_2 D}{u_1} = \frac{d\alpha_2}{d\hat{x}} \bigg|_f \frac{D}{\hat{\rho}_f \ell_d},$$

where D is the diameter of the body, ℓ_d is the characteristic reaction length and the subscript, f , refers to the frozen state immediately downstream of the translational discontinuity. The initial dissociation rate, $\frac{d\alpha_2}{d\hat{x}} \big|_f$, is determined by the exponential term of equation 4.23 for the frozen state downstream of the shock, where $\alpha_2 = \alpha_1$. Equation 4.18 gives the frozen solution for the density

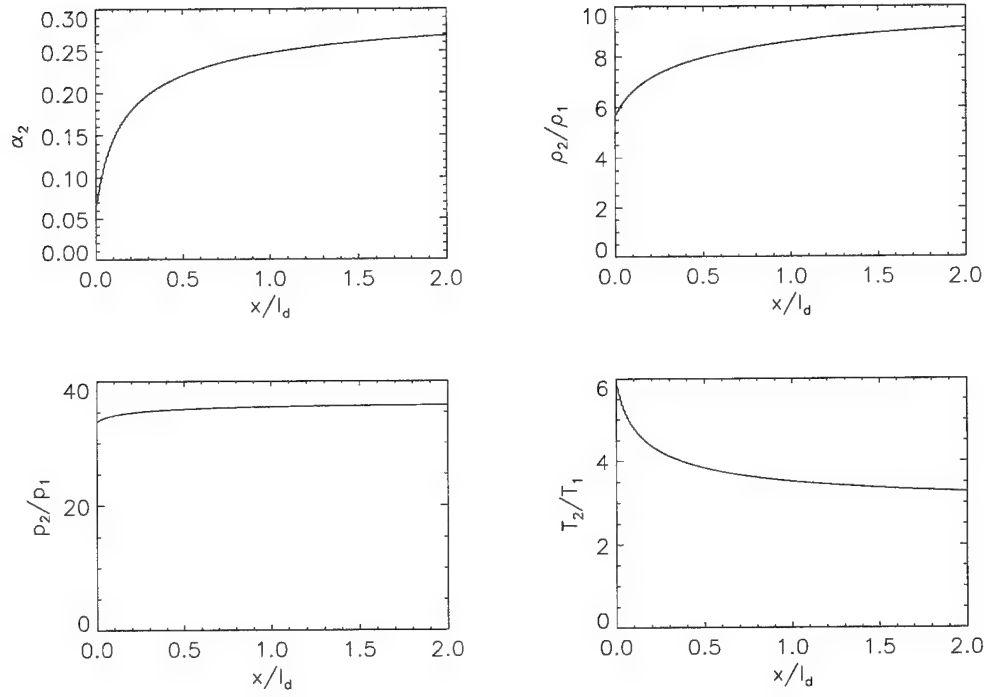


Figure 4.4: NONEQUILIBRIUM SOLUTION FOR THE RELAXATION DOWNSTREAM OF A TRANSLATIONAL DISCONTINUITY IN AN IDEAL DISSOCIATING GAS. The free-stream conditions are $P = 0.0254$, $H_0 = 0.56$, $\hat{p}_d = 8.3 \times 10^6$, $\alpha_1 = 0.051$, $\eta = -2.5$. These conditions are equivalent to the high enthalpy test condition C that was used in the experimental portion of this investigation. For these conditions the characteristic length, $\ell_d = 0.544\text{mm}$, so that for a model diameter of 40 mm the flow is close to equilibrium.

$\theta_d = 113200 \text{ K}$
$\rho_d = 130000 \text{ kg m}^{-3}$
$m = 14.0 \times 10^{-3} / 6.023 \times 10^{23} \text{ kg}$
$C = 2.7 \times 10^{21} \text{ m}^3 \text{ kg}^{-1} \text{ s}^{-1} \text{ K}^{2.5}$
$\eta = -2.5$

Table 4.1: Constants for IDG model.

and the temperature dependence follows from 4.24;

$$\Delta = \frac{D}{\ell_d} \hat{\rho}_f \left(\frac{\Theta}{\hat{T}_f} \right)^{-\eta} (1 - \alpha_1) e^{-\Theta/\hat{T}_f}. \quad (4.25)$$

This parameter is linearly dependent on the ratio of the body size, D , to the characteristic reaction length, ℓ_d . The remaining terms are most strongly dependent on the stagnation enthalpy, H_0 . This may be demonstrated in the hypersonic limit, $P \rightarrow 0$, with $\alpha_1 = 0$. The frozen density ratio reduces to $\hat{\rho}_f \rightarrow 7/(1 + 8P) \rightarrow 7$ and hence $\Theta/\hat{T} \rightarrow 7^2/12K \rightarrow 7^2/12H_0$. In this limit we obtain,

$$\Delta \simeq 7 \frac{D}{\ell_d} \left(\frac{49}{12H_0} \right)^{-\eta} e^{-49/12H_0}. \quad (4.26)$$

This is a good approximation for a wide range of the parameters since the general form, given by equations 4.25 and 4.24, depends only weakly on P and α_1 . The rationale for binary scaling that is used in hypervelocity shock tunnels is apparent from the form of equation 4.26 since this gives similarity in terms of H_0 and Δ .

4.2.5 Physical constants for the IDG model

The physical constants for the IDG model of nitrogen that were used for all computations in this report are given in table 4.1.

4.3 Extension to oblique shock waves

4.3.1 Normal components of the free stream parameters

The extension to oblique waves is obtained by the conventional technique of applying the previous solutions to the component of velocity normal to the shock front. If β is the angle of the oblique shock wave, then from the definitions of P and K we obtain the normal components,

$$P_{1N} = \frac{p_1}{\rho_1 u_1^2 \sin^2 \beta} = \frac{P_1}{\sin^2 \beta}, \quad (4.27)$$

$$K_{1N} = \frac{mu_1^2 \sin^2 \beta}{k\theta_d} = K_1 \sin^2 \beta. \quad (4.28)$$

The identity 4.15 then gives the normal component of the enthalpy,

$$H_{0_{1N}} = K_{1N} \left(1 + 2P_{1N} \frac{4 + \alpha_1}{1 + \alpha_1} \right) + \alpha_1. \quad (4.29)$$

Given $H_{0_{1N}}$, P_{1N} and α_1 the variation of density downstream of the oblique shock is then determined by equation 4.17. Solving simultaneously with equation 4.19 gives the equilibrium solution and integrating the ODE 4.23 determines the intermediate states. Once the density is known the momentum equation, 4.6, gives the pressure variation along the streamline. The variation of the flow deflection angle, δ , is determined from continuity and the conservation of velocity tangential to the shock to be,

$$\tan(\beta - \delta) = \frac{\tan \beta}{\hat{\rho}}. \quad (4.30)$$

This result carries over directly from the perfect gas case and here it applies throughout the relaxation zone.

4.3.2 Variation of parameters across an oblique shock wave

To facilitate the computation of multiple shock jumps for the interaction problem we must find a convenient means of determining P and H_0 downstream of the oblique shock. Since stagnation enthalpy is conserved,

$$H_{0_2} = H_{0_1}. \quad (4.31)$$

In order to determine P_2 observe that $u_2^2 = u_{2T}^2 + u_{2N}^2$ and so $K_2 = K_{2T} + K_{2N}$. Further, since $u_{1T} = u_{2T}$ and $\hat{\rho}u_N = 1$, it follows that

$$K_2 = K_1 \left(\cos^2 \beta + \frac{\sin^2 \beta}{\hat{\rho}^2} \right). \quad (4.32)$$

Identity 4.15 then yields P_2 and the computation for the downstream shock wave proceeds as before using P_2 , H_{0_2} and α_2 as the new upstream condition. Downstream of the shock we must adjust the equilibrium constant according to,

$$\hat{\rho}_{d_2} = \frac{\hat{\rho}_{d_1}}{\hat{\rho}}. \quad (4.33)$$

Again, these relations apply throughout the relaxation zone.

4.3.3 Features of IDG oblique shock waves

The parametric dependence of some arbitrary quantity, ϕ , downstream of an oblique shock wave may then be summarized as,

$$\phi = \phi[P, H_0, \alpha_1, \hat{\rho}_d, x/\ell_d, \eta, \beta];$$

where P behaves as $P \sim 1/M_\infty^2$, H_0 is the dimensionless stagnation enthalpy, α_1 is the upstream dissociation level, $\hat{\rho}_d$ is the equilibrium constant, x/ℓ_d is the dimensionless distance normal to the shock front, η is the temperature exponent of the reaction rate and β is the shock wave angle. To gain some insight into the behavior of the solutions, consider the limit of infinite Mach number with the upstream kinetic energy equal to the dissociation energy; $P = 0$, $H_0 = 1$, $\alpha_1 = 0$. We will consider only the frozen and equilibrium limits and so the dependence on x/ℓ_d and η disappears. The density ratio across the shock wave for such a condition is illustrated in figure 4.5. The dual mechanisms of compressibility and dissociation cause non-monotonic behavior of the shock density ratio with increasing shock angle. Even for very weak shock waves the Mach number normal to the shock wave is sufficient to cause the density to approach the strong shock limit for frozen chemistry. Only at larger shock angles do the frozen and equilibrium solutions deviate as the exponential dependence of the reaction rate and the equilibrium dissociation fraction on the normal component of the enthalpy becomes significant. For the typical shock tunnel test condition that is illustrated in figure 4.6 the distinction between the two mechanisms is less obvious however the conclusion remains valid. For weak waves the density rises faster than the dissociation level and the dissociation rate rises at a still slower rate. The important observation is that for waves of moderate strength that produce low dissociation levels, the reaction rate remains small.

4.4 IDG oblique shock loci in the p - δ plane

4.4.1 Features of oblique shock loci

Shock interaction problems are conventionally represented graphically in the p - δ plane. The influence of real gas effects on this construction is illustrated for a single oblique shock wave in figure 4.7. Real gas effects cause the frozen and equilibrium loci to be separated in proportion to the enthalpy.

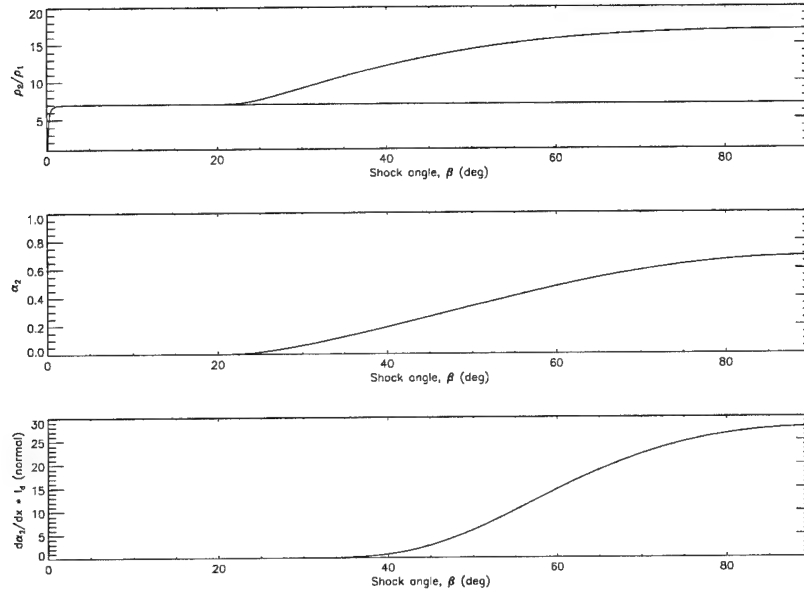


Figure 4.5: Frozen and equilibrium density ratio, equilibrium dissociation level, and initial dissociation rate as functions of shock angle for an oblique wave in an ideal dissociating gas. The free-stream conditions are $P = 1 \times 10^{-6}$, $H_0 = 1.0$, $\alpha_1 = 0$, $\hat{\rho}_d = 1 \times 10^8$.

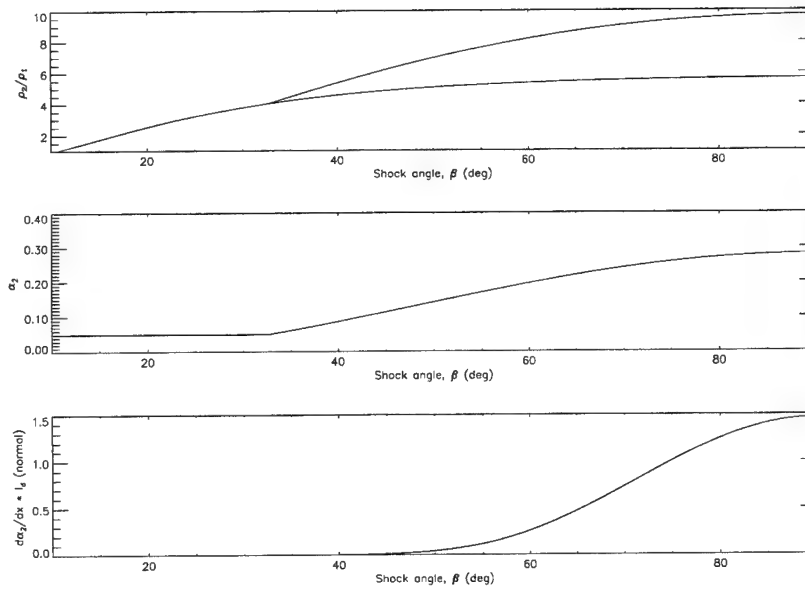


Figure 4.6: Frozen and equilibrium density ratio, equilibrium dissociation level, and initial dissociation rate as functions of shock angle for an oblique wave in an ideal dissociating gas. The free-stream conditions are $P = 0.025$, $H_0 = 0.55$, $\alpha_1 = 0.05$, $\hat{\rho}_d = 1 \times 10^7$. The discontinuity in slope at $\beta = 33^\circ$ arises intentionally as a consequence of the frozen free-stream dissociation level, α_1 .

For endothermic reactions both the pressure and flow deflection angle increase across the relaxation zone. The relative insensitivity of the pressure to real gas effects is evident. Nonequilibrium effects are most pronounced in the flow deflection behind strong waves where the normal component of the enthalpy is large. For nearly normal waves the tangential component of velocity is of the same order as the normal velocity and so relaxation produces a large change in the flow deflection angle. This may be observed in the streamlines that are mapped into the p - δ plane in figure 4.7. Streamlines are defined by equation 4.17 and are parameterized in terms of α_2 ; where $\alpha_2 \in [\alpha_1, \alpha_{2eq}]$ for each β . The pressure and flow deflection angle are given by equations 4.6 and 4.30. In the weak shock limit the origin of the loci in figure 4.7 do not coincide when α_1 is nonzero and sufficiently large. This is a consequence of relaxation of the nonequilibrium upstream state that is demonstrated by the behavior of the second solution branches in figures 4.1 and 4.2.

4.4.2 Mapping of the frozen sonic line

The definition of the speed of sound for a reacting gas is ambiguous since the manner in which the composition changes across the disturbance must be specified (Vincenti & Kreuger [45]). The governing partial differential equations for the steady flow of an inviscid reacting gas exhibit a change from elliptic to hyperbolic type when the local flow velocity exceeds the frozen speed of sound. Thus it is appropriate to consider the Mach number with respect to the frozen speed sound in both the frozen and equilibrium limits behind the shock front. Using the current notation the frozen Mach number is,

$$M_f = \frac{u}{a_f} = \left(\frac{3}{(4 + \alpha)P} \right)^{\frac{1}{2}};$$

where the variation of P through the shock layer is given by equations 4.31, 4.32 and 4.15. The mapping of the sonic line into the p - δ plane is indicated in figure 4.7. A streamline that intersects this sonic line describes an initially subsonic flow that relaxes to a supersonic equilibrium state as the temperature falls behind the shock front. This fact was exploited by Hornung & Smith [22] to explain observations of the detachment of an oblique shock wave from a wedge. It is also indicative of a downstream stretching of the sonic line behind the bow shock on a blunt body.

4.4.3 Shock wave interaction problems in the p - δ plane

The use of the p - δ plane representation to solve shock interaction problems has been discussed in section A.3. Here solutions may be constructed using loci for either the frozen or equilibrium equations of state. The resulting solutions apply directly at the intersection point or far from the shock fronts respectively. Near and far are interpreted relative to the characteristic reaction length, ℓ_d . The nonequilibrium solution 4.23 that applies for length scales intermediate to the frozen and equilibrium limits remains valid in regions where the flow is one-dimensional normal to the shock

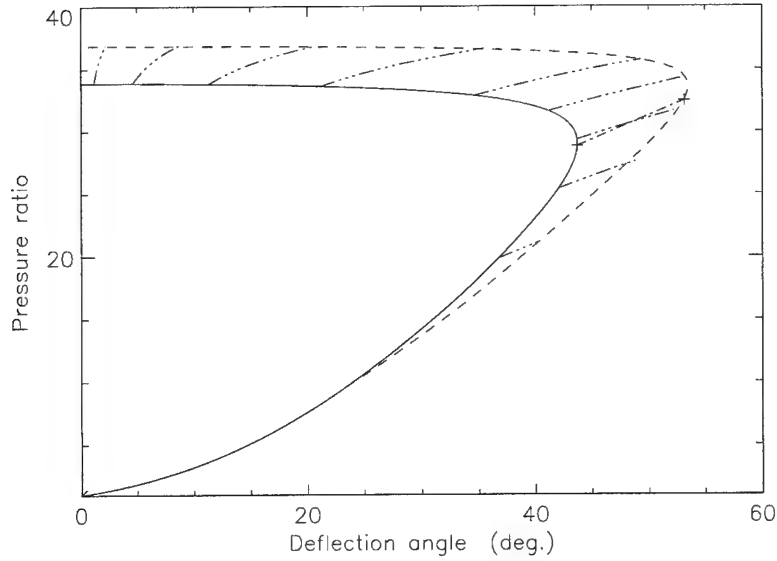


Figure 4.7: p - δ PLANE REPRESENTATION OF AN OBLIQUE SHOCK WAVE FOR AN IDEAL DISSOCIATING GAS. Solid curve is the frozen locus. Dashed curve is the equilibrium locus. — · — are streamlines for shock angles $\beta = 40^\circ, 50^\circ, 60^\circ, 68.5^\circ, 75^\circ, 80^\circ, 85^\circ, 87.5^\circ, 89^\circ$ and 89.75° respectively. — · — is the mapping of the frozen sonic line connecting the frozen and equilibrium limits (+). The free stream conditions approximate test condition C that was used in the experimental investigation; $P = 0.025, H_0 = 0.55, \hat{p}_d = 1 \times 10^7, \alpha_1 = 0.05$.

fronts (Figure 4.8). A typical computation of the loci illustrating the asymmetrical interaction of two oblique shock waves is illustrated in figure 4.9. Although chemical nonequilibrium causes subtle differences in the Mach reflection transition mechanisms, these effects are small since the waves remain relatively weak up to the transition point.

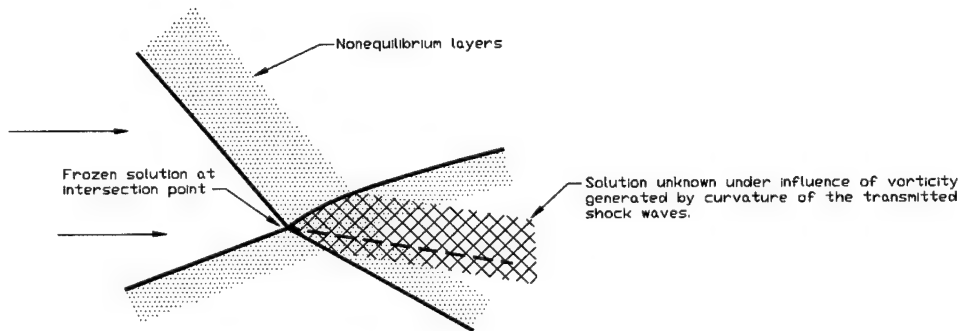


Figure 4.8: Extent of validity of p - δ plane representation for the interaction of oblique shock waves in an ideal dissociating gas.

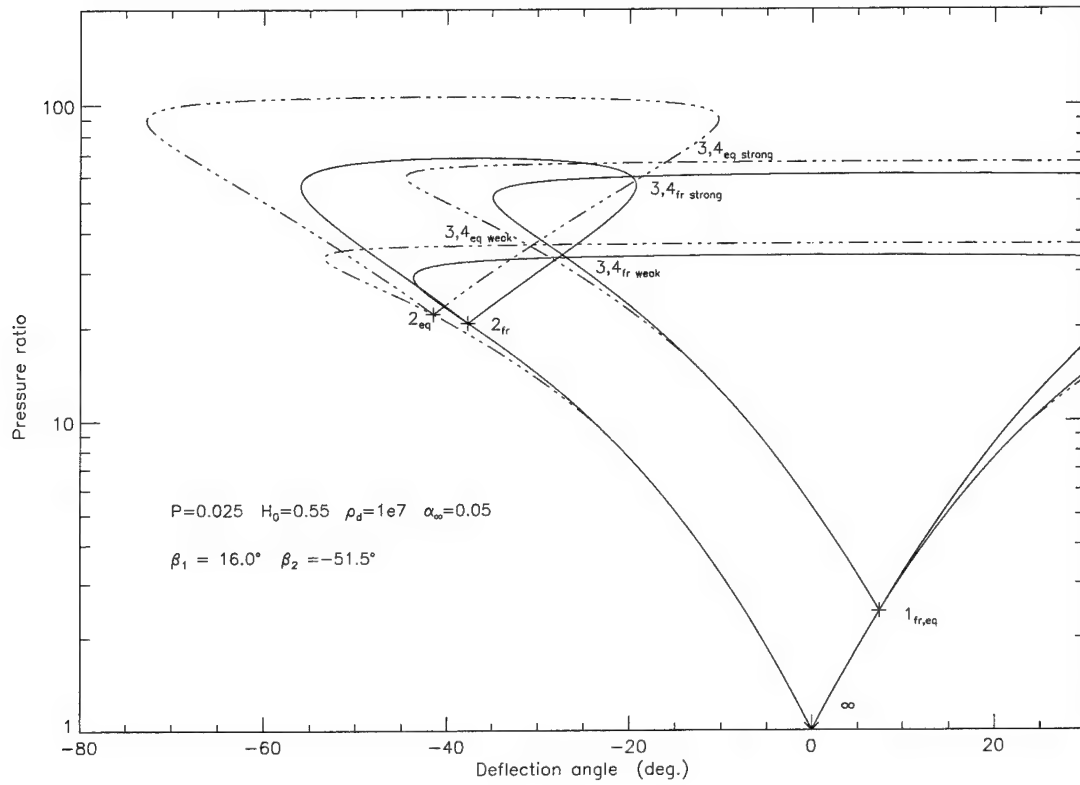


Figure 4.9: p - δ PLANE REPRESENTATION OF THE INTERACTION OF OBLIQUE SHOCK WAVES IN AN IDEAL DISSOCIATING GAS. The shock angles are $\beta_1 = 16^\circ$, $\beta_2 = -51.5^\circ$ and the numbering of the states is given in figure A.3. The free-stream conditions are $P = 0.025$, $H_0 = 0.55$, $\rho_d = 1 \times 10^7$, $\alpha_1 = 0.05$. Solid curves are the frozen shock loci. — · · · — are the equilibrium shock loci.

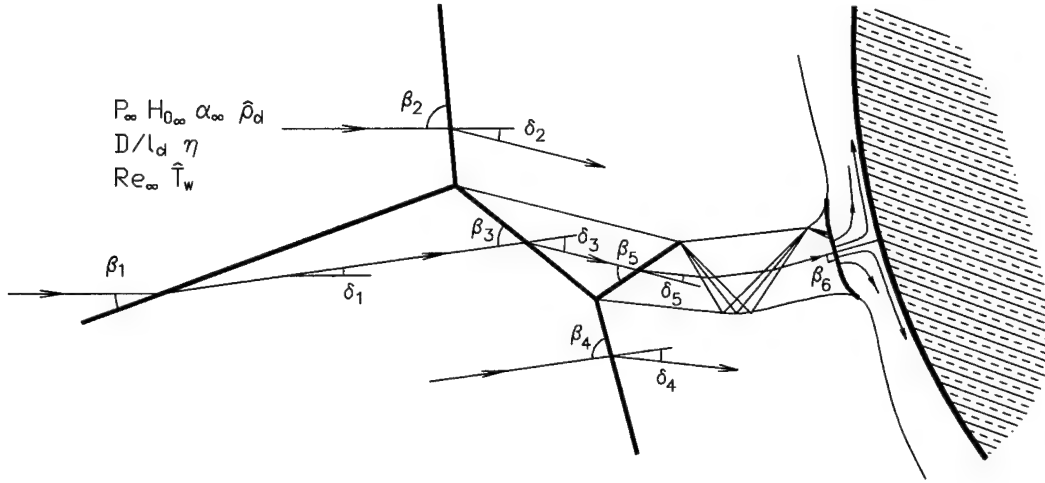


Figure 4.10: Schematic of flow field and shock wave notation for the type IV interaction in the vicinity of the impingement point.

4.5 λ -shock configuration for an ideal dissociating gas

4.5.1 Introduction

The λ -pattern of shock waves that is observed to form where the shock wave impinges on the leading edge of the blunt body is one of the most clearly recognizable features of the type IV flow field. For a given free-stream condition and incident shock angle, the remaining quantities are determined entirely by local satisfaction of the conservation equations at the impingement point. This is the fundamental mechanism that causes the formation of the type IV jet and so analysis of the influence of real gas effects on the shock angles and density field is appropriate. The idealized flow field and the notation for the shock waves are shown in figure 4.10. We proceed by mapping the interaction problem into the p - δ plane in order to obtain the frozen, equilibrium and approximate nonequilibrium solutions.

4.5.2 Formulation of the problem

A methodology for determination of the generic states A and B across a shock wave was described in section 4.3. Here it is described functionally by the relationship,

$$(\hat{p}_B, \hat{p}_B, \delta_B, P_B, H_{0B}, \alpha_B) = \mathcal{J}(P_A, H_{0A}, \alpha_A, \hat{p}_d, \beta).$$

The shock jump conditions, \mathcal{J} , are obtained from equation 4.17 combined with equation 4.18 in the frozen limit or with equation 4.19 in the equilibrium limit. The equilibrium solution is only valid sufficiently far from the intersection point that curvature of the shock waves due to relaxation may be neglected (Section 4.4.3). Normal components of the parameters are used as determined in

section 4.3. The solution of the λ -shock problem is then given by the system of equations,

$$(\hat{\rho}_2, \hat{p}_2, \delta_2, P_2, H_{0_2}, \alpha_2) = \mathcal{J}(P_\infty, H_{0_\infty}, \alpha_\infty, \hat{\rho}_d, \beta_2), \quad (4.34)$$

$$(\hat{\rho}_1, \hat{p}_1, \delta_1, P_1, H_{0_1}, \alpha_1) = \mathcal{J}(P_\infty, H_{0_\infty}, \alpha_\infty, \hat{\rho}_d, \beta_1), \quad (4.35)$$

$$(\hat{\rho}_3, \hat{p}_3, \delta_3, P_3, H_{0_3}, \alpha_3) = \mathcal{J}(P_1, H_{0_1}, \alpha_1, \hat{\rho}_d/\hat{\rho}_1, \beta_3). \quad (4.36)$$

Matching the pressure and flow deflection angle across the shear layer that originates at the intersection point we have,

$$\hat{p}_2 = \hat{p}_1 \hat{p}_3, \quad (4.37)$$

$$\delta_2 = \delta_1 + \delta_3. \quad (4.38)$$

Collectively, equations 4.34, 4.35, 4.36, 4.37 & 4.38 represent 20 equations in the 20 variables $\hat{\rho}_{1,2,3}$, $\hat{p}_{1,2,3}$, $\delta_{1,2,3}$, $P_{1,2,3}$, $H_{0_{1,2,3}}$, $\alpha_{1,2,3}$, $\beta_{2,3}$ and for convenience we choose β_1 , P_∞ , H_{0_∞} , α_∞ and $\hat{\rho}_d$ as parameters. For a given free-stream condition and shock angle this system describes a path of solutions for each H_{0_∞} from which we may study the influence of real gas effects. The equations are solved using Newton's method for the cases of frozen and equilibrium chemistry and the solution is continued in H_{0_∞} . Solution curves for the density, dissociation levels, shock wave angles, flow deflection angles, and reaction rates are plotted in figure 4.11. The uniqueness of the solution that is obtained is not guaranteed however the solution branch that we study is consistent with the experimental observations.

Consider next the computation of the initial reaction rates downstream of the translational discontinuities. Observe that the free stream conditions for the computation of shock, 3, given by equation 4.36, are based on state 1. The normalization of the reaction rates must therefore be adjusted to a common basis for comparison and this is chosen to be the characteristic reaction length for the free stream, ℓ_{d_∞} . For the i -th shock we then have,

$$\frac{d\alpha_i}{d\hat{x}_\infty} = \frac{d\alpha_i}{d\hat{x}_{i_N}} \frac{d\hat{x}_{i_N}}{dx_{i_N}} \frac{dx_\infty}{d\hat{x}_\infty} \frac{dx_{i_N}}{dx_\infty}, \quad (4.39)$$

where the subscript, N , refers to the distance normal to the shock front. The first term on the right-hand side, $\frac{d\alpha_i}{d\hat{x}_{i_N}}$, is given by equation 4.23 using the normal components of the parameters for the i -th shock. The remaining terms that adjust the normalization are;

$$\frac{d\hat{x}_{i_N}}{dx_{i_N}} = \frac{1}{\ell_{d_{i-1N}}} = \frac{\rho_{i-1} \theta_d^\eta C}{u_{i-1N}},$$

$$\frac{dx_\infty}{d\hat{x}_\infty} = \ell_{d_\infty} = \frac{u_\infty}{\rho_\infty \theta_d^\eta C},$$

$$\frac{dx_{i_N}}{dx_\infty} = \sin(\beta_i + \sum_{j=1}^{i-j=1} \delta_{i-j}).$$

The notation, i_{-j} , refers to the sequence of upstream shocks involved in the normalization (e.g. for shock $i = 6$; $i_{-j} \in [5, 3, 1]$ with $i_{-1} = 5$, $i_{-2} = 3$ etc.). Substituting these relations into equation 4.39 and using the definition of the dimensionless specific kinetic energy, K , we obtain the consistently normalized reaction rate;

$$\frac{d\alpha_i}{d\hat{x}_\infty} = \frac{d\alpha_i}{d\hat{x}_{i_N}} \sqrt{\frac{K_\infty}{K_{i_{-1}N}}} \prod_{j=0}^{i-j=1} \hat{\rho}_{i-j} \sin(\beta_i + \sum_{j=1}^{i-j=1} \delta_{i-j}). \quad (4.40)$$

4.5.3 Discussion of the solution

Interpretation of the solutions that are illustrated in figure 4.11 follows from the results presented in figure 4.6. We see that the influence of real gas effects increases strongly with increasing stagnation enthalpy, H_0 . Dissociation is negligible behind the weak impinging wave and dissociation levels increase proportionally for the moderate strength wave, 3, and the nearly normal wave, 2. The corresponding increases in the density are the most important real gas effects.

A further similarity with the conclusions drawn from figure 4.6 is the behavior of the normalized reaction rates. The reaction rate behind the impinging wave, $d\alpha_1/d\hat{x}_\infty$, is negligibly small in both the frozen and equilibrium limits. The angles of the stronger shock waves, β_2 and β_3 , vary in the frozen and equilibrium limits and so produce different initial reaction rates. Behind shock 3 the initial reaction rate in the equilibrium limit is an order of magnitude smaller than that behind the nearly normal wave, 2. This is a significant effect because it controls the relaxation of the density downstream of the interaction.

The strongest effect on the measurable wave angles is observed in the deflection angle, $\delta_{2,3} = \delta_2 = \delta_1 + \delta_3$, of the shear layer generated at the impingement point. We see from the mapping of the streamlines into the p - δ plane in figure 4.7 that the strongest effects on the flow deflection angle are apparent for nearly normal waves. This causes the strong initial effect on the flow deflection angle as H_0 increases. The effect reduces as the dissociation level behind shock 3 rises at still larger values of H_0 .

4.5.4 Representation of the nonequilibrium approximation in the p - δ plane.

Since the reaction rates downstream of the weaker oblique waves, 1 and 3, at a λ -point are significantly less than that downstream of the strong wave, 2, we introduce the nonequilibrium approximation, $d\alpha_2/d\hat{x}_\infty \gg d\alpha_3/d\hat{x}_\infty$. It is assumed that waves 1 and 3 remain frozen whilst wave 2 is allowed to relax to equilibrium. This provides a simple means of assessing the impact of thermochemical nonequilibrium on the flow field, within the constraints of the current local model that is predicate

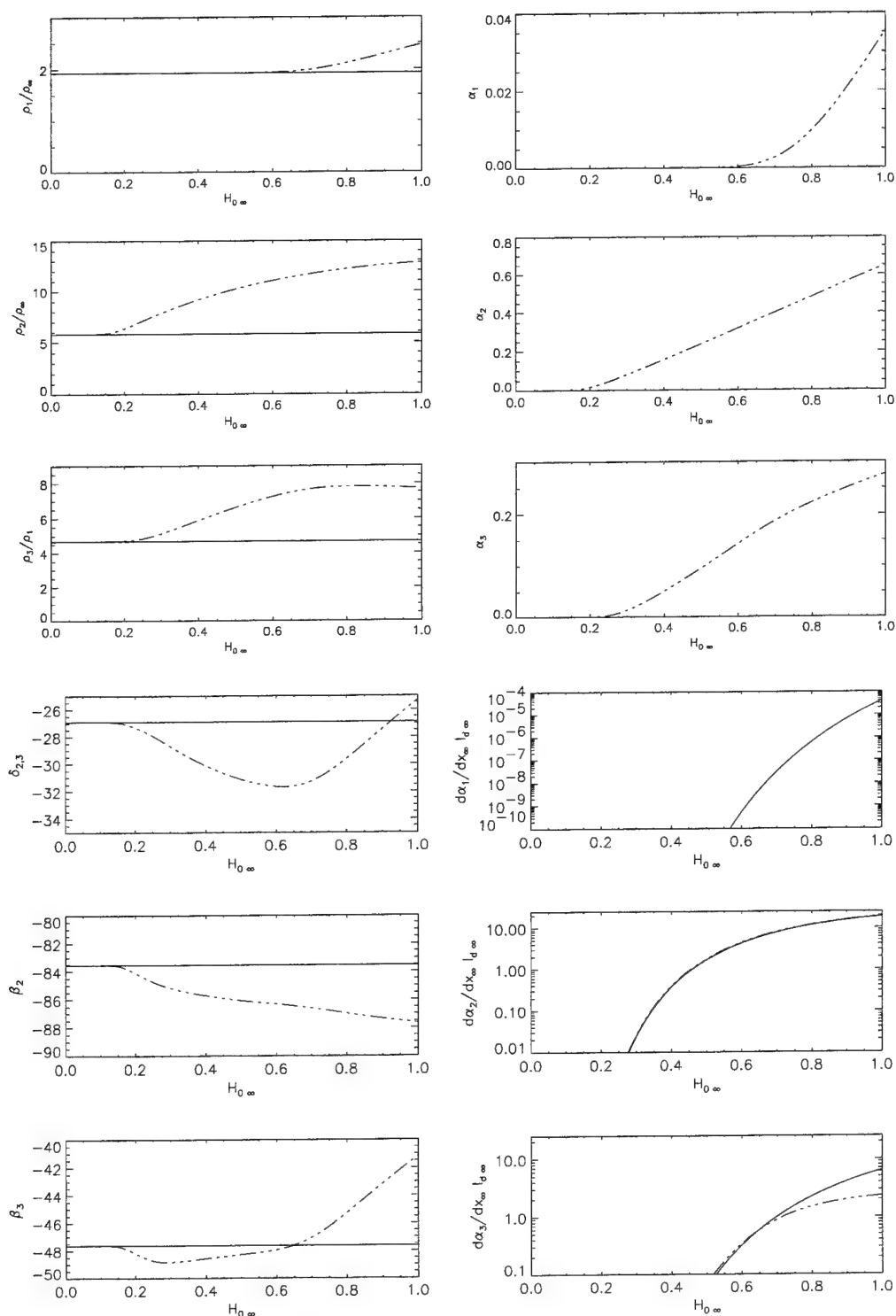


Figure 4.11: DENSITY VARIATIONS, DISSOCIATION LEVELS, SHOCK WAVE ANGLES, STREAMLINE DEFLECTION, AND REACTION RATES AS FUNCTIONS OF STAGNATION ENTHALPY, $H_{0\infty}$, AT A λ -SHOCK POINT IN AN IDEAL DISSOCIATING GAS. The free-stream conditions are $P_\infty = 0.025$, $\hat{p}_d = 1 \times 10^7$, $\alpha_\infty = 0$, $\beta_1 = 16^\circ$. Solid curves are the frozen solutions. — · · · — are the equilibrium solutions.

on the assumption of one-dimensional flow normal to the shock fronts.

Although the strong wave, 2, is curved we can still map certain regions of the flow into the p - δ plane with validity. Three valid solutions may be obtained;

1. The frozen solution that applies at the intersection point.
2. The intermediate solution that applies under the above approximation where only the strong wave, 2, is allowed to relax to equilibrium.
3. The equilibrium limit that applies far from the intersection point.

These limits are mapped into the p - δ plane in figure 4.12 along with their representation in the physical plane that is shown in figure 4.13. The approximation $d\alpha_2/d\hat{x}_\infty \gg d\alpha_3/d\hat{x}_\infty$ amounts to the requirement that the shock fronts remain straight over length scales that are intermediate to the two disparate relaxation lengths. Therefore the one-dimensional solution for the relaxation behind a straight shock front may be used to map the streamlines in this region. The extent of validity of this solution is limited by the subsequent relaxation of the supersonic region, 3. Sufficiently far downstream the equilibrium solution is obtained.

Since $P_2 \gg P_3$ it is also possible to infer the shear layer departure angle from the frozen limit in the p - δ plane. Note the interpretation of $P = p/\rho u^2$ as the ratio of pressure force to inertia force (c.f. $P \sim 1/M^2$). Since $p_2 = p_3$ and $P_2 \gg P_3$ it follows that the inertia of the frozen supersonic flow, 3, dominates the pressure of the relaxing subsonic flow behind the strong shock. This determines the vertical departure of the stream line from the frozen intersection point in figure 4.12. Extrapolating upward towards the intermediate limit we see that this effect produces a further curvature of the strong shock, 2, towards normal. This is addition to that caused by the difference in the relaxation lengths.

Numerical calculations of the three limits are shown in figure 4.14. Points of inflection are produced on both transmitted wave fronts whilst the shear layer curves monotonically at this level of approximation. These arguments lead to the flow field that is sketched in figure 4.13. These slight changes in the shock angles are of secondary importance in comparison to the density and reaction rate variations.

The aim of the nonequilibrium approximation is to provide an indication of the influence of finite rate effects without recourse to full numerical simulation. An additional possibility, that is not pursued here, follows from the observation that the partial differential equations that describe the steady flow in the supersonic jet are hyperbolic. Numerical simulations of the nonequilibrium jet flow using space marching techniques are possible if the shear layers are treated as constant pressure boundaries. This approach shares the limitations of the current local model whereby the scale of the interaction region and the location of the terminating jet shock remain indeterminate.

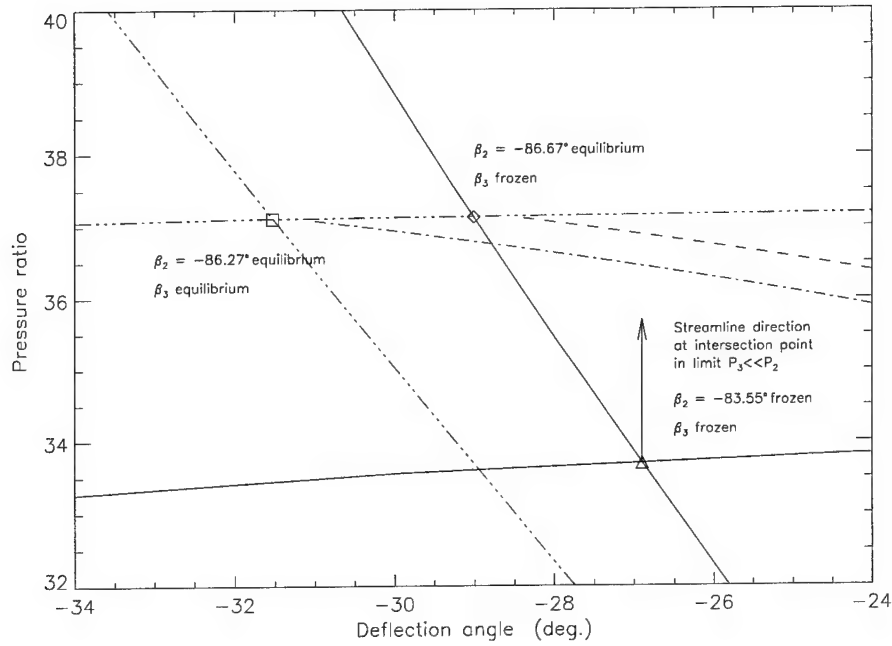


Figure 4.12: REPRESENTATION OF THE IDG λ -SHOCK CONFIGURATION IN THE p - δ PLANE. Solid curves are the frozen shock loci. — · — curves are the equilibrium shock loci. Solution points are; Δ -frozen limit, \diamond -nonequilibrium approximation, square-equilibrium limit. — — — and — · — are the streamlines behind shock 2 in the nonequilibrium approximation and equilibrium limit respectively. Free-stream conditions are $P = 0.025$, $H_{0\infty} = 0.56$, $\alpha_\infty = 0$, $\hat{p}_d = 1 \times 10^7$, $\beta_1 = 16^\circ$.

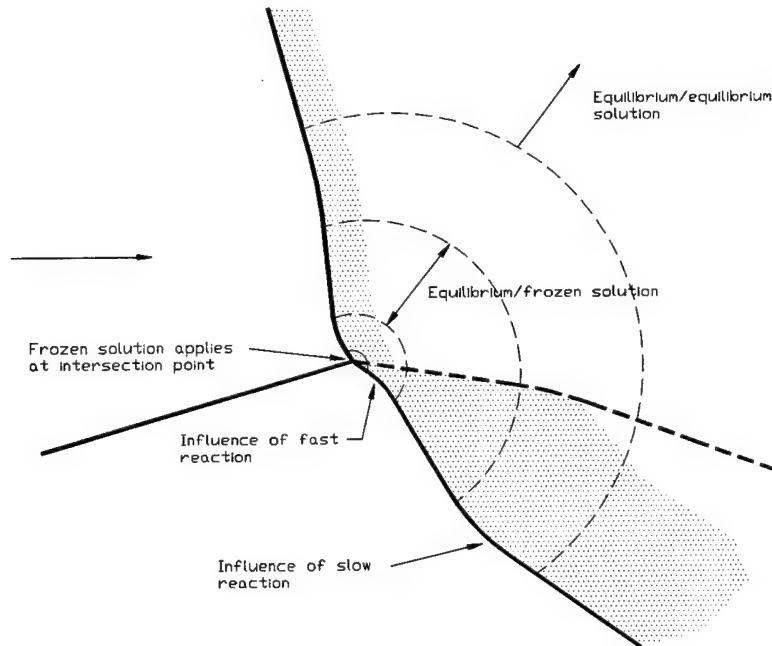


Figure 4.13: Schematic representation of the effects of finite rate dissociation on the λ -shock configuration.

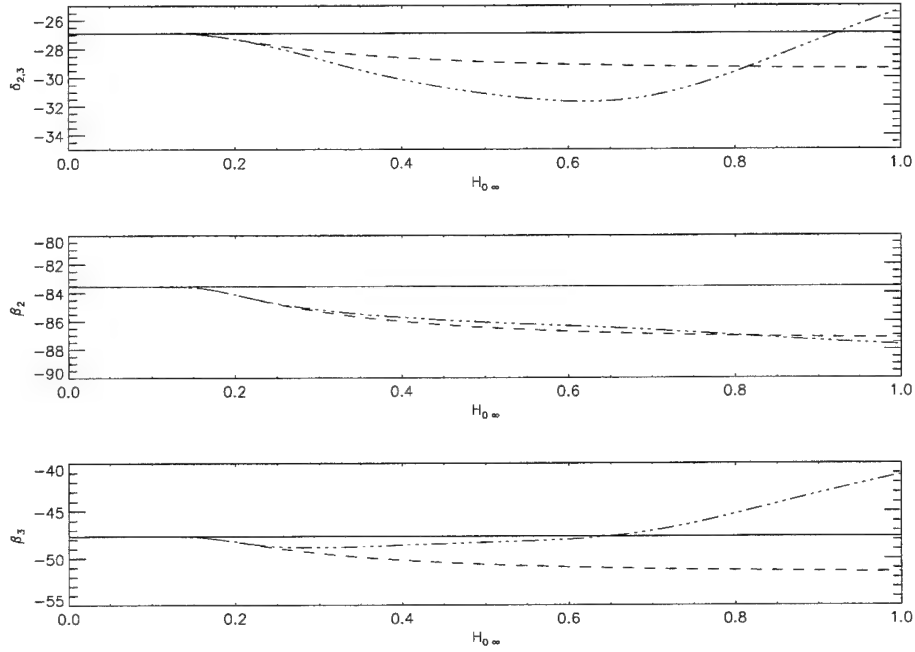


Figure 4.14: EFFECT OF FINITE RATE DISSOCIATION ON THE SHOCK WAVE ANGLES AND FLOW DEFLECTION DOWNSTREAM OF A λ -SHOCK CONFIGURATION. Solid curves are the frozen solutions, — — — curves are the nonequilibrium approximations, — · — · — curves are the equilibrium solutions. Free-stream conditions are $P = 0.025$, $\alpha_\infty = 0$, $\hat{\rho}_d = 1 \times 10^7$, $\beta_1 = 16^\circ$.

4.6 Type IV inverted λ -shock for an ideal dissociating gas

The preceding analysis for the λ -shock configuration may be extended to account for the second inverted λ -shock that is observed to appear in the type IV interaction. The flow geometry and additional notation are described in figure 4.10. The system of equations 4.34–4.38 is extended by the addition of,

$$(\hat{\rho}_4, \hat{p}_4, \delta_4, P_4, H_{04}, \alpha_4) = \mathcal{J}(P_1, H_{01}, \alpha_1, \hat{\rho}_d/\hat{\rho}_1, \beta_4). \quad (4.41)$$

$$(\hat{\rho}_5, \hat{p}_5, \delta_5, P_5, H_{05}, \alpha_5) = \mathcal{J}(P_3, H_{03}, \alpha_3, \hat{\rho}_d/(\hat{\rho}_1\hat{\rho}_3), \beta_5). \quad (4.42)$$

$$\hat{p}_4 = \hat{p}_3\hat{p}_5, \quad (4.43)$$

$$\delta_4 = \delta_3 + \delta_5. \quad (4.44)$$

Equations 4.41–4.44 represent an additional 14 equations in the 14 variables $\hat{\rho}_{4,5}$, $\hat{p}_{4,5}$, $\delta_{4,5}$, $P_{4,5}$, $H_{04,5}$, $\alpha_{4,5}$ and $\beta_{4,5}$ that are decoupled from the solution of the preceding system 4.34–4.38. Again, this system describes a path of solutions for each $H_{0\infty}$ where the remaining parameters, P_∞ , α_∞ , $\hat{\rho}_d$ & β_1 , are held constant. Since the two systems of equations decouple, the λ -shock solutions illustrated in figure 4.11 apply at the impingement point for the type IV configuration. Solutions

of the additional system of equations 4.41–4.44 that apply at the downstream inverted λ -shock are illustrated using the same format in figure 4.15.

The behavior is somewhat different from that shown in figure 4.11 for the particular values of the parameters that have been chosen. Here the incident wave, 3, is stronger than the reflected wave, 5. In the equilibrium case the reaction rate behind wave 5 is very small since the wave is weak and the flow behind the stronger wave upstream of it has already relaxed. In the frozen case the reaction rate is much higher because of the departure from equilibrium caused by the now frozen wave, 3, upstream of it. In either case the reaction rates for the weaker waves, 3 and 5, remain an order of magnitude smaller than that for the nearly normal wave, 4. Figures 4.11 and 4.15 combine to describe a particular instance of a type IV jet in which the intermediate wave, 3, is stronger than the surrounding waves, 1 and 5. We will return to this important point later.

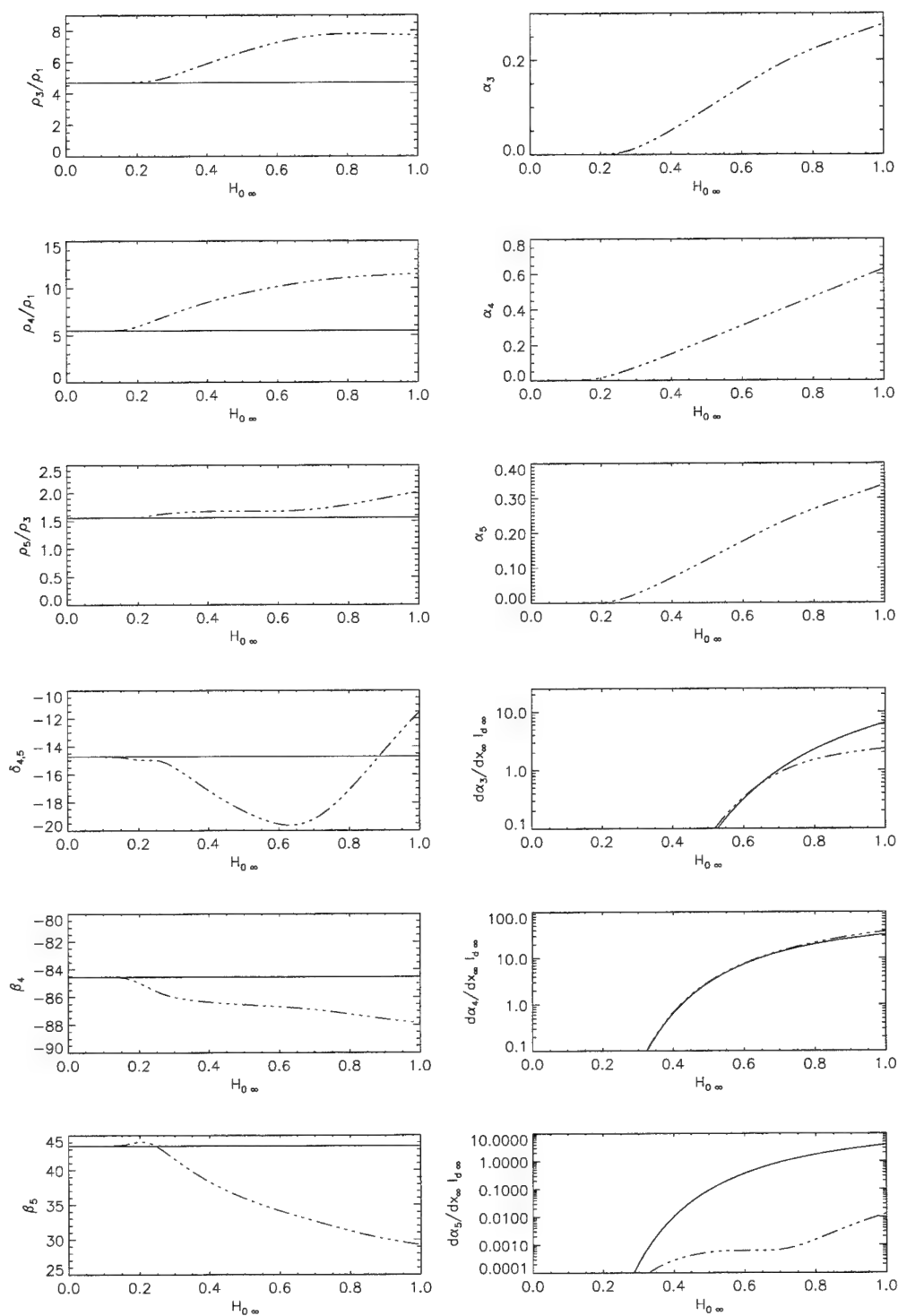


Figure 4.15: DENSITY VARIATIONS, DISSOCIATION LEVELS, SHOCK WAVE ANGLES, STREAMLINE DEFLECTION, AND REACTION RATES AS FUNCTIONS OF STAGNATION ENTHALPY, $H_{0\infty}$, AT A TYPE IV INVERTED λ -SHOCK POINT IN AN IDEAL DISSOCIATING GAS. The free-stream conditions are $P_\infty = 0.025$, $\hat{p}_d = 1 \times 10^7$, $\alpha_\infty = 0$, $\beta_1 = 16^\circ$. Solid curves are the frozen solutions. — · · · — are the equilibrium solutions.

4.7 Heat transfer model

4.7.1 Introduction

The preceding sections describe the use of the IDG model to study the thermochemical processes that occur in the inviscid type IV jet flow. The solutions that are obtained determine the state of the gas that impinges on the surface of the body. The following section describes the reacting flow stagnation point model that is used to estimate the heat transfer rates. In subsequent sections the two models are combined to obtain the final result.

4.7.2 Fay & Riddell stagnation point heat transfer solution

The stagnation point heat transfer solution of Fay & Riddell [11] represents the canonical example of the influence of finite rate chemistry on blunt body heat transfer. By applying the Illingworth transformation to the boundary layer equations for a compressible, non-equilibrium reacting flow, Fay & Riddell demonstrated that self similar solutions are admitted at the stagnation point for arbitrary chemical reaction rates. Fay & Riddell implicitly formulated the problem including the source terms and outer solution for axisymmetric bodies. This affects the coefficients of the similarity equations and therefore the dimensionless velocity and enthalpy profiles across the boundary layer. To rework the Fay & Riddell solution and re-correlate the computations for planar flows of nitrogen is non trivial and has not been undertaken here. The transport properties for nitrogen are assumed to be sufficiently similar to Fay & Riddell's binary mixture approximation for air that the results are adequate to describe any flow phenomena observed here.

The stagnation point heat transfer rate when the boundary layer is in chemical equilibrium is correlated by an expression of the form (Fay & Riddell [11]);

$$\dot{q} = \zeta_1 (\rho_w \mu_w)^{0.1} (\rho_e \mu_e)^{0.4} \sqrt{\left. \frac{du_e}{dx} \right|_0} (h_e - h_w) \left[1 + (Le^{0.52} - 1) \frac{h_d}{h_e} \right]. \quad (4.45)$$

Here \dot{q} is the heat transfer per unit area and time, μ is the viscosity, $\left. \frac{du_e}{dx} \right|_0$ is the transverse velocity gradient at the outer edge of the boundary layer, Le is the Lewis number, h_d is the chemical enthalpy of the dissociated gas at the edge of the boundary layer and the remaining symbols are defined as before. The subscripts, w and e , denote conditions at the wall and at the outer edge of the boundary layer respectively. The constant of proportionality is $\zeta_1 = 0.94$ for axisymmetric bodies. For planar bodies the value $\zeta_1 = 0.70$ is obtained by extrapolation of results for non-reacting flow (White [47]).

4.7.3 Outer flow solutions

In order to apply this result we must assess the velocity gradient term, du_e/dx , at the stagnation point. Conventionally this is done by application of the Newtonian approximation for thin shock layers. Since the density of the outer flow at the stagnation point is constant we have,

$$p_e(x) + \frac{1}{2}\rho_e u_e(x)^2 = p_e(0).$$

The x coordinate is measured along the surface of the body with its origin at the stagnation point. Applying L'Hopital's rule in the limit as $x \rightarrow 0$ gives the conventional result,

$$\left[\frac{du_e}{dx} \right]_0^2 = \frac{-\frac{d^2 p}{dx^2}|_0}{\rho_e}.$$

The Newtonian approximation gives the pressure distribution as, $p_e(x) = \rho_\infty u_\infty^2 \sin^2 \beta(x)$. For thin shock layers where the shock inclination, β , is closely approximated by the local surface slope, x/R , the stagnation point velocity gradient becomes;

$$\frac{du_e}{dx} \Big|_0 = \frac{u_\infty}{R} \sqrt{2\rho_\infty/\rho_e} \quad (4.46)$$

where R is the radius of curvature of the planar or axisymmetric body. Writing the result in this form, the influences of real gas effects are evident in terms of the free-stream velocity and the shock density ratio.

The thin shock layer approximation used to obtain equation 4.46 fails in the limit $R \rightarrow \infty$. This case is important since it is required for analysis of the blunt cylinder heat transfer data and also as an approximation for the impingement of the type IV jet where the jet width is much smaller than the body diameter. On dimensional grounds the dependence of the velocity gradient must be;

$$\frac{\frac{du_e}{dx} \Big|_0 R}{u_\infty} = \text{func} \left(M_\infty, \frac{\rho_e}{\rho_\infty} \right).$$

In the perfect gas case, that is discussed in some detail by White [47], the density ratio is determined uniquely by the Mach number and in the hypersonic limit this asymptotes to $\frac{\gamma+1}{\gamma-1}$. White (Figure 7-7) cites computational and experimental results that give,

$$\frac{\frac{du_e}{dx} \Big|_0 R}{u_\infty} = 0.15,$$

in the limit $M \rightarrow \infty$ for flow of a perfect gas ($\gamma = 1.4$) over a blunt faced body. On the basis of the density dependence exhibited by equation 4.46 we extrapolate to the case of a dissociating gas at

high Mach numbers;

$$\left. \frac{du_e}{dx} \right|_0 = \zeta_2 \frac{u_\infty}{R} \sqrt{2\rho_\infty/\rho_e} \quad (4.47)$$

with,

$$\zeta_2 = \begin{cases} 1, & 1/R > 0, \\ 0.15 \times \sqrt{6/2} = 0.26, & 1/R = 0. \end{cases} \quad (4.48)$$

The discontinuous limit that is indicated in equation 4.48 is unrealistic and the question of appropriate scalings for the velocity gradient in this regime remains open. This level of approximation is considered adequate for the current conceptual model. Only ratios of the parameters ζ_1 and ζ_2 are contained in the final result and they arise in a form that is not critical to the conclusions of the model.

4.7.4 Stagnation point recombination rate parameter

The key conclusion drawn from the nonequilibrium solutions of Fay & Riddell [11] is that if the recombination rate is sufficiently high, so that the gas remains close to equilibrium throughout the boundary layer, or if the wall is catalytic and the Lewis number remains close to unity, so that the diffusive and conductive mechanisms of energy transport in the layer are similar in magnitude, then the influence of recombination on the boundary layer is adequately represented by the chemical component of the total enthalpy that is used as the forcing gradient in correlations of the heat flux. Nonequilibrium effects were observed as a decrease in the heat transfer rate to the wall only under conditions when the recombination rate was slow and the wall was non-catalytic. Wall catalyticity was unimportant at high recombination rates.

Following Fay & Riddell [11], the departure of the stagnation point boundary layer from equilibrium may be assessed by comparing the lifetime of an atom at the outer edge of the boundary layer with the diffusion time scale across the boundary layer. For the ideal dissociating gas model that we use here the time rate of change of the mass of atoms per unit mixture mass due to recombination is given by the second term of the rate equation 4.21,

$$\left. \frac{d\alpha}{dt} \right|_{recomb} = -C\rho^2 T^\eta \frac{\alpha^2}{\rho_d} = -\ell_d^{-1} \hat{\rho}^2 \left(\frac{\hat{T}}{\hat{\Theta}} \right)^\eta \frac{\alpha^2}{\hat{\rho}_d} u_\infty. \quad (4.49)$$

The dimensionless notation and parameters that are used here are developed in section 4.2. The lifetime of an atom in the boundary layer scales with $\left. \frac{d\alpha}{dt} \right|_{recomb}^{-1}$. If this is evaluated at the outer edge of the boundary layer and normalized by the velocity gradient (equation 4.47) at the stagnation point we define the recombination rate parameter,

$$\Sigma = \frac{d\alpha/dt_{recomb_e}}{\alpha_e^2} \left[\left. \frac{du_e}{dx} \right]_0^{-1} = \frac{D}{\ell_d} \frac{\hat{\rho}_e^{5/2} \left(\frac{\hat{T}_e}{\hat{\Theta}} \right)^\eta}{2\sqrt{2}\zeta_2 \hat{\rho}_d}. \quad (4.50)$$

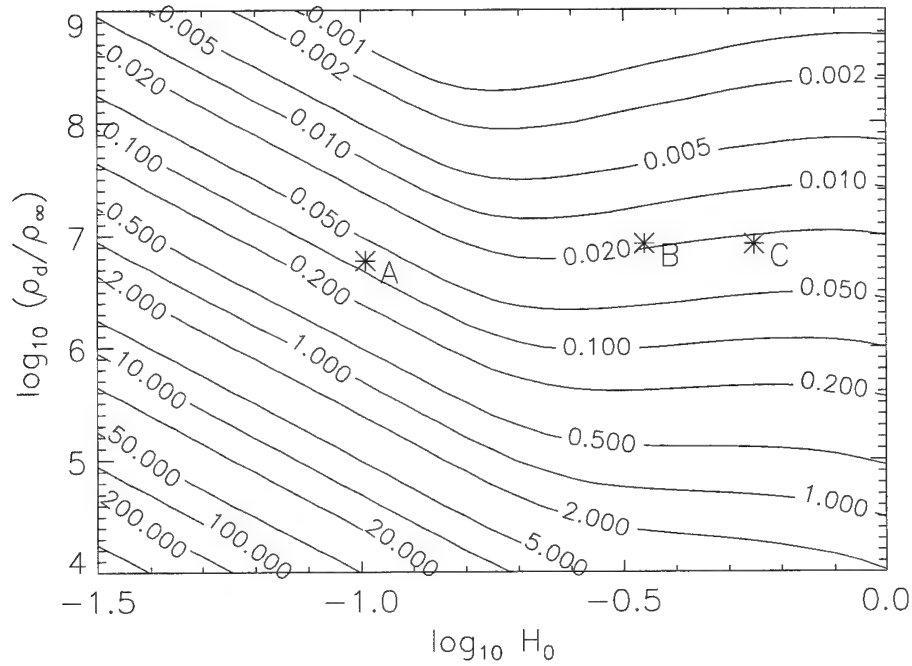


Figure 4.16: CONTOUR PLOT OF THE RECOMBINATION RATE PARAMETER, $\Sigma \frac{\zeta_{2\ell_d}}{D}$, AS A FUNCTION OF DIMENSIONLESS STAGNATION ENTHALPY, H_0 , AND EQUILIBRIUM DENSITY RATIO, ρ_d . The contours values are indicated on the plot and the remaining parameters are taken as $P = 0$, $\alpha_\infty = 0$, $\eta = -2.5$. The dependence on P for large Mach numbers is weak. At low enthalpies where the dissociation levels are low the contours asymptote to slope η . At higher enthalpies Σ is insensitive to H_0 and exhibits an inverse power dependence on ρ_d . The three test conditions used for the current experiments are indicated.

Only the dimensional terms of equation 4.49 multiplying the dissociation level, α^2 , have been included since this leads to the form that arises in the similarity formulation. The temperature ratio at the edge of the boundary layer is approximated by the solution for the equilibrium shock layer 4.24,

$$\frac{\Theta}{\hat{T}} = \frac{\hat{\rho}^2(1 + \alpha)}{2K[\hat{\rho}(P + 1) - 1]}.$$

The boundary layer tends to equilibrium for $\Sigma \gg 1$ and is frozen for $\Sigma \ll 1$. The nonequilibrium solutions of Fay & Riddell [11] indicate that nonequilibrium effects become significant only for values of $\Sigma < 0.1$ when the wall is non catalytic to the recombination reaction. Contours of the recombination rate parameter in the universal form, $\Sigma \frac{\zeta_{2\ell_d}}{D}$, are indicated in figure 4.16 along with the values for the three test conditions that were used in the experimental investigation. Table 4.2 indicates the values of the recombination rate parameter for the current experiments and in all cases the boundary layer is justifiably treated as equilibrium since $\Sigma \gg 0.1$.

Test condition	A	B	C
$\Sigma \frac{\zeta_2 \ell_d}{D}$	0.080	0.018	0.025
ζ_2	1	1	1
ℓ_d	0.19 mm	0.46 mm	0.54 mm
D	40.6 mm	40.6 mm	40.6 mm
Σ	17.	1.6	1.9

Table 4.2: Predicted recombination rate parameters for test conditions A, B & C.

4.7.5 Normalization of the stagnation point heat flux

The similarity solution of Fay & Riddell [11] given by equation 4.45 may be expressed as a Stanton number,

$$St_{body} = \zeta_1 \frac{(\rho_w \mu_w)^{0.1} (\rho_e \mu_e)^{0.4}}{\rho_\infty u_\infty} \left[1 + 0.2 \frac{\alpha_e}{H_{0\infty}} \right] \sqrt{\frac{du_e}{dx}} \Big|_0,$$

where the small wall enthalpy has been neglected in the definition of the Stanton number,

$$St_{body} = \frac{\dot{q}}{\rho_\infty u_\infty h_{0\infty}}.$$

The Lewis number has been taken as $Le = 1.4$ and the enthalpy of dissociation is given by,

$$\frac{h_d}{h_e} = \frac{\alpha_e \left(\frac{2m}{k\theta_d} \right)^{-1}}{h_e} = \frac{\alpha_e}{H_{0\infty}}.$$

If the velocity gradient is introduced from equation 4.47 this becomes,

$$St_{body} = 2^{3/4} \sqrt{\frac{\zeta_1^2 \zeta_2}{Re_\infty}} (\hat{\rho}_w \hat{\mu}_w)^{0.1} \hat{\mu}_e^{0.4} \hat{\rho}_e^{0.15} \left[1 + 0.2 \frac{\alpha_e}{H_{0\infty}} \right]. \quad (4.51)$$

The Reynolds number is defined with respect to the body diameter and the free-stream conditions, $Re_\infty = \rho_\infty u_\infty D / \mu_\infty$. The Sutherland viscosity formula is used to evaluate μ_∞ . In order to simplify treatment of the type IV jet model a power law model is used for the viscosity across the boundary layer;

$$\hat{\mu}_w = \hat{T}_w^{0.7} \quad \hat{\mu}_e = \hat{T}_e^{0.7}.$$

The power law dependence is taken from the empirical data summarized by White [47]. Since the pressure at the edge of the boundary layer is given by the Newtonian approximation we obtain $\hat{p}_e = \rho_\infty u_\infty^2 / p_\infty = 1/P_\infty$ and using the IDG thermal equation of state 4.16,

$$\hat{T}_e = \frac{1 + \alpha_\infty}{P_\infty \hat{\rho}_e (1 + \alpha_e)}.$$

Further, the pressure across the boundary layer is constant, $\hat{p}_w = \hat{p}_e = 1/P_\infty$, and the thermal equation of state gives the wall density ratio,

$$\hat{\rho}_w = \frac{1 + \alpha_\infty}{P_\infty \hat{T}_w}.$$

Since the wall temperature is low and the boundary layer is in equilibrium we have taken $\alpha_w = 0$. Substituting these dependencies into equation 4.51 we obtain the Stanton number as a function of the relevant dimensionless parameters,

$$St_{body} = 2^{3/4} \sqrt{\frac{\zeta_1^2 \zeta_2}{Re_\infty}} \left(\frac{1 + \alpha_\infty}{P_\infty} \right)^{0.38} (1 + \alpha_e)^{-0.28} \hat{T}_w^{-0.03} \hat{\rho}_e^{-0.13} \left[1 + 0.2 \frac{\alpha_e}{H_{0\infty}} \right]. \quad (4.52)$$

The complete dimensionless dependence of the stagnation point heating problem as it is modeled here becomes $St_{body}(P_\infty, H_{0\infty}, \alpha_\infty, \hat{\rho}_d, D/\ell_d, \eta, Re_\infty, \hat{T}_w)$. The remaining variables, α_e and $\hat{\rho}_e$, are determined from the equilibrium normal shock solution in terms of the same set of parameters. Variation of the flow variables as the subsonic flow decelerates to the stagnation point is neglected since the Mach number is low.

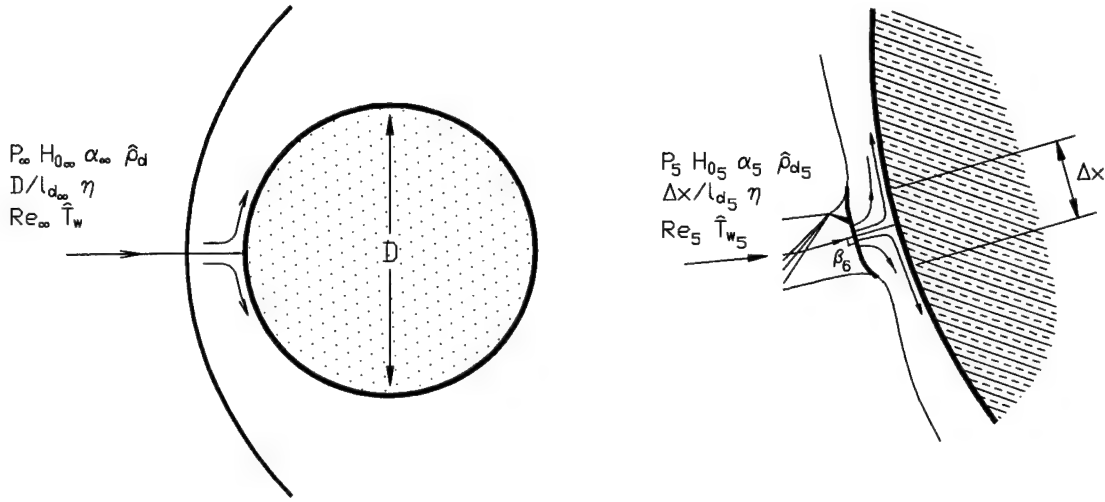


Figure 4.17: Adaption of the Fay & Riddell stagnation point solution to the jet impingement problem.

4.8 Type IV jet heat transfer solution

4.8.1 Introduction

In this section we combine the stagnation point heat transfer model with the free-stream conditions provided by the inviscid type IV jet solution. The results of the model will be expressed in terms of the ratio of the heat transfer rate at the jet impingement point with respect to the undisturbed stagnation point value. Whilst equation 4.52 applies at the undisturbed stagnation point, its validity at the jet impingement point requires further consideration.

If the local vorticity and out-of-plane strain rate at the type IV jet stagnation point remain small, then the deformed stagnation streamline meets the wall symmetrically at 90° . Under these restrictions we may adapt the Fay & Riddell solution 4.52 to study the jet impingement problem as shown in figure 4.17. The conditions of zero vorticity and out-of-plane strain rate are sensibly satisfied for streamlines that pass through the jet in a two-dimensional shock impingement problem (Figure 4.10). Vorticity produced by curvature of the oblique jet shocks or the terminating normal wave is neglected.

Differences in the flow topology for three-dimensional shock impingement configurations were discussed in section 2.3.3. Here we note an additional difference whereby out-of-plane vortex stretching and diffusion alter the form of the stagnation point at the base of the impinging jet. The current results cannot therefore be applied to non-planar configurations such as the shock-on-fin problem. Despite this, it is reasonable to assume that the generic influences of real gas effects are similar for both two and three-dimensional flows.

The following model also assumes quasi-steady, slowly varying conditions at the stagnation point.

4.8.2 Heat transfer intensification due to jet impingement

We now proceed to apply the Fay & Riddell [11] solution at the jet impingement point. The parameters describing the free-stream conditions are given by the inviscid shock interaction solution (Sections 4.5 & 4.6). The conditions upstream of the normal shock at the base of the jet are taken to be those existing at state, 5, behind the third wave produced at the inverted λ -shock. Any additional waves in the supersonic jet are neglected as discussed in section 1.2. We then have,

$$St_{jet} = 2^{3/4} \sqrt{\frac{\zeta_{1jet}^2 \zeta_{2jet}}{Re_5}} \left(\frac{1 + \alpha_5}{P_5} \right)^{0.38} (1 + \alpha_6)^{-0.28} \hat{T}_{w_5}^{-0.03} \hat{\rho}_6^{-0.13} \left[1 + 0.2 \frac{\alpha_6}{H_{0_5}} \right]. \quad (4.53)$$

The Reynolds number, Re_5 , is based on the width of the supersonic jet, Δx . As before, subsonic variations of the equilibrium state, 6, behind the terminating jet shock are neglected as the flow decelerates to the stagnation point. The intensification of the heat transfer as a result of jet impingement is,

$$\frac{\dot{q}_{jet}}{\dot{q}_{body}} = \frac{St_{jet} \rho_5 u_5 h_{0_5}}{St_{body} \rho_\infty u_\infty h_{0_\infty}} = \frac{St_{jet}}{St_{body}} \hat{\rho}_5 \hat{\rho}_3 \hat{\rho}_1 \sqrt{\frac{K_5}{K_\infty}}. \quad (4.54)$$

All of the terms in equations 4.52 and 4.53 that are necessary to evaluate this expression are available from the inviscid jet solution with the exception of Re_5 . The ratio, $\hat{T}_{w_5}/\hat{T}_{w_\infty}$, arises and this is determined by the thermal equation of state, 4.16, to be,

$$\frac{\hat{T}_{w_5}}{\hat{T}_{w_\infty}} = \frac{T_\infty T_1 T_3}{T_1 T_3 T_5} = \frac{\hat{\rho}_5 \hat{\rho}_3 \hat{\rho}_1}{\hat{\rho}_5 \hat{\rho}_3 \hat{\rho}_1} \left(\frac{1 + \alpha_5}{1 + \alpha_\infty} \right). \quad (4.55)$$

The ratio of the Reynolds numbers is similarly determined since we have assumed a power law dependence for the viscosity;

$$\frac{Re_5}{Re_\infty} = \frac{\rho_5 u_5 \mu_\infty \Delta x}{\rho_\infty u_\infty \mu_5 D} = \hat{\rho}_5 \hat{\rho}_3 \hat{\rho}_1 \sqrt{\frac{K_5}{K_\infty}} \frac{\Delta x}{D} \left(\frac{\hat{T}_{w_5}}{\hat{T}_{w_\infty}} \right)^{0.7}. \quad (4.56)$$

Substituting equations 4.53, 4.52, 4.55 and 4.56 into equation 4.54 we obtain the following expression for the heat transfer intensification;

$$\frac{\dot{q}_{jet}}{\dot{q}_{body}} = \sqrt{\frac{\zeta_{1jet}^2 \zeta_{2jet}}{\zeta_{1body}^2 \zeta_{2body}}} \frac{D}{\Delta x} \left(\frac{K_5}{K_\infty} \right)^{0.63} (\hat{\rho}_5 \hat{\rho}_3 \hat{\rho}_1)^{0.5} \left(\frac{1 + \alpha_6}{1 + \alpha_e} \right)^{-0.28} \left(\frac{\hat{\rho}_6}{\hat{\rho}_e} \right)^{-0.13} \left[\frac{H_0 + 0.2\alpha_6}{H_0 + 0.2\alpha_e} \right]. \quad (4.57)$$

Observe that although the heat transfer rate varies inversely with the square root of the Reynolds number in equation 4.53, the intensification of the heat transfer due to jet impingement in equation 4.57 is independent of the Reynolds number. This is consistent with the experimental observations

of Wieting & Holden [48] at low enthalpies. No variation in the heat transfer amplification was observed as the Reynolds number was changed with the remaining parameters held nearly constant.

The last three factors of equation 4.57 are close to unity. This is a consequence of the conservation of stagnation enthalpy at all points in the flow and the weak additional dependence of the stagnation point dissociation level on density. To a very good approximation $\alpha_6 \approx \alpha_e$. The ratio of the normal shock density ratios, $\frac{\hat{\rho}_6}{\hat{\rho}_e}$, is somewhat less than unity however the small exponent, -0.13 , reduces its influence. The square root dependence on the geometrical factors, $\frac{D}{\Delta x}$ and $\frac{\zeta_{1jet}^2 \zeta_{2jet}}{\zeta_{1body}^2 \zeta_{2body}}$, is explicit. The remaining two factors in the center demonstrate intensification caused by increases in the jet specific kinetic energy and density respectively.

4.8.3 Numerical solutions

The factors of equation 4.57 representing jet density and kinetic energy intensification control most of the interesting effects. Their behavior is determined by the two λ -shock solutions of sections 4.5 and 4.6. Equations 4.34–4.38, 4.41–4.44 and 4.57 determine the solution which has the form,

$$\frac{\dot{q}_{jet}}{\dot{q}_{body}} \sqrt{\frac{\Delta x}{D} \frac{\zeta_{1body}^2 \zeta_{2body}}{\zeta_{1jet}^2 \zeta_{2jet}}} = \text{func}(P_\infty, H_{0\infty}, \hat{\rho}_d, \alpha_\infty, \beta_1). \quad (4.58)$$

The equations are solved using Newton's method and the solution is continued in one parameter ($H_{0\infty}$ or β_1) for typical values of the remaining parameters. The term, $\frac{\Delta x}{D} \frac{\zeta_{1body}^2 \zeta_{2body}}{\zeta_{1jet}^2 \zeta_{2jet}}$, specializes the result for a particular geometry and remains indeterminate.

The influence of dissociation chemistry appears principally through the parameter $H_{0\infty}$. Finite rate effects are considered in the approximate intermediate limit, $\frac{d\alpha_1}{d\hat{x}_\infty}, \frac{d\alpha_3}{d\hat{x}_\infty}, \frac{d\alpha_5}{d\hat{x}_\infty} \ll \frac{d\alpha_2}{d\hat{x}_\infty}, \frac{d\alpha_4}{d\hat{x}_\infty}, \frac{d\alpha_6}{d\hat{x}_\infty}$. This approximation leads to three solutions;

1. the frozen solution,
2. the nonequilibrium solution under the above approximation where only shocks 2, 4 and 6 are allowed to come to equilibrium,
3. the full equilibrium solution.

The validity of the nonequilibrium approximation is assessed from the requirement that the reaction rate downstream of the jet shocks (1, 3 & 5) be small relative to that behind the undisturbed bow shock (i.e. $\frac{d\alpha_5}{d\hat{x}_\infty} / \frac{d\alpha_e}{d\hat{x}_\infty} \ll 1$). The influences of α_∞ and $\hat{\rho}_d$ are numerically significant but secondary in terms of demonstrating the essential behavior. The claim therefore is that the solution curves plotted using the universal form, 4.58, in figures 4.18–4.22, illustrate the main mechanisms involved.

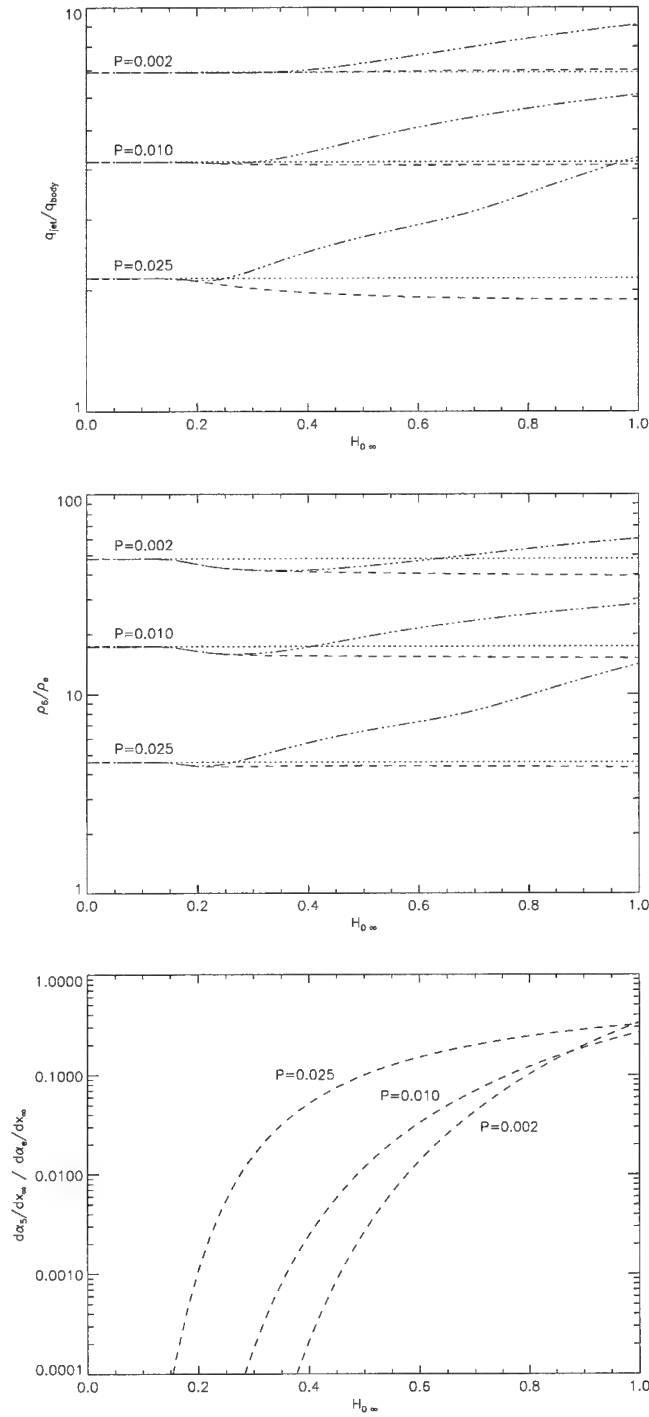


Figure 4.18: INFLUENCE OF DIMENSIONLESS STAGNATION ENTHALPY, $H_{0\infty}$, MACH NUMBER, $\sim 1/\sqrt{P_\infty}$ AND REACTION RATE ON TYPE IV HEAT TRANSFER INTENSIFICATION. From top: Heat transfer intensification, $\frac{\dot{q}_{jet}}{\dot{q}_{body}} \sqrt{\frac{\Delta x}{D} \frac{\zeta_{1body}^2 \zeta_{2body}}{\zeta_{1jet}^2 \zeta_{2jet}}}$, stagnation density intensification, $\frac{\hat{p}_0}{\hat{p}_e}$ and jet reaction rate ratio, $\frac{d\alpha_5/d\hat{x}_\infty}{d\alpha_e/d\hat{x}_\infty}$ curves are the frozen solutions. — · — curves are the equilibrium solutions. --- curves are the nonequilibrium solutions in the limit $\frac{d\alpha_1}{d\hat{x}_\infty}, \frac{d\alpha_3}{d\hat{x}_\infty}, \frac{d\alpha_5}{d\hat{x}_\infty} \ll \frac{d\alpha_2}{d\hat{x}_\infty}, \frac{d\alpha_4}{d\hat{x}_\infty}, \frac{d\alpha_6}{d\hat{x}_\infty}$. The parameters are $P_\infty = 0.002, 0.010, 0.025$, $\hat{p}_d = 1 \times 10^7$, $\alpha_\infty = 0$ and $\beta_1 = 16^\circ$.

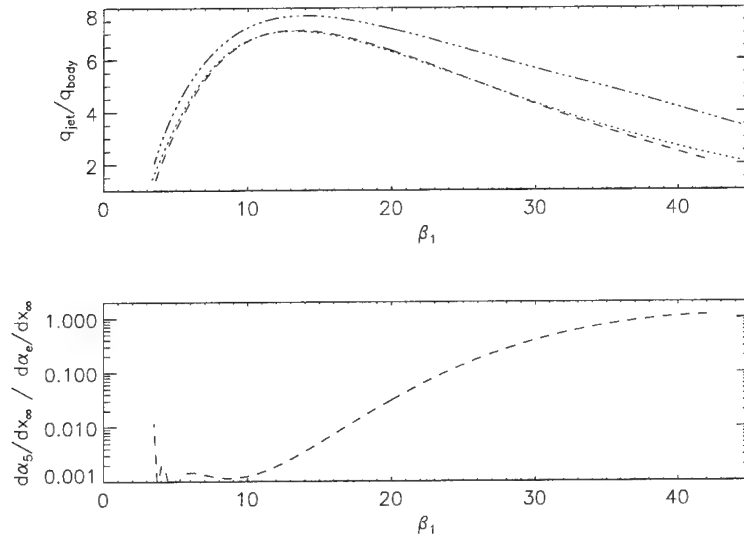


Figure 4.19: INFLUENCE OF IMPINGING SHOCK WAVE ANGLE, β_1 , AND REACTION RATE ON TYPE IV HEAT TRANSFER INTENSIFICATION AT VERY HIGH MACH NUMBER; $P_\infty = 0.002$. From top: Heat transfer intensification, $\frac{\dot{q}_{jet}}{\dot{q}_{body}} \sqrt{\frac{\Delta x}{D} \frac{\zeta_{1body}^2 \zeta_{2body}}{\zeta_{1jet}^2 \zeta_{2jet}}}$ and jet reaction rate ratio, $\frac{d\alpha_5}{dx_\infty} / \frac{d\alpha_e}{dx_\infty}$ curve is the frozen solution. — · — curve is the equilibrium solution. --- curve is the nonequilibrium solution in the limit $\frac{d\alpha_1}{dx_\infty}, \frac{d\alpha_3}{dx_\infty}, \frac{d\alpha_8}{dx_\infty} \ll \frac{d\alpha_2}{dx_\infty}, \frac{d\alpha_4}{dx_\infty}, \frac{d\alpha_6}{dx_\infty}$. The parameters are $H_{0\infty} = 0.6$, $\hat{\rho}_d = 1 \times 10^7$ and $\alpha_\infty = 0$.

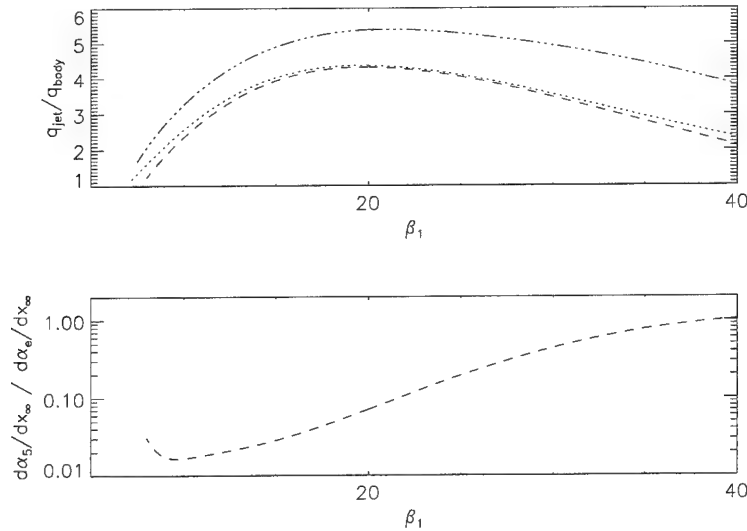


Figure 4.20: INFLUENCE OF IMPINGING SHOCK WAVE ANGLE, β_1 , AND REACTION RATE ON TYPE IV HEAT TRANSFER INTENSIFICATION AT HIGH MACH NUMBER; $P_\infty = 0.010$. The remaining parameters and format are the same as figure 4.19.

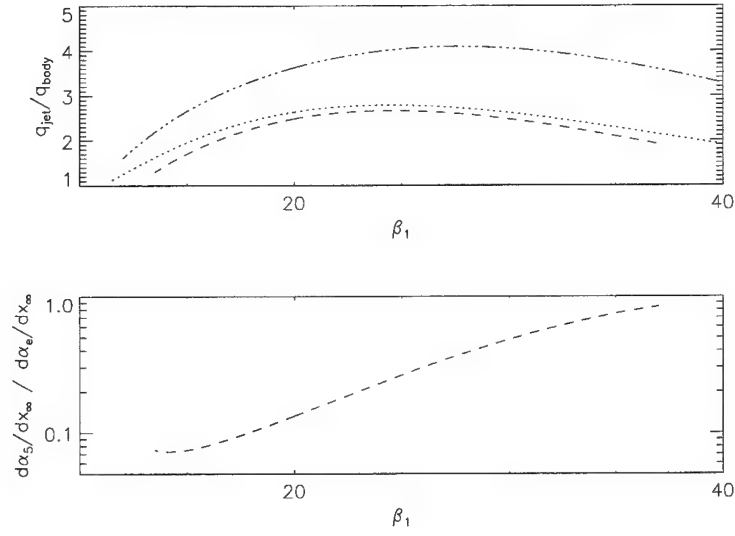


Figure 4.21: INFLUENCE OF IMPINGING SHOCK WAVE ANGLE, β_1 , AND REACTION RATE ON TYPE IV HEAT TRANSFER INTENSIFICATION AT MODERATE MACH NUMBER; $P_\infty = 0.025$. The remaining parameters and format are the same as figure 4.19.

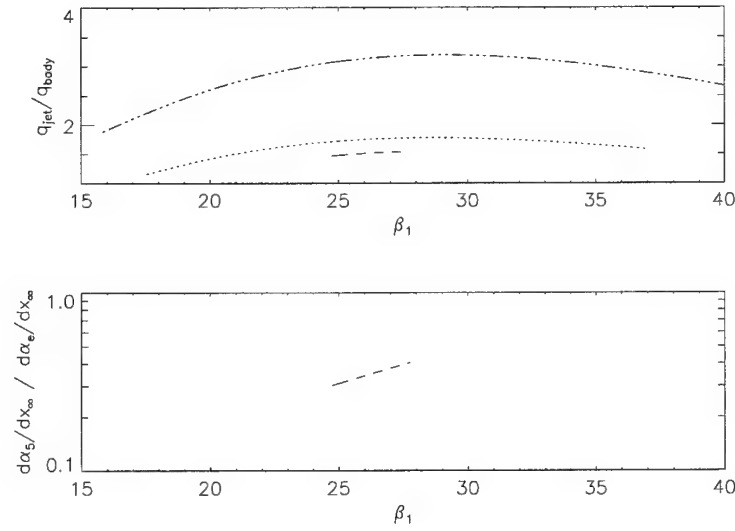


Figure 4.22: INFLUENCE OF IMPINGING SHOCK WAVE ANGLE, β_1 , AND REACTION RATE ON TYPE IV HEAT TRANSFER INTENSIFICATION AT LOW SUPERSONIC MACH NUMBER; $P_\infty = 0.050$. The remaining parameters and format are the same as figure 4.19.

4.8.4 Discussion

The influence of real gas effects on the shock impingement problem may be observed in figure 4.18. The frozen, nonequilibrium and equilibrium solutions are plotted as a function of dimensionless stagnation enthalpy, $H_{0\infty}$. Naturally, the frozen solutions do not vary with stagnation enthalpy. The difference between the equilibrium and frozen solutions increases with stagnation enthalpy as dissociation produces increasing density ratios across the jet shocks, 3 and 5. This effect is absent in the nonequilibrium solution that in fact decreases slightly with respect to the frozen solution. Since $\alpha_6 \approx \alpha_e$ and $\alpha_5 = 0$ in the nonequilibrium approximation, the effects of dissociation on the normal wave, 6, and the undisturbed bow shock are similar. This limits the deviation of the frozen and nonequilibrium heat transfer ratios. The significance of real gas effects is seen to increase with decreasing Mach number (or increasing P_∞). The lower plot in figure 4.18 demonstrates that the validity of the nonequilibrium approximation improves with increasing Mach number and decreasing stagnation enthalpy.

The existing perfect gas model (Edney [8], Keyes & Hains [24]) considers the effects of three parameters;

1. the free-stream Mach number,
2. the impinging shock angle, β_1 ,
3. the ratio of specific heats, γ .

This model predicts that the heat transfer intensification increases with the free-stream Mach number and peaks at a modest value of the impinging shock strength. These trends are reproduced by the frozen solutions in figures 4.19–4.22 that correspond to free-stream Mach numbers of $M_\infty = 19.$, 8.7, 5.5 and 3.9 respectively ($\gamma = 4/3$). As the Mach number increases, and as β_1 approaches the maxima in figures 4.19–4.22, the influence of real gas effects declines. The relative influence of real gas effects is quite large for shock angles either side of the maxima.

The reaction rate curves shown in figures 4.19–4.22 indicate that nonequilibrium effects are most significant for weak (but finite) strength waves. For vanishingly weak waves the jet reaction rate increases and this effect becomes more abrupt as the Mach number increases. At higher Mach numbers (Figures 4.19 & 4.20) the reaction rate in the jet is depressed over a wide range of shock angles.

End points of the various solution curves correspond to conditions at which the flow downstream of shock 5 becomes subsonic with respect to the frozen speed of sound. The differing end points of the frozen, nonequilibrium and equilibrium solutions are a manifestation of the behavior of the sonic line that was discussed in section 4.4.2. The limited extent of the nonequilibrium solution in figure 4.22 indicates that finite width subsonic regions become important features of the flow at

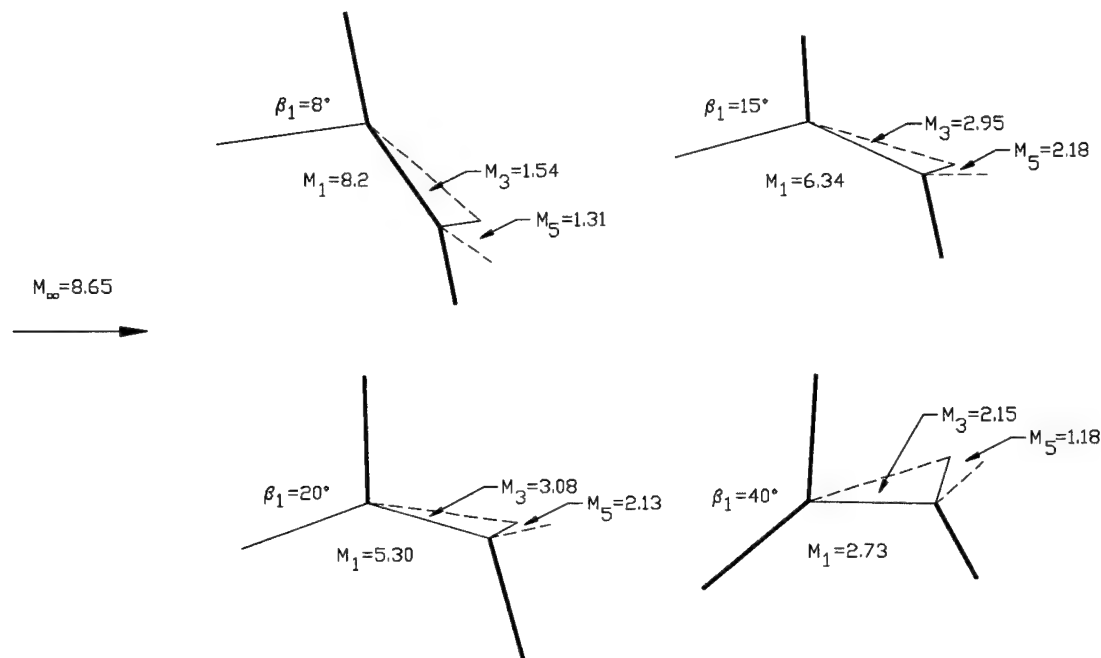


Figure 4.23: VARIATION OF TYPE IV JET SHOCK STRENGTHS WITH IMPINGING SHOCK ANGLE, β_1 . Free stream conditions for the frozen solutions are $P_\infty = 0.010$, $\alpha_\infty = 0$; $\beta_1 = 8^\circ, 15^\circ, 20^\circ, 40^\circ$. The shock angles and flow deflection angles shown are to scale.

lower Mach numbers.

4.8.5 Interpretation of the mechanisms

The thermochemical effects that are observed in figures 4.18–4.22 may be understood from the variations of the jet shock strengths that are demonstrated in figure 4.23. At the intermediate shock angles, $\beta_1 = 15^\circ$ and $\beta_1 = 20^\circ$, the strengths of the jet shocks (1,3 & 5) are balanced to produce the maximum compression and heat transfer intensification. For very weak impinging waves, $\beta_1 = 8^\circ$, we see that the shock connecting the two λ -points becomes disproportionately strong. In the case of a strong impinging wave, $\beta_1 = 40^\circ$, the compression across the incident wave dominates. Maximum heating results therefore from a balancing of the jet shock strengths. The key conclusion is that this balance simultaneously reduces the relative influence of equilibrium real gas effects and depresses the jet reaction rate. This follows from consideration of figures 4.5 and 4.6 which demonstrate the limited extent and rate of the dissociation reaction downstream of moderate strength shock waves. Real gas effects become significant at lower Mach numbers and away from the peak heating shock angle when at least one of the jet shocks causes significant dissociation.

4.9 Comparison with existing models

Edney [8] presented the type IV model data in terms of the jet pressure ratio because this quantity is sensitive to variations in the Mach number and ratio of specific heats. For the current model, density and heat transfer ratios were better measures of the influence of real gas effects. Provided that the jet Mach number remains high we can approximate the intensification of the stagnation pressure by,

$$\frac{p_{6_0}}{p_e} = \frac{\rho_5 u_5^2}{\rho_\infty u_\infty^2} = \hat{\rho}_5 \hat{\rho}_3 \hat{\rho}_1 \frac{K_5}{K_\infty}.$$

Using this form, figure 1.7 compares the current frozen solution with the results of Edney [8]. The real gas solution has been verified against independent calculations for a single oblique shock wave.

The curve for $\gamma = 1.2$ in figure 1.7 demonstrates Edney's prediction of greatly increased heat transfer at high enthalpies. This value is typical for stagnation temperatures in the range 8000–12000K that are studied here. Comparing figure 1.7 with figure 4.20 we see that the variable γ model considerably over-estimates the difference between the frozen and equilibrium solutions of the IDG model at the same Mach number. This occurs because the density ratio across all shock waves is increased uniformly as γ is reduced. This includes the jet shock waves that determine the heat transfer intensification and across these waves the influence of real gas effects is limited.

4.10 Comparison with experimental data

Tables 4.3–4.5 contain the detailed predictions of the model for the free-stream conditions that were used in the experimental portion of this work. The parameters for the computation, P_∞ , H_{0_∞} , $\hat{\rho}_d$, α_∞ and β_1 , are given in tables B.1 and B.5. No other adjustable parameters appear in the model, other than the indeterminate geometrical terms that are estimated below.

The heat transfer rate is predicted by the model in the universal form, $\frac{\dot{q}_{jet}}{\dot{q}_{body}} \sqrt{\frac{\Delta x}{D} \frac{\zeta_{1body}^2 \zeta_{2body}}{\zeta_{1jet}^2 \zeta_{2jet}}}$. Both the undisturbed body flow and the impinging jet are planar so that, $\zeta_{1body} = \zeta_{1jet} = 0.70$ (Equation 4.45). Equation 4.48 gives $\zeta_{2body} = 1$ and $\zeta_{2jet} = 0.26$. During discussion of the experimental results it was noted that the maximum heat transfer occurs when the inverted λ -shock lies close to the surface of the body (Figures 3.3 & 3.4). Noting this we propose the following as an unbiased scaling of the jet width to body diameter ratio;

$$\frac{\Delta x}{D} = \frac{\chi}{D} \sin(|\beta_3 + \delta_1 - \delta_2|). \quad (4.59)$$

This relationship scales the jet width with the undisturbed shock standoff distance, χ , and the divergence angle of the oblique wave and shear layer at the λ -shock (Figure 4.10). All of the quantities appearing in equation 4.59 may be predicted apriori. The undisturbed shock standoff

	Frozen	Nonequilibrium	Equilibrium
β_1	14.25°	14.25°	14.25°
β_2	-87.1°	-87.1°	-87.1°
β_3	-33.1°	-33.1°	-33.1°
δ_1	10.2°	10.2°	10.2°
δ_2	-15.5°	-15.5°	-15.5°
$\frac{\bar{p}_e}{\bar{p}_e}$	21.5	21.5	21.5
$\frac{d\alpha_s}{d\bar{x}_\infty} / \frac{d\alpha_e}{d\bar{x}_\infty}$	-	-	-
$\frac{\dot{q}_{jet}}{\dot{q}_{body}} \left(\frac{\Delta x}{D} \frac{\zeta_{1body}^2 \zeta_{2body}}{\zeta_{1jet}^2 \zeta_{2jet}} \right)^{1/2}$	4.63	4.63	4.63
χ/D	0.218	0.218	0.218
$ \beta_3 + \delta_1 - \delta_2 $	7.4°	7.4°	7.4°
$\frac{\dot{q}_{jet}}{\dot{q}_{body}}$	14.1	14.1	14.1

Table 4.3: Model predictions for condition A.

	Frozen	Nonequilibrium	Equilibrium
β_1	15°	15°	15°
β_2	-84.7°	-86.3°	-86.2°
β_3	-43.5°	-45.1°	-44.9°
δ_1	8.12°	8.12°	8.12°
δ_2	-24.3°	-25.5°	-25.7°
$\frac{\bar{p}_e}{\bar{p}_e}$	7.05	6.53	7.13
$\frac{d\alpha_s}{d\bar{x}_\infty} / \frac{d\alpha_e}{d\bar{x}_\infty}$	-	0.0089	-
$\frac{\dot{q}_{jet}}{\dot{q}_{body}} \left(\frac{\Delta x}{D} \frac{\zeta_{1body}^2 \zeta_{2body}}{\zeta_{1jet}^2 \zeta_{2jet}} \right)^{1/2}$	2.66	2.54	2.75
χ/D	0.186	0.186	0.186
$ \beta_3 + \delta_1 - \delta_2 $	11.1°	11.5°	11.1°
$\frac{\dot{q}_{jet}}{\dot{q}_{body}}$	7.16	6.73	7.41

Table 4.4: Model predictions for condition B.

distances were obtained from table B.6

Examination of the jet divergence angle, $|\beta_3 + \delta_1 - \delta_2|$, in table 4.5 reveals an additional influence of finite rate effects whereby the decreased density of the jet causes a divergence of the shock and shear layer. This translates into a further reduction in the heat flux that is not encompassed by the universal form, $\frac{\dot{q}_{jet}}{\dot{q}_{body}} \sqrt{\frac{\Delta x}{D} \frac{\zeta_{1body}^2 \zeta_{2body}}{\zeta_{1jet}^2 \zeta_{2jet}}}$.

Although the calculations were based on the measured incident shock angles, β_1 , the flow deflection angles computed from them are somewhat larger than the actual shock generator angle of 6°. The discrepancy is consistent with the discussion of nozzle flow nonuniformity and Mach number over-prediction in appendix B. Observe the decline of the discrepancy with increasing stagnation enthalpy that is consistent with figures B.1–B.3.

	Frozen	Nonequilibrium	Equilibrium
β_1	16°	16°	16°
β_2	-83.1°	-86.1°	-85.7°
β_3	-48.4°	-51.6°	-49.3°
δ_1	7.31°	7.31°	7.31°
δ_2	-27.2°	-29.2°	-31.5°
$\frac{\rho_e}{\rho_\infty}$	4.12	3.59	5.61
$\frac{\frac{d\rho_e}{d\alpha_\infty}}{\frac{d\rho_\infty}{d\alpha_\infty}}$	-	0.119	-
$\frac{\dot{q}_{jet}}{\dot{q}_{body}} \left(\frac{\Delta x}{D} \frac{\zeta_{1body}^2 \zeta_{2body}}{\zeta_{1jet}^2 \zeta_{2jet}} \right)^{1/2}$	2.03	1.82	2.52
χ/D	0.173	0.173	0.173
$ \beta_3 + \delta_1 - \delta_2 $	13.9°	15.1°	10.5°
$\frac{\dot{q}_{jet}}{\dot{q}_{body}}$	5.07	4.37	7.23

Table 4.5: Model predictions for condition C.

4.10.1 Heat flux data

At condition A the dissociation levels are negligible and so the frozen, nonequilibrium and equilibrium solutions contained in table 4.3 are indistinguishable. The peak heat transfer rate agrees remarkably with the heat transfer measurements that are summarized in table 4.6.

Nonequilibrium effects are most pronounced for condition B where the reaction rate in the supersonic jet is two orders of magnitude less than that behind the undisturbed bow shock (Table 4.4). The influence of this on the measurable quantities is only slight since the dissociation levels remain small. Despite the limited number of data points obtained at this condition, the trends predicted by the model are confirmed by the data in table 4.6.

The effect of dissociation chemistry is most obvious at condition C (Table 4.5). Significant dissociation occurs and this is reflected in the differing peak density and heat transfer ratios. Chemical nonequilibrium produces a decrease in these quantities however the depression of the jet reaction rate is only moderate. Since the reaction rate parameter is large for the undisturbed flow ($\Delta = 21.$), the jet should remain close to equilibrium. Table 4.6 indicates experimental heat transfer rates that are consistent with this interpretation. Although the model appears to predict the heating rates for the current conditions quite reliably, further experiments spanning a range of reaction rate parameters would be required to discern the nonequilibrium behavior.

4.10.2 Density data

The peak interferometric fringe shift for the type IV flow was measured from the holograms shown in figures C.8, C.15 and C.34. Table 4.7 lists the ratios of the peak fringe shifts relative to the stagnation point values without shock impingement. Estimates of the error include only the precision of the

Test condition	A	B	C
Peak measured $\frac{q_{jet}}{q_{body}}$			
Instantaneous	15.2	10.8	7.9
100 μ s averaged	13.5	7.6	6.0
Predicted $\frac{q_{jet}}{q_{body}}$			
Frozen	14.1	7.2	5.1
Nonequilibrium	14.1	6.7	4.4
Equilibrium	14.1	7.4	7.2

Table 4.6: COMPARISON OF MEASURED AND PREDICTED HEAT TRANSFER INTENSIFICATION FOR TYPE IV FLOWS WITH CYLINDRICAL MODEL. The experimental heat transfer rates are obtained from figures 3.6–3.8

Test condition	A	B	C
Undisturbed fringe shift	13 ± 1	10.5 ± 1	9 ± 1
Type IV fringe shift	55 ± 2	29.5 ± 1	27 ± 1
Ratio	4.2 ± 0.5	2.81 ± 0.4	3.0 ± 0.4
Predicted $\frac{\rho_0}{\rho_e}$			
Frozen	21.5	7.05	4.12
Nonequilibrium	-	6.53	3.59
Equilibrium	-	7.13	5.61

Table 4.7: Comparison of measured fringe shift and predicted stagnation density intensification for type IV flows with cylindrical model.

measurement. Additional systematic error was introduced through line of sight integration of span-wise variations of the jet structure. The peak fringe shift ratios are therefore smaller than the density ratios predicted by the model.

Figures C.48 and C.50 illustrate the flow over a blunt ended cylinder at conditions A and C. Since the chord length across the face of the model was similar in both cases, the peak fringe shifts of 17 ± 1 and 8 ± 1 can be meaningfully compared. Weighted by the free-stream densities, the ratio of these values is 3.0. Although three-dimensional effects were still present, this ratio approaches that of the peak densities predicted by the model in the equilibrium limit; 3.8.

4.11 Dissociation and recombination rate parameters for the type IV jet.

As a final check on the validity of the assumptions of the model we consider the dissociation and recombination rate parameters for the type IV jet. The definitions of these parameters follow from equations 4.25 and 4.50 where the free-stream conditions are now taken to be those downstream of the jet shock system (Figure 4.17). It is convenient to represent these parameters as ratios of the

form,

$$\frac{\Delta_5}{\Delta_\infty} \cdot \frac{D}{\Delta x} = \frac{d\alpha_6/d\hat{x}_5}{d\alpha_e/d\hat{x}_\infty} \sqrt{\frac{K_\infty}{K_5}} \hat{\rho}_5 \hat{\rho}_3 \hat{\rho}_1 \left(\frac{\hat{\rho}_{f_e}}{\hat{\rho}_{f_s}} \right), \quad (4.60)$$

where the characteristic reaction lengths have been renormalized according to equation 4.40. The reaction rates, $d\alpha_6/d\hat{x}_5$ and $d\alpha_e/d\hat{x}_\infty$, along with the frozen shock density ratios, $\hat{\rho}_{f_e}$ and $\hat{\rho}_{f_s}$, are obtained from the type IV jet solution given in sections 4.5 and 4.6.

The ratio of the recombination rate parameters follows from equation 4.50;

$$\frac{\Sigma_5}{\Sigma_\infty} \cdot \frac{D\zeta_{2_{jet}}}{\Delta x\zeta_{2_{body}}} = \frac{\sigma_5}{\sigma_\infty} \sqrt{\frac{K_\infty}{K_5}} \hat{\rho}_5 \hat{\rho}_3 \hat{\rho}_1, \quad (4.61)$$

where $\sigma_5 = \hat{\rho}_6^{5/2} (\hat{T}_6/\Theta_5)^\eta / \hat{\rho}_{d_5}$ and $\sigma_\infty = \hat{\rho}_e^{5/2} (\hat{T}_e/\Theta_\infty)^\eta / \hat{\rho}_{d_\infty}$ are determined from the type IV jet solution. The temperature ratios in these expressions are given by equation 4.24.

Figure 4.24 shows the jet dissociation rate parameter for the free-stream conditions that correspond to figure 4.20. Increases in the dissociation rate due to the higher density at the jet impingement point are offset by the ratio $\Delta x/D$. The net effect is that the jet shock dissociation rate parameter is similar to the undisturbed bow shock rate parameter. Due to relaxation that occurs in the jet, the equilibrium curve lies below the nonequilibrium curve. This also explains the strong dip in the equilibrium solution for weak impinging waves where the unbalanced oblique jet shock system causes significant dissociation.

The recombination rate parameter ratios are observed to vary with the square of the dissociation rate parameter ratios. This is consistent with the scaling of the recombination rate with the square of the density. We conclude that the jet boundary layer lies significantly closer to equilibrium than that on the undisturbed blunt body. For conditions where $\Sigma_\infty \ll 1$ but $\Sigma_5 \approx 1$, this may produce an increase in the heat transfer rate if the body surface is non-catalytic to the recombination reaction.

4.12 Summary

The current experiments exposed deficiencies in existing variable γ models of the shock impingement phenomenon. These models over-predict the experimentally observed heat transfer rates and densities at high enthalpy. Improved models of the inviscid jet shock system and the impingement point boundary layer were introduced in order to explain the discrepancies.

The main real gas effects on the inviscid jet shock system arise because of the widely differing shock strengths produced at the λ -points. Rapid dissociation occurs downstream of the strong waves whereas the extents and rates of dissociation for the weak jet shocks are depressed. It was further demonstrated that peak heating occurs when the strengths of the oblique shock waves in the supersonic jet are balanced. This minimizes the entropy rise along the stagnation streamline. These

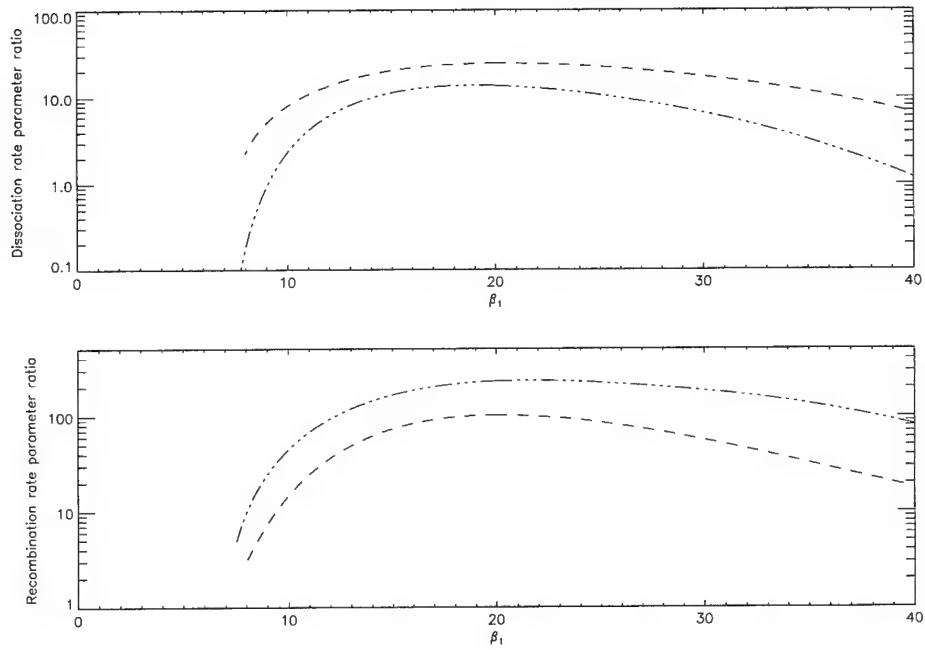


Figure 4.24: REACTION RATE PARAMETERS FOR THE TYPE IV JET STAGNATION POINT. Upper plot is the ratio of the dissociation rate parameters in the form, $\frac{\Delta_s}{\Delta_\infty} \cdot \frac{D}{\Delta x}$. Lower plot is the ratio of the recombination rate parameters, $\frac{\Sigma_s}{\Sigma_\infty} \cdot \frac{D\zeta_{jet}}{\Delta x\zeta_{body}}$. — · — curves are the equilibrium solutions. — — — curves are the nonequilibrium solutions. The free-stream conditions are $P_\infty = 0.010$, $H_{0\infty} = 0.6$, $\hat{\rho}_{d\infty} = 1 \times 10^7$, $\alpha_\infty = 0$.

effects combine to greatly reduce the influence of thermochemistry at the peak heating condition. Real gas effects were shown to be important when the balance of the oblique shock waves is disturbed. This occurs for impinging shock strengths greater or less than that which produces maximum heating and for lower free stream Mach numbers.

A nonequilibrium approximation was introduced that applies when the oblique jet shocks are weak with respect to the undisturbed bow shock. Within the scope of the approximation, non-monotonic behavior with the reaction rate is predicted.

The model successfully reproduced the experimentally observed heat transfer rates. Accurate predictions of the heat transfer rates should be possible for conditions where turbulent diffusion of the supersonic jet is unimportant. Further experimentation is necessary to resolve the prediction of non-monotonic behavior with the reaction rate parameter.

Chapter 5 Conclusions

A series of experiments was conducted in the T5 free piston driver shock tunnel to determine the quantitative effects of high enthalpy thermochemistry on the shock impingement heating problem. By studying the nominally two-dimensional mean flow about a cylinder with a coplanar impinging shock wave the topology of the problem was simplified so that it could be observed directly by holographic interferometry. Interferograms obtained for three different test conditions and a range of shock impingement locations demonstrated the controlling influence of the inertia of the supersonic jet and indicated that existing predictions of greatly increased stagnation density at high enthalpy were not realized. Time resolved heat transfer measurements confirmed this observation and agreed accurately with existing low enthalpy experimental investigations.

Temporal fluctuations of the impinging jet were observed at all test conditions and Strouhal numbers were estimated from the power spectra of the heat transfer data. Variations of the tunnel test conditions during the test time limited the quality of the spectra at high enthalpies. Whilst it was not possible to conclusively discount the effect of free-stream perturbations, the data exhibited features that have been observed in recent numerical studies. The Strouhal numbers were consistent with the limited existing data.

New instrumentation developed for this project has allowed critical assessment of the flow quality produced by the T5 facility. Measurements of the flow over blunt bodies without shock impingement agreed with established theories within experimental uncertainty. Flow contamination that was detectable with this instrumentation did not become apparent until times beyond the period of test flow that was used to obtain the data. This confirmed the validity of the current measurements.

In order to reconcile the experimental observations with existing analyses the influence of thermochemistry on the jet shock system was modeled using the ideal dissociating gas approximation. Careful nondimensionalization of the problem led to a tractable formulation and identification of the important parameters. The results were used to demonstrate generic influences of real gas effects on the shock impingement problem. The central conclusion was that peak heating arises from a balancing of the jet shock strengths. This balance was demonstrated to simultaneously reduce the relative influence of equilibrium real gas effects and depress the jet reaction rate. Real gas effects were shown to be important at lower Mach numbers (< 7.5) and for impinging shock angles away from that which produces peak heating. The model accurately reproduced the experimentally observed heat transfer rates using apriori estimated parameters. Interferometric comparisons were hindered by variations in the impingement location across the span of the model. Relative trends of the interferometric data at the different conditions were consistent with the model predictions.

A non-equilibrium approximation was introduced that applies under conditions where the jet shocks remain weak with respect to the undisturbed bow shock. Within the scope of the approximation non-monotonic behavior was predicted with the reaction rate parameter. Discrimination of finite rate effects was not possible in the current investigation since the reaction rate was not varied as an independent parameter.

Bibliography

- [1] AMBROSIO, A. & WORTMAN, A. 1962 Stagnation point shock detachment distance for flow around spheres and cylinders. *American Rocket Society Journal*, **28**, 281.
- [2] BURCHAM, F. W. & NUGENT, J. 1970 Local flow field around a pylon mounted dummy ramjet engine on the X-15-2 airplane for Mach numbers from 2.0 to 6.7. NASA TN D-5638.
- [3] CARLSON, A. B. & WILMOTH, R. G. 1994 Monte Carlo simulation of a near continuum shock-shock interaction problem. *Journal of Spacecraft and Rockets*, **31**(1), 25-30.
- [4] CAULFIELD, H. J. *ed.* 1979 *Handbook of Optical Holography*. Academic Press.
- [5] COHEN, C. B. & RESHOTKO, E. 1956 Similar solutions for the compressible laminar boundary layer with heat transfer and pressure gradient. NACA Report 1293.
- [6] COURANT, R. & FRIEDRICHS, K. O. 1948 *Supersonic Flow and Shock Waves*. Interscience.
- [7] DELERY, J. & MARVIN, J. G. 1986 Shock-wave boundary layer interactions. AGARDograph No. 280.
- [8] EDNEY, B. E. 1968 Anomalous heat transfer and pressure distributions on blunt bodies at hypersonic speeds in the presence of an impinging shock. FFA Report 115.
- [9] EDNEY, B. E. 1968 Effects of shock impingement on the heat transfer around blunt bodies. *AIAA J*, **6**(1), 15-21.
- [10] EMRICH, R. J. *ed.* 1981 *Methods of Experimental Physics*, **18** Pt. A. 392-396. Academic Press.
- [11] FAY, J. A. & RIDDELL, F. R. 1958 Theory of stagnation point heat transfer in dissociated air. *Journal of the Aeronautical Sciences*, **25**(2), 73-85.
- [12] FONTENOT, J. E. 1965 A method of estimating the effect of shock interaction on stagnation line heating. *AIAA J*, **3**(3), 562.
- [13] FRANCIS, W. L. 1965 Experimental heat transfer study of shock impingement on fins in hypersonic flow. *Journal of Spacecraft and Rockets*, **2**(4), 630.
- [14] FREEMAN, N. C. 1958 Non-equilibrium flow of an ideal dissociating gas. *JFM*, **4**, 407-425.
- [15] GAITONDE, D. 1993 Calculations on unsteady type IV interaction at Mach 8. Wright Laboratory, WL-TR-93-3002.

- [16] HANNEMANN, K., BRÜCK, S. & BRENNER, G. 1993 Numerical simulation of reacting flows related to the HEG. *19th Int. Sym. Shock Waves*, Marseille.
- [17] HENDERSON, L. F. 1966 Experiments on the impingement of a supersonic jet on a flat plate. *ZAMP*, **17**(5), 553–569.
- [18] HIERS, R. S. & LOUBSKY, W. J. 1967 Effects of shock-wave impingement on the heat transfer on a cylindrical leading edge. NASA TN D-3859.
- [19] HORNING, H. G. 1972 Non-equilibrium dissociating nitrogen flow over spheres and circular cylinders. *JFM*, **53**, 149.
- [20] HORNING, H. G. 1986 Regular and Mach reflection of shock waves. *Annual Review of Fluid Mechanics*, **18**, 33–58.
- [21] HORNING, H. G., OERTEL, H. & SANDEMAN, R. J. 1979 Transition to Mach reflexion of shock waves in steady and pseudosteady flow with and without relaxation. *JFM*, **90**(3), 541–560.
- [22] HORNING, H. G. & SMITH, G. H. 1979 The influence of relaxation on shock detachment. *JFM*, **93**, 225.
- [23] HORNING, H. G., STURTEVANT, B., BELANGER, J., SANDERSON, S. R., BROUILLETTE, M. & JENKINS, M. 1991 Performance data of the new free-piston shock tunnel T5 at GALCIT. *18th Int. Sym. Shock Waves*, Sendai.
- [24] KEYES, J. W. & HAINS, F. D. 1973 Analytical and experimental studies of shock interference heating in hypersonic flows. NASA TN D-7139.
- [25] KLOPFER, G. H. & YEE, H. C. 1988 Viscous hypersonic shock-on-shock interaction on blunted cowl lips. AIAA-88-0233.
- [26] KORKEGI, R. H. 1971 Survey of viscous interactions associated with high Mach number flight. *AIAA J*, **9**(5), 771.
- [27] KORTZ, S. 1993 Zum Einfluß der Stickstoffdissoziation auf die Wechselwirkung zwischen Stoßwellen in Hochenthalpieströmungen. DLR-Forschungsbericht 93-57.
- [28] KORTZ, S., MCINTYRE, T. J. & EITELBERG, G. 1993 Experimental investigation of shock on shock interactions in the high enthalpy shock tunnel Göttingen (HEG). *19th Int. Sym. Shock Waves*, Marseille.
- [29] LIGHTHILL, M. J. 1957 Dynamics of a dissociating gas. Part I. Equilibrium flow. *JFM*, **2**, 1–32.

- [30] LORDI, J. A., MATES, R. E. & MOSELLE, J. R. 1966 Computer program for solution of nonequilibrium expansions of reacting gas mixtures. NASA CR-472.
- [31] MCINTOSH, M. K. 1968 Computer program for the numerical calculation of frozen and equilibrium conditions in shock tunnels. Department of Physics, School of General Studies, Australian National University, Canberra, ACT.
- [32] MERZKIRCH, W. 1974 *Flow Visualization*. Academic Press.
- [33] NONWEILER, T. R. F. 1959 Aerodynamic problems of manned space vehicles. *Journal of the Royal Aeronautical Society*, 521-528.
- [34] PAPOULIS, A. 1984 *Probability, Random Variables and Stochastic Processes*. Mc-Graw Hill.
- [35] PERRY, A. E. & CHONG, M. S. 1987 A description of eddying motions and flow patterns using critical-point concepts. *Annual Review of Fluid Mechanics*, **19**, 125-155.
- [36] PRABHU, R. K., STEWART, J. R. & THAREJA, R. R. 1990 Shock interference studies on a circular cylinder at Mach 16. AIAA 90-0606.
- [37] PRESS W. H., FLANNERY B. P., TEUKOLSKY S. A. & VETTERLING W. T. 1988 *Numerical Recipes in C*. Cambridge University Press.
- [38] REIN, M. 1989 Surf:A program for calculating inviscid supersonic reacting flows in nozzles. GALCIT FM89-1.
- [39] SANDERSON, S. R. & SIMMONS, J. M. 1991 Drag balance for hypervelocity impulse facilities. *AIAA J*, **29**(12), 2185.
- [40] SCHULTZ D. L. & JONES T. V. 1973 Heat-transfer measurements in short-duration hypersonic facilities. AGARDograph No. 165.
- [41] STALKER, R. J. 1967 A study of the free piston shock tunnel. *AIAA J*, **5**(12), 2160.
- [42] SYKES, D. M. 1962 The supersonic and low-speed flows past circular cylinders of finite length supported at one end. *JFM*, **12**, 367.
- [43] TANNEHILL, J. C., HOLST, T. L. & RAKICH, J. V. 1976 Numerical computation of two dimensional viscous blunt body flows with an impinging shock. *AIAA J*, **14**(2), 204-211.
- [44] VEMAGANTI, G. R. 1994 Laminar and turbulent flow computations of type IV shock-shock interference aerothermal loads using unstructured grids. NASA CR-195008.
- [45] VINCENTI, W. G. & KRUGER, C. H. 1965 *Introduction to physical gas dynamics*. Robert E. Krieger Publishing Company.

- [46] WEN, C. Y. 1994 Hypervelocity flow over spheres. Ph.D. Thesis, California Institute of Technology.
- [47] WHITE, F. M. 1974 *Viscous Fluid Flow*. McGraw-Hill.
- [48] WIETING, A. R. & HOLDEN, M. S. 1989 Experimental shock wave interference heating on a cylinder at Mach 6 and 8. *AIAA J*, **27**(11), 1557–1565.
- [49] YEUNG, S. L. B. & HALL, I. M. 1993 Shock wave interactions in hypersonic flow. *19th Int. Sym. Shock Waves*, Marseille.
- [50] ZHONG, X. 1994 Application of essentially non-oscillatory schemes to unsteady hypersonic shock-shock interference heating problems. *AIAA J*, **32**(8), 1606–1616.

Appendix A Review of shock impingement flow field models

A.1 Introduction

It is appropriate to include a brief review of the seminal observations of Edney [8] since these form the basis of what follows. Schlieren cinematography of shock wave impingement flow fields allowed Edney to categorize six distinct flow regimes known as types I–VI. These six interaction patterns arise for different locations of the impinging shock wave with respect to the blunt body, as indicated in figure 1.3. The sequence of interactions, obtained by Edney for a hemispherical body, is illustrated in figures A.1 and A.2. These flow fields were observed for a variety of model geometries and so the classification appears to be universal.

A.2 Shock loci methods for a perfect gas

The flow in smooth regions of the shock impingement flow field and across shock discontinuities is, in principle, understood. The predominant concern is then points where surfaces of discontinuity intersect and here local analysis about intersection points in the pressure – flow deflection angle (p - δ) plane provides a useful tool. These techniques were developed in the study of Mach reflection problems and reviews are given by Courant & Friedrichs [6] and Hornung [20] who reviews recent developments. In this method the solution is represented graphically by the intersection in the p - δ plane of the loci of possible downstream states for the interacting waves.

In the absence of viscous effects, the usual Mach reflection problems may be mirrored about the surface of reflection. They are therefore degenerate symmetrical cases in which two shock surfaces of opposite families interact. Although the asymmetric case has received relatively little attention, many of the ideas in the literature carry over in modified form to the shock on leading edge problem. Edney [8] used these methods to interpret the shock impingement flow fields and justify the type I–VI classification. The key conclusion drawn from this analysis was the role of the three shock solutions (or λ -shocks). Our approach here is to briefly review the existing methods before extending them to study the influence of real gas effects.

For a perfect gas the mapping of an oblique shock wave into the p - δ plane is determined by

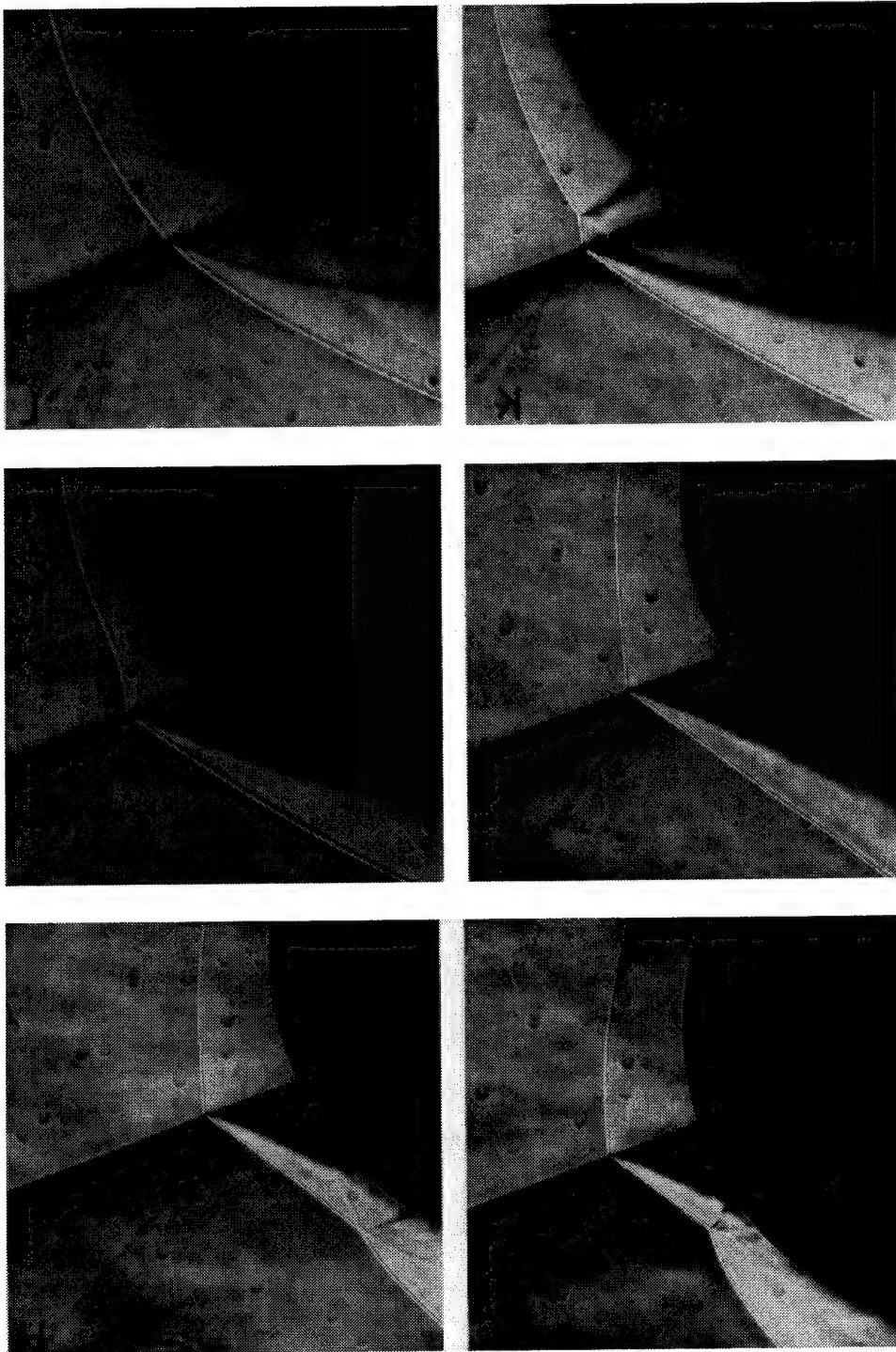


Figure A.1: Interference types I–III for supersonic flow about a hemisphere; $M_\infty = 4.6$ (Edney [8]). Sequence of interactions is left–right, top–bottom.

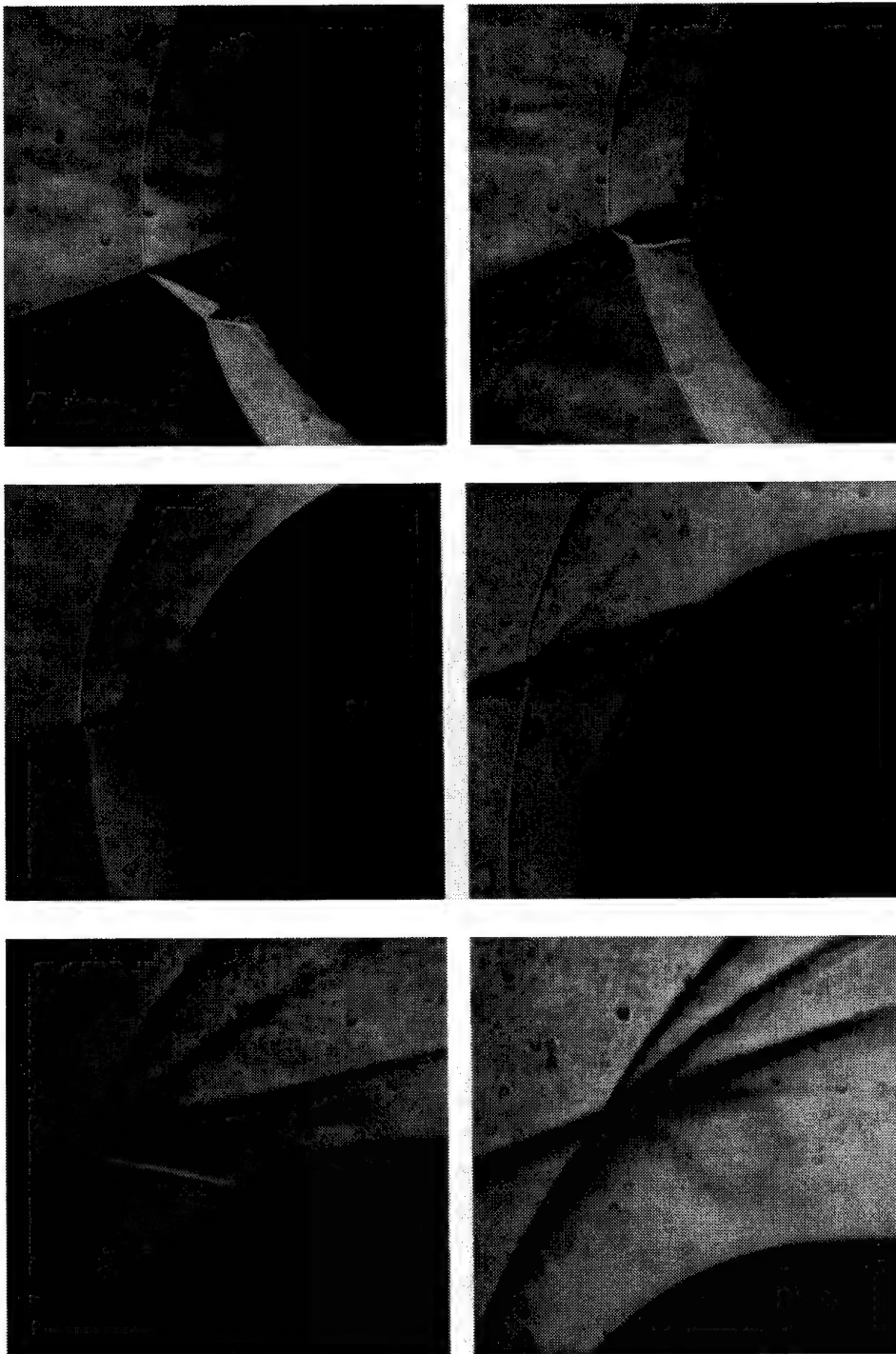


Figure A.2: Interference types IV–VI for supersonic flow about a hemisphere; $M_\infty = 4.6$ (Edney [8]). Sequence of interactions is left–right, top–bottom.

conservation of mass, momentum and energy normal to the shock front to be,

$$\hat{\rho} = \frac{(\gamma + 1)M_\infty^2 \sin^2 \beta}{(\gamma - 1)M_\infty^2 \sin^2 \beta - 2},$$

$$\hat{p} = 1 + \frac{\hat{\rho} - 1}{\gamma \hat{\rho} M_\infty^2 \sin^2 \beta},$$

$$\frac{\tan \beta}{\tan(\beta - \delta)} = \hat{\rho},$$

where $\hat{\rho}$ and \hat{p} are the density and pressure ratios across the shock. The free-stream Mach number is M_∞ and γ is the ratio of specific heats. For a given free-stream condition the above equations determine the locus of possible downstream states. This forms a curve in the p - δ plane that is parameterized in terms of the shock angle, β .

A.3 The type I–VI classification

A.3.1 Type I

Type I interference is observed in the first frame of figure A.1 and this is the well known regular solution for the interaction of weak oblique shock waves. The type I flow field is illustrated schematically in figure A.3 along with its mapping into the p - δ plane. Enhanced heating occurs as a result of the shock wave boundary layer interaction that occurs at the body surface. Results from the literature (Delery & Marvin [7]) may be expected to yield reasonable estimates of the heating rates.

A.3.2 Type II

As the impingement point moves upward towards the lower sonic line a type II interaction is observed in the second frame of figure A.1. In this configuration the oblique shock loci (Figure A.4) do not intersect and a subsonic region is observed behind a Mach stem connecting the two mutually inverted λ -pattern shock intersection points. The transition mechanism from type I is similar to the Mach reflection problem however the strengths of the interacting waves are unequal. Edney's criterion for transition was equivalent to the maximum deflection condition in Mach reflection (Hornung [20]). Mechanisms for enhanced heating in type II flows are similar to those for type I flows however the shock that interacts with the boundary layer is generated at the upper λ -point (Figure A.4).

A.3.3 Type III

When the Mach stem merges with the subsonic portion of the bow shock ahead of the body a type III flow results (Figure A.1, frames 3 & 4). During the type II–III transition the locus representing the

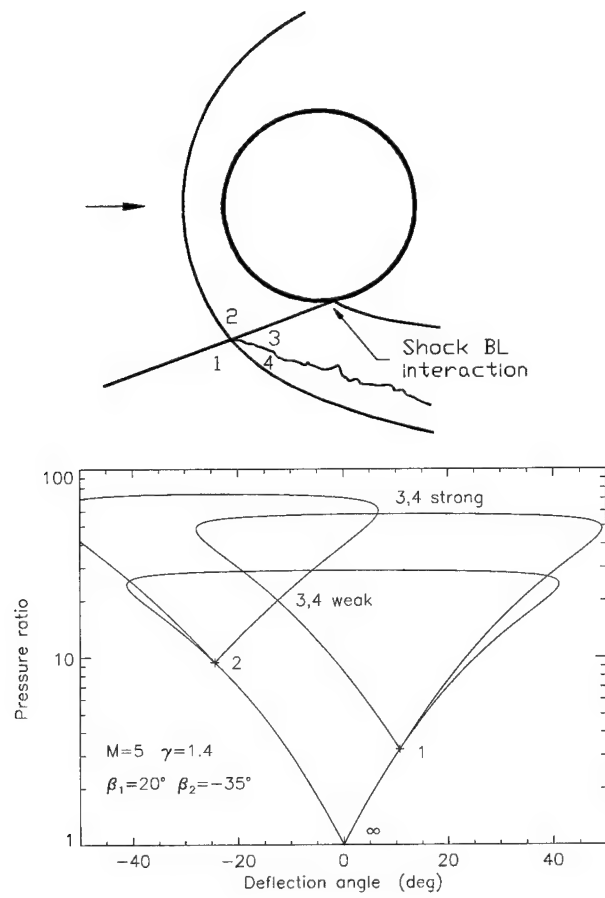


Figure A.3: Schematic of type I interference flow and its representation in the p - δ plane.

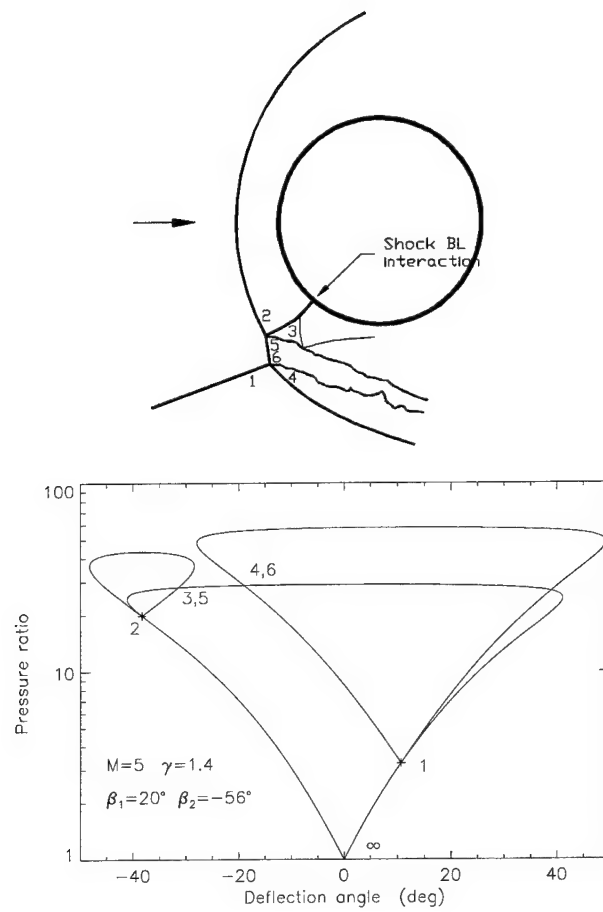


Figure A.4: Schematic of type II interference flow and its representation in the p - δ plane.

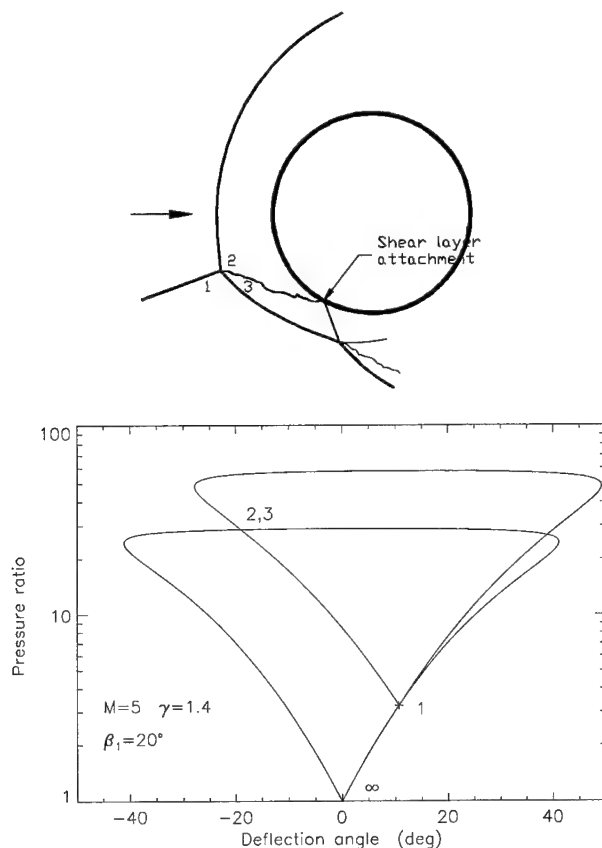


Figure A.5: Schematic of type III interference flow and its representation in the p - δ plane.

upper λ -point in Figure A.4 becomes vanishingly small. The influence of the impinging wave is now global since it impinges on the subsonic portion of the bow wave. Both the radius of curvature and the standoff distance of the asymmetrical upper portion of the bow shock increase to match the λ -point solution (Figure A.5). In frame 5 of figure A.1 the shear layer that is generated at the shock impingement point is seen to deflect where it meets the body. The shear layer is assumed to attach to the surface of the body and a compression wave is generated that overtakes and steepens the third wave produced at the impingement point. As this secondary interaction becomes stronger (Figure A.1, frame 6) the transition to type IV begins. Transition to type IV is presumed to occur at the detachment angle for the compression wave. Observe that a parallel exists between this process and the mechanism of complex Mach reflection of a propagating shock from the surface of a wedge.

A.3.4 Type IV

The supersonic jet that characterizes the type IV flow field is observed to form in the first frame of figure A.2. An extensive description of the type IV flow field is contained in section 1.2. Type IV interactions produce severe pressure loads and heat transfer rates where the supersonic jet im-

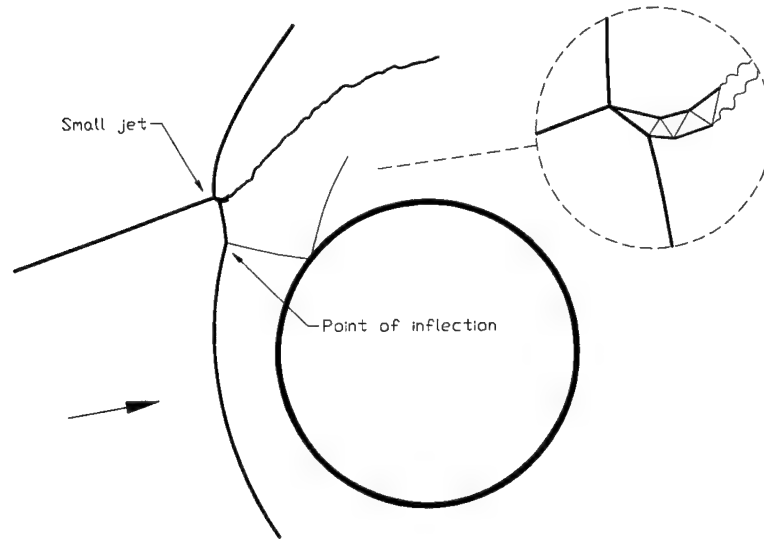


Figure A.6: Schematic of type V interference flow.

pings on the body. The width of the type IV jet reduces as the impingement point moves upward (Figure A.2, frames 2–4) and a point of inflection is induced on the bow shock below the interaction region. At the highest impingement point the supersonic jet is barely distinguishable.

A.3.5 Type V

The width of the supersonic jet decreases rapidly as the impingement point moves toward the upper sonic line. Although the jet structure was not resolvable Edney [8] assumed that this remains unchanged from the type IV solution. No other local solution appears to exist. Since the bow shock angle immediately below the jet is fixed by the local solution, a point of inflection is induced on the wave front for sufficiently high impingement points (Figure A.6). The type V flow is characterized by the appearance of a third λ -point that causes a weak wave to impinge on the surface of the body (Figure A.2, frame 5).

Type V flows are observed more clearly in shock-on-fin impingement problems where the curvature of the bow shock in the plane of symmetry is greatly reduced.

A.3.6 Type VI

For impingement points lying well above the upper sonic line a type VI flow is observed (Figure A.2, frame 6). This is analogous to the conventional overtaking intersection of oblique shock waves with a weak reflected expansion fan. The representation of the type VI flow in the p - δ plane is shown in figure A.7. Relatively little is known about the transition mechanism for this overtaking intersection in comparison with the body of literature that exists for the Mach reflection problem. Edney used the limit of tangential intersection of the p - δ loci as the transition mechanism between regimes V

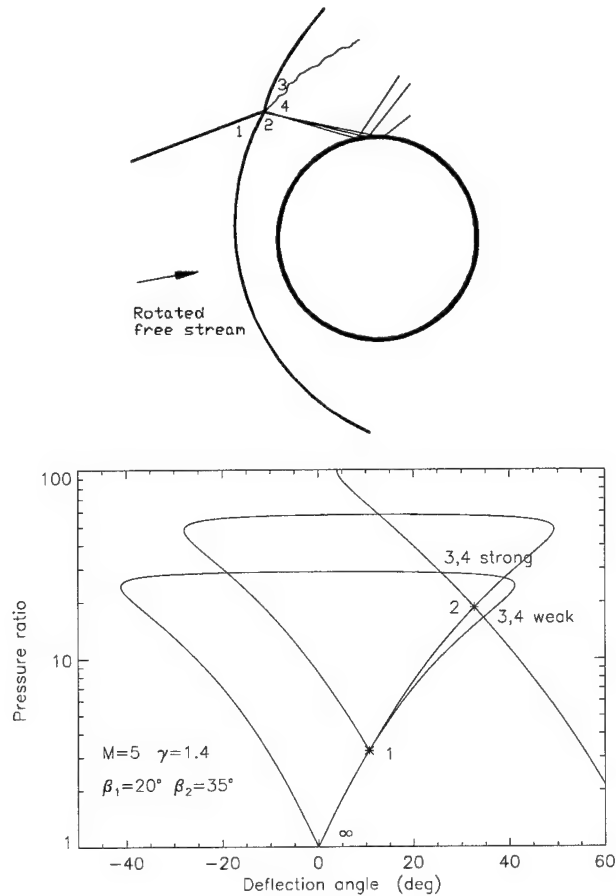


Figure A.7: Schematic of type VI interference flow and its representation in the p - δ plane.

and VI. Minor heating occurs where the reflected expansion interacts with the boundary layer. The interaction occurs downstream of the sonic line so that flow over the upstream part of the body is equivalent to that for a blunt body immersed in the rotated flow behind the impinging shock.

Appendix B Test section conditions

B.1 Summary

Three different test conditions were used in the experiments described here and these were chosen to highlight the influence of real gas effects on the shock impingement phenomenon. Specific values for the flow parameters are given in table B.1. The first case, A, represents a low enthalpy control condition where the only real gas effects were a partial excitation of the vibrational modes in the stagnant regions of the flow. Control of the T5 piston dynamics was optimized for high enthalpy flows and prevented the operation of the facility at lower enthalpies with the current 120 kg piston. Case C represents a high enthalpy condition that was chosen to highlight the influence of thermochemistry on the problem. Case B is an intermediate enthalpy condition that was designed to aid interpretation of the differences in the flow mechanisms for cases A and C.

B.2 Prediction of the test section conditions

T5 was operated as a reflected mode shock tunnel whereby the reservoir conditions upstream of the nozzle were generated by the reflection of the incident shock wave from the end wall of the shock tube. The volume of double shock heated gas was then expanded through a contoured nozzle into the test section. Prediction of the test section conditions was based on a two-step process whereby the reservoir conditions and nozzle flow were computed sequentially.

Given the initial filling conditions of the shock tube and the measured velocity of the incident shock wave, the reservoir condition was calculated using an inviscid equilibrium chemistry model of the incident and reflected waves. The stagnant reservoir state was then expanded isentropically to the measured reservoir pressure in order to account for subsequent weak waves reflected from the driver gas interface, propagated influences that arose from the unsteady motion of the piston and the expansion of the reservoir volume supplying the nozzle. This computation was performed using the ESTC code described by Macintosh [31] where the reader may obtain further details of the technique. The thermodynamics of the system were modeled using harmonic oscillator approximations at temperatures below 5000K and polynomial fits above this threshold.

Flow through the nozzle was calculated using the 2D supersonic inviscid reacting nozzle flow code (SURF) developed by Rein [38]. The thermodynamic models were similar to those described above with the addition that the nonequilibrium gas was described as a mixture of thermally perfect components. Reaction rates were described using Arrhenius forms and vibrational excitation was

Test condition		A	B	C
Shock tube conditions	Fill pressure (kPa ± 0.5 kPa)	75	32.5	20
	Fill temperature (K ± 4 K)	297	297	297
	Shock speed (m/s)	1890	3500	4360
		± 100	± 245	± 255
Nozzle reservoir conditions	Pressure (MPa)	14.6	22.3	28.3
	Temperature (K)	± 0.7	± 1.3	± 1.9
	Enthalpy (MJ/kg)	3210	7550	8960
		3.88	12.0	19.1
Test section conditions	Velocity (m/s)	2540	4450	5350
	Density (kg/m ³)	0.0218	0.0155	0.0157
	Pressure (kPa)	1.03	5.48	11.4
	N concentration (mole/kg)	9.9×10^{-5}	6.9×10^{-1}	3.65×10^0
Test section dimensionless parameters	IDG P_∞	7.32×10^{-3}	1.79×10^{-2}	2.54×10^{-2}
	IDG $H_{0\infty}$	0.102	0.346	0.560
	IDG α_∞	1.4×10^{-6}	9.7×10^{-3}	0.051
	IDG $\hat{\rho}_d$	6.0×10^6	8.4×10^6	8.3×10^6
	IDG Δ per mm	$4. \times 10^{-13}$	3.4×10^{-2}	0.525
	Re per mm	5540	1630	1350

Table B.1: SUMMARY OF THE FREE-STREAM CONDITIONS. Test conditions were computed on the basis of measurements of the initial shock tube fill pressure and temperature, incident shock speed prior to reflection, and nozzle reservoir pressure after shock reflection. The dimensionless parameters for the ideal dissociating gas (IDG) model are defined in section 4.2. Error estimates given for the fill conditions represent the accuracy of the pressure gauge and the variation of the ambient temperature. Error estimates for the measured shock speed and reservoir pressure are the standard deviation of the quantities sampled over the entire sequence of shots. The error in the computed quantities may be inferred from these estimates.

		ESTC/SURF	IDG/NENZF
Shock tube conditions	Fill pressure (kPa)	25	25
	Fill temperature (K)	300	300
	Shock speed (m/s)	5600	5600
Nozzle reservoir conditions	Pressure (MPa)	90.	90.1
	Temperature (K)	11350	11880
	Enthalpy (MJ/kg)	32.9	33.4
Test section conditions	Velocity (m/s)	6650	6930
	Density (kg/m ³)	0.034	0.033
	Pressure (kPa)	55.5	50.0
	Atomic N (mole/kg)	9.3	17.5
Test section dimensionless parameters	IDG P_∞	3.7×10^{-2}	3.1×10^{-2}
	IDG $H_{0\infty}$	0.98	0.99
	IDG α_∞	0.130	0.245
	IDG \hat{p}_d	3.82×10^6	3.94×10^6

Table B.2: Verification of ESTC/SURF computations by comparison with simplified IDG/NENZF model.

modeled using a simple switch from frozen to equilibrium at 3000K. Verification of the results was obtained by comparison with a simplified calculation using the IDG model for the reflected shock and the one-dimensional nonequilibrium nozzle flow code of Lordi et al. [30] (Table B.2).

B.3 Variation of the free-stream conditions across the test section

Since the flow in the nozzle was chemically reacting, a contour optimized to produce axial flow at high enthalpy produced nonuniform flow at other off design conditions. The variations across the test section were obtained at the nozzle exit plane from the SURF code and these computations are shown in figures B.1, B.2 and B.3. Spatial nonuniformity of the flow increases at low enthalpies as expected. Further evolution of the profile must be expected downstream of the nozzle exit plane, however it was not possible to compute this with the current implementation of the SURF code. The conditions given in table B.1 were based on conditions 35mm above the nozzle centerline. This represented the approximate location of the model for the type IV impingement flow.

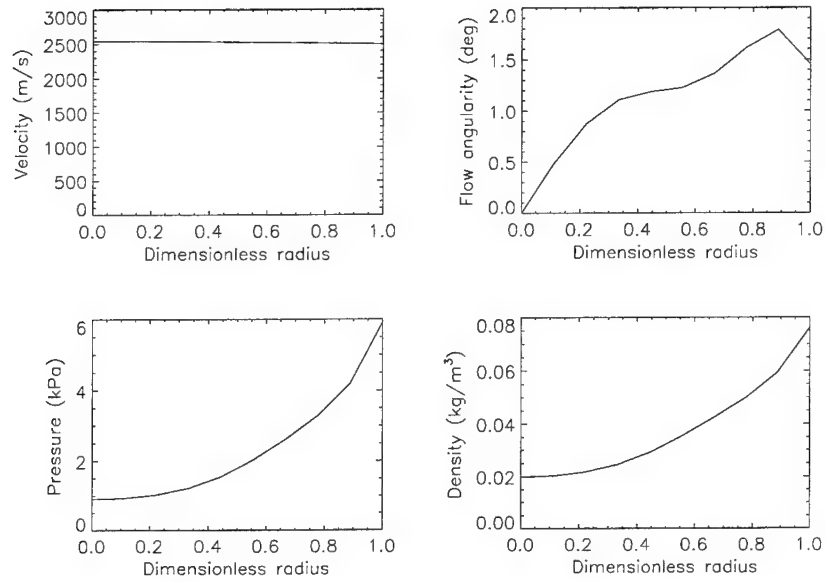


Figure B.1: Flow nonuniformity in the nozzle exit plane for test condition A.

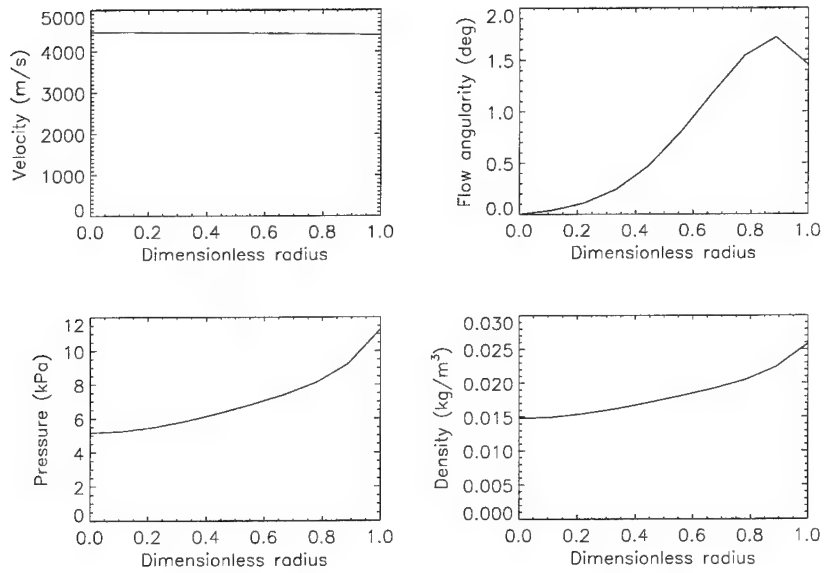


Figure B.2: Flow nonuniformity in the nozzle exit plane for test condition B.

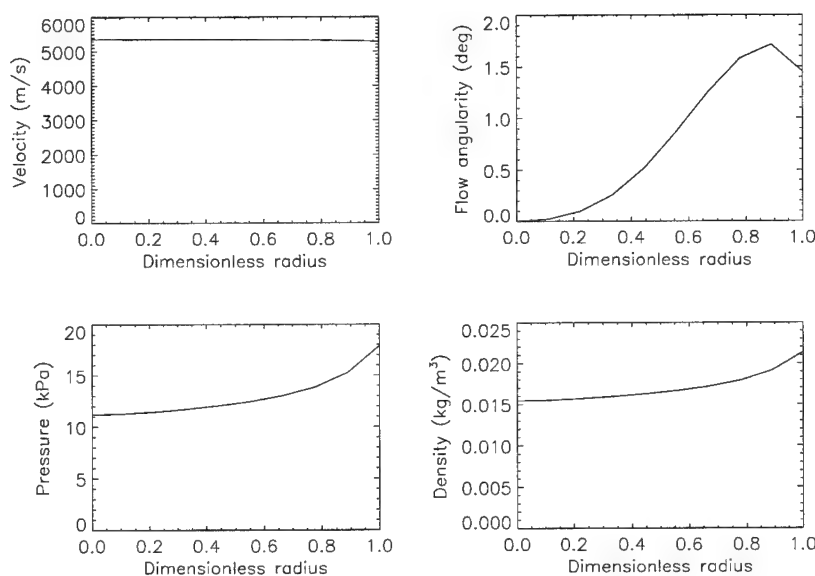


Figure B.3: Flow nonuniformity in the nozzle exit plane for test condition C.

B.4 Experimental verification of the flow density

B.4.1 Interferometric measurements for a finite aspect ratio cylinder

The accuracy of the prediction of the test conditions and the quality of the flow in the facility may be assessed from the holograms and stagnation point heat transfer measurements obtained without shock impingement. Consider first the stagnation density data contained in figures C.1, C.14 and C.20 that correspond to test conditions A, B and C respectively. The variation of density behind the normal portion of the bow shock was computed for condition C using the IDG model presented in section 4.2. The curvature of the shock was neglected and the results are shown in figure 4.4. Observe that the density asymptotes to its equilibrium value in a distance that is small compared to the shock standoff distance. In the strong shock limit for a perfect gas with $\gamma = 7/5$ the density rises by a further factor of 1.08 between the bow shock and the stagnation point. We extrapolate this result to the high enthalpy cases with sufficient accuracy for the present comparison. We may therefore compare the fringe shift calculated from,

$$\frac{\theta_{calc}}{2\pi} = (1.08\rho_{\infty}\hat{\rho}_{eq} - \rho_{\infty})[K_{N_2}(1 - \alpha_{eq}) + K_N\alpha_{eq}]\frac{L}{\lambda}, \quad (B.1)$$

with that observed in the interferograms (Table B.3). Here $\theta_{calc}/2\pi$ is the predicted fringe shift, ρ_{∞} is the free-stream density predicted by SURF, $\hat{\rho}_{eq}$ is the equilibrium IDG post shock density ratio, α_{eq} is the equilibrium dissociated mass fraction, K_{N_2} and K_N are the Gladstone–Dale constants for molecular and atomic nitrogen, L is the span of the cylinder and λ is the wavelength of light. The

Test condition	A	B	C
ρ_{∞} (SURF kg/m ³)	0.0218	0.0155	0.0157
\hat{p}_{fr} (IDG model)	6.61	6.08	5.61
\hat{p}_{eq} (IDG model)	6.61	8.59	9.67
α_{fr} (IDG model)	1.4×10^{-6}	0.010	0.051
α_{eq} (IDG model)	2.0×10^{-6}	0.114	0.285
Calculated fringe shift (fr)	11.1	7.17	6.67
Calculated fringe shift (eq)	11.1	11.0	13.2
Measured fringe shift	$13. \pm 1$	10.5 ± 1	$9. \pm 1$

Table B.3: INTERFEROMETRIC VERIFICATION OF THE STAGNATION DENSITY. Physical constants used were; $L = 0.180\text{m}$, $\lambda = 532\text{nm}$, $K_N = 3.1 \times 10^{-4} \text{ m}^3\text{kg}^{-1}$, $K_{N_2} = 2.45 \times 10^{-4} \text{ m}^3\text{kg}^{-1}$.

slight effect of variation of the refractivity of the gas mixture at the free-stream conditions has been neglected.

Table B.3 shows that at low enthalpy the stagnation density is under-predicted. This was probably due to the strong variation in density and pressure, and hence Mach number, across the nozzle exit. At an enthalpy of 12MJ/kg the measured stagnation density agrees with the computation within the established uncertainty. Condition C, which corresponds to an enthalpy of 19.1MJ/kg, demonstrated a stagnation density somewhat lower than that predicted by the ESTC/SURF computation. The uncertainty of ± 1 fringe indicated in table B.3 is based on the difficulty of sub-fringe resolution and the slight deviations from infinite fringe conditions that are observed in the holograms. Additional computations with SURF indicated that the error of $\pm 250 \text{ m/s}$ in the measured shock speed and $\pm 2 \text{ MPa}$ in the measured reservoir pressure constitute an error of ± 0.5 fringes in the calculated value for high enthalpy condition C. Three-dimensional flow over the ends of the cylinder introduces additional systematic error.

B.4.2 Abel transform interferometric measurements for a blunted cylinder

For axisymmetric flow fields the true density field may be deconvolved from the holographic data by use of Abel transform methods. A recursive, direct solution algorithm was used to reconstruct the density field in a stepwise manner from the edge of the flow-field (Emrich et al. [10]). Holographic data was available for the flow over a blunt faced cylinder at test conditions A and C (Figures C.47 & C.49). The fringe shift was measured along the face of the body at the quarter fringe points and cubic splines were used to interpolate between them. The density fields deconvolved from the spline fitted data are shown in figures B.4 and B.5. A comparison with the conditions computed using the ESTC/SURF codes is indicated in table B.4. The measurements and predictions agree within experimental uncertainty if potential error in the prediction of the test conditions is included. These

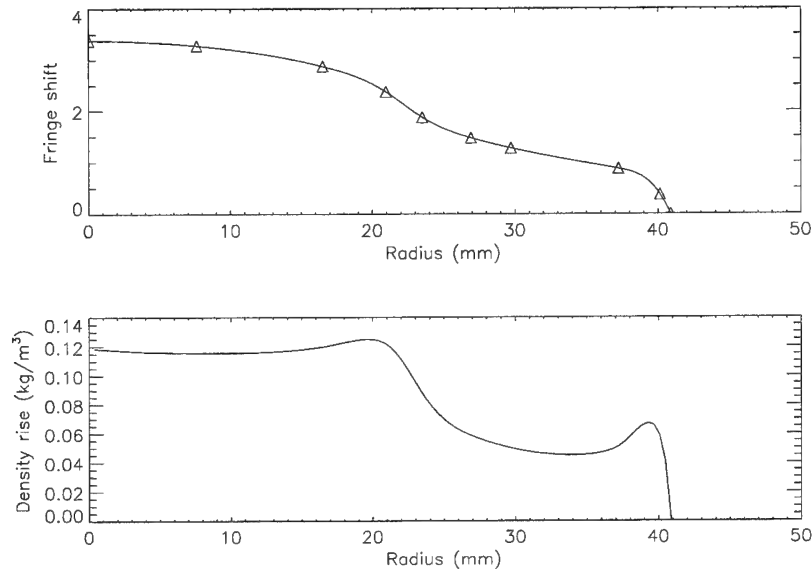


Figure B.4: Abel transformation of density field for flow over the blunt faced cylinder at test condition A; Shot T5-819.

Test condition	A	C
ρ_{∞} (SURF kg/m^3)	0.0218	0.0157
$\hat{\rho}_{fr}$ (IDG model)	6.61	5.61
$\hat{\rho}_{eq}$ (IDG model)	6.61	9.67
Calculated $\Delta\rho_{fr}$ (kg/m^3)	0.122	0.072
Calculated $\Delta\rho_{eq}$ (kg/m^3)	0.122	0.136
Measured $\Delta\rho$ (kg/m^3)	0.117 ± 0.02	0.110 ± 0.02

Table B.4: INTERFEROMETRIC VERIFICATION OF THE STAGNATION DENSITY USING ABEL TRANSFORM METHODS. The calculated values are obtained from the ESTC/SURF computations. Error estimates for the measured values are based on a sub-fringe resolution of ± 0.5 with respect to the fringe shift at the stagnation point.

results confirm those for the nominally two-dimensional cylinder flow discussed above.

B.4.3 Density variation across the incident shock wave

Further information on the free-stream conditions can be obtained from the jump in density that was observed across the incident shock wave. The results of section 4.5 indicate that the extent of chemical reaction across the weak impinging shock wave was negligible. If we also assume vibrational freezing then the density ratio across the wave is given by the perfect gas result,

$$\hat{\rho} = \frac{(\gamma + 1)M_{\infty}^2 \sin^2 \beta}{(\gamma - 1)M_{\infty}^2 \sin^2 \beta + 2}.$$

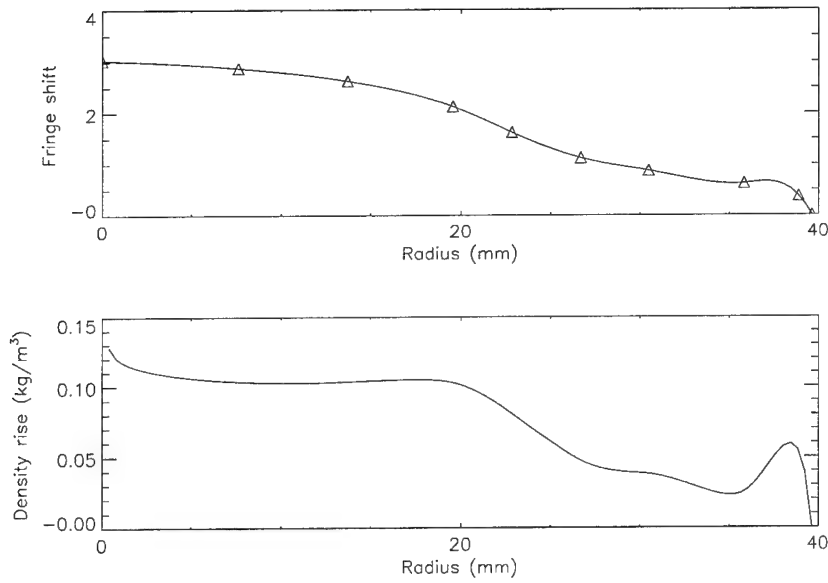


Figure B.5: Abel transformation of density field for flow over the blunt faced cylinder at test condition C; Shot T5-820.

Test condition	A	B	C
ρ_{∞} (SURF kg/m ³)	0.0218	0.0155	0.0157
M_{∞} ($\gamma = 1.4$)	9.9	6.33	5.31
Shock angle; β ($\pm 1^{\circ}$)	14.25	15.0	16.0
$\hat{\rho}$	3.3	2.1	1.8
Calculated fringe shift	5.6	1.9	1.5
Measured fringe shift ± 0.5	4.5	2.	2.

Table B.5: Density rise across the impinging shock wave.

This level of approximation is sufficient given the large uncertainty in the interferometric data when the fringe shift is small. Measurements of the fringe shift that are indicated in table B.5 may be repeatably obtained from any of the holograms contained in appendix C. Cases A and B are consistent with the earlier measurements of the stagnation point density. At the low enthalpy condition the density is slightly over-predicted and the medium enthalpy condition is predicted very accurately. In the high enthalpy case the density is under-predicted whereas the stagnation point density was over-predicted. This suggests that the nature of the discrepancy is more complicated than a simple over-prediction of the free-stream density. It is not possible to draw any further conclusions on the basis of the current measurements.

Test condition	A	B	C
M_∞ ($\gamma = 1.4$)	9.9	6.33	5.31
$\hat{\rho}_{fr}$ (IDG model)	6.61	6.08	5.61
$\hat{\rho}_{eq}$ (IDG model)	6.61	8.59	9.67
$\frac{\chi}{D_{ref}}$	0.202	0.217	0.228
$\frac{\chi}{D_{eq}}$	0.202	0.154	0.132
Measured $\frac{\chi}{D}$ (± 0.0025)	0.218	0.186	0.173

Table B.6: Experimental verification of the shock standoff distance.

B.5 Experimental verification of the shock standoff distance

An additional check on the density ratio across the bow shock wave is provided by measurements of the shock standoff distance. For hypersonic flows, where the shock layer ahead of the body is thin and approximately constant density;

$$\frac{\chi}{D} \sim \frac{1}{2\hat{\rho}}. \quad (\text{B.2})$$

Here $\frac{\chi}{D}$ is the shock standoff distance normalized with respect to the cylinder diameter and $\hat{\rho}$ is the density ratio across the normal portion of the bow shock. This correlation, which arises from conservation of the mass flux entering the shock layer across the bow shock, has been successfully extended to the case of multicomponent reacting mixtures by Wen [46]. Wen used the classical perfect gas correlation of Ambrosia & Wortman [1] to determine the similarity constant in equation B.2. Using an approximate solution for the nonequilibrium flow along the stagnation streamline, Wen [46] determined an average value for the density in the shock layer as a function of dimensionless kinetic energy and reaction rate parameter.

Here we consider only the frozen and equilibrium limits of such a correlation for the flow over cylinders. Ambrosia & Wortman [1] accurately correlated the shock standoff distance from a cylinder by the expression,

$$\frac{\chi}{D_{ref}} = 0.193 \times e^{4.67/M_\infty^2}. \quad (\text{B.3})$$

This applies in the frozen limit for the reacting flow. Accounting for the increase in density caused by relaxation using the IDG solution we combine equations B.2 and B.3 to obtain,

$$\frac{\chi}{D_{eq}} = \frac{\chi}{D_{ref}} \frac{\hat{\rho}_{fr}}{\hat{\rho}_{eq}}. \quad (\text{B.4})$$

The predicted and measured values for the shock standoff distance are indicated in table B.6.

At low enthalpies, where the original correlation should be quite accurate, the discrepancy in the shock stand-off distance is attributed to nonuniformity of the nozzle flow. Reference to the numerical results of Wen [46] suggests that the reaction rate parameter for test condition B ($\Delta = 0.034 \text{ mm}^{-1}$

Test condition	A	B	C
Stanton number (Equation 4.52)	0.0123	0.0172	0.0167

Table B.7: Predicted stagnation point Stanton numbers.

$\times 40.6 \text{ mm} = 1.4$) is sufficiently large at moderate enthalpy to cause the measured standoff distance to approach the equilibrium limit. This is confirmed here by the measured shock standoff distance and is consistent with the holographic data. The reaction rate parameter for the high enthalpy case C ($\Delta=21.$), combined with the prediction of a further increase in the shock layer density ratio, should cause a further reduction in the stand-off distance. Whilst the the measured shock position moves proportionally closer to the equilibrium limit, the standoff distance remains somewhat larger than that predicted by the correlation. These facts are consistent with the over-prediction of the stagnation point fringe shift that has been discussed earlier.

B.6 Stagnation point heat transfer rate

The stagnation point heat transfer rate was modeled using the Fay & Riddell [11] equilibrium similarity solution in the form discussed in section 4.7. Predictions of the Stanton number are shown in table B.7. Figures C.1, C.14 and C.20 demonstrate tolerable agreement with this correlation at all three test conditions.

Appendix C Holographic interferograms and heat transfer data

The data that are presented in this appendix comprise the main results obtained from the experimental investigation conducted in the T5 free piston shock tunnel. Experiments were conducted at the three test conditions that are described in appendix B. For each shot a holographic interferogram is presented along with the heat transfer distribution around the circumference of the model. The data have been arranged by test condition and in order according to the position of the model. Due to slight variations in the incident shock angle, some of the interferograms appear to be out of order. The position of the model was measured by gauging the distance between flat reference surfaces on the model traverse. Values of this distance, g/D , that are indicated for each of the figures, have been normalized by the model diameter. The zero point of this quantity was arbitrary but repeatable to within ± 0.001 .

The effects of variation of the shock impingement location were visualized using the double pulse holographic interferometer that is described in appendix D. Quantitative interpretation of the density field is possible and the necessary physical constants are contained in table C.1. The reader will observe some limitations in the quality of images that were obtained during the early development of the interferometer. They are presented here for completeness. Repeated magnified views are also presented where appropriate.

Time resolved heat transfer measurements were made at 24 locations around the circumference of the model. Geometrical details of the test section apparatus and sensor locations are contained in appendix F. Sensor locations have been overlayed on the holographic interferograms and the dimensions of the symbols correspond to the sensitive area of the thermocouples. The instantaneous heat transfer distribution was plotted for each interferogram along with an average value taken over an interval of width $100 \mu\text{s}$. The instantaneous profile and the center of the averaging interval correspond to the time at which the hologram was recorded. Superimposed on these plots are the standard deviations of the time histories over the averaging interval. This gives an indication of the

Wavelength	$\lambda = 532\text{nm}$
Path length	$L = 0.180\text{m}$
Gladstone-Dale constants	$K_N = 3.1 \times 10^{-4} \text{ m}^3\text{kg}^{-1}$
	$K_{N_2} = 2.45 \times 10^{-4} \text{ m}^3\text{kg}^{-1}$

Table C.1: Physical constants for holographic interferograms.

temporal fluctuations of the heat transfer rates at various locations on the model surface.

The final set of points on each plot is the envelope of the maximum heat transfer rate recorded at each circumferential location during the shot. The first 500 μs of the time records were excluded from this maximization so that tunnel starting transients did not influence the profiles. The records were scanned until 4 ms after primary shock reflection. This interval spans the period of useful test flow. Whilst the utility of a maximum level measurement inevitably depends on the temporal and spatial resolution of the device, these factors remained constant for all data presented here. This statistic has proven useful for the interpretation of the effect of variation of the stagnation enthalpy. Further details of the specialized techniques used to obtain this data, along with an assessment of the accuracy of the sensors, are contained in appendix E.

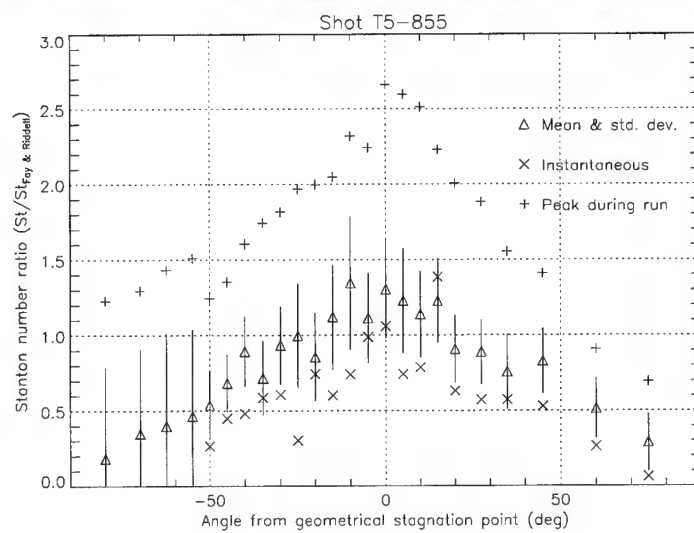
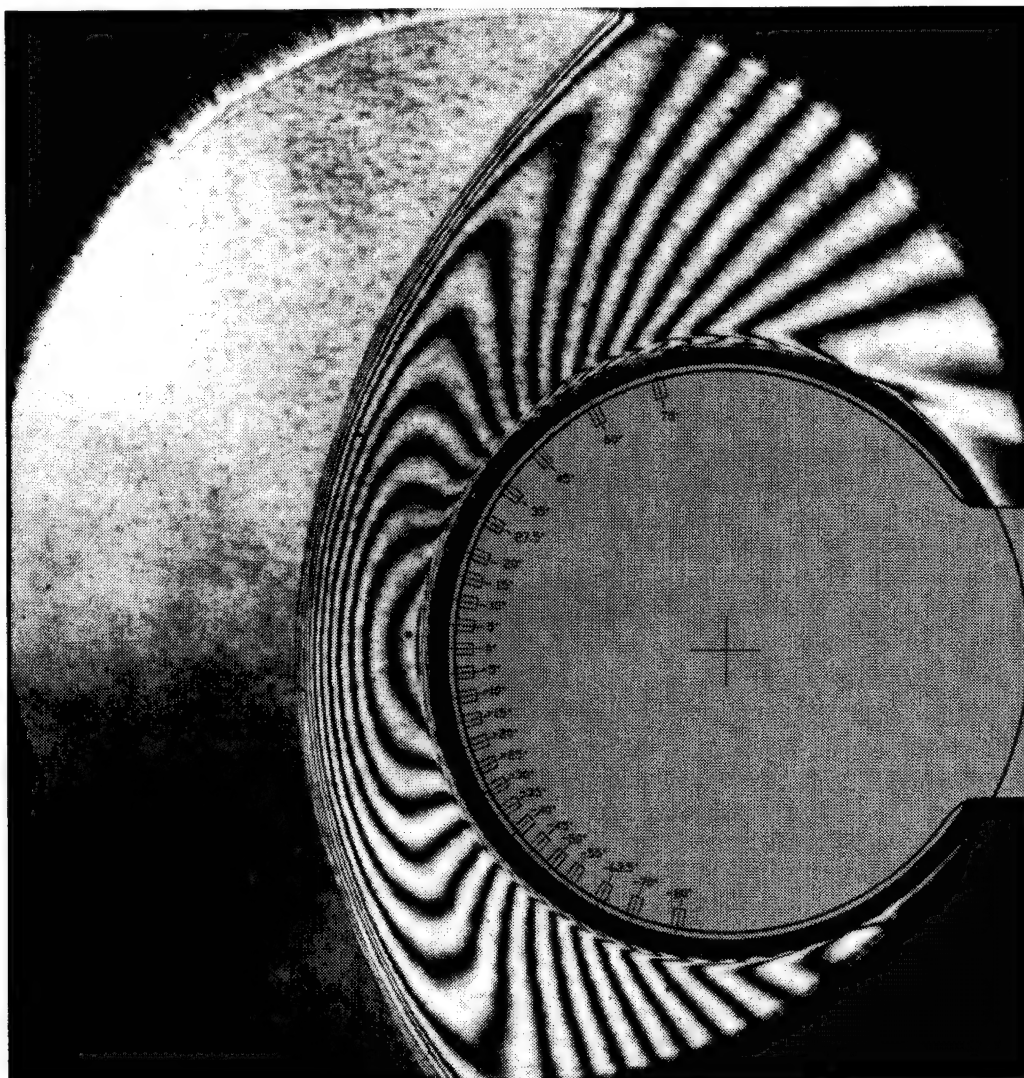


Figure C.1: Shot T5-855; condition A, $g/D = 2.168$.

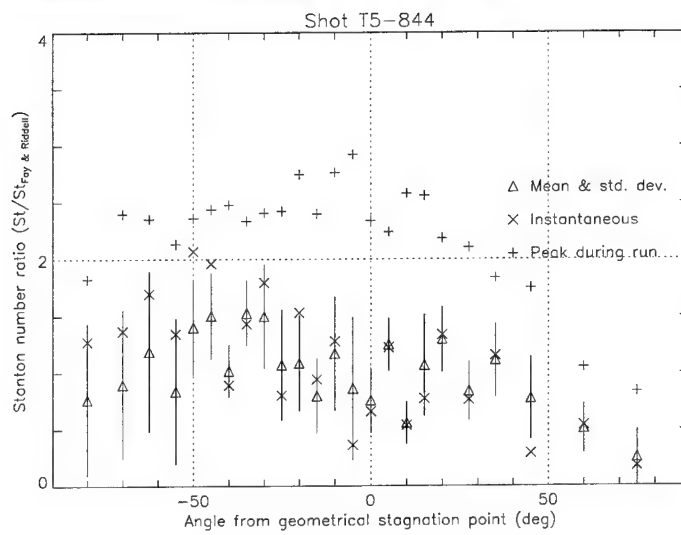
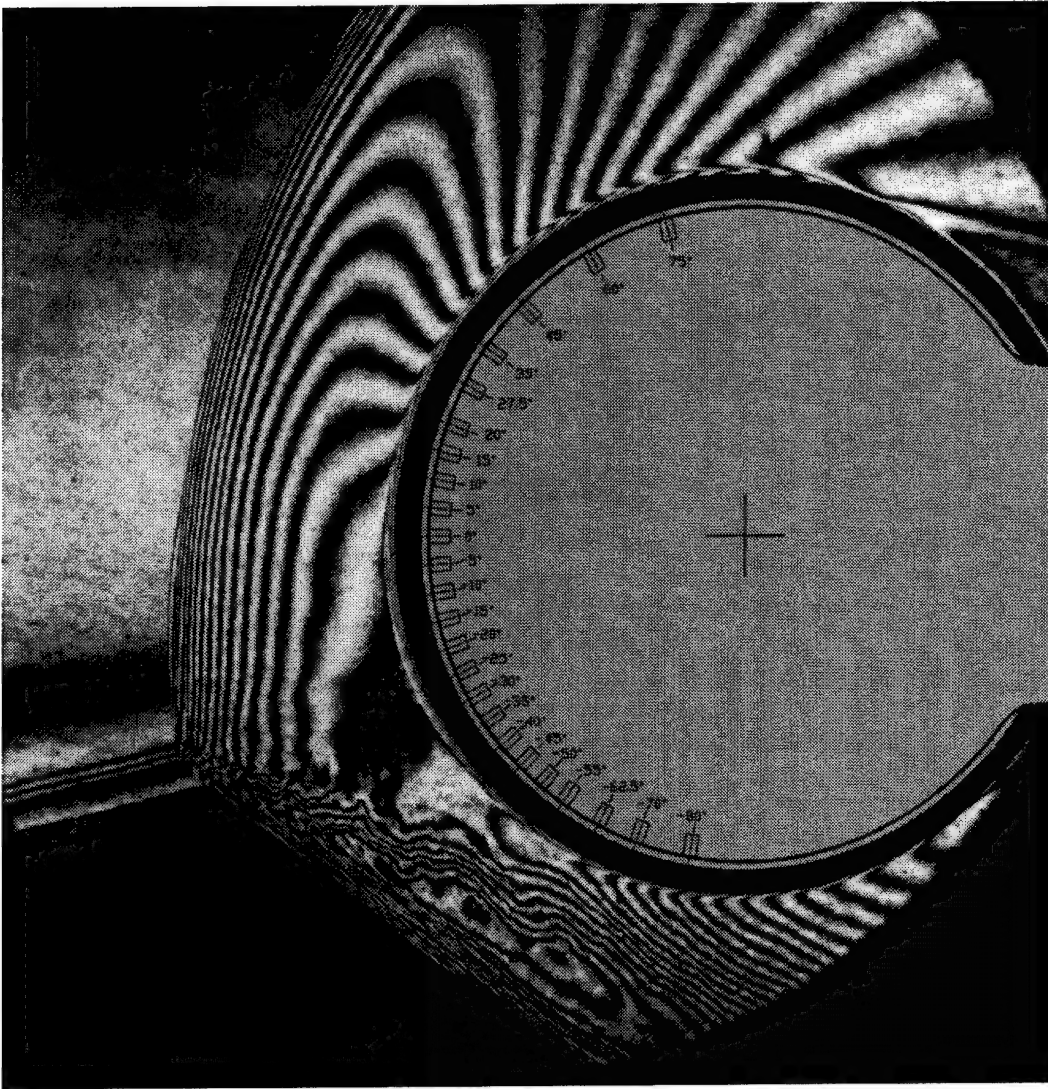


Figure C.2: Shot T5-844; condition A, $g/D = 2.128$.

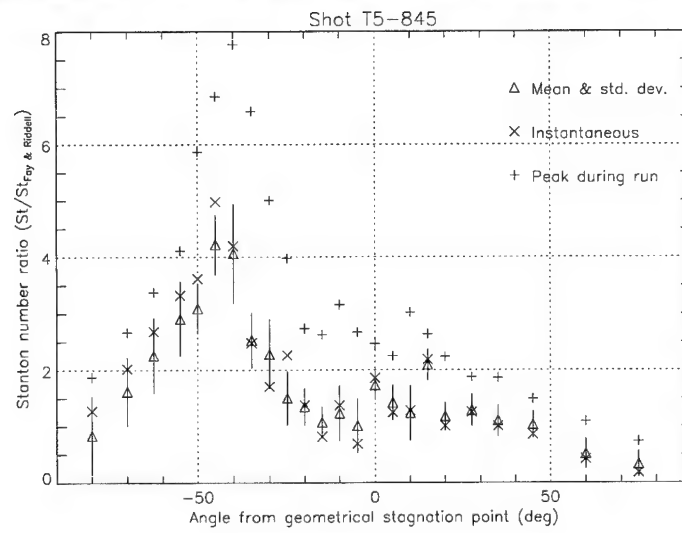
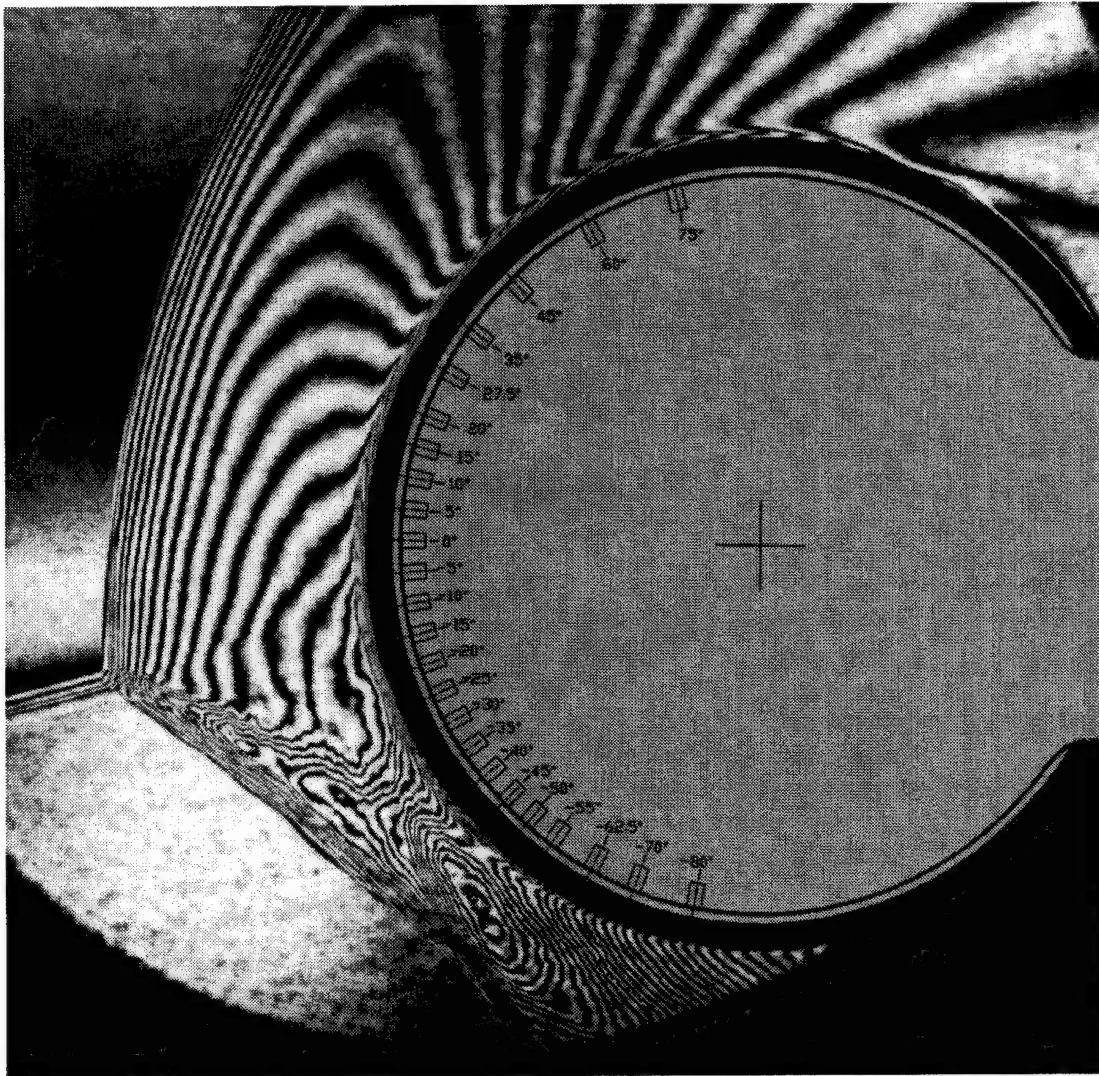


Figure C.3: Shot T5-845; condition A, $g/D = 2.254$.

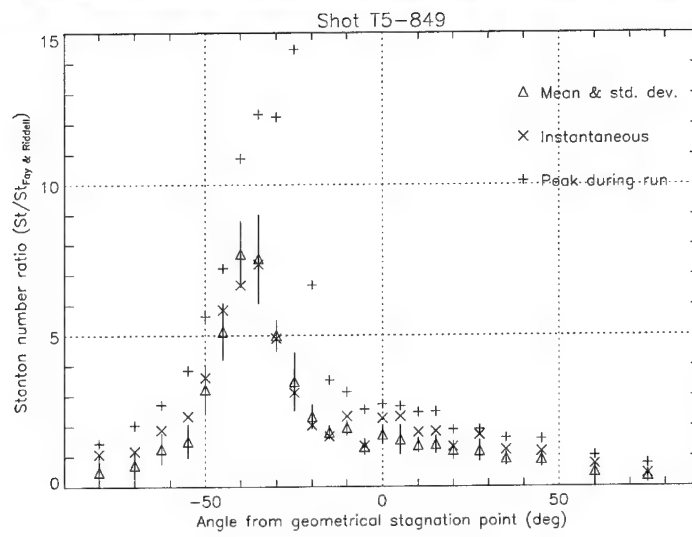
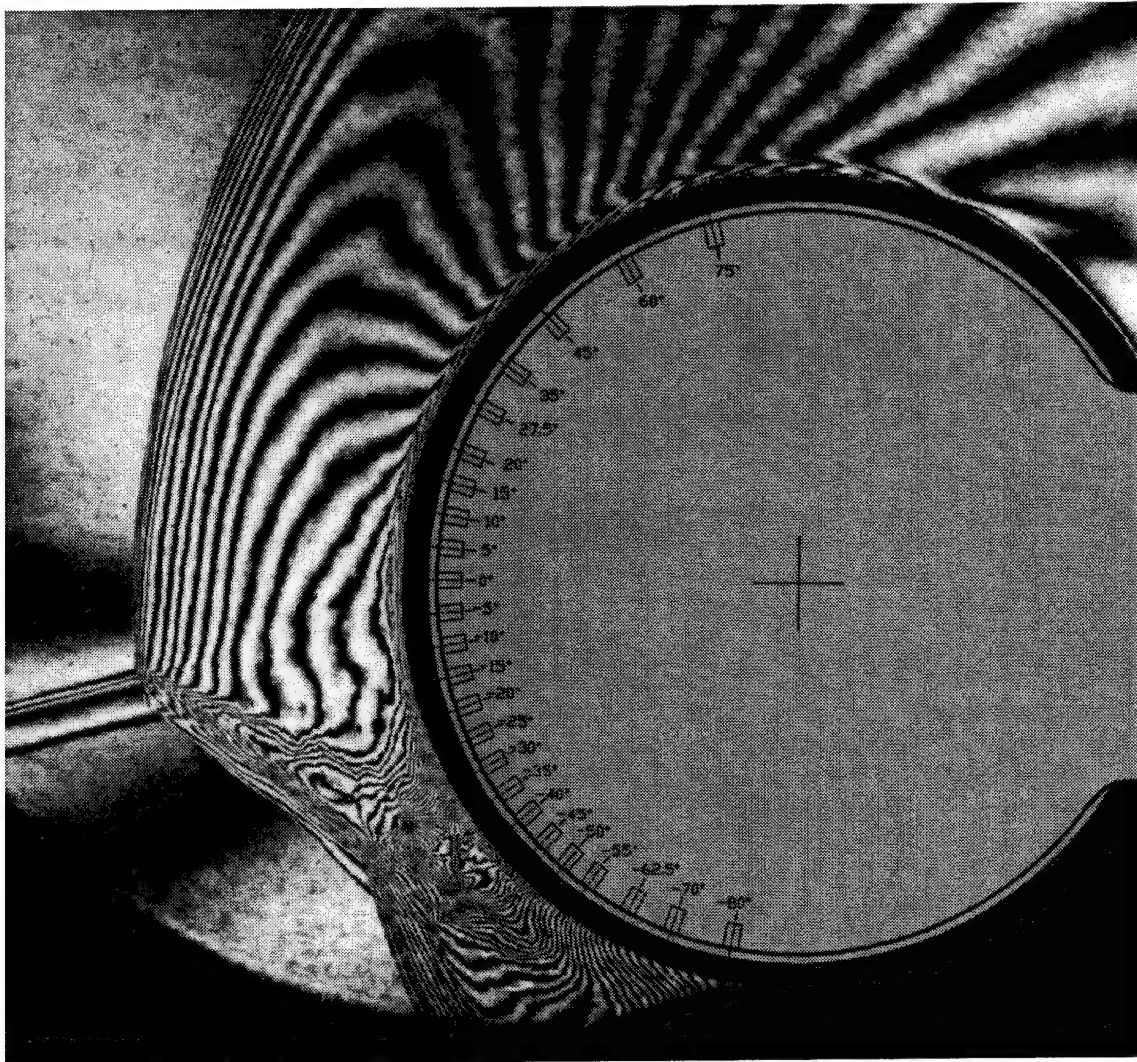


Figure C.4: Shot T5-849; condition A, $g/D = 2.339$.

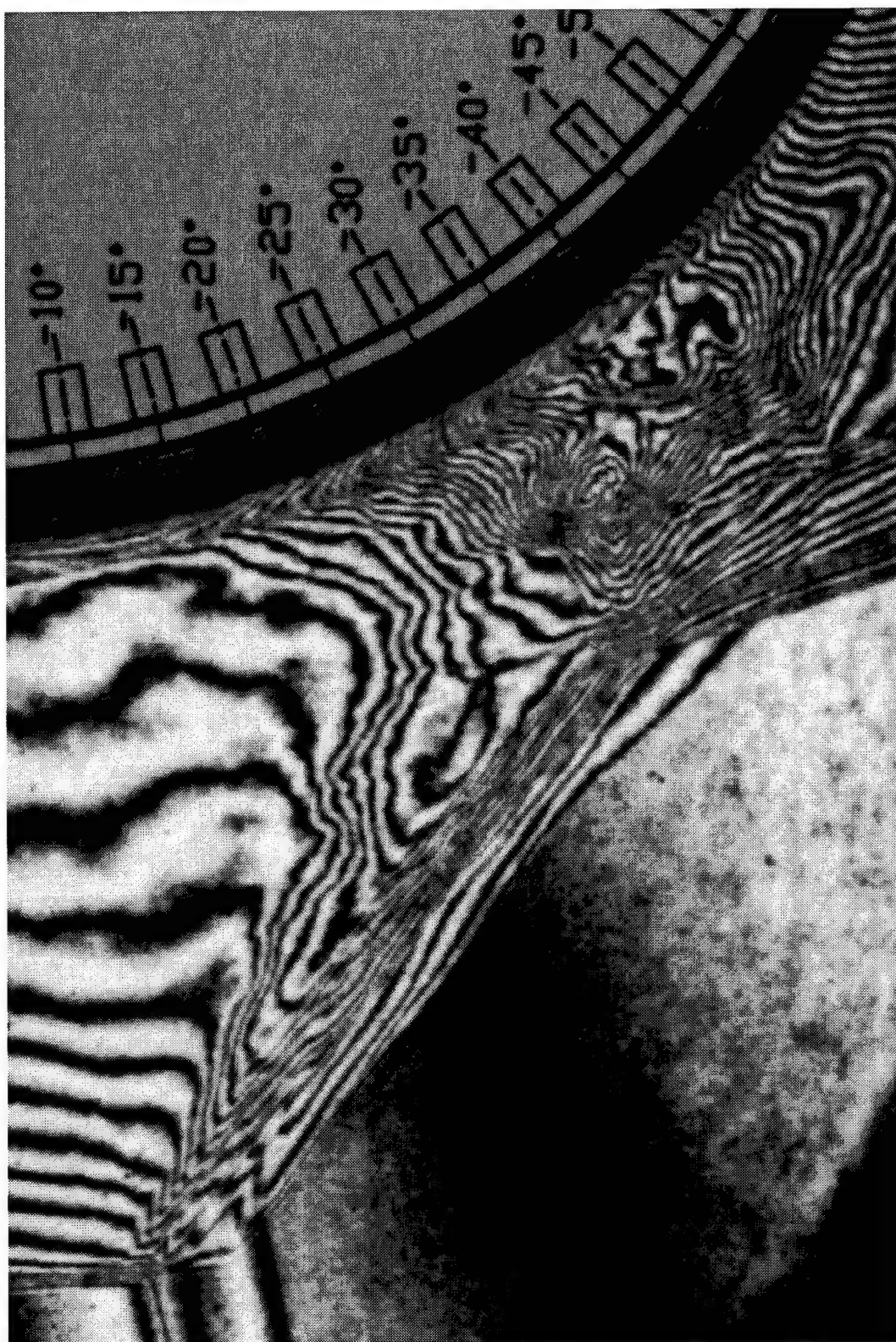


Figure C.5: Magnified view of holographic interferogram; Shot T5-849

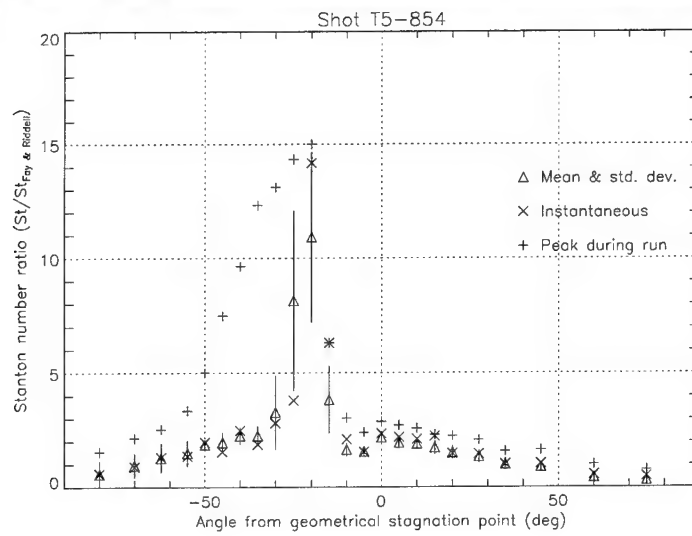
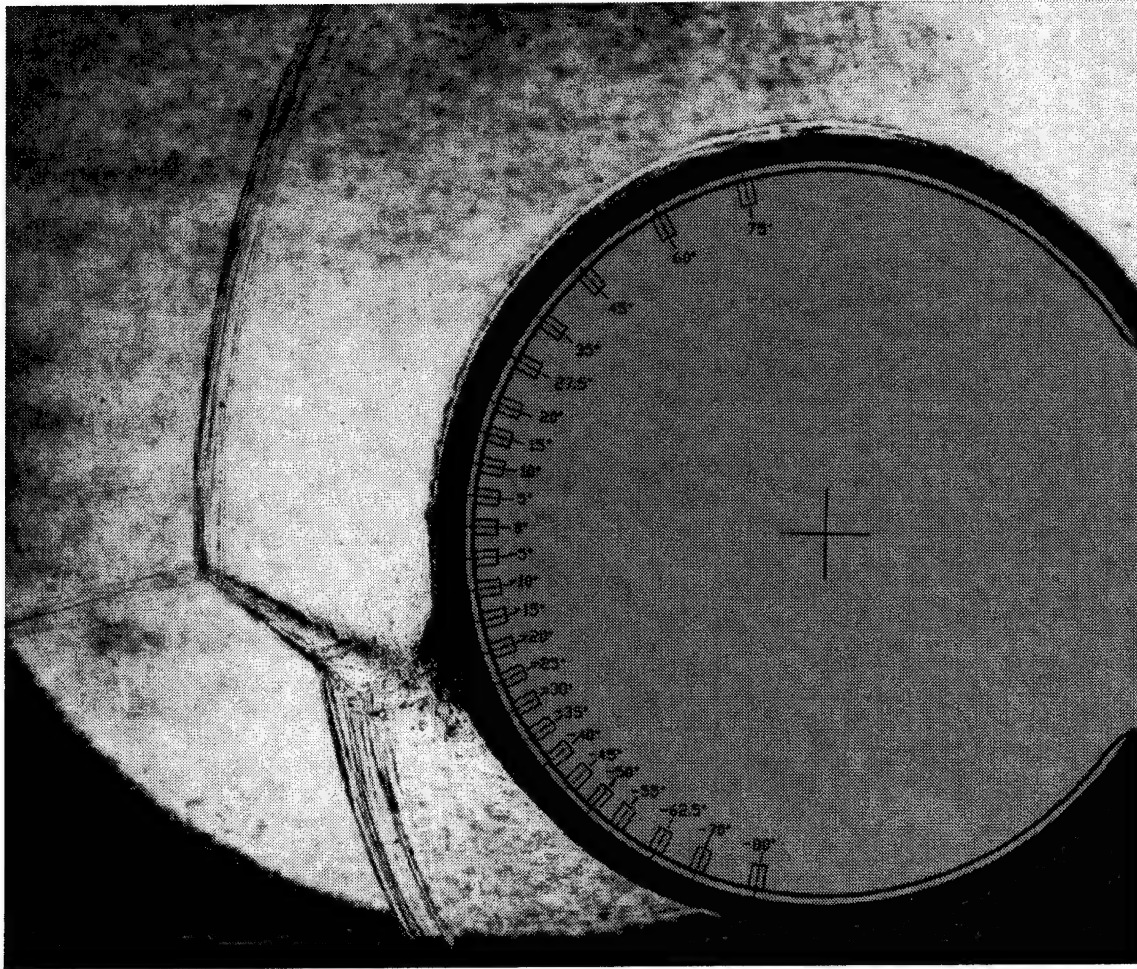


Figure C.6: Shot T5-854 (holographic shadowgraph); condition A, $g/D = 2.368$.

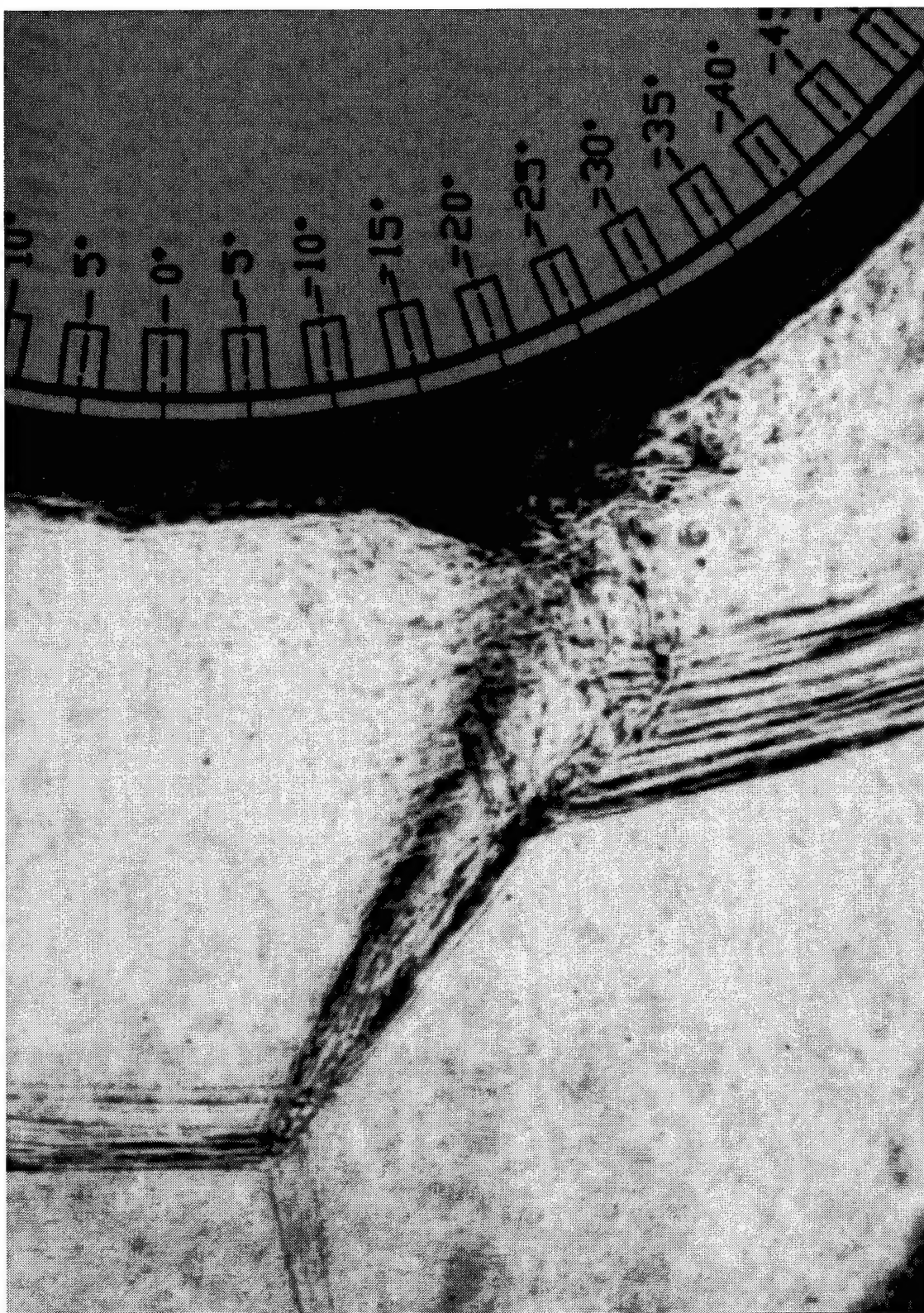


Figure C.7: Magnified view of holographic shadowgraph; Shot T5-854

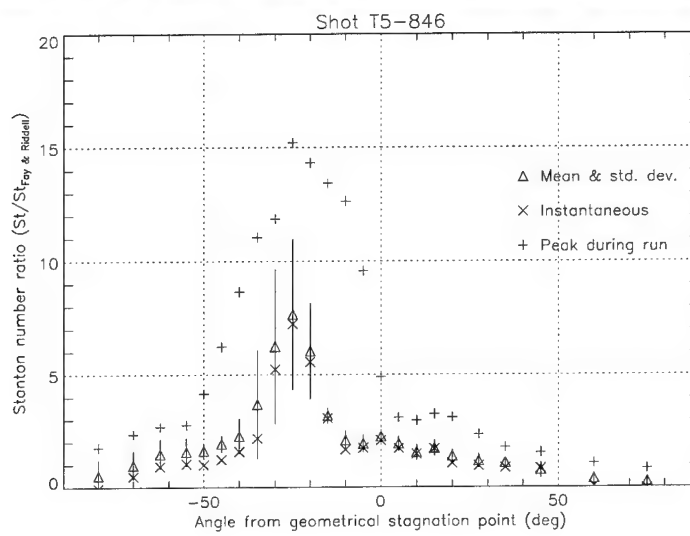
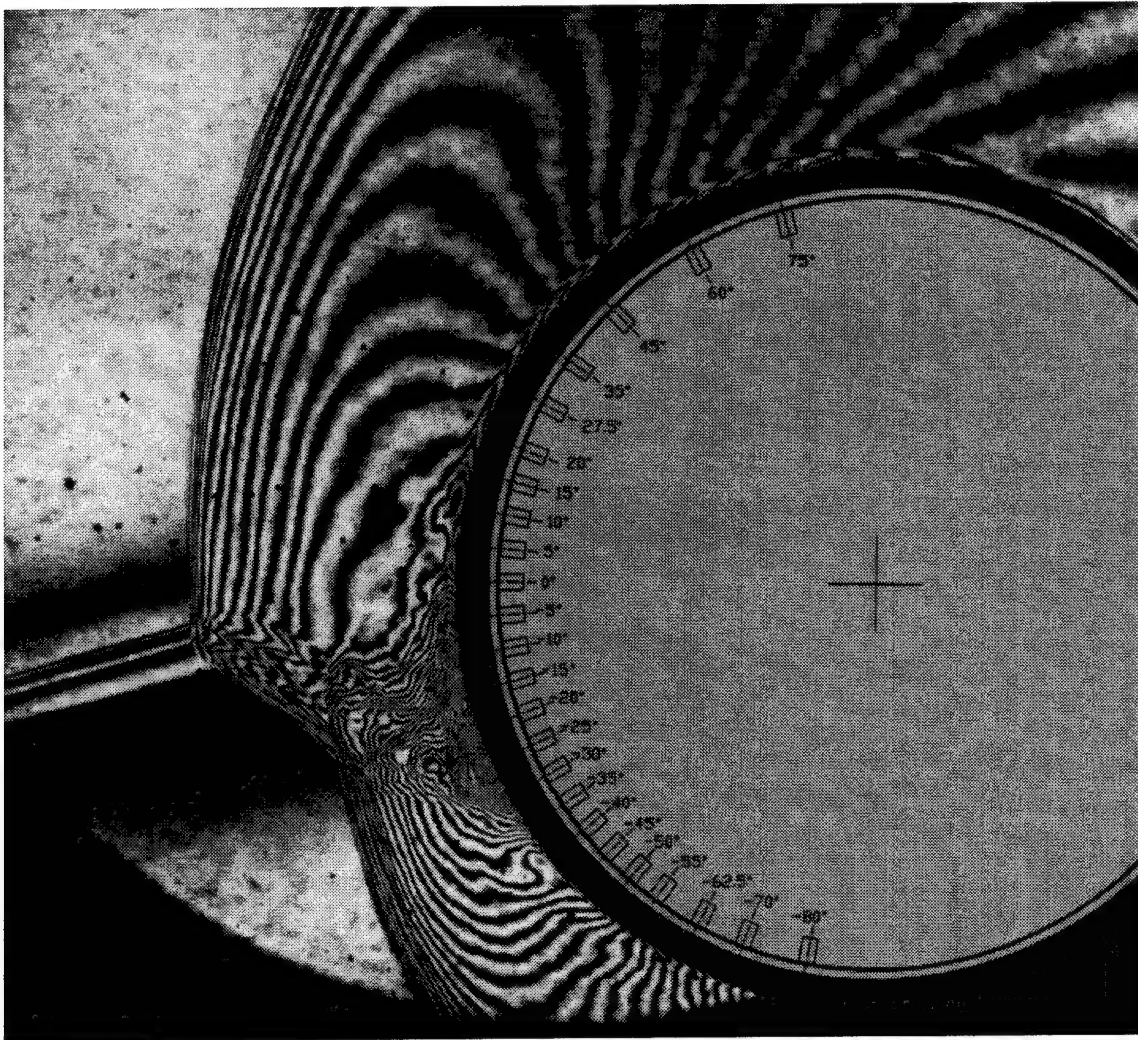


Figure C.8: Shot T5-846; condition A, $g/D = 2.371$.

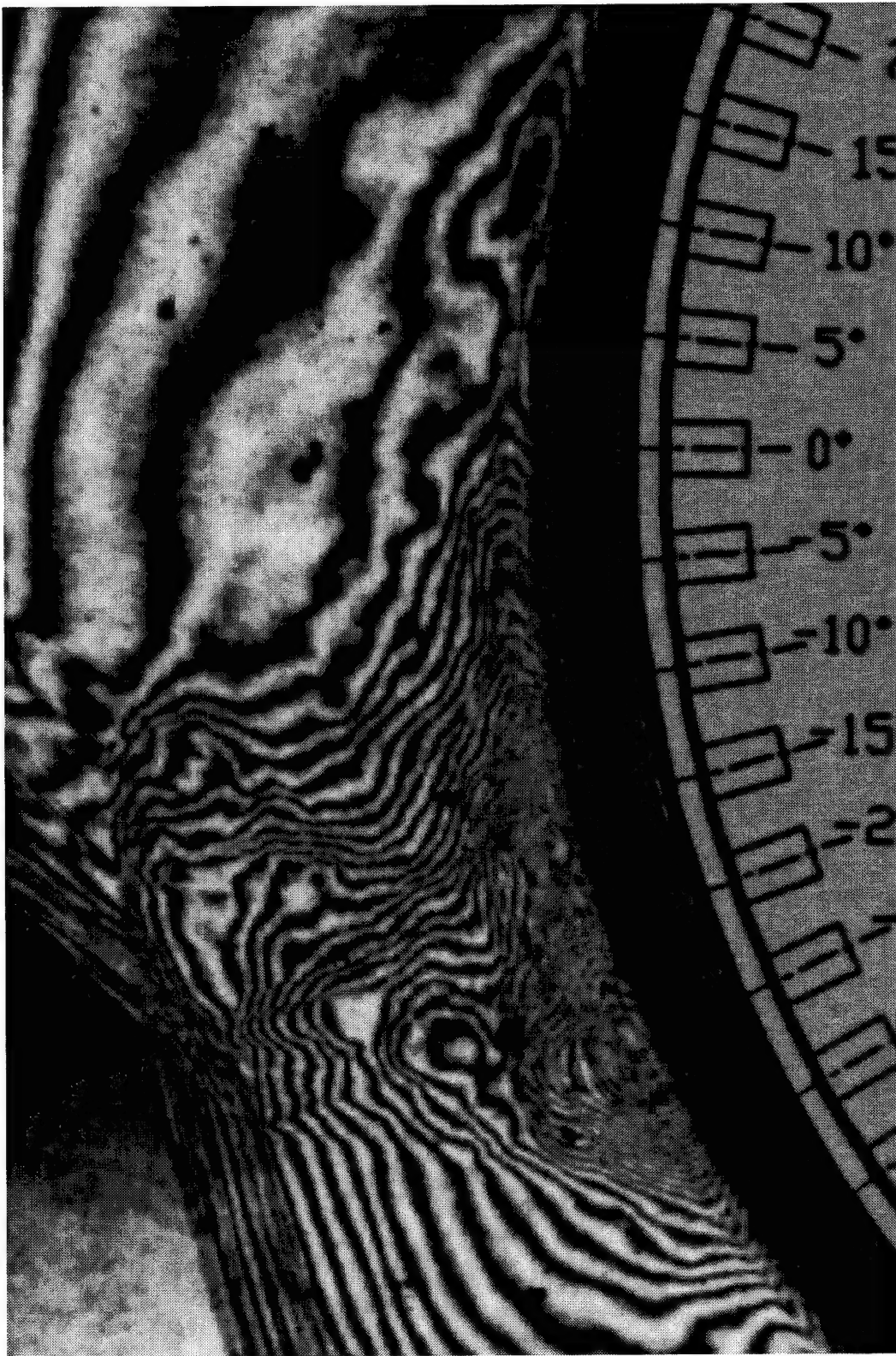


Figure C.9: Magnified view of holographic interferogram; Shot T5-846

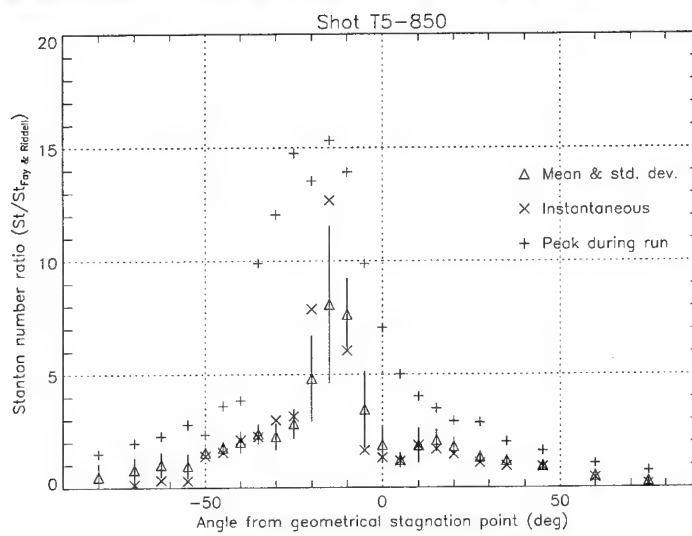
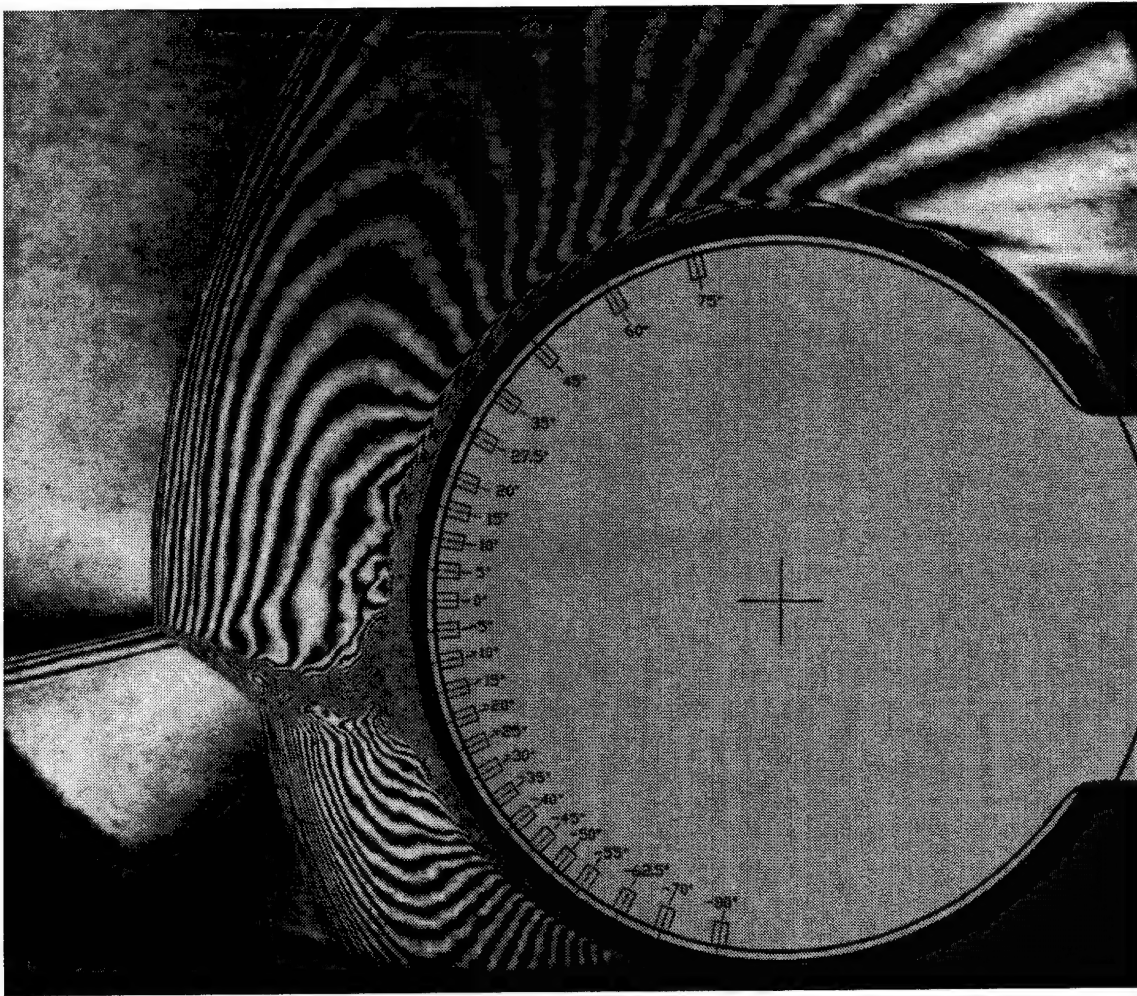


Figure C.10: Shot T5-850; condition A, $g/D = 2.396$.

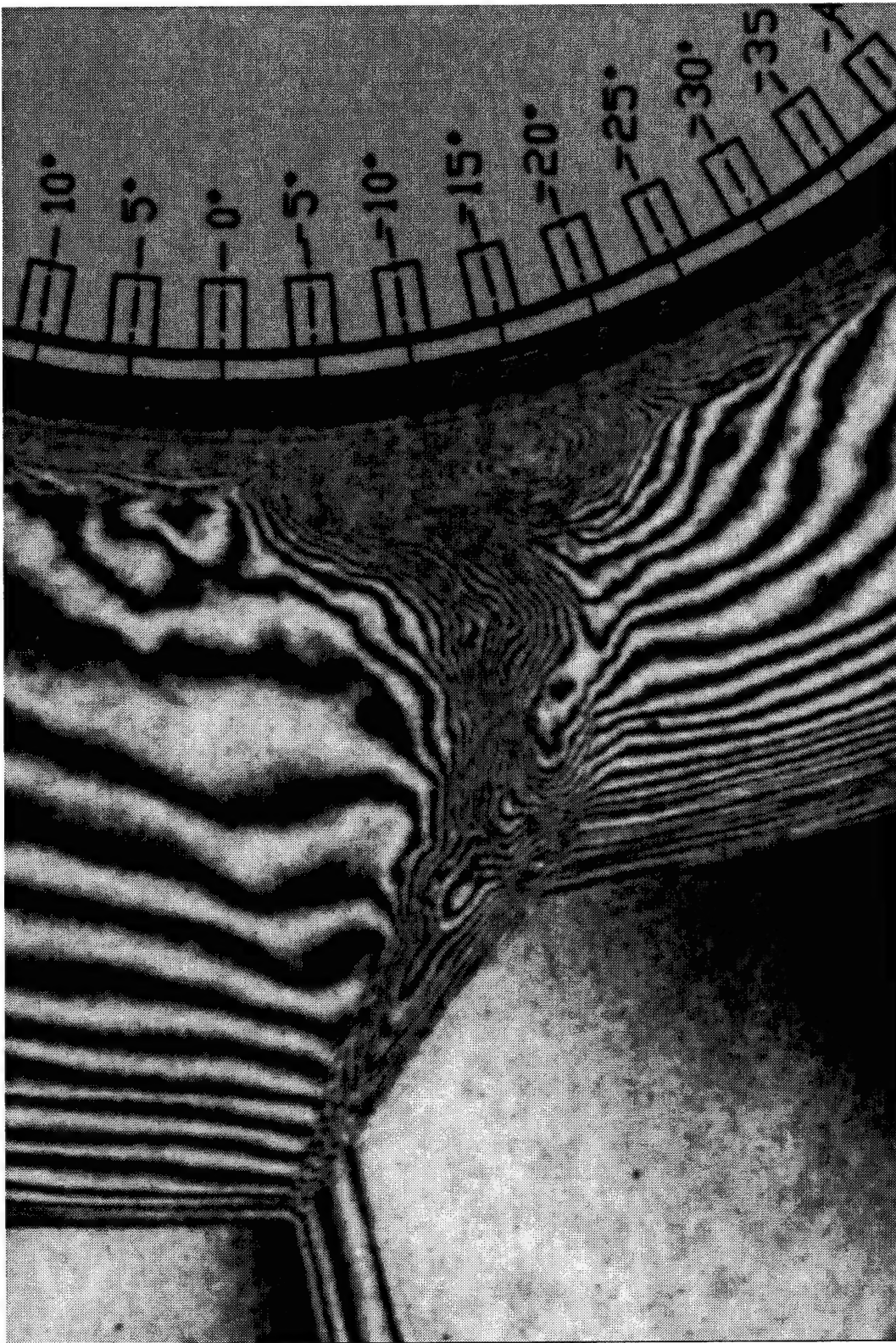


Figure C.11: Magnified view of holographic interferogram; Shot T5-850

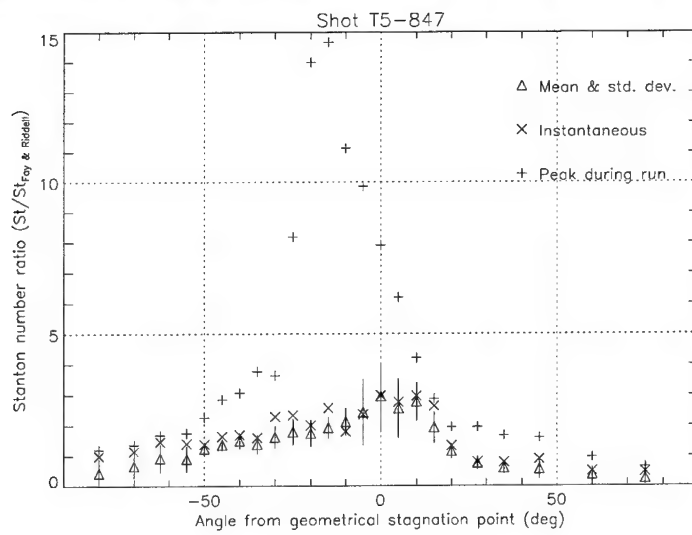
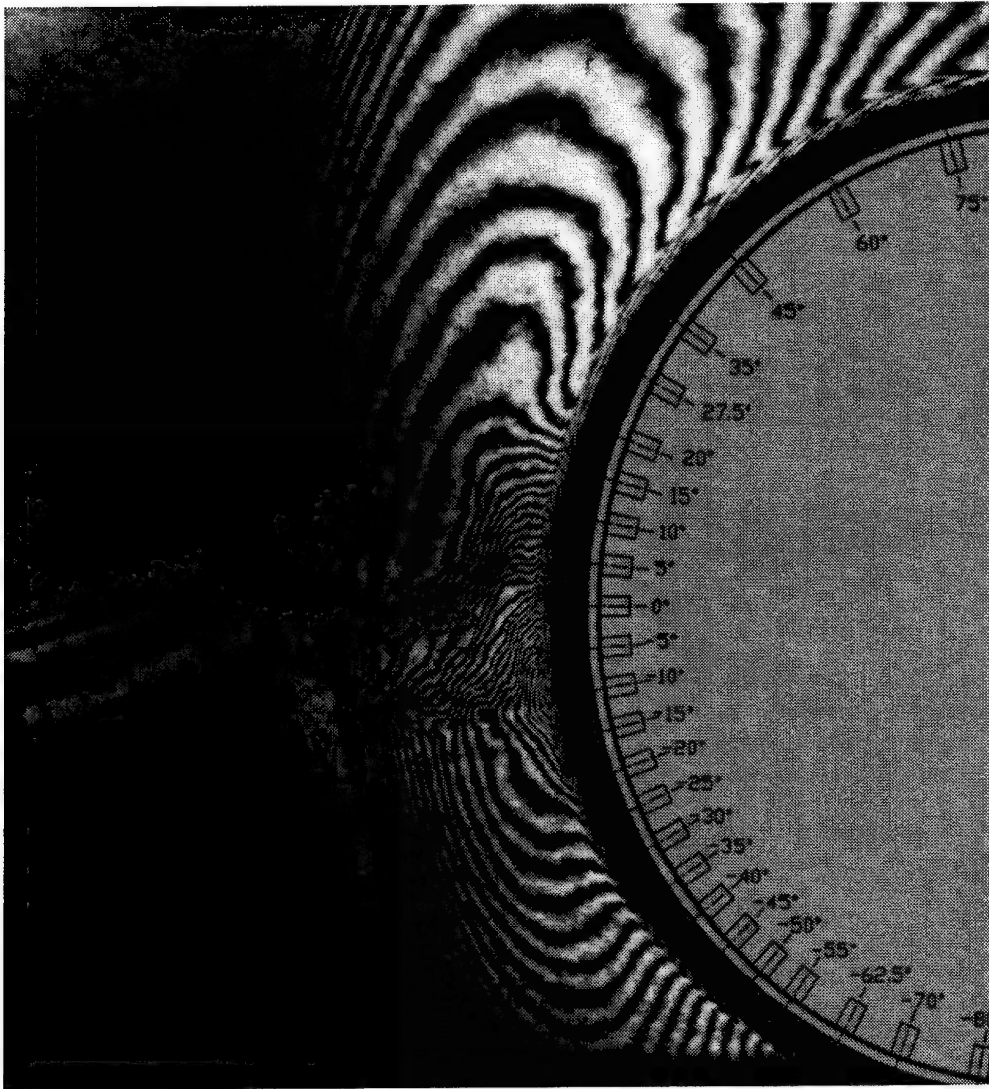


Figure C.12: Shot T5-847; condition A, $g/D = 2.450$.

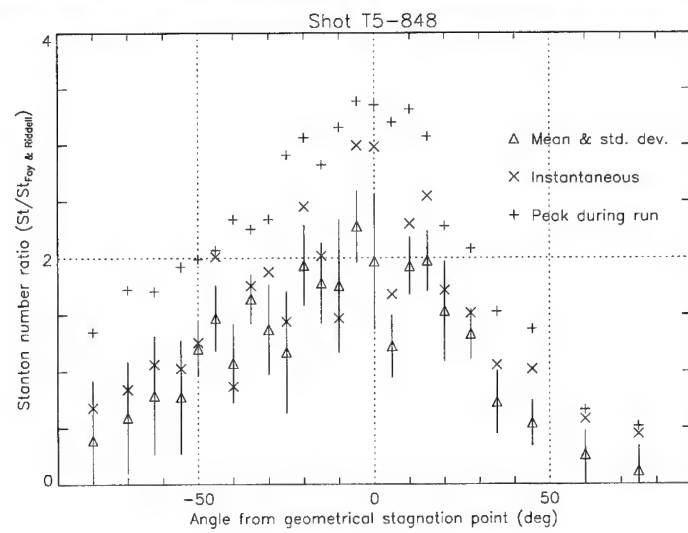
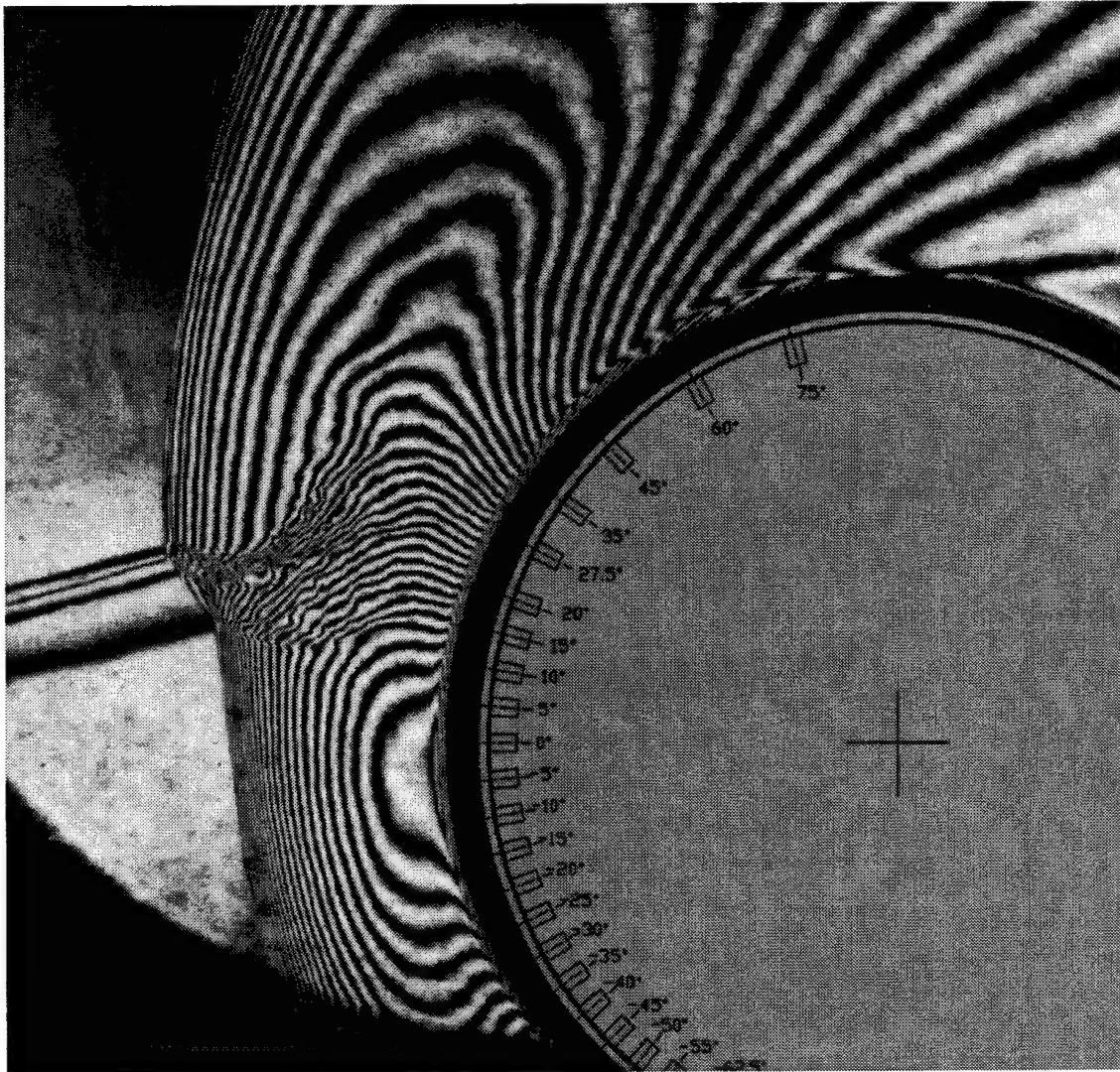


Figure C.13: Shot T5-848; condition A, $g/D = 2.565$.

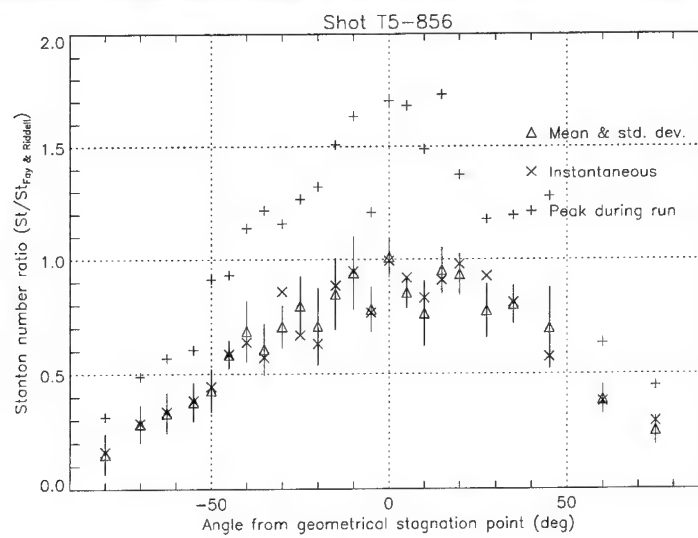
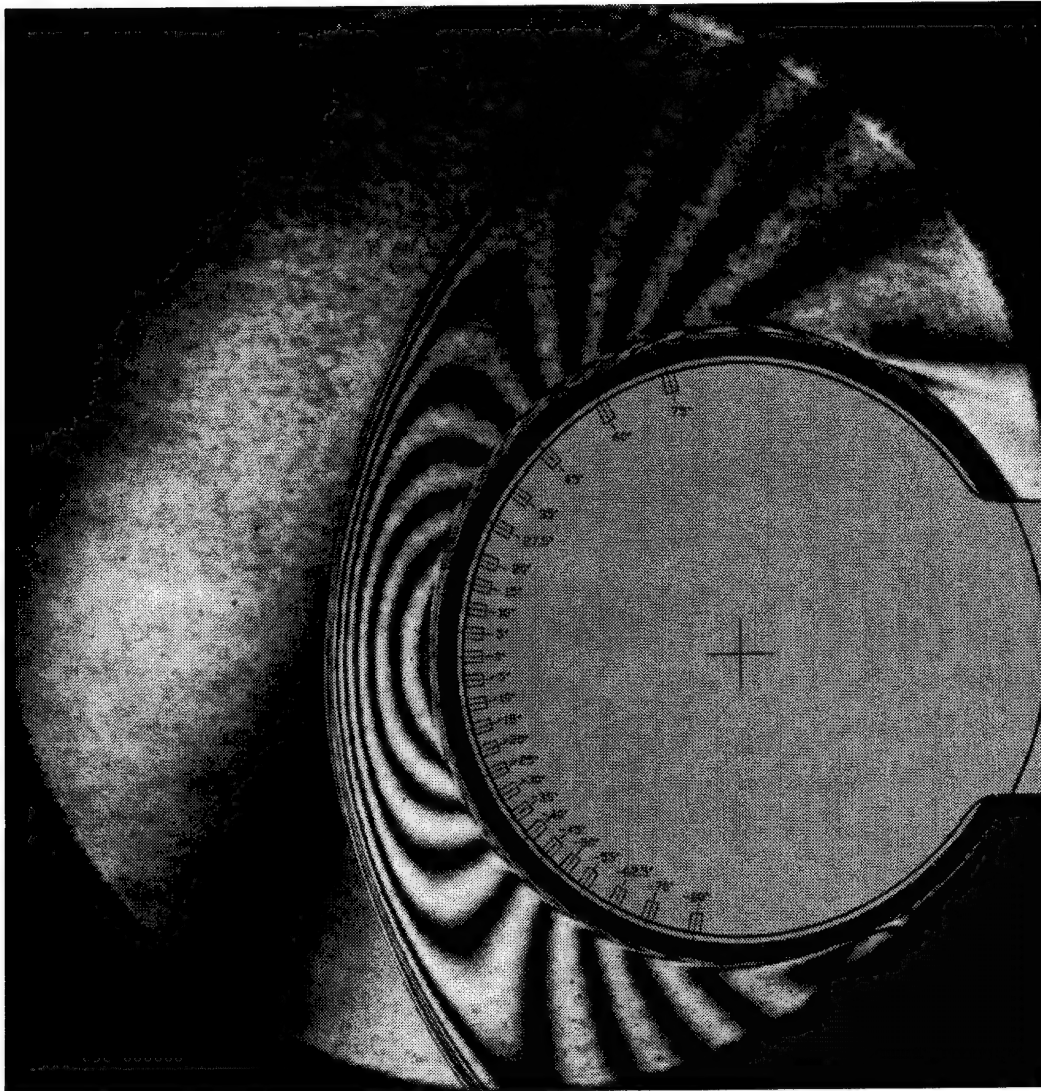


Figure C.14: Shot T5-856; condition B, $g/D = 2.185$.

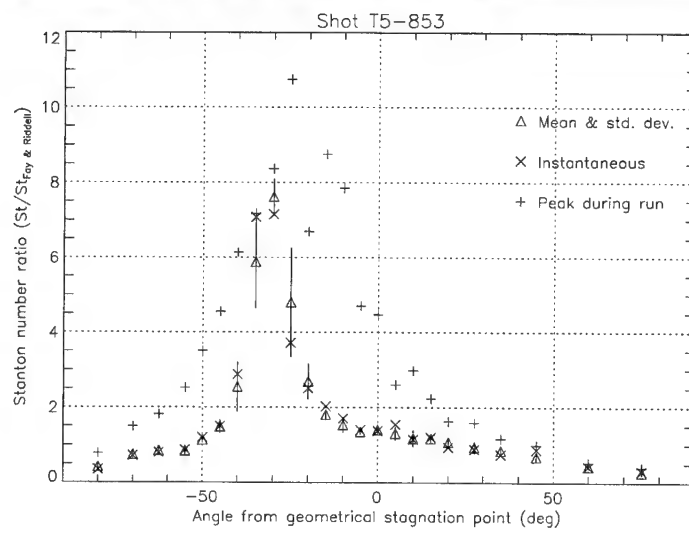
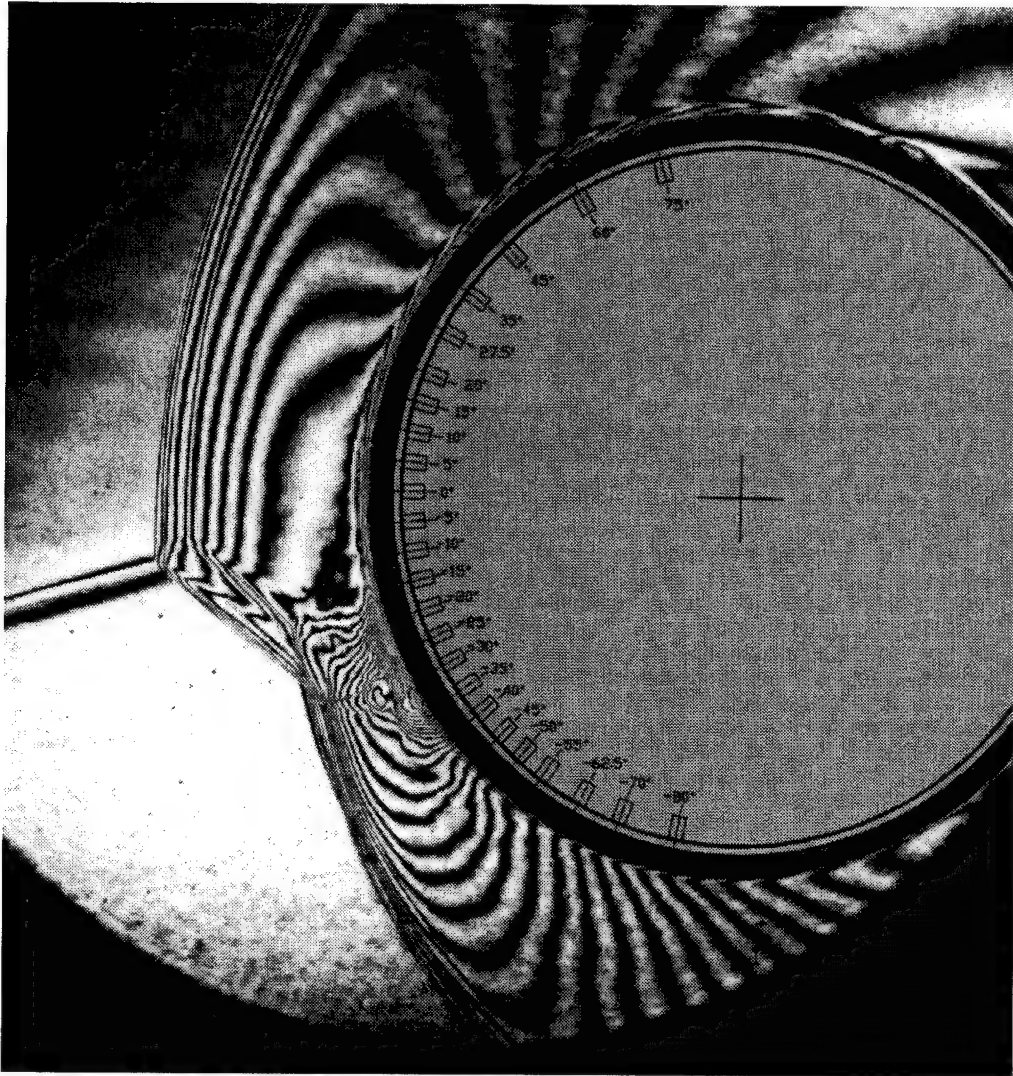


Figure C.15: Shot T5-853; condition B, $g/D = 2.163$.



Figure C.16: Magnified view of holographic interferogram; Shot T5-853

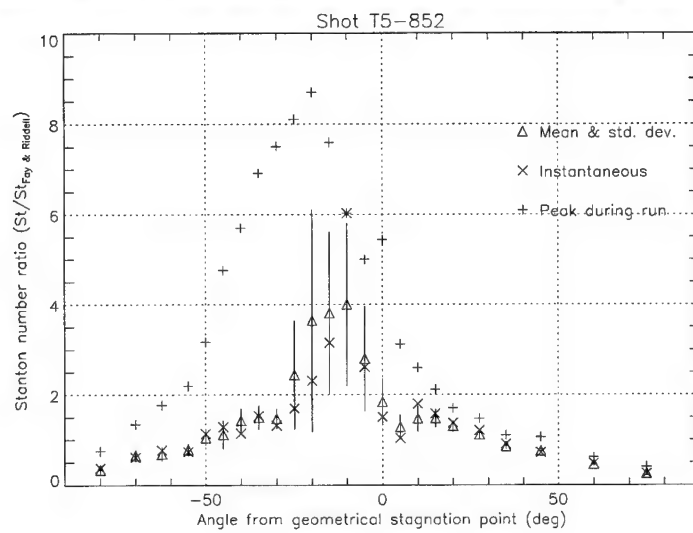
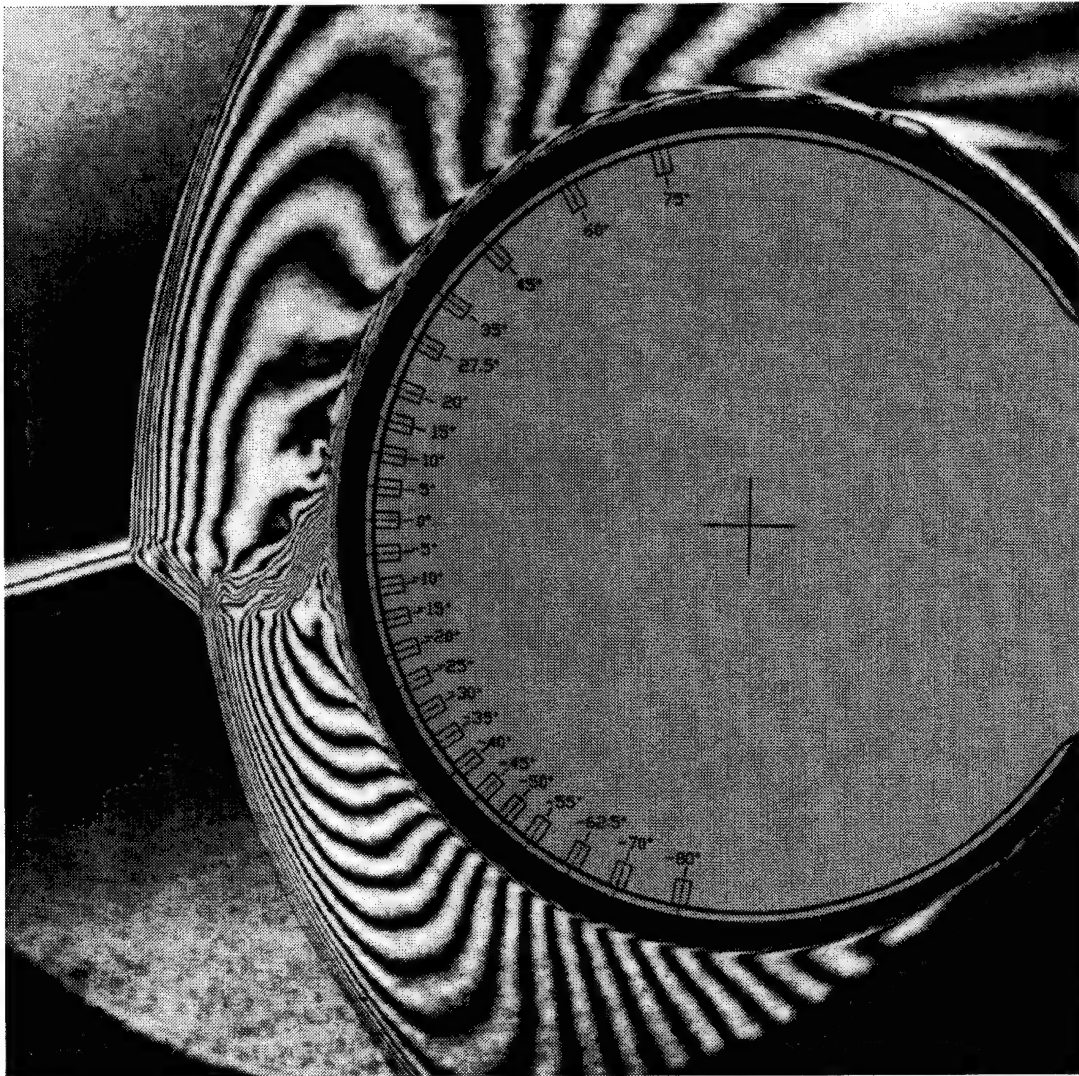


Figure C.17: Shot T5-852; condition B, $g/D = 2.197$.

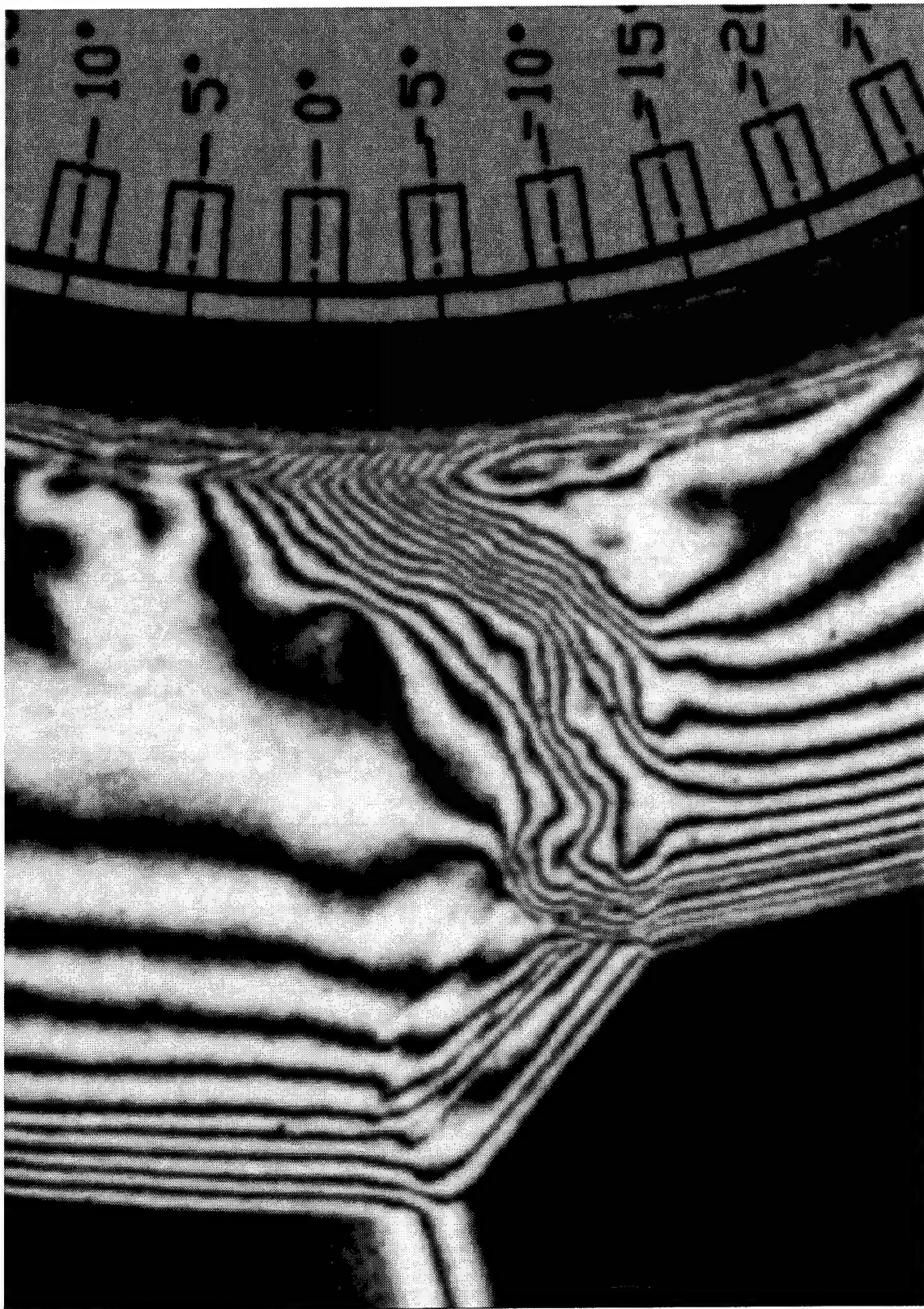


Figure C.18: Magnified view of holographic interferogram; Shot T5-852

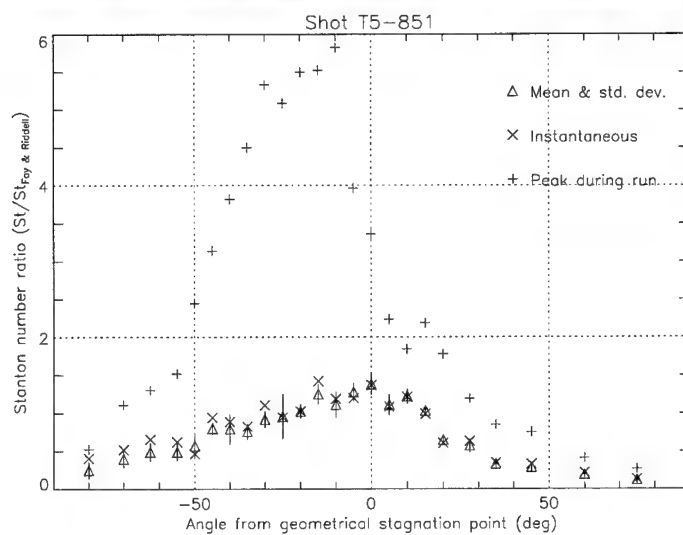
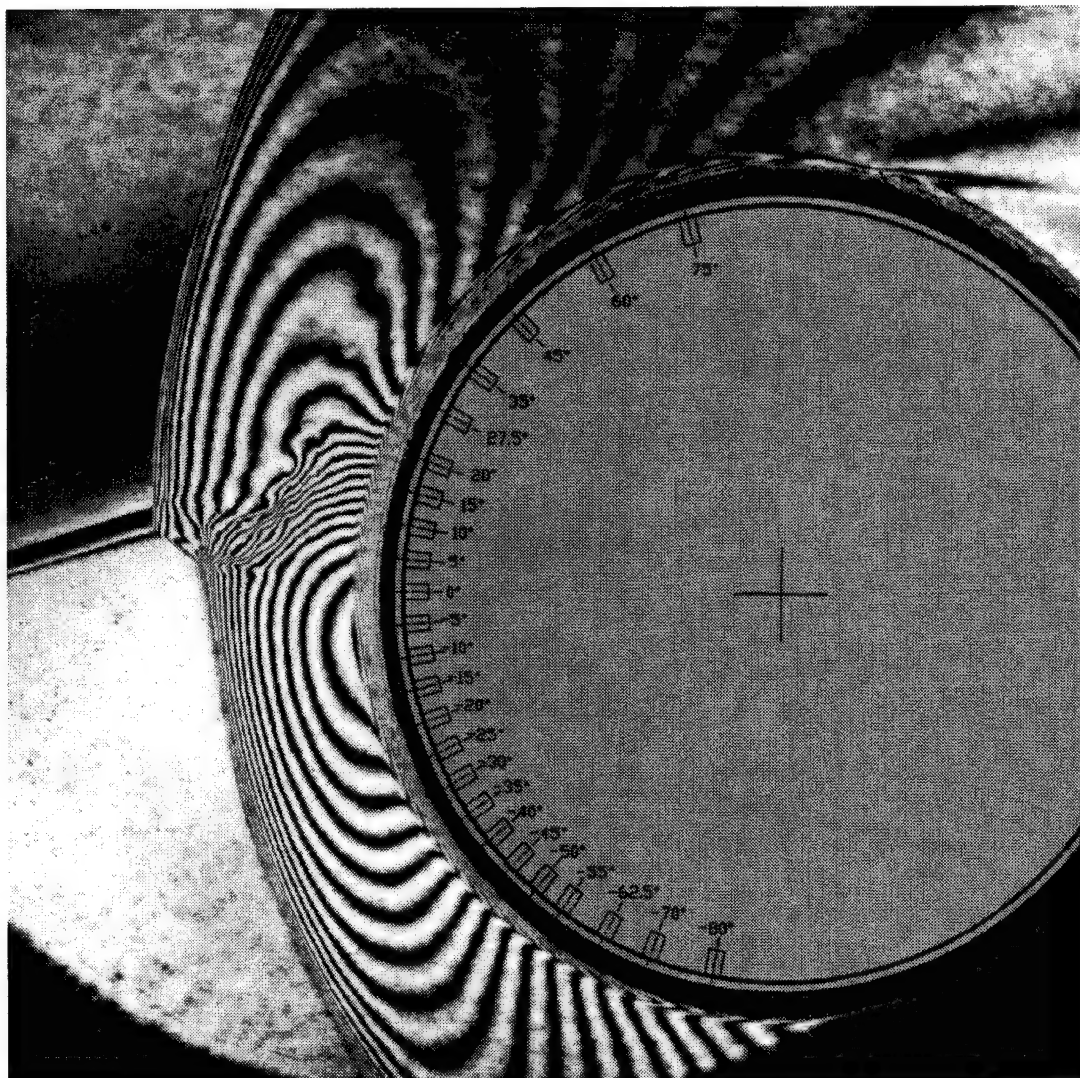


Figure C.19: Shot T5-851; condition B, $g/D = 2.281$.

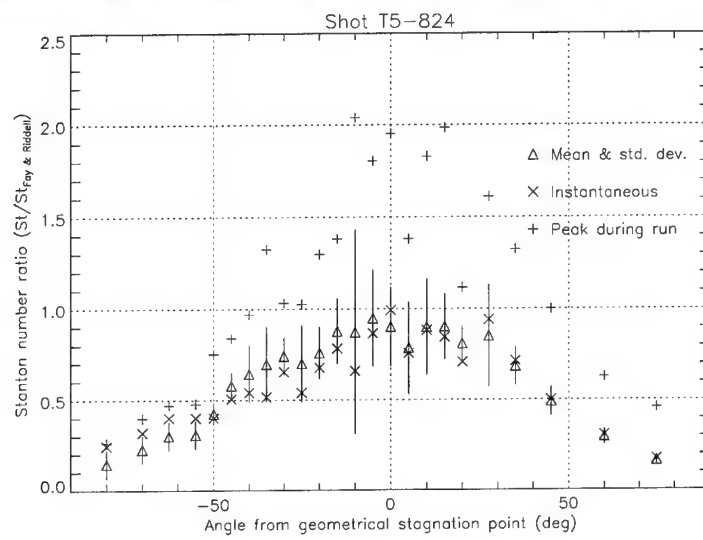
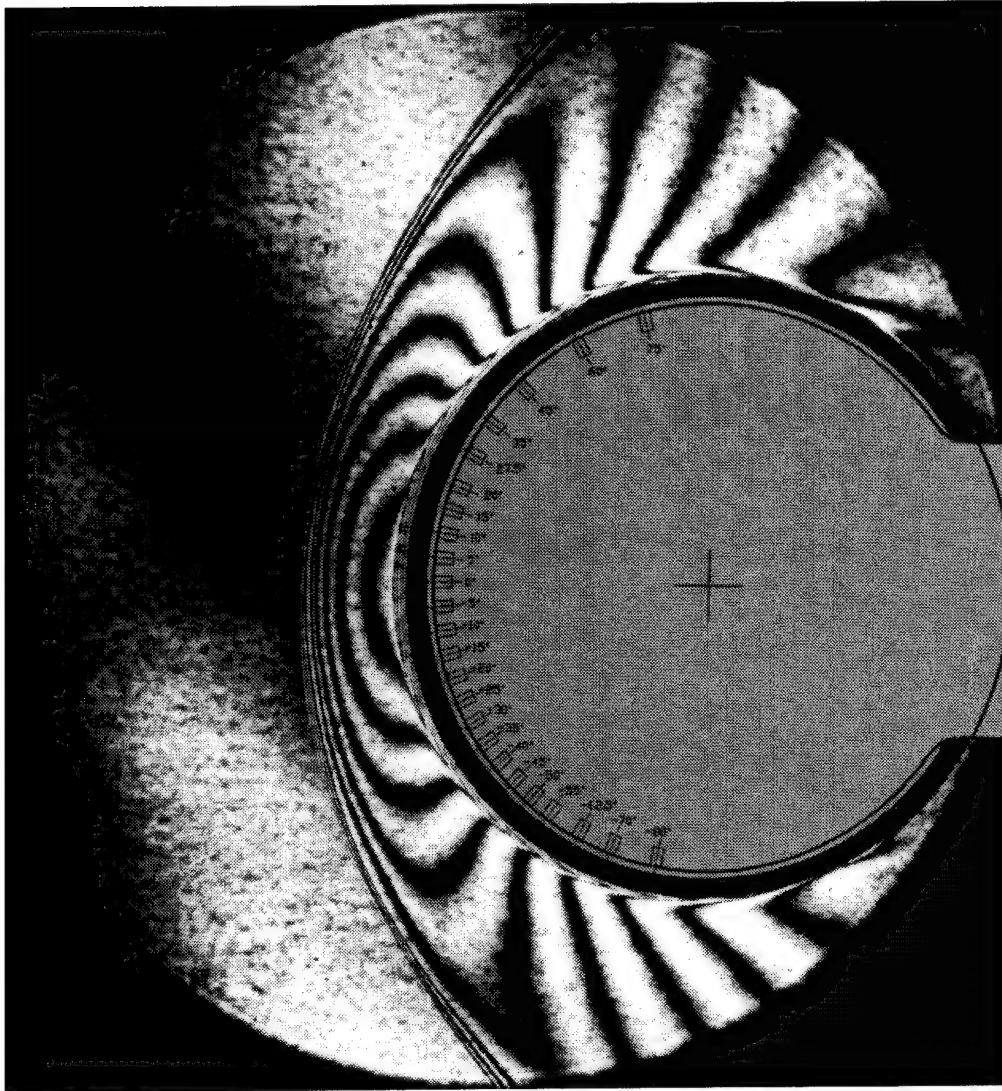


Figure C.20: Shot T5-824; condition C, $g/D = 2.081$.

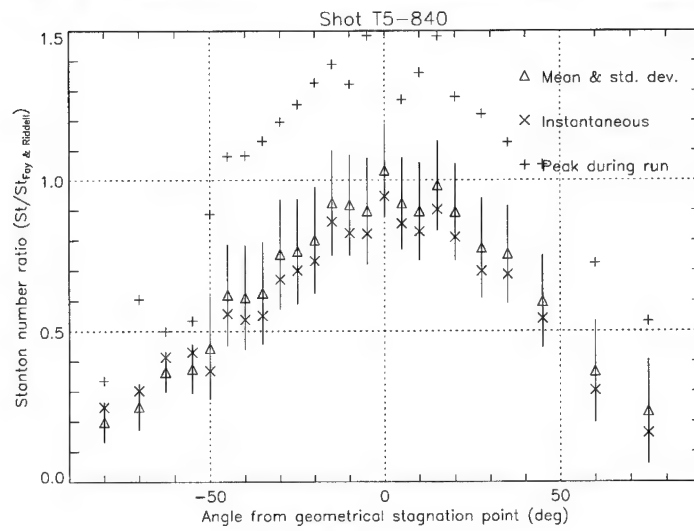
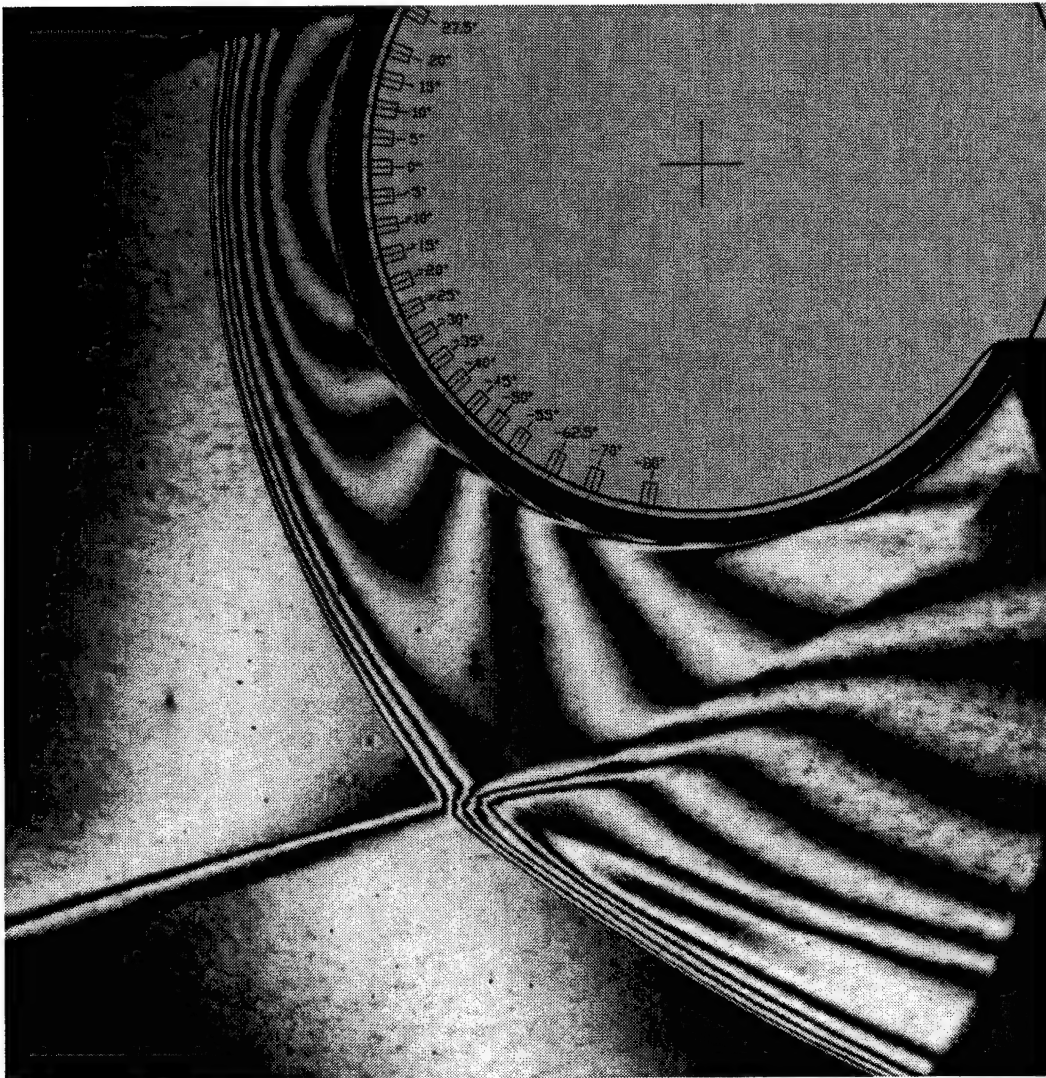


Figure C.21: Shot T5-840; condition C, $g/D = 1.361$.

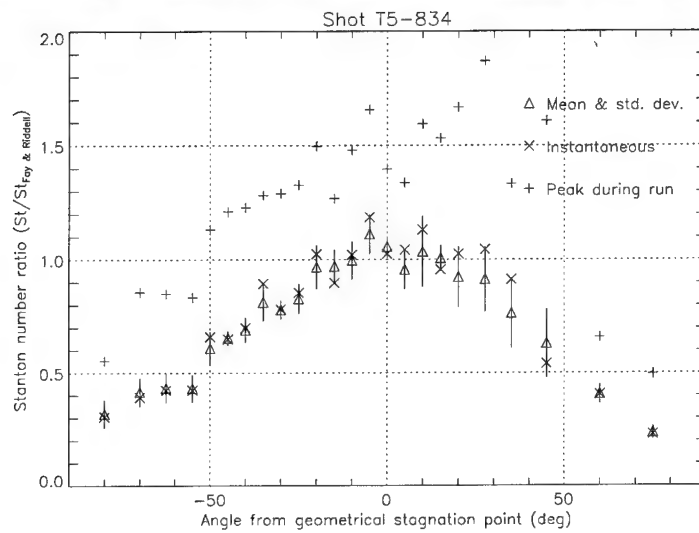
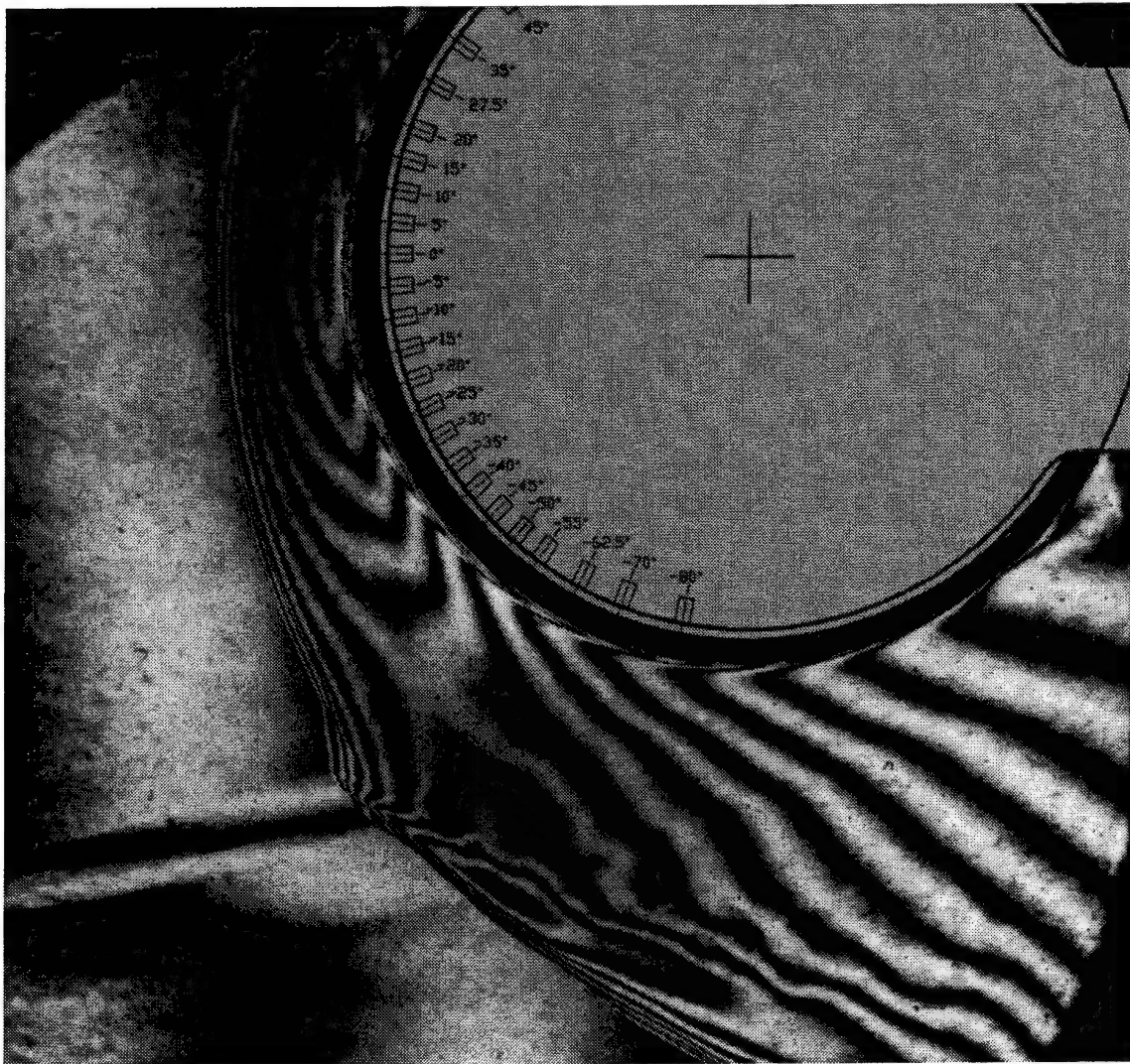


Figure C.22: Shot T5-834; condition C, $g/D = 1.485$.

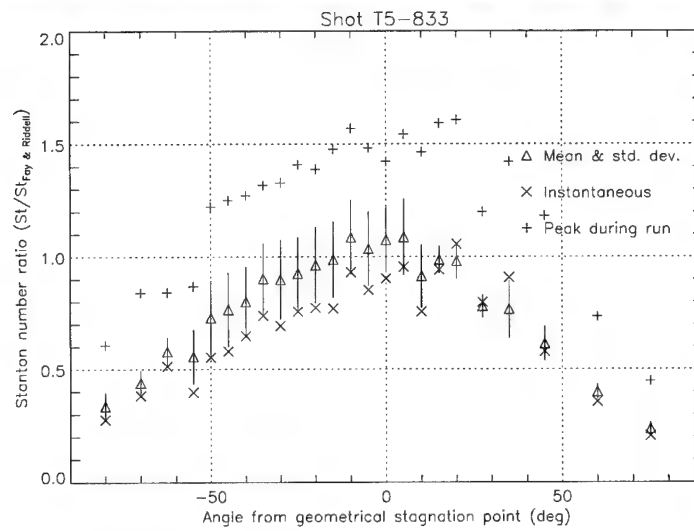
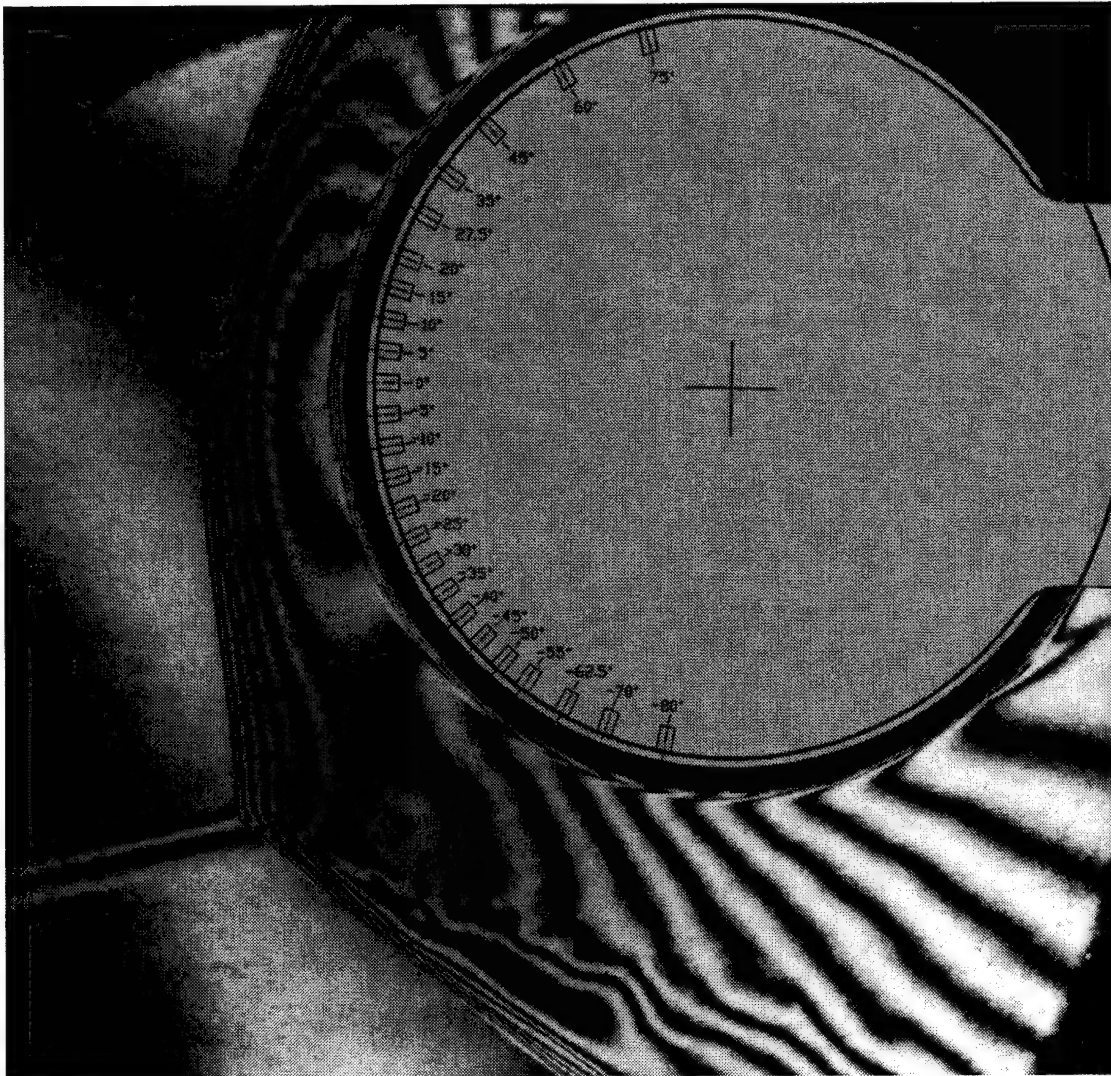


Figure C.23: Shot T5-833; condition C, $g/D = 1.622$.

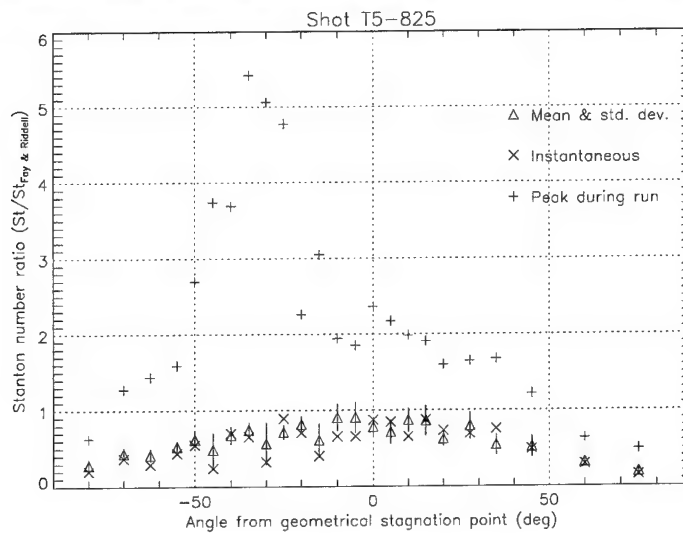
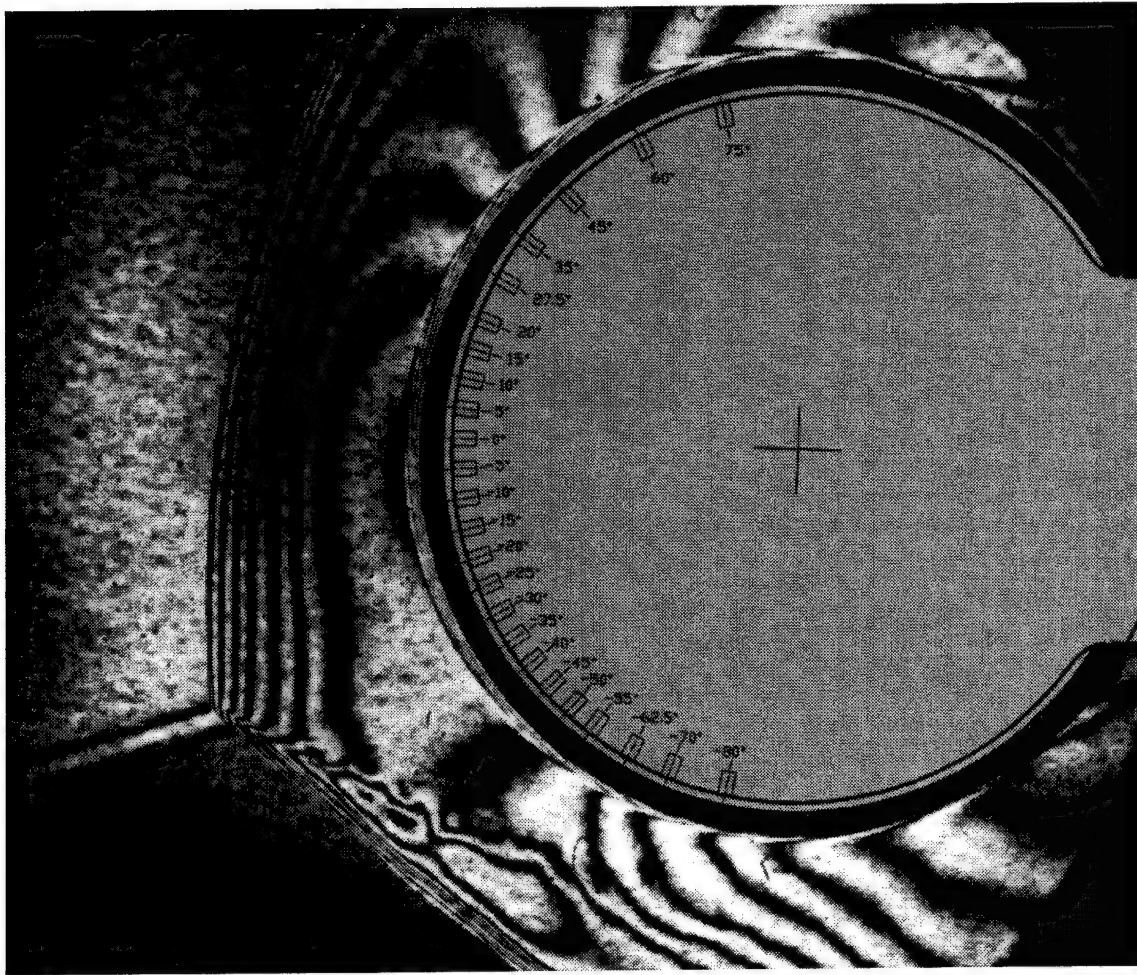


Figure C.24: Shot T5-825; condition C, $g/D = 1.926$.

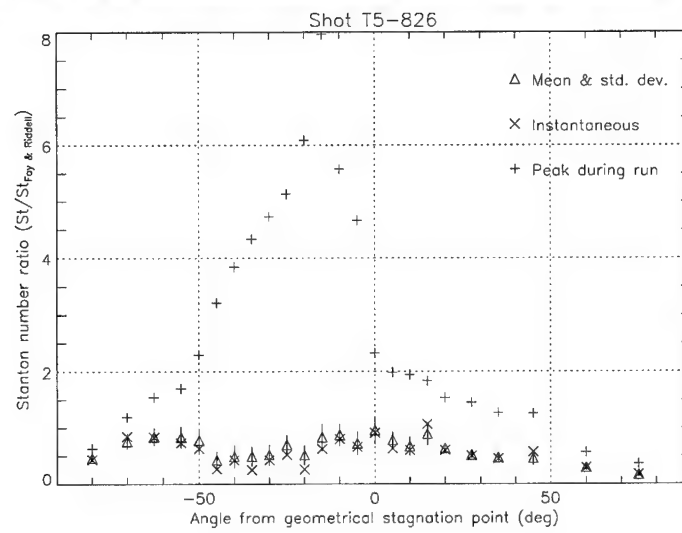
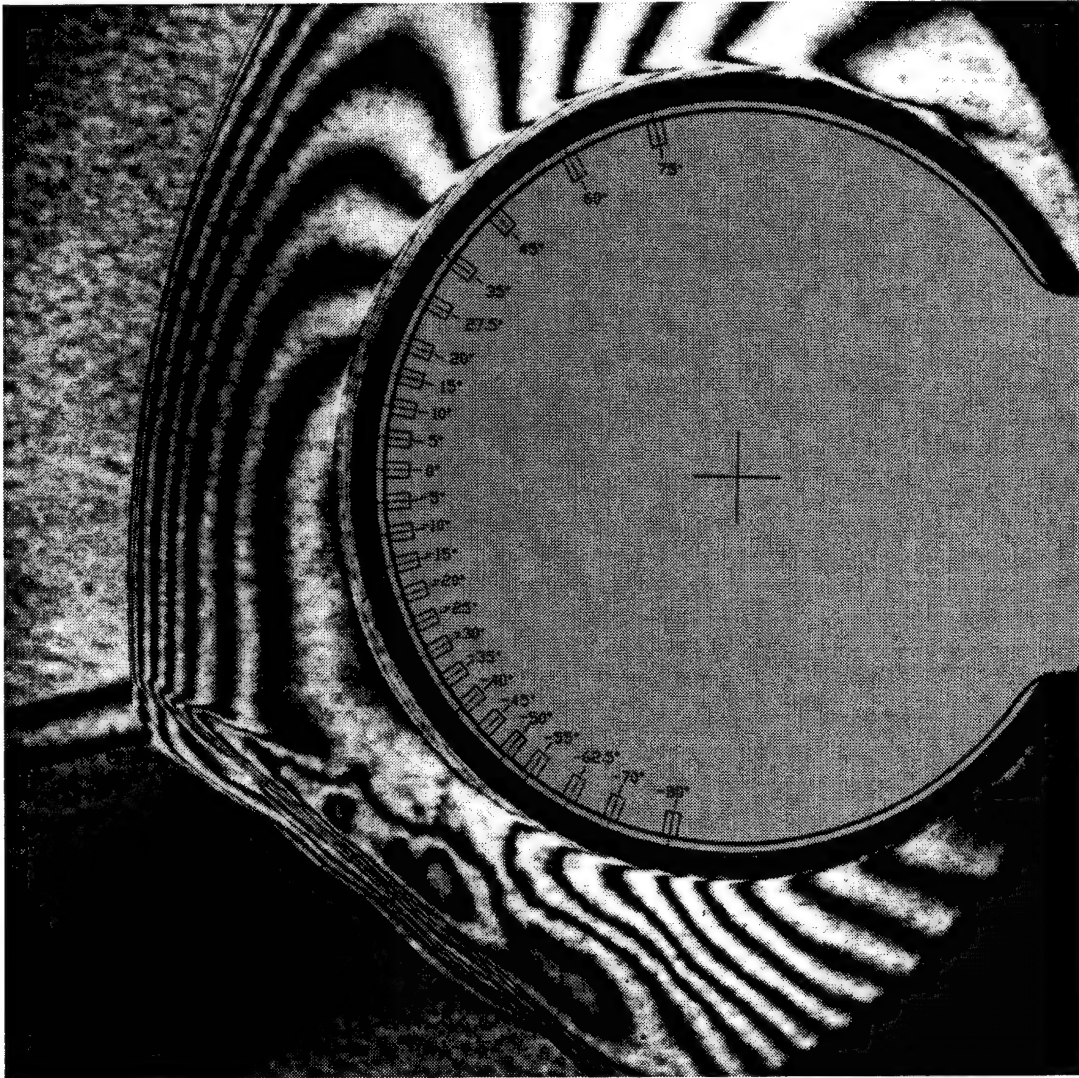


Figure C.25: Shot T5-826; condition C, $g/D = 2.036$.

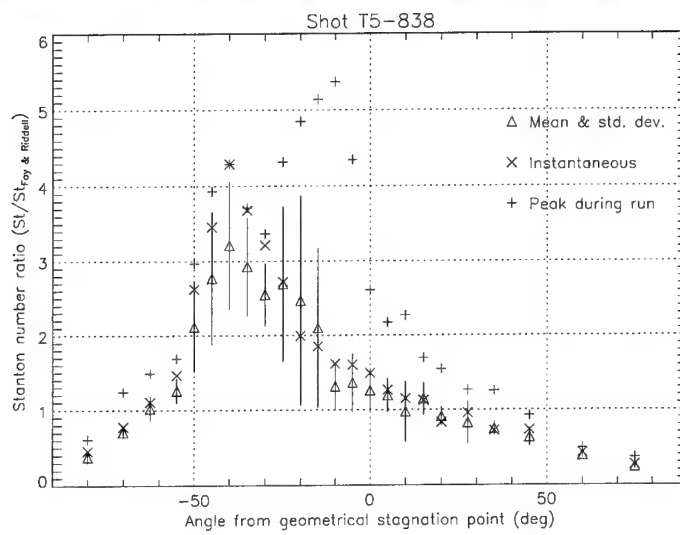
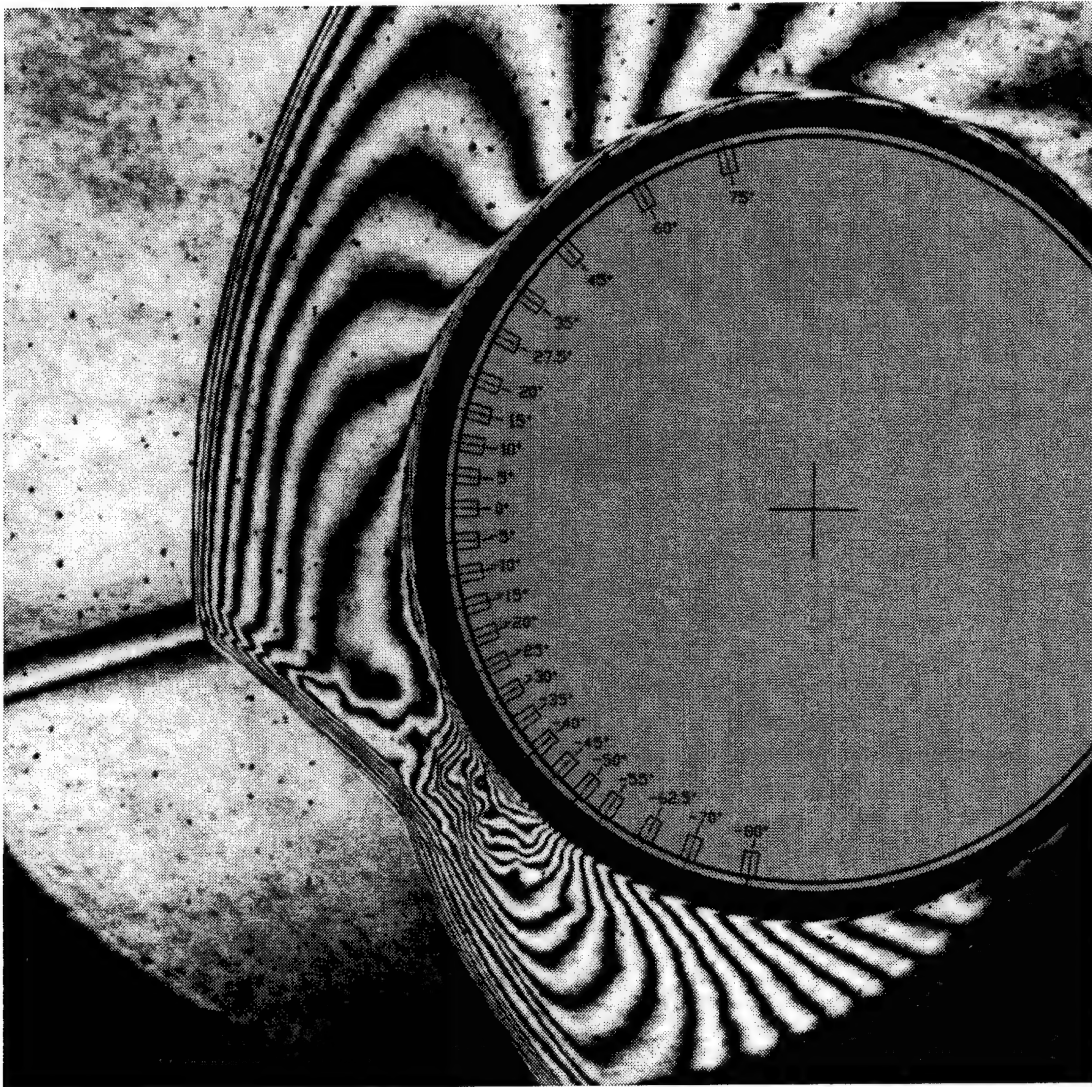


Figure C.26: Shot T5-838; condition C, $g/D = 2.113$.

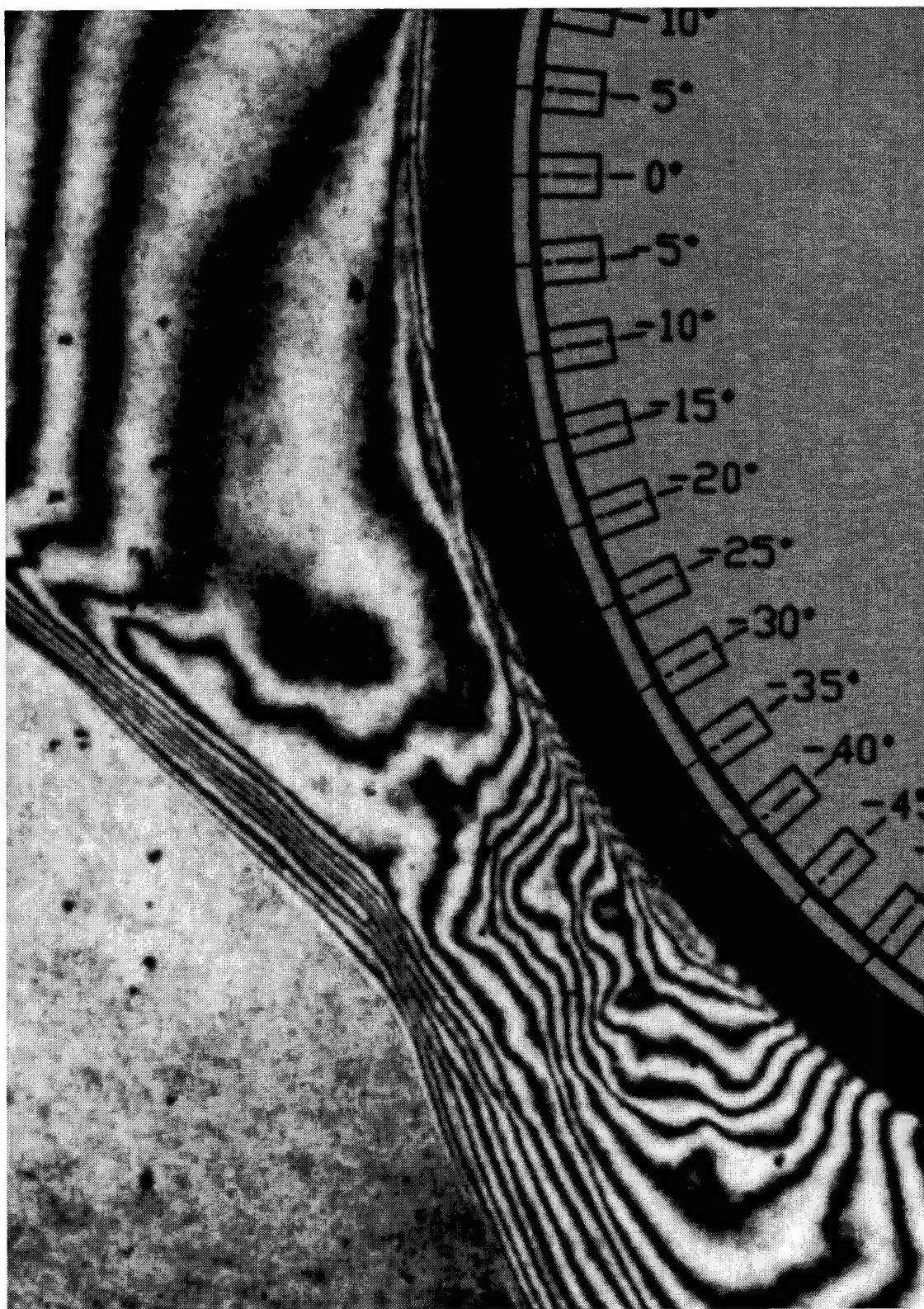


Figure C.27: Magnified view of holographic interferogram; Shot T5-838

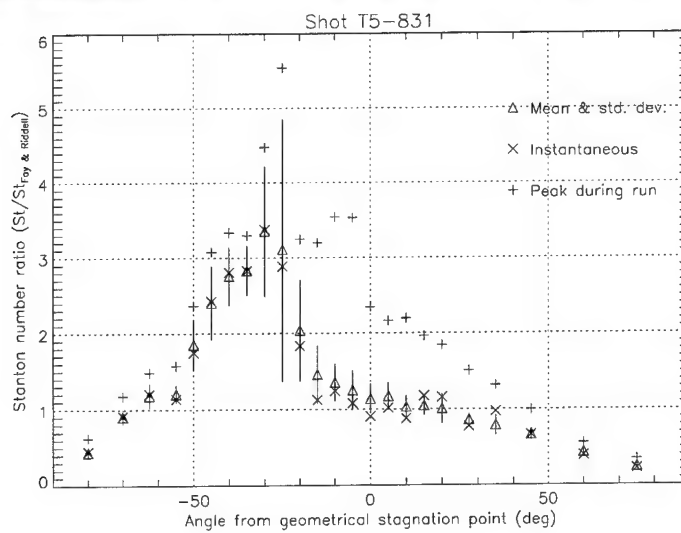
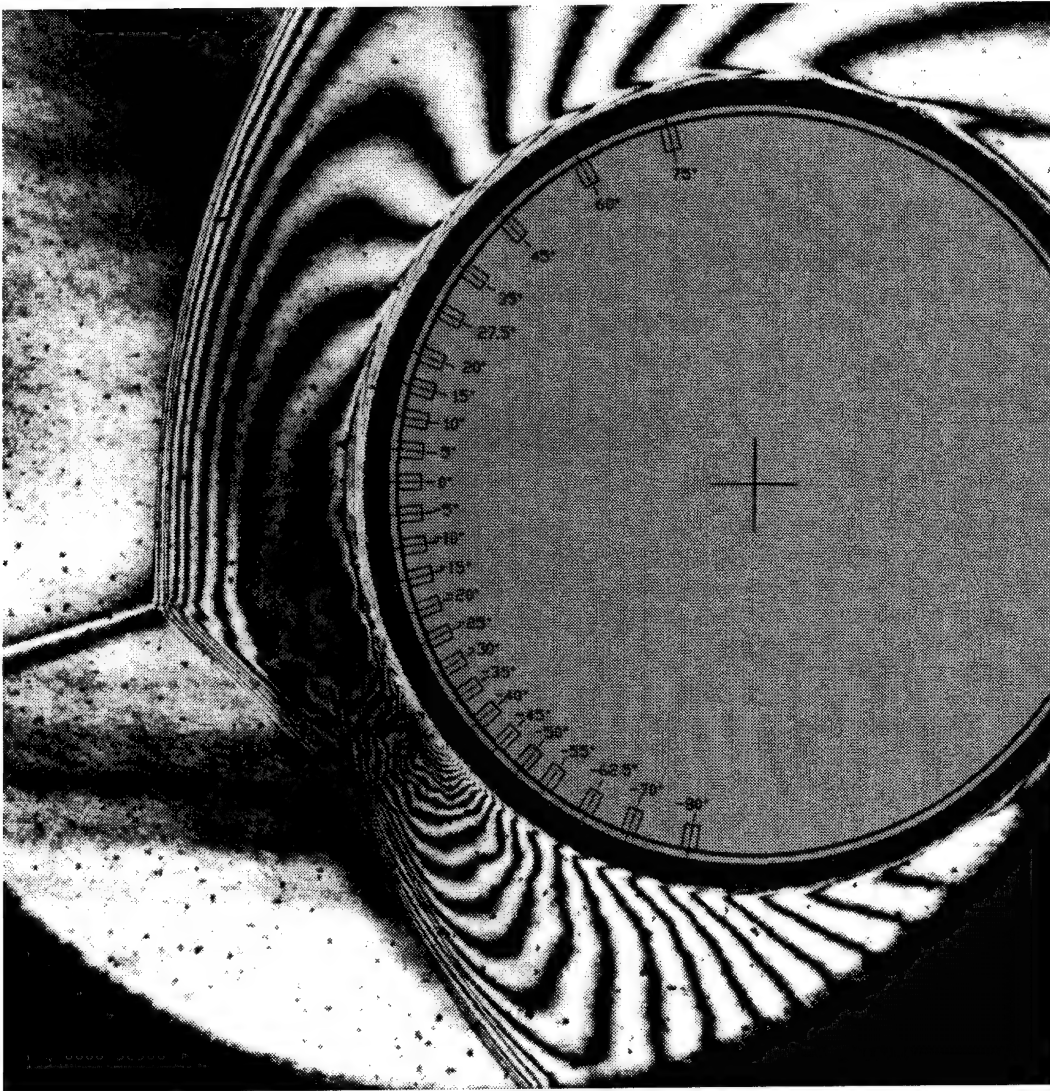


Figure C.28: Shot T5-831; condition C, $g/D = 2.149$.

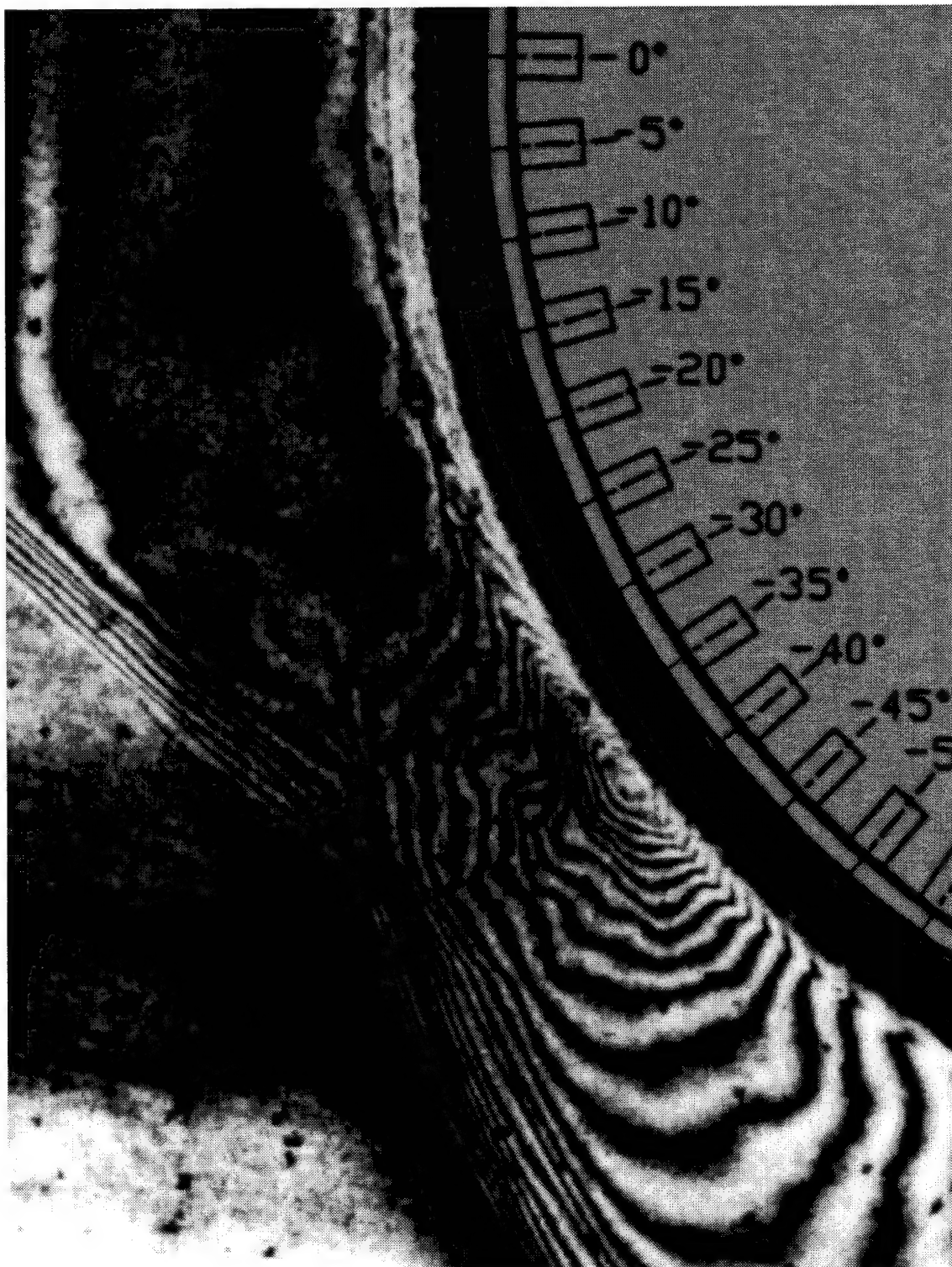


Figure C.29: Magnified view of holographic interferogram; Shot T5-831

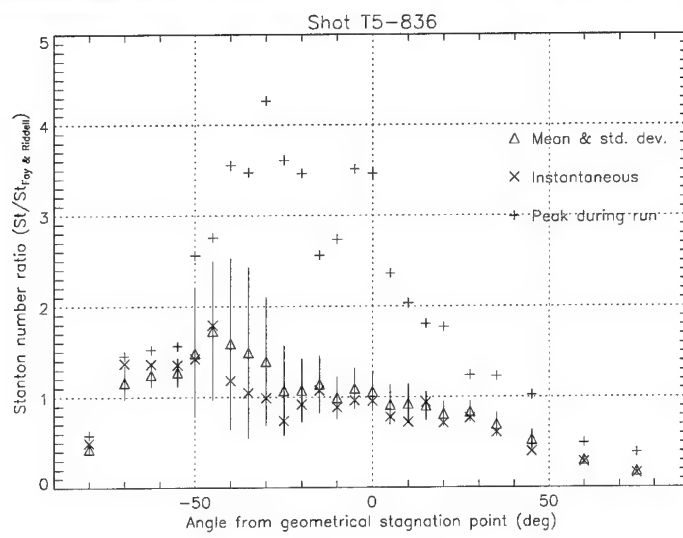
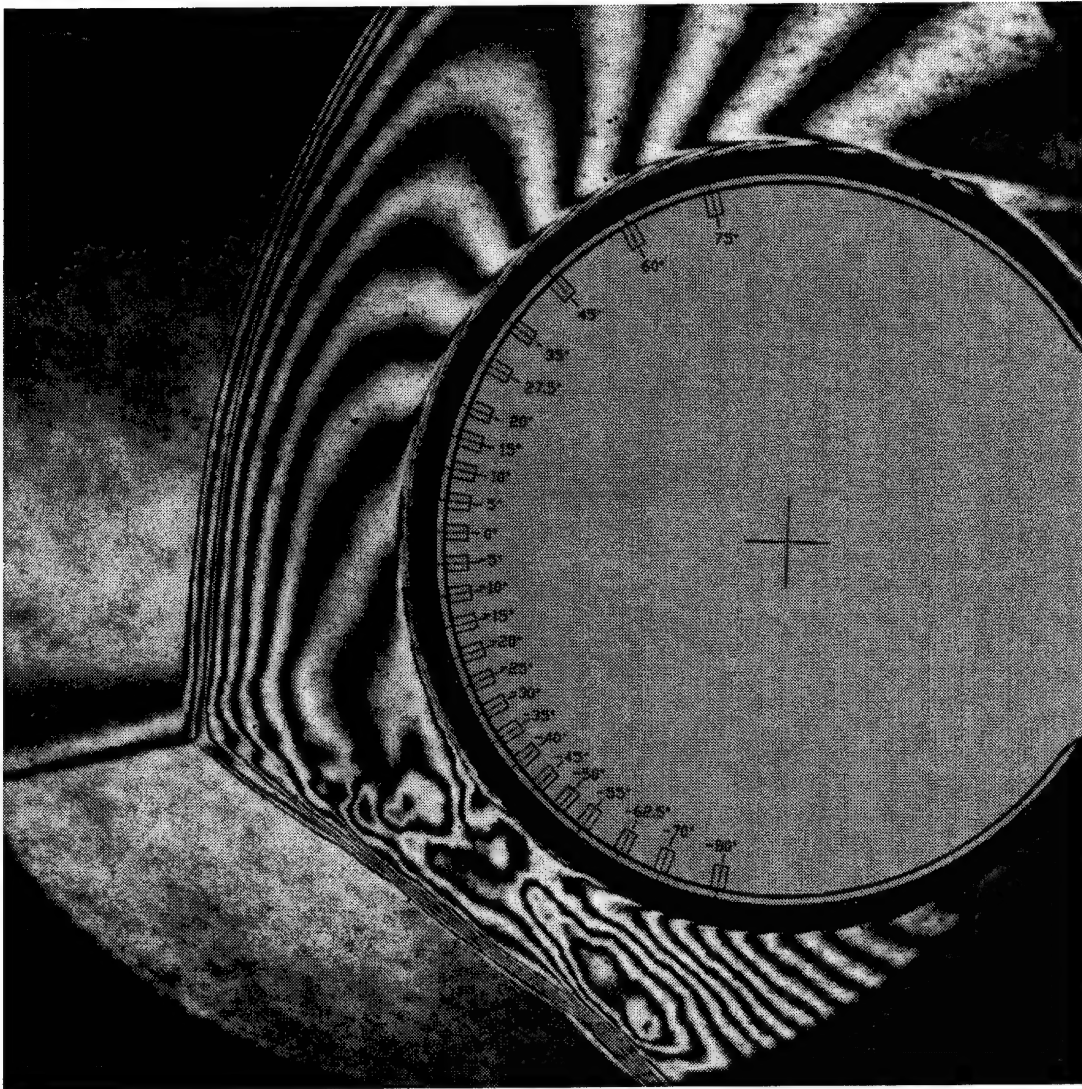


Figure C.30: Shot T5-836; condition C, $g/D = 2.162$.

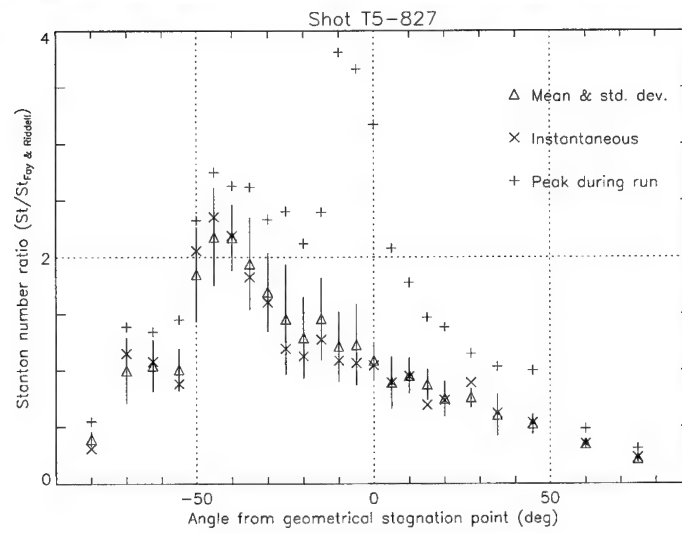
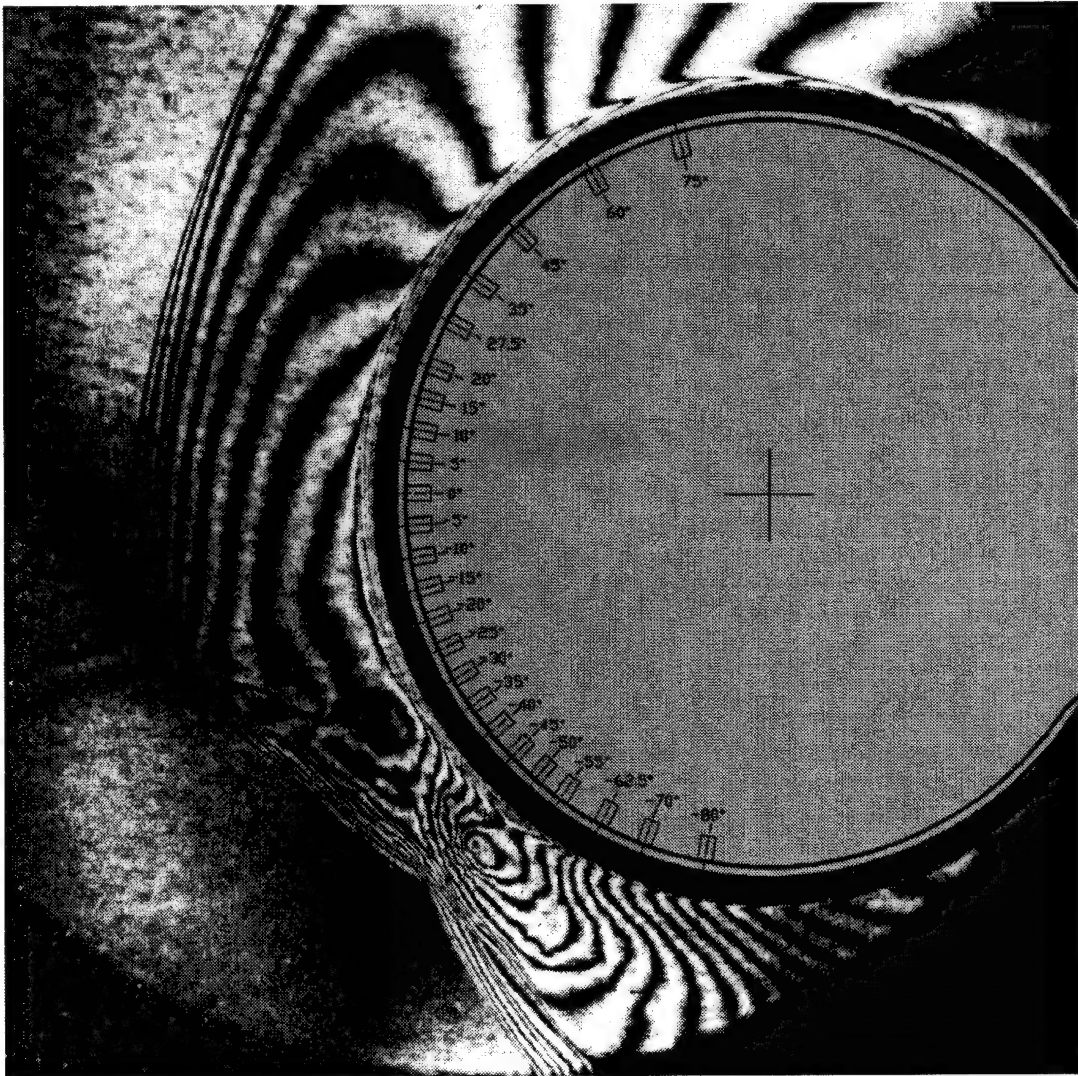


Figure C.31: Shot T5-827; condition C, $g/D = 2.179$.

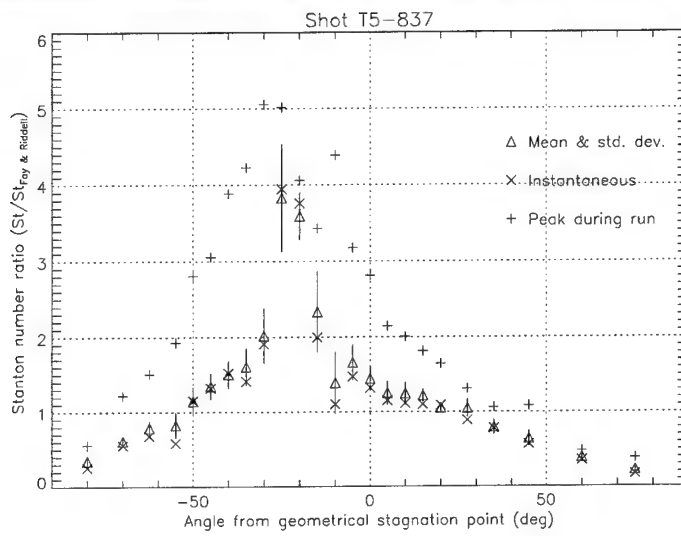
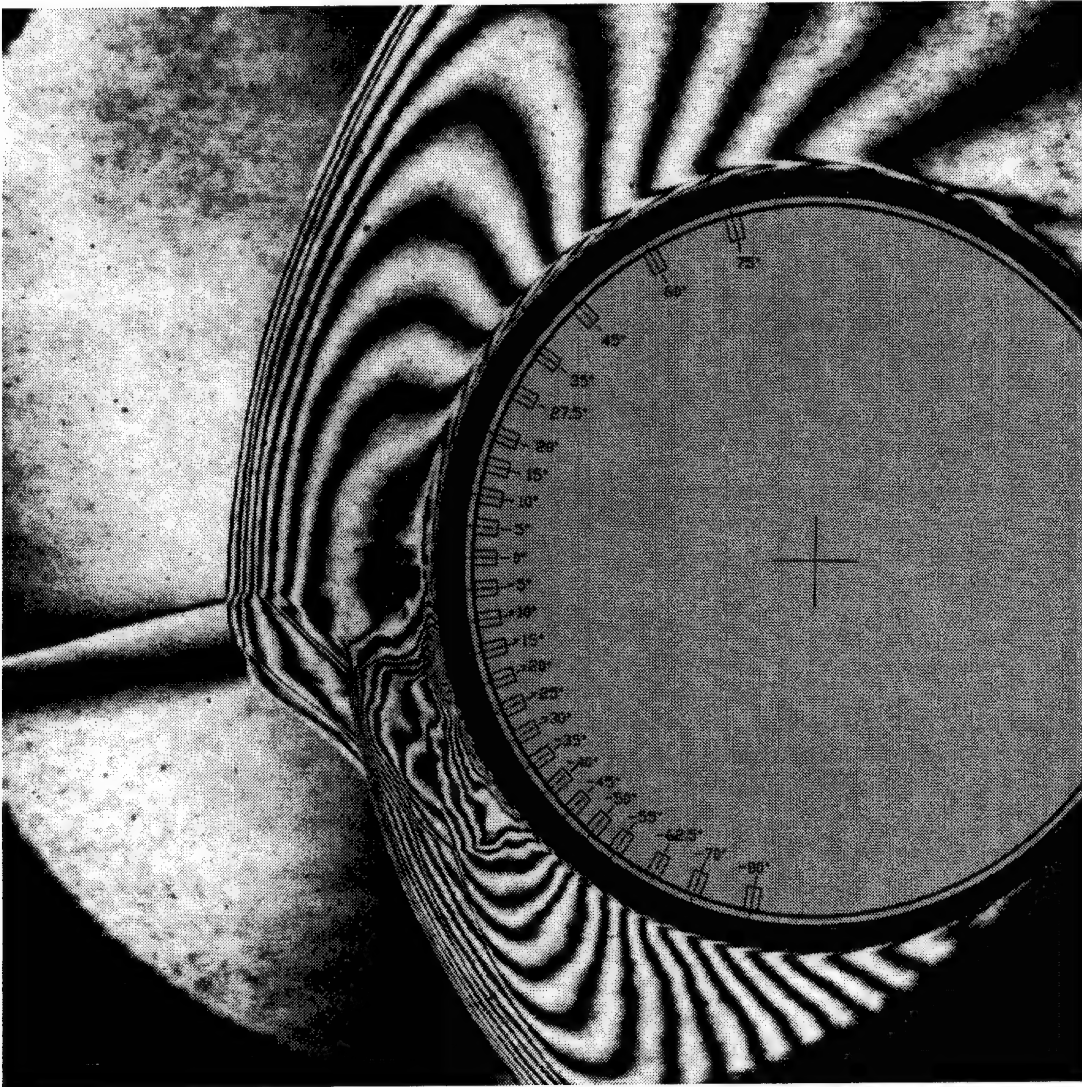


Figure C.32: Shot T5-837; condition C, $g/D = 2.189$.

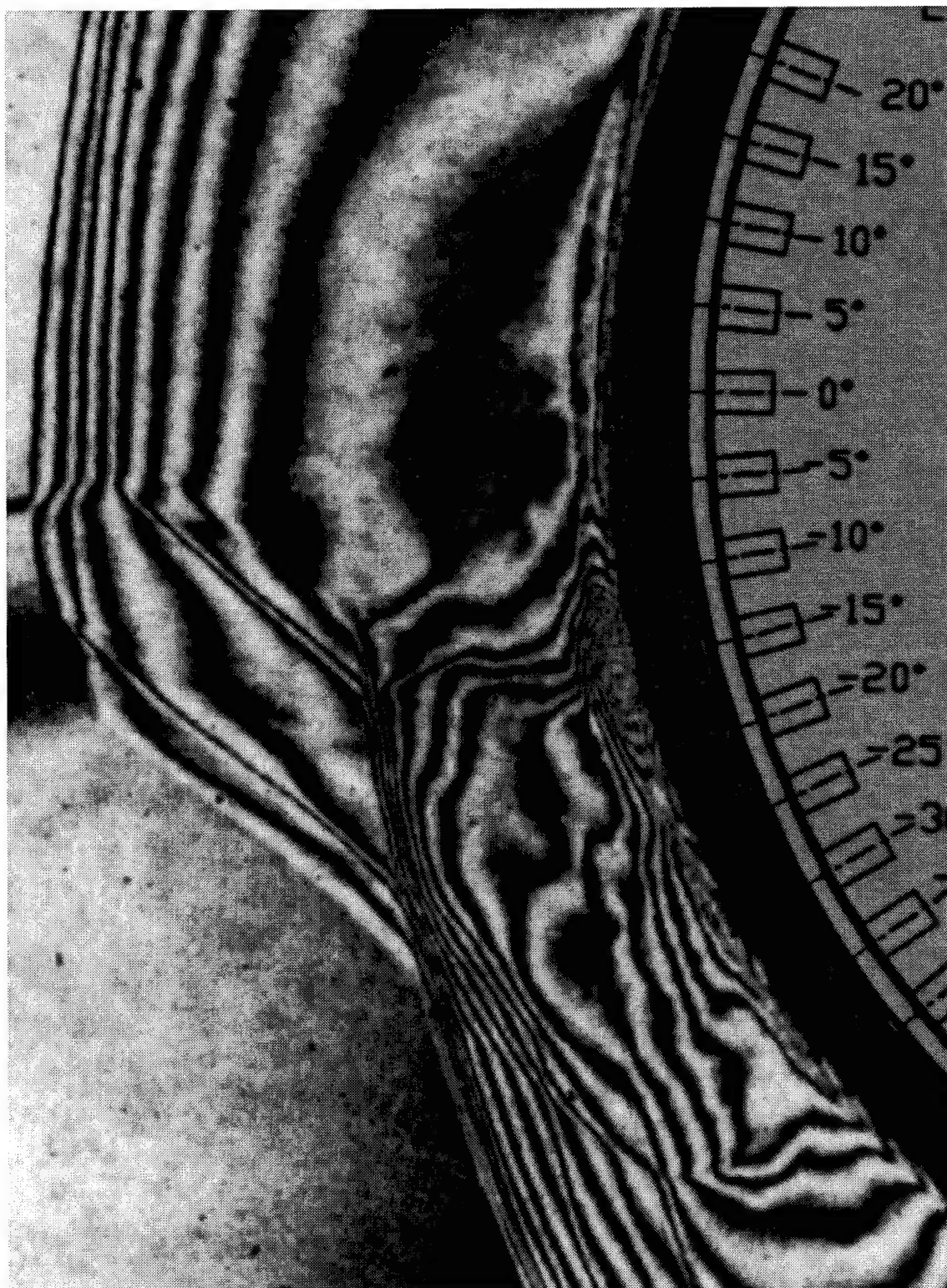


Figure C.33: Magnified view of holographic interferogram; Shot T5-837

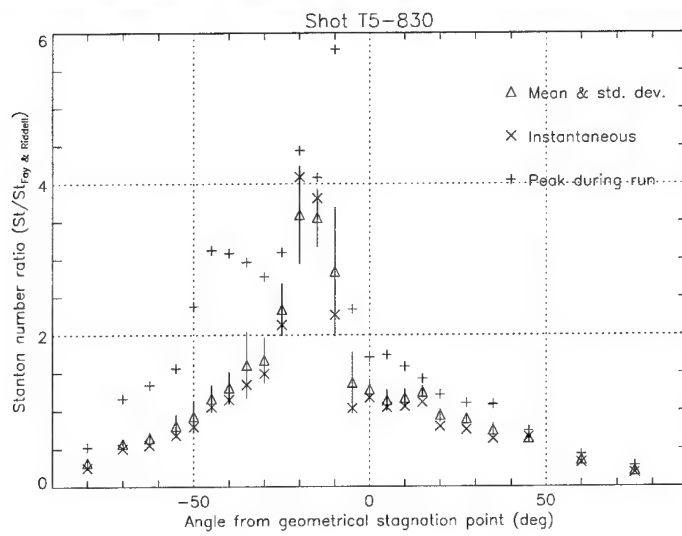
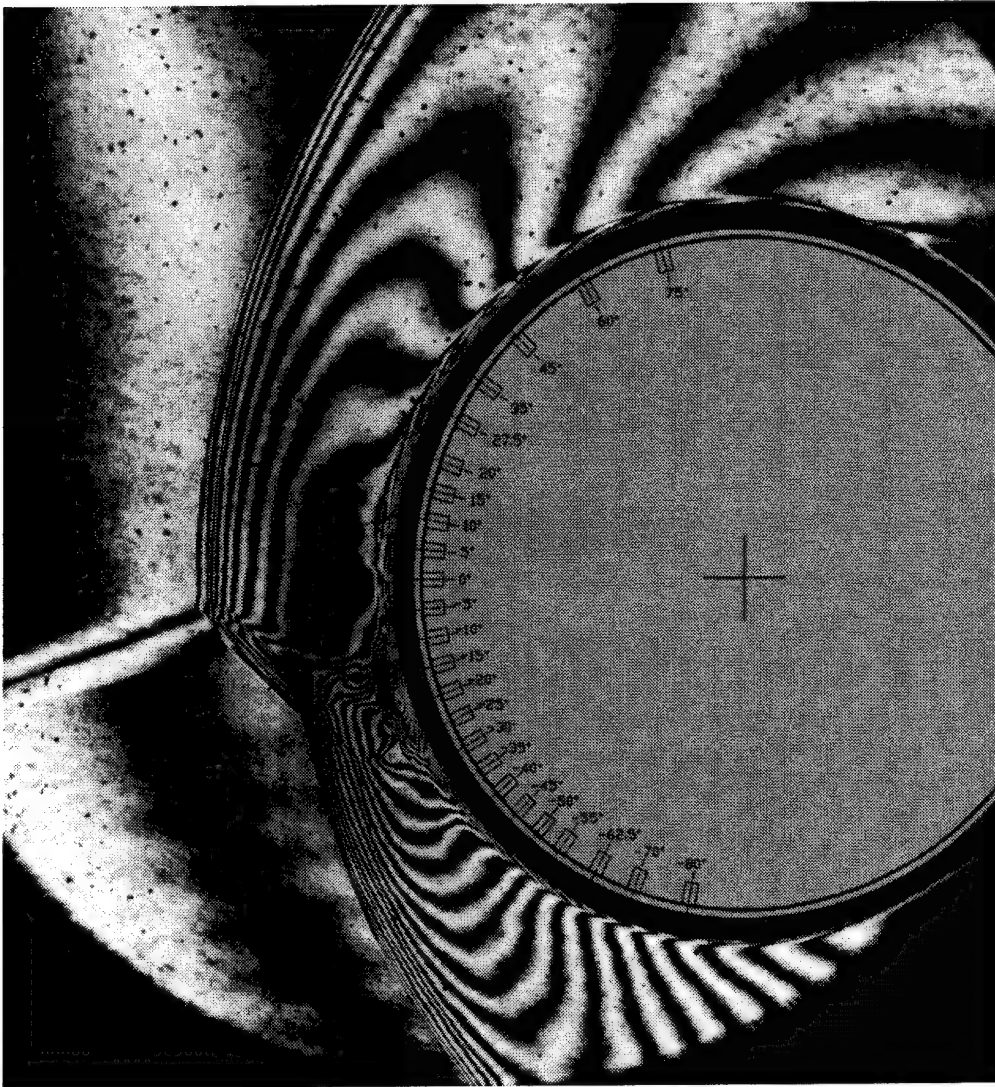


Figure C.34: Shot T5-830; condition C, $g/D = 2.198$.

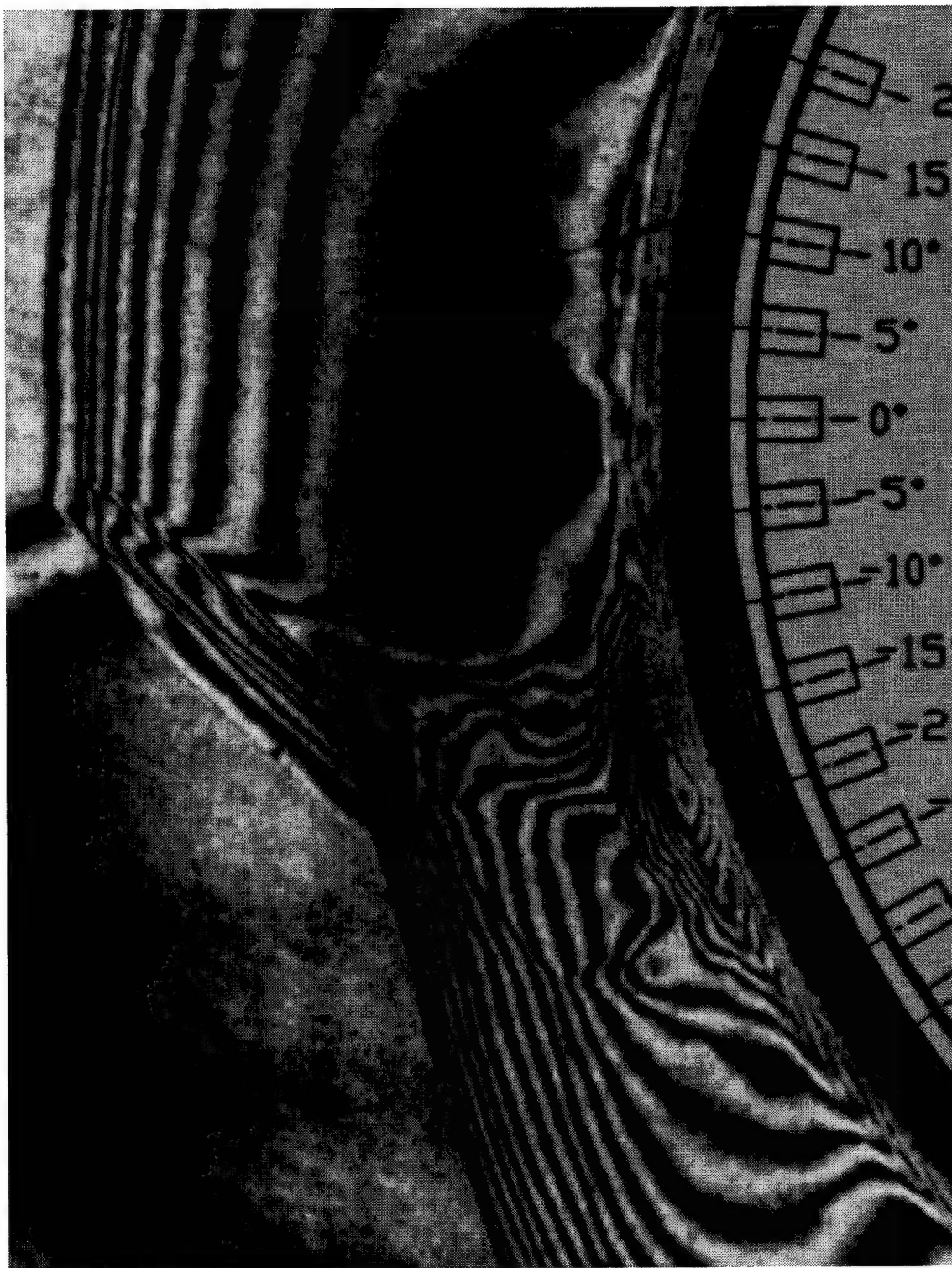


Figure C.35: Magnified view of holographic interferogram; Shot T5-830

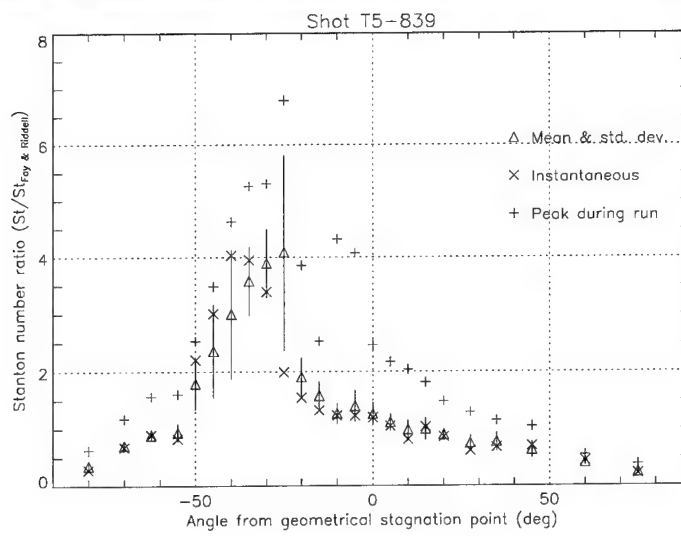
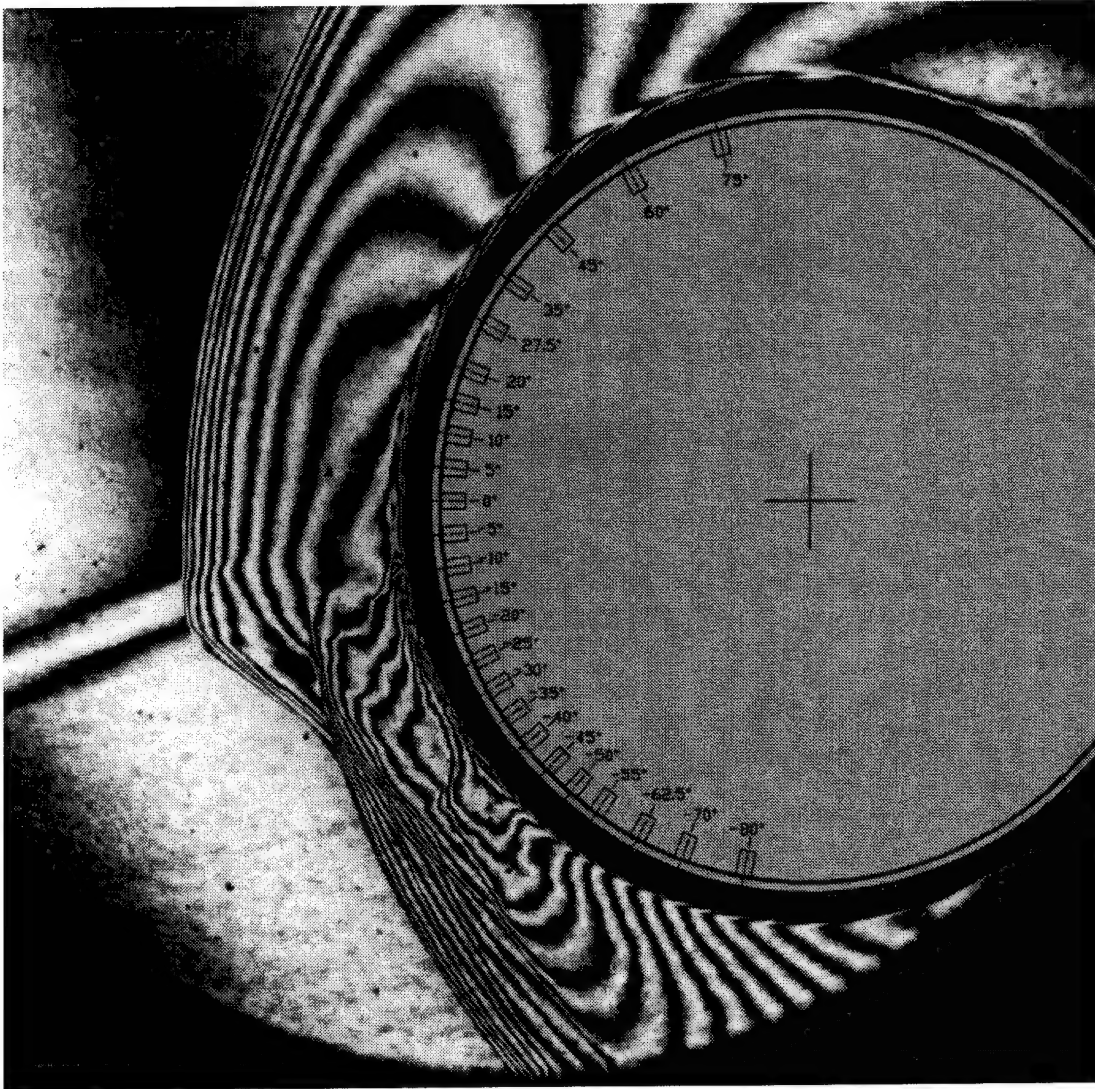


Figure C.36: Shot T5-839; condition C, $g/D = 2.211$.

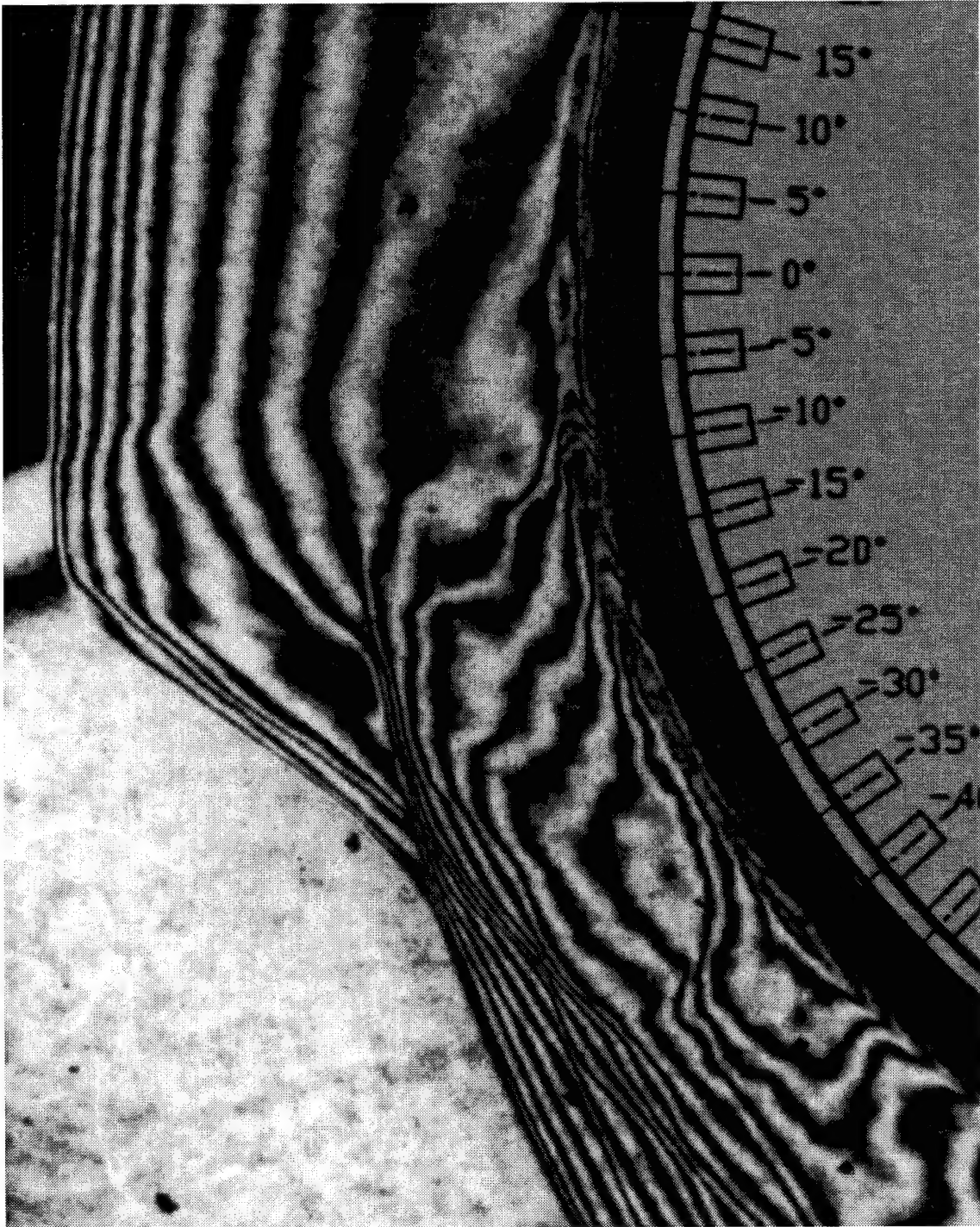


Figure C.37: Magnified view of holographic interferogram; Shot T5-839

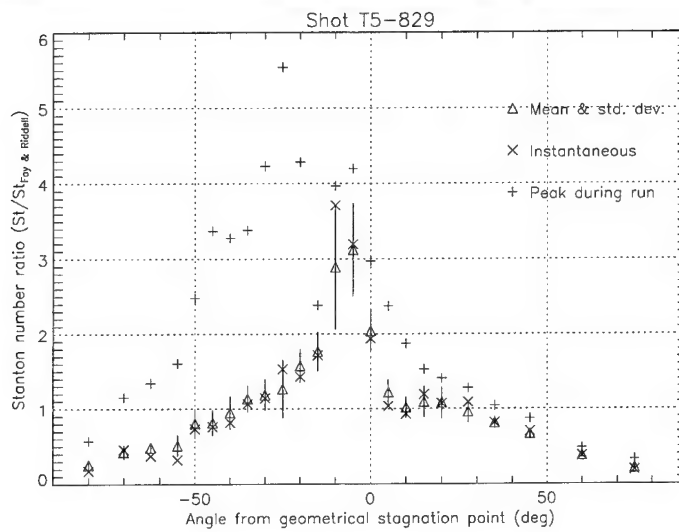
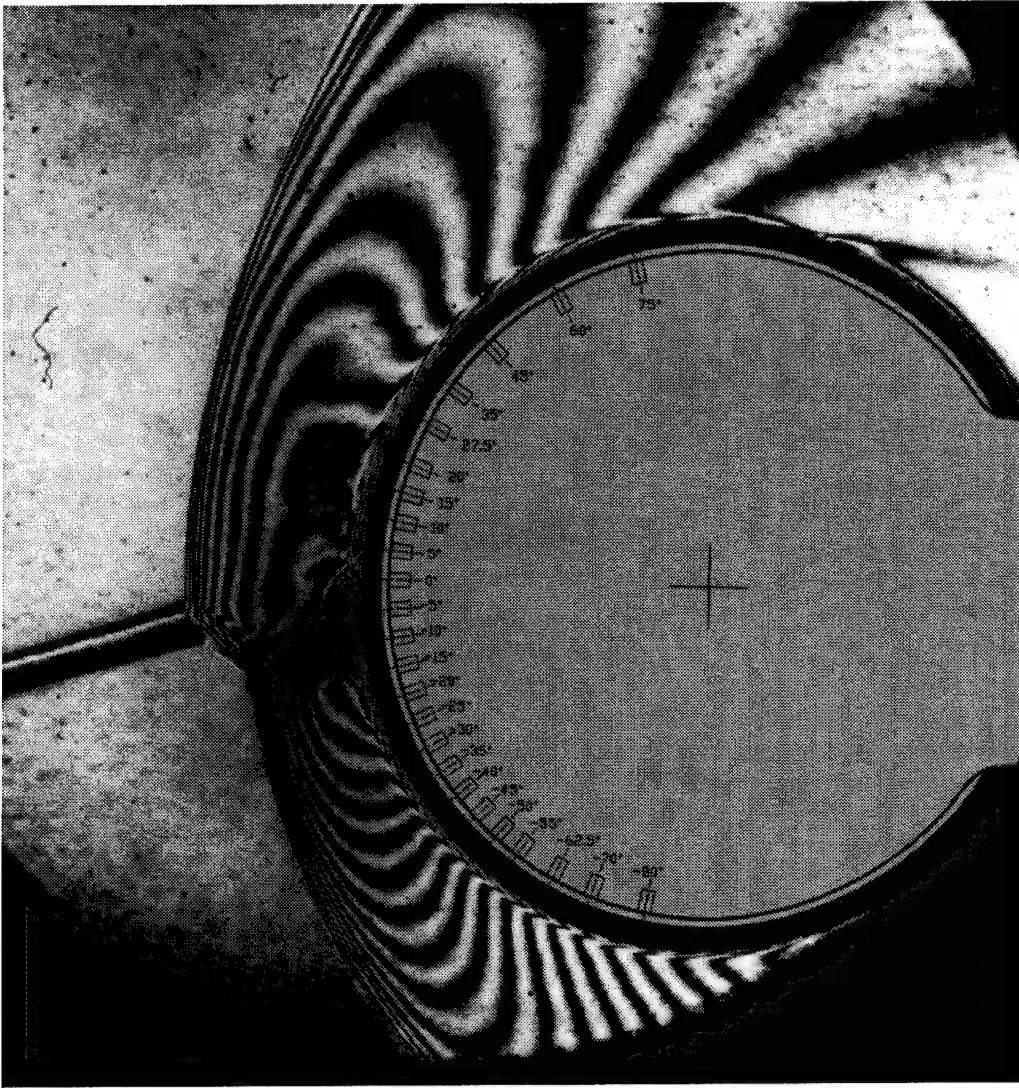


Figure C.38: Shot T5-829; condition C, $g/D = 2.246$.



Figure C.39: Magnified view of holographic interferogram; Shot T5-829

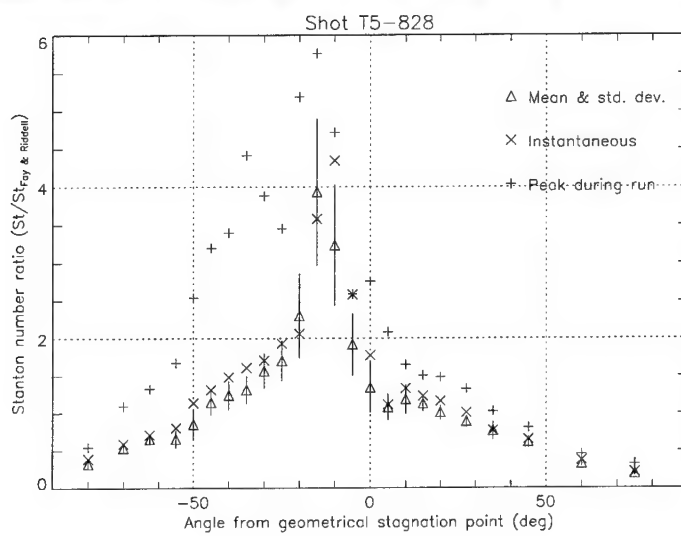
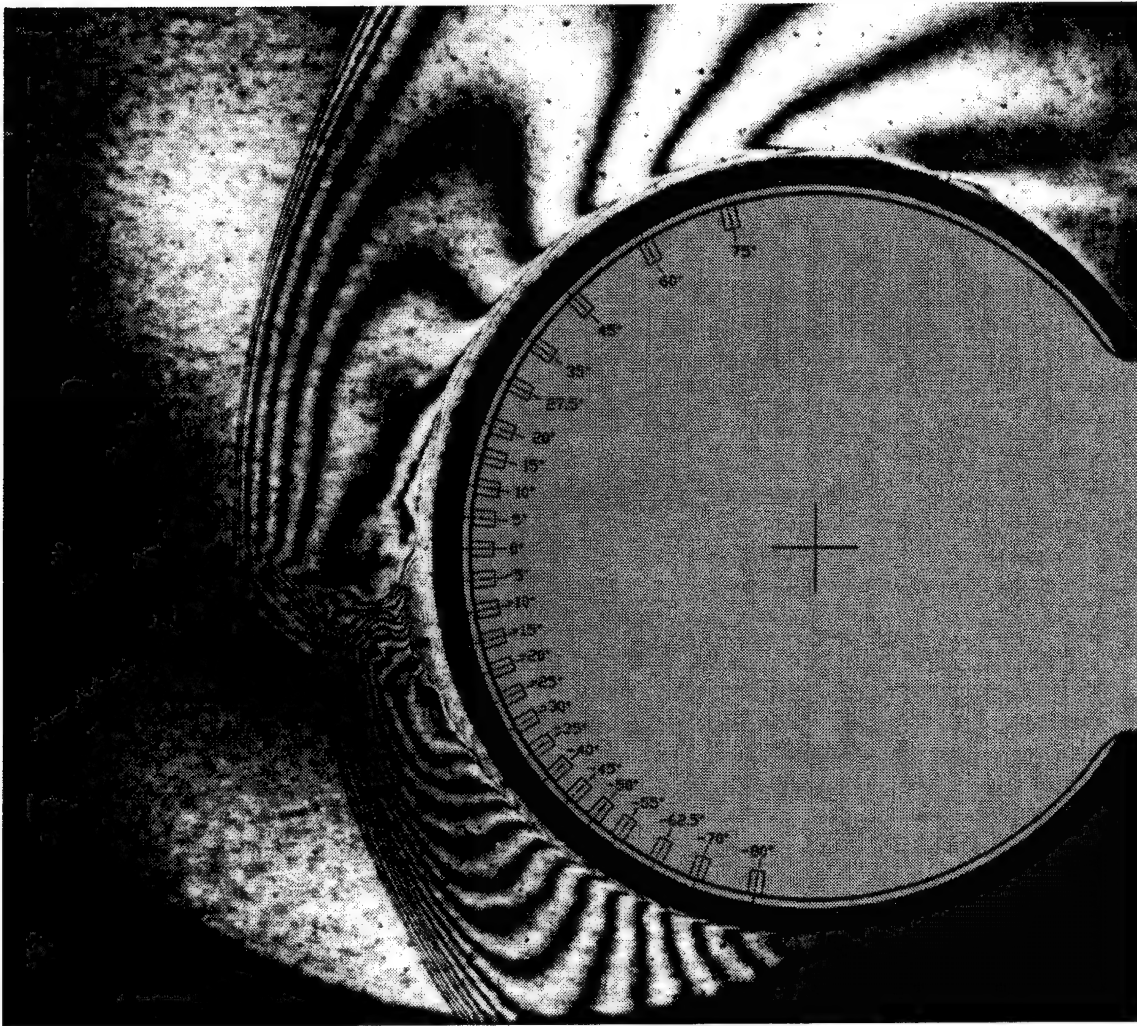


Figure C.40: Shot T5-828; condition C, $g/D = 2.274$.

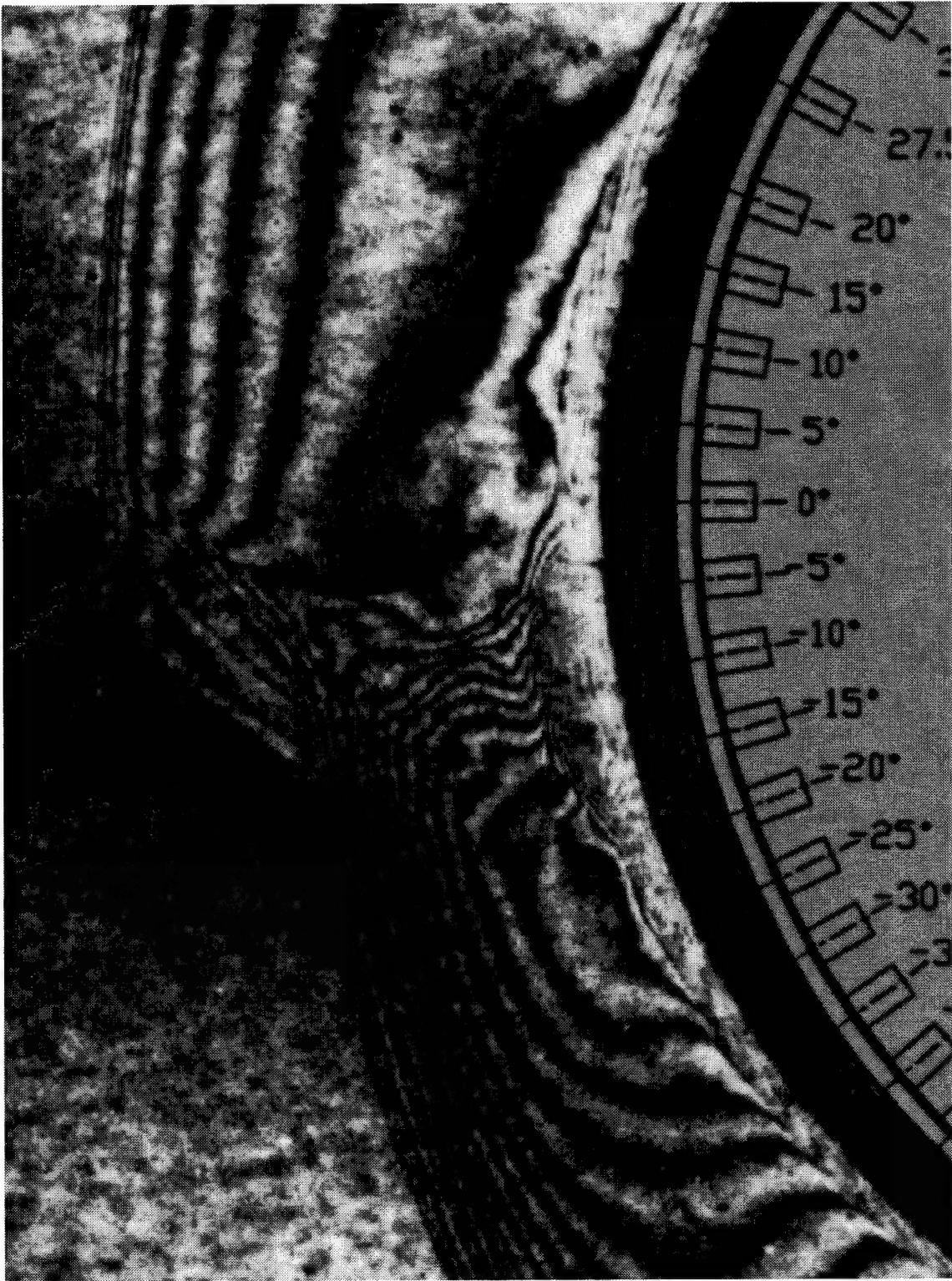


Figure C.41: Magnified view of holographic interferogram; Shot T5-828

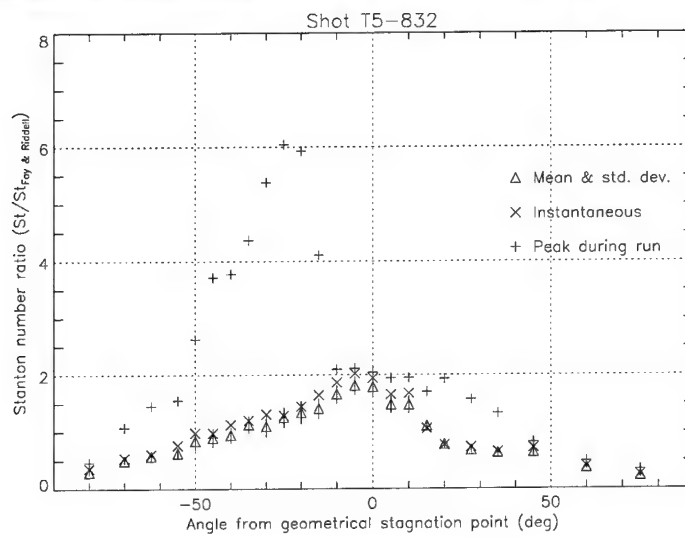
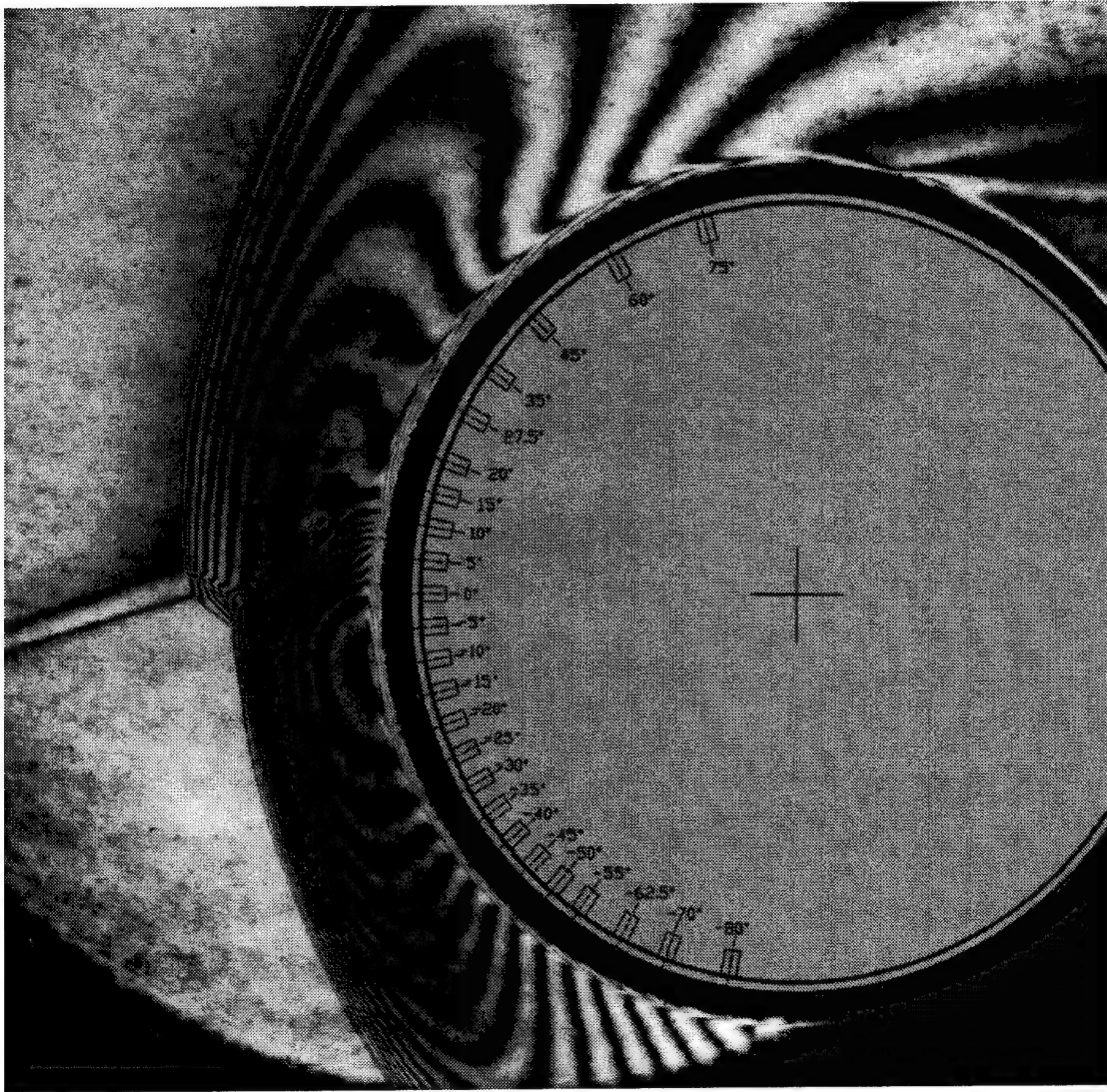


Figure C.42: Shot T5-832; condition C, $g/D = 2.307$.

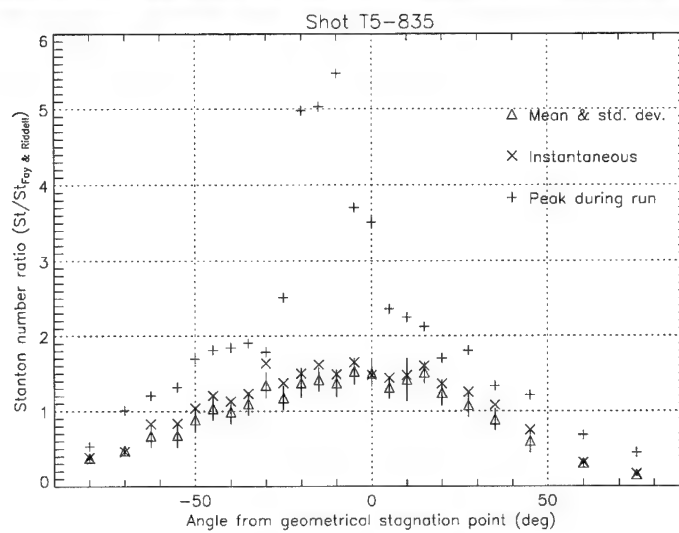
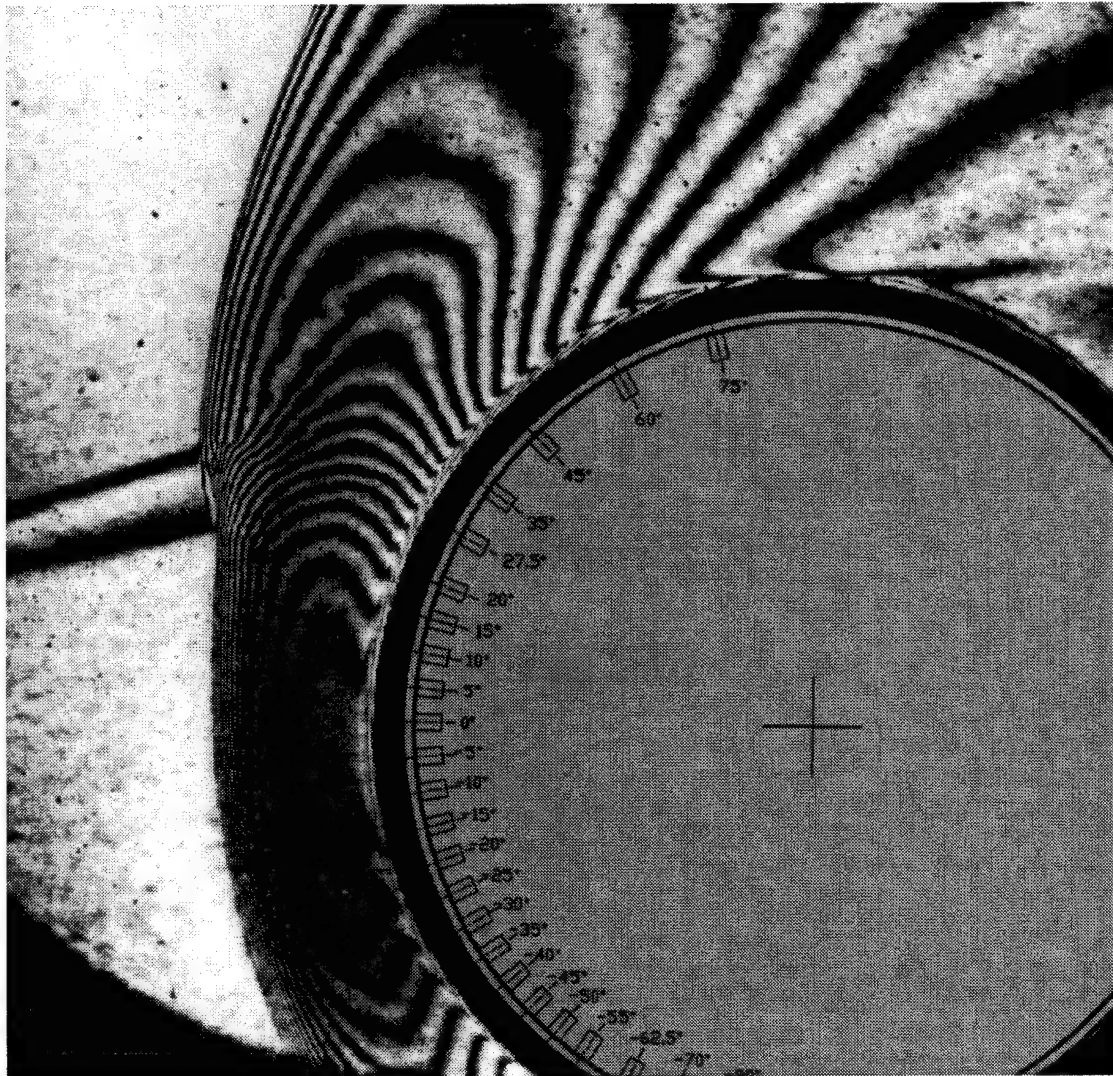


Figure C.43: Shot T5-835; condition C, $g/D = 2.481$.

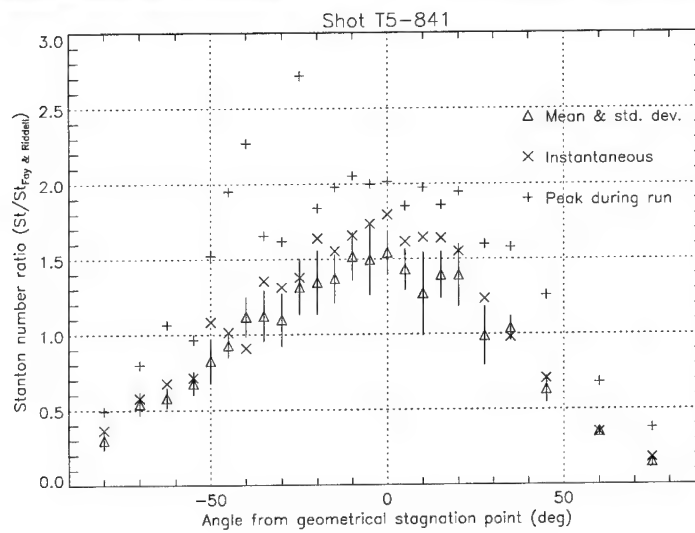
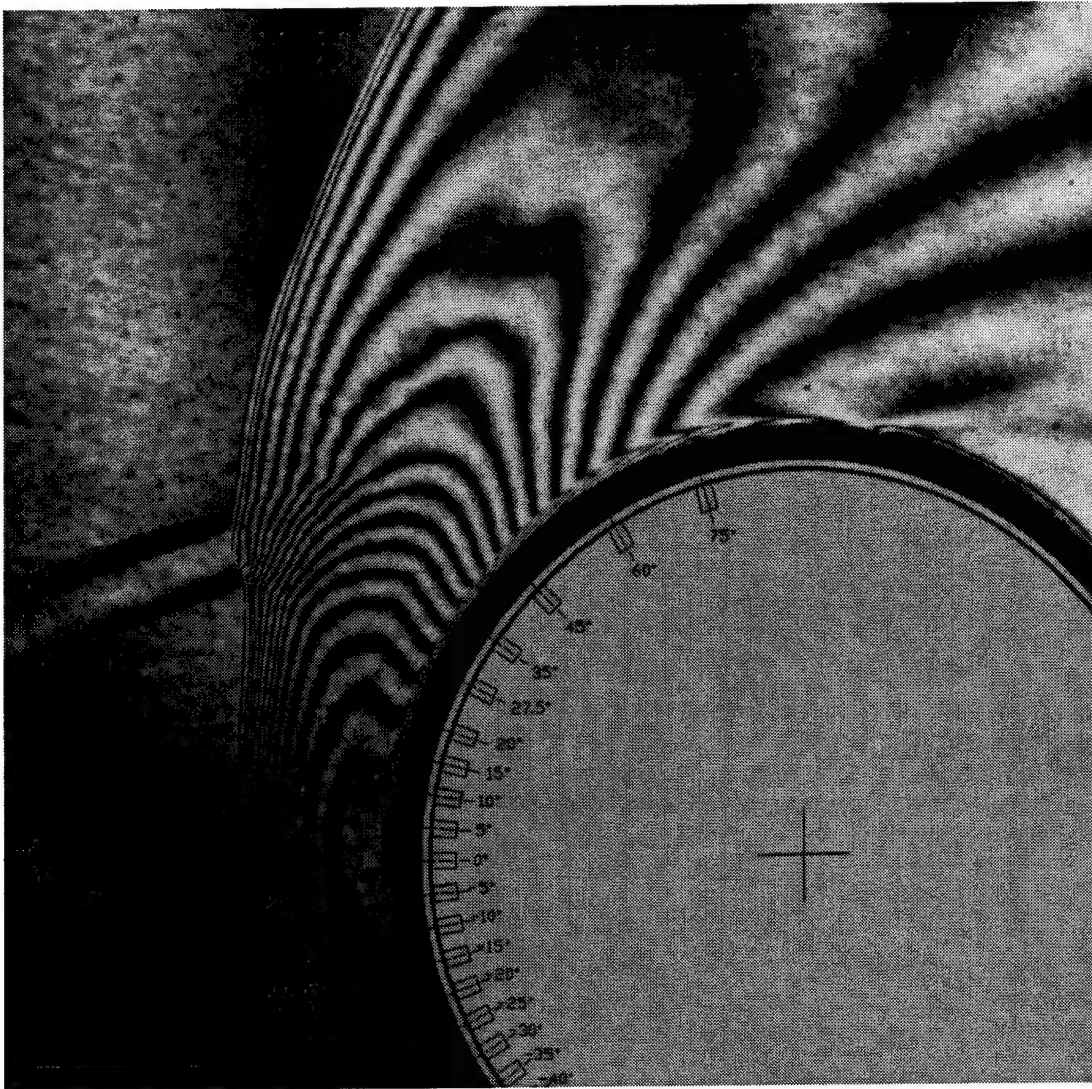


Figure C.44: Shot T5-841; condition C, $g/D = 2.620$.

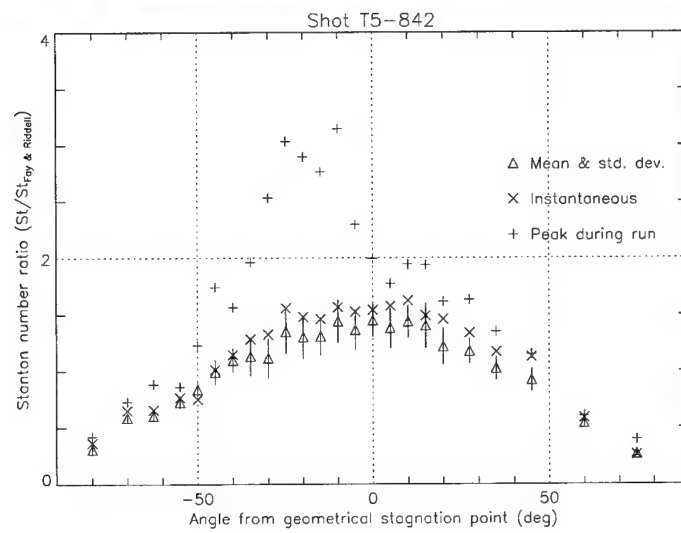
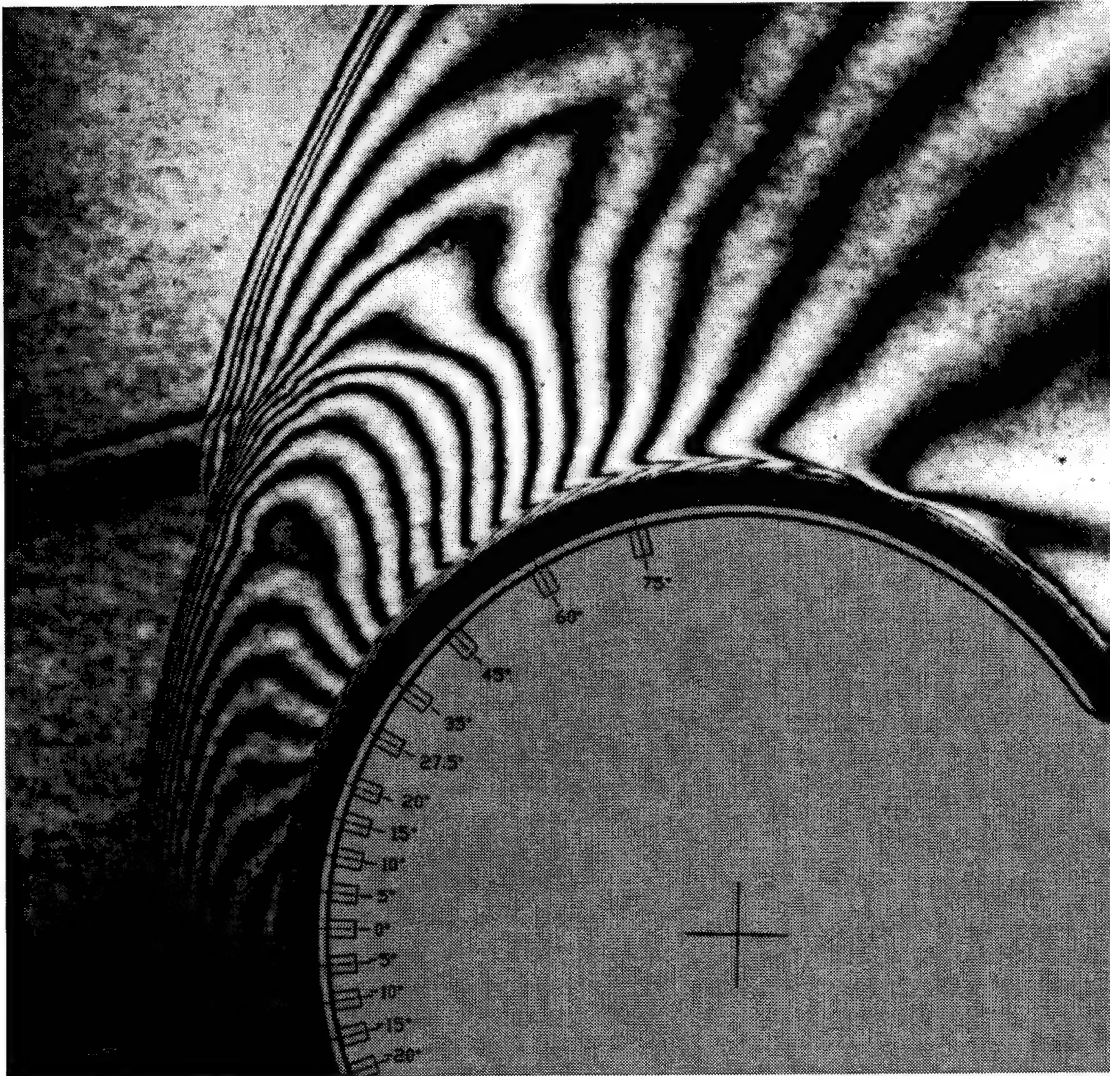


Figure C.45: Shot T5-842; condition C, $g/D = 2.764$.

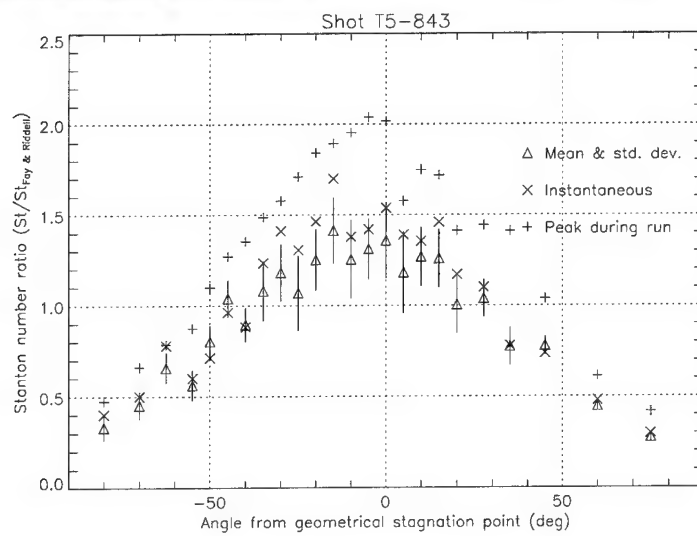
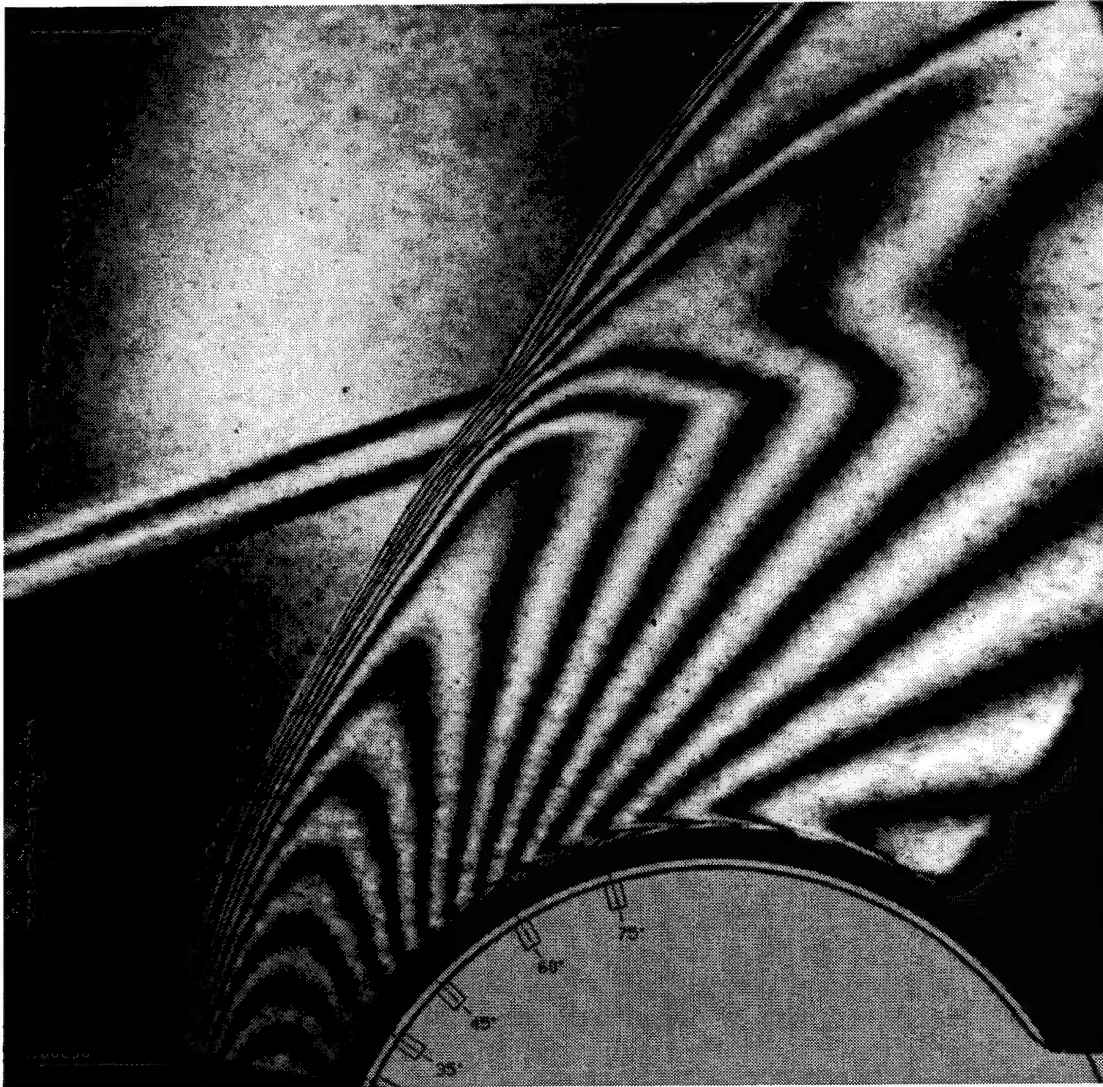


Figure C.46: Shot T5-843; condition C, $g/D = 3.074$.

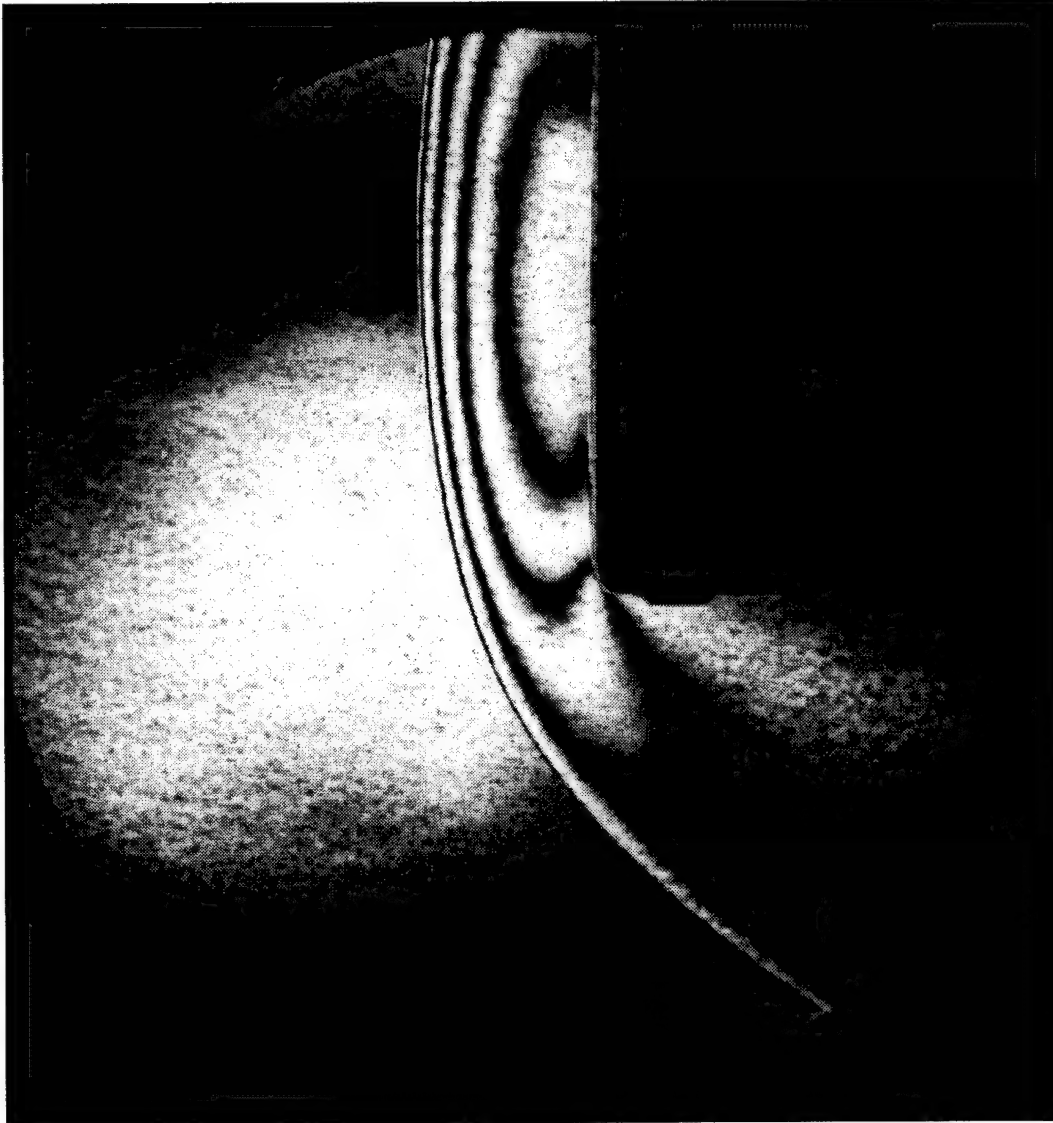


Figure C.47: Flow over a $\phi 50\text{mm}$ blunt cylinder without shock impingement. Shot T5-819; condition A.

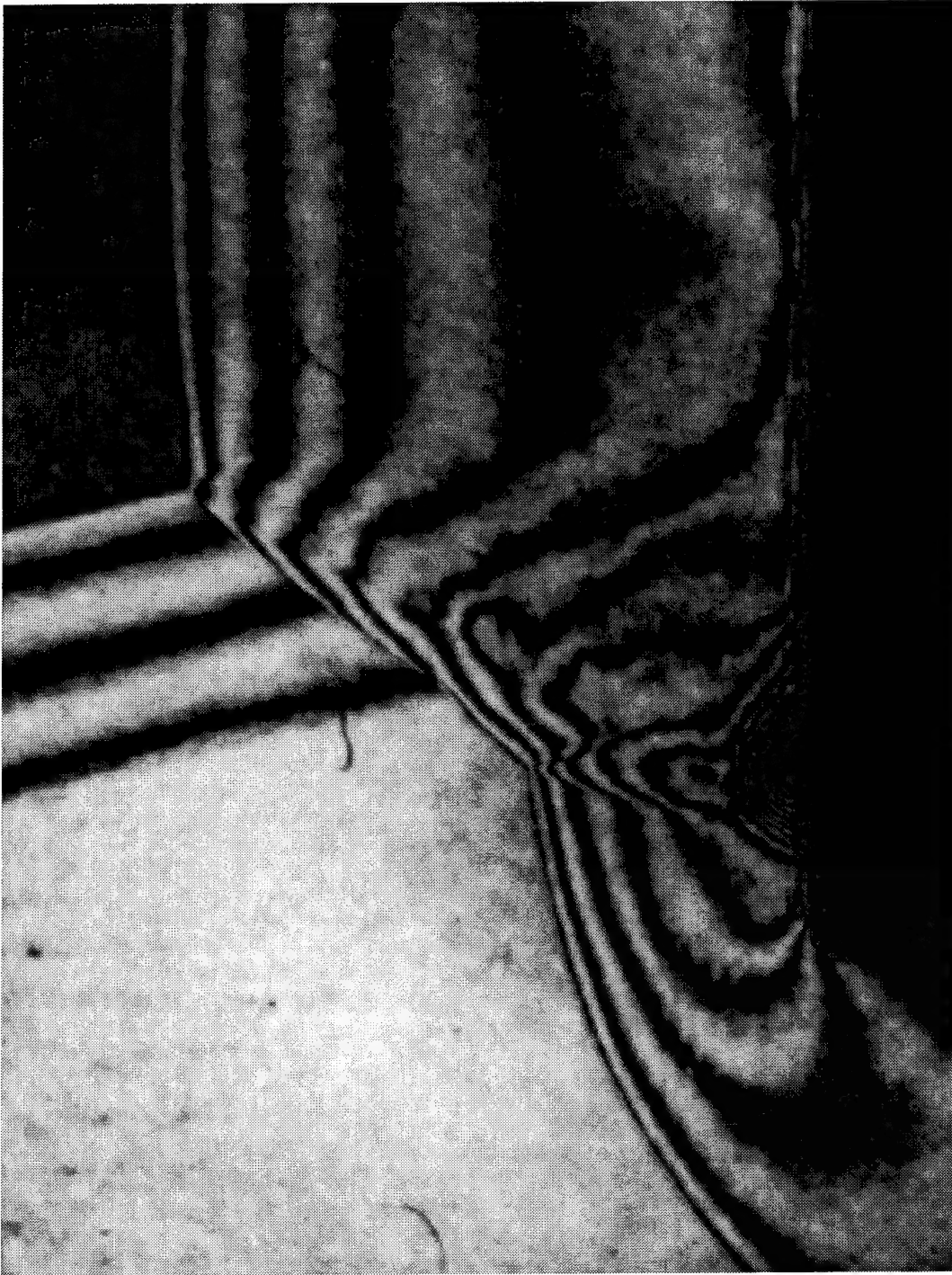


Figure C.48: Flow over a $\phi 50\text{mm}$ blunt cylinder with type IV shock impingement. Condition A.



Figure C.49: Flow over a $\phi 50\text{mm}$ blunt cylinder without shock impingement. Shot T5-820; condition C.



Figure C.50: Flow over a $\phi 50\text{mm}$ blunt cylinder with type IV shock impingement. Condition C.

Appendix D Holographic interferometer

The main features of the design of this device were a consequence of the desire to provide maximum resolution of features at the test section. Consequently, short focal length multi-element lenses were used for the imaging optics and these were placed as close as possible to the test section. The device also incorporates an unusually small crossing angle between the test section and reference beams. This allowed the use of relatively low resolution photographic media and short coherence length lasers. Diffraction minima about the images of shock waves were suppressed by the use of Fourier plane conjugate image separation and Gaussian apodizing filters. White light reconstruction suppressed the appearance of laser speckle.

D.1 Description of optical apparatus

The optical arrangement is shown in Figure D.1 and the technique used was off axis reference beam image plane holography. A frequency doubled NdYAG laser ($\lambda=532$ nm) with a coherence length of 10 mm and 30 ns pulse duration was used as the light source. The source beam was passed vertically downward into the top of the interferometer by a periscope arrangement. A dielectric cube beam splitter then separated the reference and test section beams.

The test section beam was expanded through a diverging-converging singlet lens pair and folded to pass through the test section. A doublet lens focused the modulated beam so that it passed through an aperture stop of diameter $d \approx 5$ mm. Since this stop was an image at infinity with respect to the test section, the f -number was large ($f/d \approx 120$) with respect to the diffuse test section luminosity. An interference filter ($\Delta\lambda=10$ nm) further reduced the background level. A second doublet objective re-collimated and minified the beam before it was recombined with the reference beam at the plate beam splitter.

The unexpanded reference beam was reflected through a path length adjuster before being passed around the test section through the interior of the interferometer support beam. Several beam steering prisms were used to align the beam with the singlet pair reference beam expander. The reference beam formed a 5° angle as it interfered with the test section beam. Image plane holograms were obtained by focusing the test section onto the film plane. The rejected beams emerging from the plate beam splitter were arranged to fall on a ground glass screen placed in front of an exposure control photo diode. A rotating dichroic polarizer was mounted on the camera body to regulate the ratio of the beam intensities. Custom built programmable digital timing circuitry was used to thermally stabilize the laser prior to the shot and to synchronize the laser pulses and electromechanical shutter

when the tunnel was fired. The two interferometric pulses were generated from separate flash-lamp cycles.

Holograms were recorded on Kodak SO-253 plastic based film that was mounted in a modified 35 mm camera body. Film development was optimized to best accommodate the double pulses within the linear portion of the emulsion characteristic curve. The developed images were bleached in a solution of potassium permanganate and sulfuric acid to produce phase modulated holograms with improved diffractive efficiency.

By replacing the developed hologram at its position during exposure, the reference beam was used to reconstruct the hologram. A folding mirror passed the reconstructed beams through a pair of lenses that imaged the hologram at unity magnification onto a secondary camera mount where the interferogram was recorded. Multiple diffracted orders produced by the hologram were separated by an aperture placed at the focus of the two lenses. Low power densities during reconstruction allowed the use of an aperture with a Gaussian transmittance profile. These filters were produced photographically. It may be shown that this profile produces non-oscillatory images of the shock fronts that are free from diffraction effects. The interferograms were reconstructed using white light to reduce the appearance of laser speckle. Conventional photographic methods were used to record and print the reconstructed interferograms.

The interferometer was assembled in a U-shaped plywood cabinet to provide appropriate damping characteristics. The long term static stability of the device is unimportant since double pulse holography is sensitive only to path length differences during recording. An aluminum truss across the top of the box allowed access to the internal components whilst maintaining the stiffness of the housing. Adjustable rails were used to position the interferometer over the test section of the shock tunnel. Optical components were rigidly attached to the baseboard by custom made, nonadjustable mounts that were permanently aligned during the initial set up of the device. The interferometer is easily transportable and self contained except for the external laser.

D.2 Modes of operation

This system was used in a single shot mode for schlieren and shadowgraph reconstruction and principally in a double pulse holographic interferometry mode. In this second technique an initial hologram is recorded with no flow through the test section. An additional hologram is recorded on the same film at an appropriate time during the flow. The two waveforms are reconstructed simultaneously to produce an interferogram that displays the path length difference due to the refractivity of the gas in the test section. Note that this procedure does not provide a three-dimensional capability. Here holography is used to facilitate the sequential recording and simultaneous reconstruction of two wavefronts. The results that are produced are functionally equivalent to a Mach-Zehnder inter-

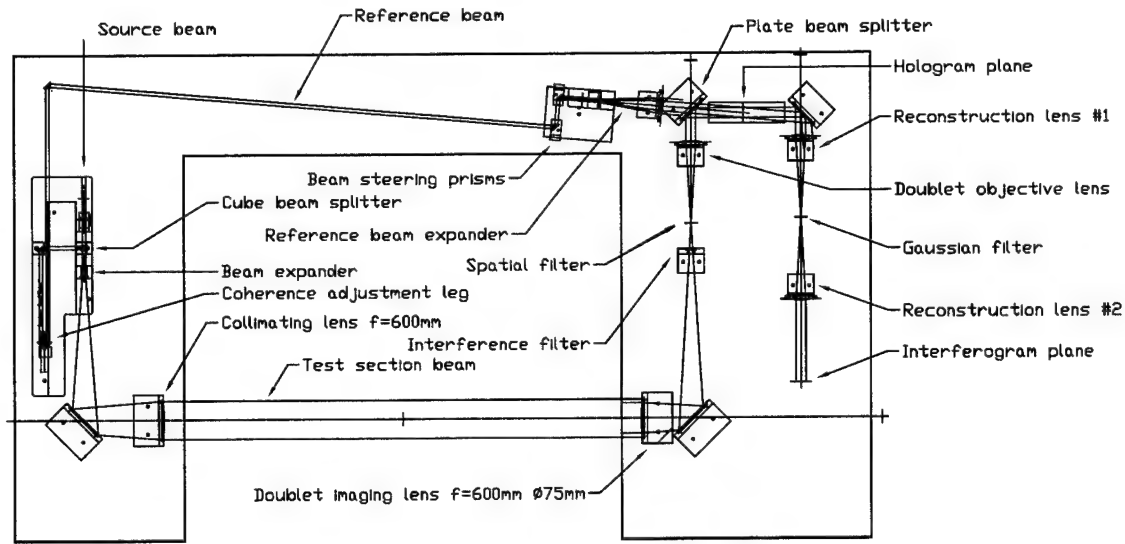


Figure D.1: Optical and mechanical layout of the holographic interferometer.

ferogram whereby the information is integrated along the line of sight. The only three-dimensional capability is the freedom to choose the plane of focus during reconstruction. This remaining freedom is removed if incoherent light is used during reconstruction.

Introducing a diffuser plate immediately before to the test section produces an infinite number of point sources. This provides three-dimensional information since the point of view, the plane of focus and the angular field of view (and hence depth of focus) may be varied arbitrarily during reconstruction. The information obtained by this technique is averaged along the line of sight and also over a conical volume either side of the plane of focus. The conical volume is determined by the solid angle subtended by the aperture of the reconstruction imaging optics. In conventional holography of solid objects this simply reduces the depth of field; however for phase objects a finite path length is still required in order to generate an image. Thus three-dimensional information is obtained at the expense of additional angular mollification of the fine flow structure. This point is not well treated in the literature and is of considerable importance in obtaining high resolution images.

D.3 Principles of operation

The physical principles of holography are described in the literature (Caulfield [4], Merzkirch [32]). Here we demonstrate the techniques of white light reconstruction and Fourier plane conjugate image separation that are features of the current device.

Consider the interference of the plane test section wavefront, T , with the reference beam, R_0

(Figure D.2). The spatial variations of the two fields in the $z = 0$ hologram plane at a given point in time are described by,

$$T = e^{i\phi(x,y)} \quad R_0 = e^{i\phi_0(x,y)},$$

where ϕ and ϕ_0 are the phases at a given instant in time. Both beams are monochromatic with wavenumber, $k_0 = 2\pi/\lambda_0$. The reference beam is planar and forms an angle θ with respect to the test section beam in the x-z plane so that,

$$\phi_0(x, y) = k_0 x \sin \theta.$$

The modulation of the phase of test section beam by the gas inhomogeneities is described by $\phi(x, y)$. At the hologram plane the media responds to the intensity of the interfering wavefronts yielding an image of density,

$$I_H(x, y) = |T + R_0|^2 = (e^{i\phi} + e^{ik_0 x \sin \theta})(e^{-i\phi} + e^{-ik_0 x \sin \theta}) = 2[1 + \cos(\phi - k_0 x \sin \theta)]. \quad (D.1)$$

Holographic fringes are therefore formed on the film according to,

$$2\pi n = \phi(x, y) - k_0 x \sin \theta.$$

In the case of a uniform test section beam, $\phi = 0$, we see that the holographic fringes are formed with spacing, $s \approx 2\pi/k_0 \theta$, for small crossing angle, θ . Phase variations are recorded as a modulation of the local fringe spacing.

Consider reconstruction of the hologram with a reference wave of the same geometry but arbitrary wavelength, $R = e^{ikx \sin \theta}$. The image formed on the film modulates the amplitude of the reconstruction beam to produce the following wavefront immediately downstream of the hologram,

$$D(x, y) = 2[1 + \cos(\phi - k_0 x \sin \theta)] e^{ikx \sin \theta} = 2e^{ikx \sin \theta} + e^{i(\phi + (k - k_0)x \sin \theta)} + e^{i(-\phi + (k + k_0)x \sin \theta)}. \quad (D.2)$$

The first term corresponds to the transmitted component of the reconstruction beam. The second term is the reconstructed test section beam and it is deflected by an angle that is proportional to the shift in wavenumber of the reconstruction beam. An additional wave, known as the conjugate wave, is symmetrically disposed with respect to the reference beam and is also deflected because of the difference in reconstruction wavelength. Additional higher order diffracted beams will be present since the actual recording process will deviate from this ideal. Each of these orders is brought to focus by the first lens shown in Figure D.2. By placing an aperture at the focus corresponding to the reconstructed test section beam, the additional unwanted images are removed. Each of the foci

broaden as the spatial frequencies recorded on the hologram increase. Overlap of the adjacent orders is prevented by the spatial filter used during recording of the hologram. Maximum resolution, for a given crossing angle, is achieved with apertures whose diameters are equal to the spacing between the foci. Note that background luminosity determines the aperture diameter and so the small crossing angle does not limit the resolution of the interferometer. Thus spatial filtering recovers the second term of equation D.2 which is the reconstructed test section beam,

$$\tilde{T} = e^{i(\phi + (k - k_0)x \sin \theta)}.$$

Double pulse holography interferes two such beams. When the second lens images the hologram onto the interferogram recording plane the original phase distribution is recovered and we have,

$$\tilde{T}_1 + \tilde{T}_2 = e^{i(\phi_1 + (k - k_0)x \sin \theta)} + e^{i(\phi_2 + (k - k_0)x \sin \theta)}.$$

Since we have recorded an image plane hologram the phase differences caused by propagation between the hologram and the interferogram planes vanish. At the interferogram recording plane the response of the media yields an image of density,

$$I_F(x, y) = |\tilde{T}_1 + \tilde{T}_2|^2 = 2[1 + \cos((\phi_2 + (k - k_0)x \sin \theta) - (\phi_1 + (k - k_0)x \sin \theta))].$$

An additional consequence of image plane recording is that the effect of the wavelength shift is common to both beams and cancels. Thus the hologram may be reconstructed with white light and the fringe shift in the final interferogram is independent of the reconstruction wavelength,

$$I_F(x, y) = 2[1 + \cos(\phi_2 - \phi_1)].$$

Fringes are observed in the interferogram at locations,

$$2\pi m = \phi_2 - \phi_1.$$

Coherence of the two polychromatic beams is ensured by accurate focusing and the use of achromatic lenses for reconstruction.

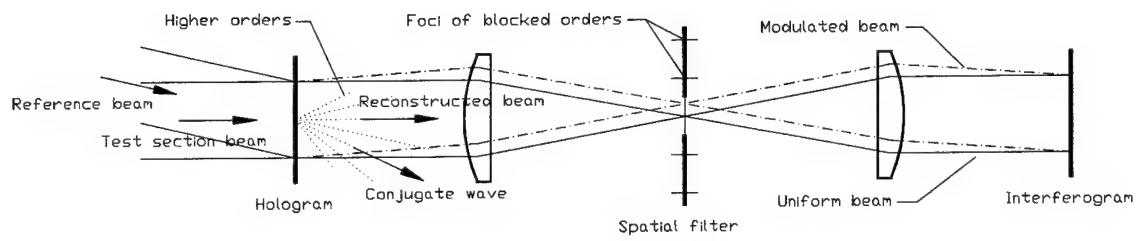


Figure D.2: Geometry of hologram reconstruction and conjugate image separation.

Appendix E Surface junction thermocouple sensors

E.1 Introduction

The measurement of aerodynamic heat transfer rates is important in the design of thermal protection systems for hypervelocity aerospace vehicles. High enthalpy flows may be created in wind tunnels for only a fraction of a second because of the high specific energies involved and the limited strength of materials at elevated temperatures. Thus the problem is transient in nature and a common measurement technique is to sense the time history of the surface temperature of the model. The unsteady conduction of heat within a solid body is described by linear partial differential equations and so the heat transfer rates at the surface of a body may be inferred from the surface temperature measurements. The operating principles, and typical sensor designs are described by Schultz & Jones [40].

We have conducted experiments in the T5 free piston driver shock tunnel at GALCIT. This facility is capable of simulating the high density hypervelocity flows about space vehicles at speeds of order 5000 m/s. Under these extreme conditions the flow in typical facilities is contaminated with the products of mechanical, physical and chemical breakdown of various materials. Some erosion of the surface of the gauge is probable under these conditions and this impacts the design of the transducer.

A commonly used technique for gauge fabrication is to deposit a thin metal film (typically Platinum) on a glass or ceramic substrate. The surface temperature is then sensed through the temperature dependence of the resistivity of the metal film. This technique yields a relatively sensitive device however the thin film is prone to damage in hostile environments. Any erosion of the metal film alters the sensitivity of the gauge and so these devices are unsuitable for some wind tunnels. Observe also that since the sensitivity of the gauge depends on the geometry of the device, calibration of each individual sensor is required.

An alternative physical mechanism for temperature measurement is the thermoelectric EMF produced at a junction of dissimilar metals. If a metallic substrate is used, the gauge is capable of tolerating a larger transient heat flux due to the higher thermal diffusivity and the larger allowable temperature. The figure of merit is $T_{max}\sqrt{\rho ck}$. A particularly robust design results when the thermocouple material itself is used as the substrate. The sensitivity of the gauge is then unaffected by surface erosion or gauge geometry and depends only on physical properties of the materials. Thus calibration of individual gauges is not required.

The design problem in producing such a gauge is to insulate the two conductors that form the thermocouple so that only a thin surface junction is formed. Common practice is to construct the gauge from coaxial cylindrical thermocouple elements that are insulated by a layer of epoxy or ceramic adhesive. The surface junction is formed by electrolytic deposition of a metal film or by abrasion of the exposed surface. In either case very fine tolerances are required to produce a small gap between the thermocouple elements and the effective depth of the junction scales with the width of the gap between the conductors.

E.2 Analysis of heat conduction in gauge substrate

In order to illustrate the principles of gauge operation and to assess the effect of the finite thickness of the surface junction, consider the unsteady conduction of heat in a one-dimensional semi-infinite solid. For small temperature gradients this process is described by the usual linear partial differential equation,

$$\frac{\partial^2 T}{\partial x^2} = \frac{1}{\alpha} \frac{\partial T}{\partial t}; \quad (\text{E.1})$$

where T is the temperature, x is the spatial coordinate normal to the surface, t is time and α is the thermal diffusivity. Note that $\alpha = \frac{k}{\rho c}$; where k is the thermal conductivity, ρ is the density and c is the specific heat of the material. For the following uniform initial condition, and instantaneously applied, constant surface heat flux, \dot{q}_0 ;

$$T(x, 0) = T_i,$$

$$\left(\frac{\partial T}{\partial x} \right)_{x=0} = \frac{-\dot{q}_0}{k}; \quad t > 0,$$

the solution is,

$$\Delta T = T - T_i = \frac{2\dot{q}_0}{k} \sqrt{\frac{\alpha t}{\pi}} \exp \frac{-x^2}{4\alpha t} - \frac{\dot{q}_0 x}{k} \left(1 - \operatorname{erf} \frac{x}{2\sqrt{\alpha t}} \right). \quad (\text{E.2})$$

Expanding this solution asymptotically in powers of t as $t \rightarrow \infty$ at constant x we obtain,

$$\Delta T = 2 \frac{\dot{q}_0}{k} \sqrt{\frac{\alpha}{\pi}} t^{\frac{1}{2}} - \frac{\dot{q}_0}{k} x + \frac{1}{2} \frac{\dot{q}_0}{k} \frac{1}{\sqrt{\alpha \pi}} x^2 t^{-\frac{1}{2}} + O\left(t^{-\frac{3}{2}}\right). \quad (\text{E.3})$$

The first term is asymptotically dominant for $\frac{x}{(\alpha t)^{\frac{1}{2}}} \ll 1$.

$$\Delta T \asymp 2 \frac{\dot{q}_0}{k} \sqrt{\frac{\alpha}{\pi}} t^{\frac{1}{2}}, \quad (\text{E.4})$$

and this expresses the usual result that the surface temperature rises with \sqrt{t} for a constant heat flux. The criterion $\frac{x}{(\alpha t)^{\frac{1}{2}}} \ll 1$ provides a limit on the thickness of the surface sensing element for practical designs. The next order term, $\frac{\dot{q}_0}{k} x$, gives the error in the surface temperature measurement

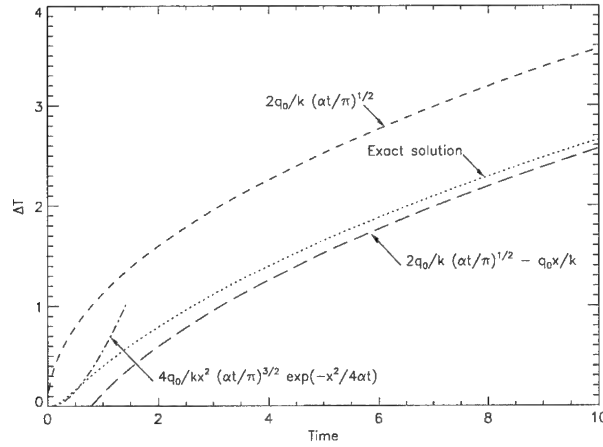


Figure E.1: ASYMPTOTIC BEHAVIOR OF A SURFACE TEMPERATURE SENSOR. For illustrative purposes $\alpha = 1$, $k = 1$, $\dot{q}_0 = 1$, $x = 1$.

associated with this finite thickness and the estimate is also asymptotically valid provided $\frac{x}{(\alpha t)^{1/2}} \ll 1$. Extracting the exponential prefactor and expanding asymptotically as $t \rightarrow 0$ at constant x , the leading order behavior is;

$$\Delta T \asymp \frac{4\dot{q}_0}{kx^2} \left(\frac{\alpha t}{\pi} \right)^{3/2} \exp \frac{-x^2}{4\alpha t}; \quad \frac{x}{(\alpha t)^{1/2}} \gg 1. \quad (\text{E.5})$$

The significance of the various terms of the expansion is illustrated in figure E.1. At long times the solution asymptotes to the true surface temperature, given by the first term in the expansion E.3, with a constant error given by the second term.

E.3 Description of new gauge design

A new gauge design has been developed and tested with the aim of simplifying the construction of surface junction thermocouple sensors. The essential feature of this design is the use of a slightly tapered center conductor. The resulting interference between the tapered center pin and the sharp edged outer conductor forms a thin surface junction and provides reliable insulation (Figure E.2). The protruding pin is severed and the surface is polished once the gauge has been assembled. This design results in a robust transducer whose sensitivity is determined solely by the physical properties of the thermocouple materials. There is a further weak dependence on the taper angle however this is constant for all gauges and is determinable by either calibration or analysis.

The effective thickness of the junction may be estimated from the surface roughness of the thermocouple components and the taper angle of the center conductor (Figure E.3). The thickness

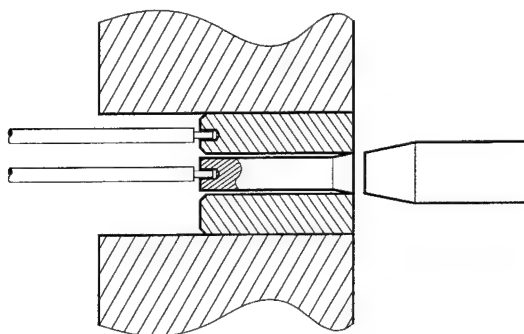


Figure E.2: Layout of new surface junction thermocouple sensor.

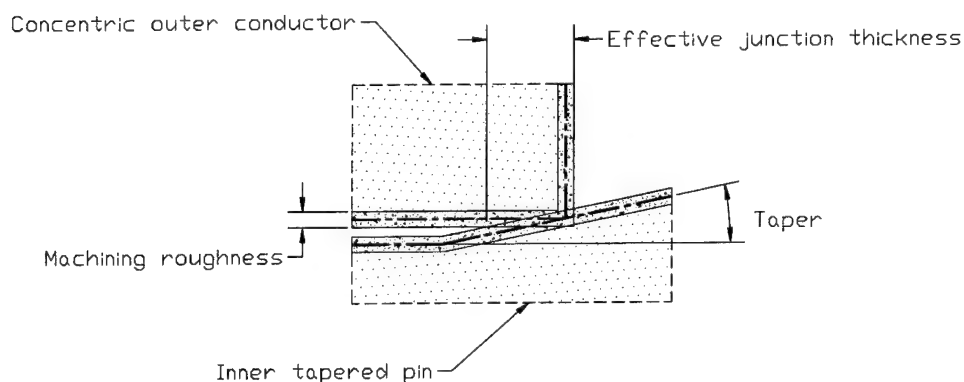


Figure E.3: Effective thickness of thermocouple junction.

of the junction, averaged over the two surfaces may be estimated to be,

$$\text{thickness} = \text{taper} \times \text{roughness}.$$

It is possible to achieve a 0.3μ finish with conventional machining operations and with a 5:1 taper the average junction depth is $1.5 \mu\text{m}$. For the gauges described here type E (Chromel-Constantan) thermocouples were used and the average thermal diffusivity for these materials is $5 \times 10^{-6} \text{ m}^2/\text{s}$. A response time of $0.5 \mu\text{s}$ follows from the condition $\frac{x}{(\alpha t)^{1/2}} \sim 1$. The test time for typical hypervelocity wind tunnels lies in the range 1–10 ms and so this was acceptable. The length of the gauge must be sufficient so that the temperature rise at the rear surface is negligible. This is determined from the condition $\frac{x}{(\alpha t)^{1/2}} \gg 1$; where here the scales are understood to be the test time and the length of the gauge.

A second dissimilar metal junction is formed between the outer conductor and the model. This junction extends along the full length of the gauge since these surfaces are not insulated and so the thermoelectric EMF is small. In the current experiments this common mode EMF and noise pickup were reduced by the use of a simple differential amplifier (Figure E.4). The cold junction was formed at ambient temperature at the amplifier circuit board. This arrangement was adequate given the

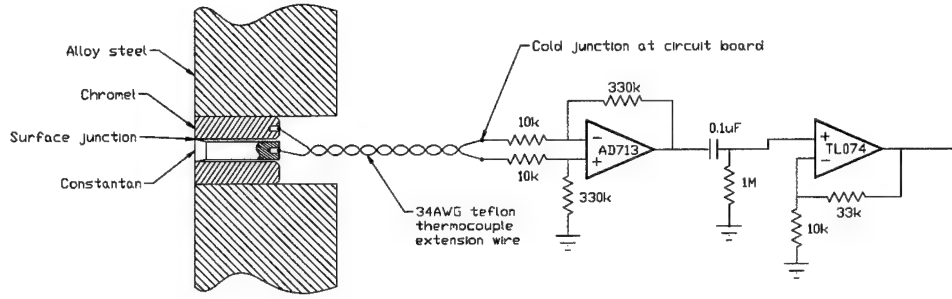


Figure E.4: Schematic of amplifier circuit.

constancy of the cold junction temperature during the short run time and the large hot junction temperature rise experienced in hypervelocity wind tunnels ($\sim 200\text{K}$).

The center pin was located in the concentric outer conductor and secured with epoxy or ceramic adhesive. Sufficient force was applied to ensure adequate registration of the mating parts however care was taken not to deform the sharp edge of the outer conductor. Thermocouple extension wires were resistance welded to the rear of the assembly by discharging a capacitor through the wire. The thermocouple was then installed flush with the outer surface of the model and the protruding center pin was removed. The excess material was removed by filing and the surface was honed to produce the surface junction. Some degradation of the adhesive bond between the conductors was anticipated however the thermal penetration depth during the test time was small so that the bond at the rear maintained the integrity of the device.

E.4 Deducing the surface heat transfer rate

If the unsteady conduction of heat in the thermocouple sensor is modeled by the analysis presented in section E.2 then given the time history of the surface temperature and the physical properties of the gauge materials it is possible to solve an inverse problem for the time history of the surface heat flux. The procedure is described by Schultz & Jones [40] whereby the calculation is performed using a problem specific quadrature scheme or by an electronic analogue.

Observe however that the governing equations are linear and hence the dynamic behavior of the system may be described by a convolution integral,

$$\Delta T(x, t) = \int_0^t g(x, t - \tau) \dot{q}(\tau) d\tau. \quad (\text{E.6})$$

The unit impulse response function, $g(x, t)$, is given by the derivative of equation E.2,

$$g(x, t) = \frac{\partial \Delta T(x, t)}{\partial t} = \sqrt{\frac{\alpha}{\pi k^2 t}} \exp \frac{-x^2}{4\alpha t}; \quad t > 0. \quad (\text{E.7})$$

Note that the integral E.6 is improper in the limit $x \rightarrow 0$ and a finite value of x is taken to regularize the problem (as estimated in section E.2). Recasting the problem in this general form allows the use of spectral deconvolution methods that provide a mean square optimal estimate of the time history of the surface heat flux. This procedure provides optimal rejection of the errors associated with the differentiation of noisy experimental data. Theoretical background is given in Papoulis [34] and the numerical implementation with discrete Fourier transform algorithms is described by Press et al. [37]. A concise description of these methods applied to an analogous problem is given by Sanderson & Simmons [39].

If the noisy experimental data in discrete time is,

$$z_i = \Delta T_i + n_i, \quad (\text{E.8})$$

then the deconvolution problem comprises determining the acausal filter, ϕ_i , that gives a mean square optimal estimate, \dot{q}_i^* , of the time history of the surface heat flux. Thus,

$$\sum_{k=0}^{N-1} \phi_{i-k} z_k = \sum_{k=0}^i g_{i-k} \dot{q}_k^*; \quad i = 0, 1 \dots N-1. \quad (\text{E.9})$$

By the convolution property of the discrete Fourier transform, and since $g_i = 0$ for $i < 0$,

$$\Phi_j Z_j = G_j \dot{Q}_j^* \quad j = 0, 1 \dots N-1. \quad (\text{E.10})$$

Upper case symbols denote the discrete Fourier transform of the corresponding lowercase quantities. It may be shown that the optimal filter is determined by,

$$\Phi_j = \frac{S_{ZZ_j} - \nu_j}{S_{ZZ_j}}, \quad (\text{E.11})$$

where S_{ZZ_j} is the discrete power spectral density of the surface temperature measurement and ν_j is the power spectral density of the signal noise. By inverse discrete Fourier transform, the optimal estimate of the time resolved surface heat flux is then,

$$\dot{q}_i^* = F^{-1} \left[\frac{\Phi_j Z_j}{G_j} \right]; \quad i, j = 0, 1 \dots N-1. \quad (\text{E.12})$$

Note that all time series must be padded to twice their length with trailing zeroes to enforce causality of the right-hand side of equation E.9 when discrete Fourier transforms are used in this manner.

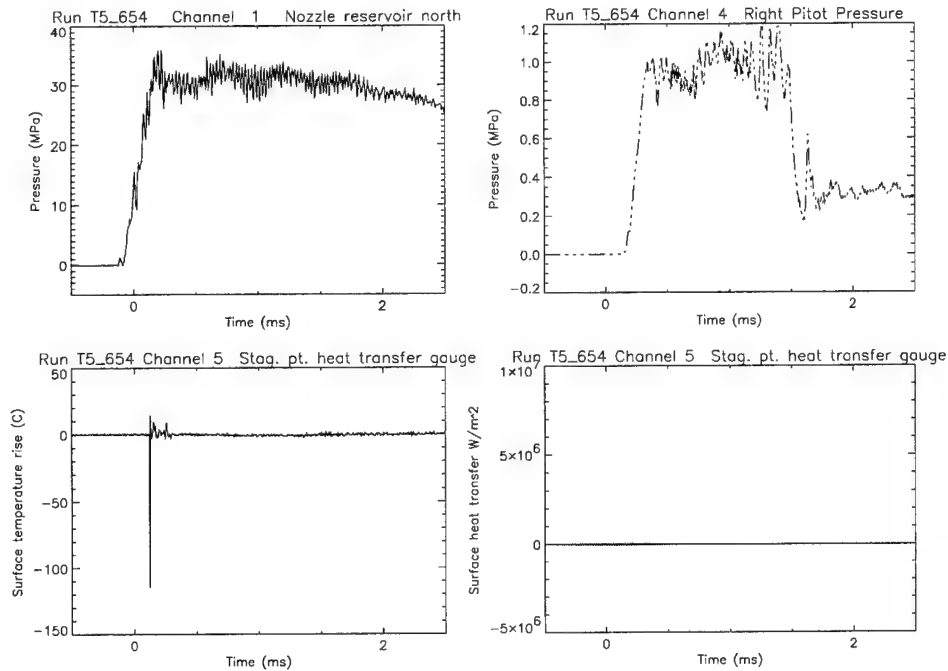


Figure E.5: STAGNATION POINT HEAT TRANSFER MEASUREMENT FOR SPHERE IN HYPERVELOCITY FLOW USING DUMMY CONSTANTAN – CONSTANTAN THERMOCOUPLE AT CONDITION C. The large drop in the pitot pressure at $t = 1.5\text{ms}$ was caused by the passage of an oblique shock wave.

E.5 Accuracy of measurements

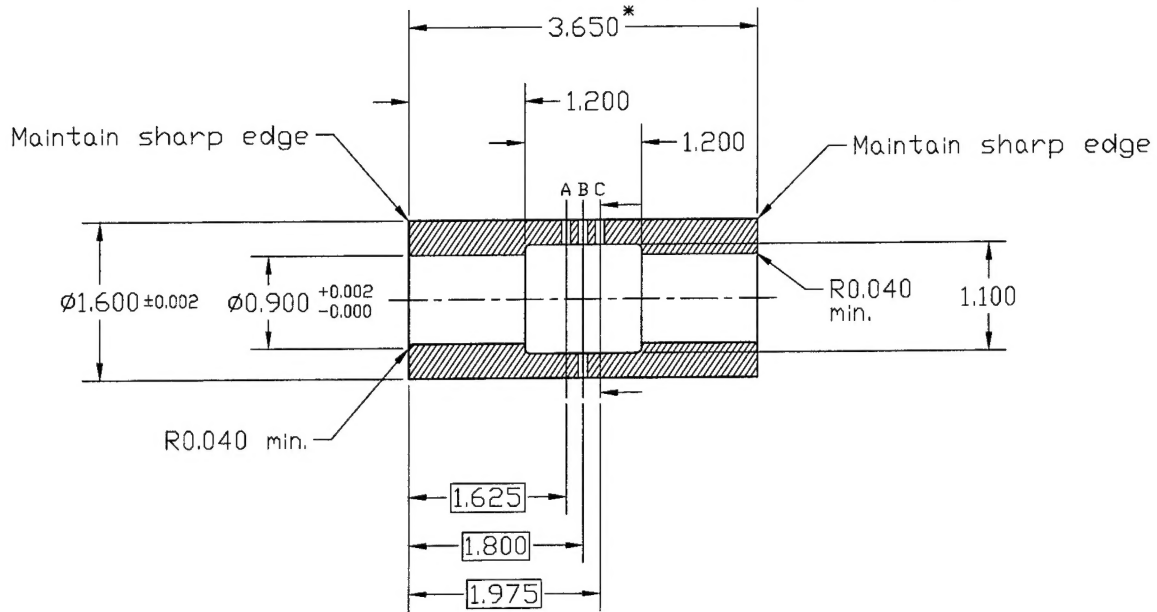
It has been demonstrated that the sensitivity of the transducer depends only on the thermo-physical properties of the materials. All transducers used in the current experiments were manufactured from the same piece of raw material. Comparison of symmetrically disposed transducers on the cylindrical model indicated that the repeatability of the measurement for individual realizations of the design was within $\pm 10\%$.

The flow environment in T5 was extremely hostile and since the thermocouple junction was electrically exposed to the flow it was necessary to demonstrate that erroneous EMFs were not generated by physical mechanisms other than the thermoelectric effect. A dummy gauge of identical design was manufactured with both conductors made of Constantan so that no thermoelectric EMF was generated. Figure E.5 shows the results obtained with this dummy gauge at a high enthalpy condition. Apart from an initial transient that decays rapidly, no erroneous EMFs are discernible on this scale. The deconvolved heat transfer rate is three orders of magnitude less than the actual heat transfer rate.

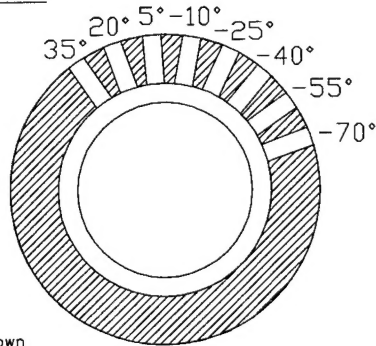
Appendix F Technical data

F-2

* Fit when assembled with mating parts
Leave 0.050" excess material on RH face

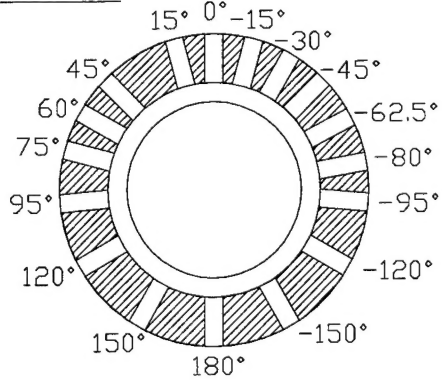


Section AA



31 holes as shown
Ream $\varnothing 3/32$ " through
Maintain sharp edge at
outer end

Section BB



Section CC

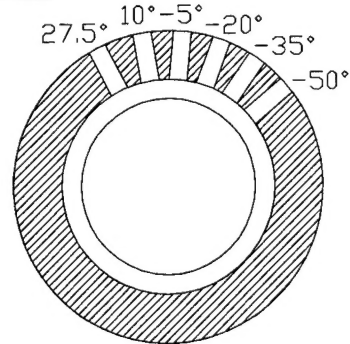


Figure F.1: Layout of thermocouple sensors.

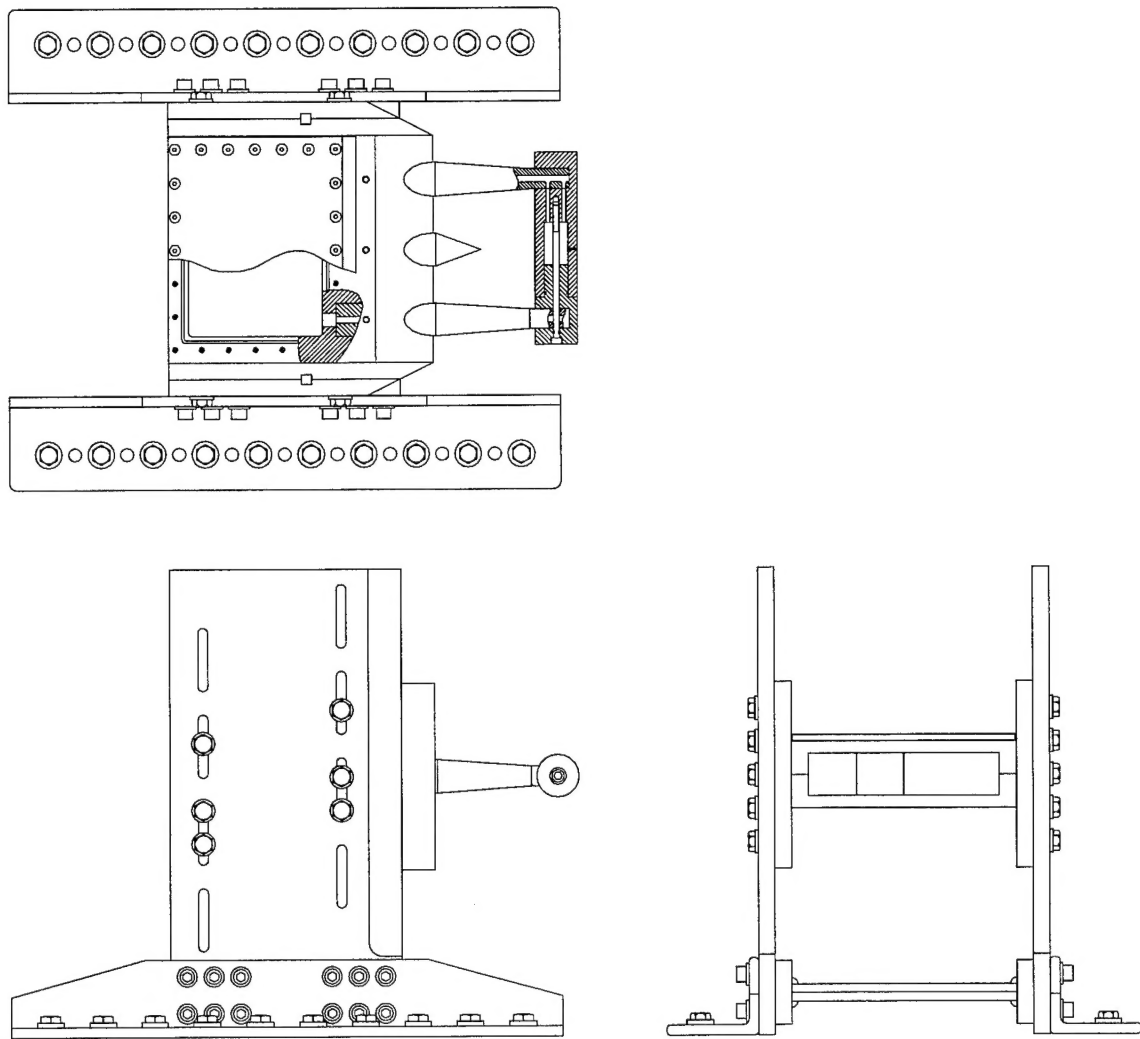


Figure F.2: Arrangement drawing of model support.

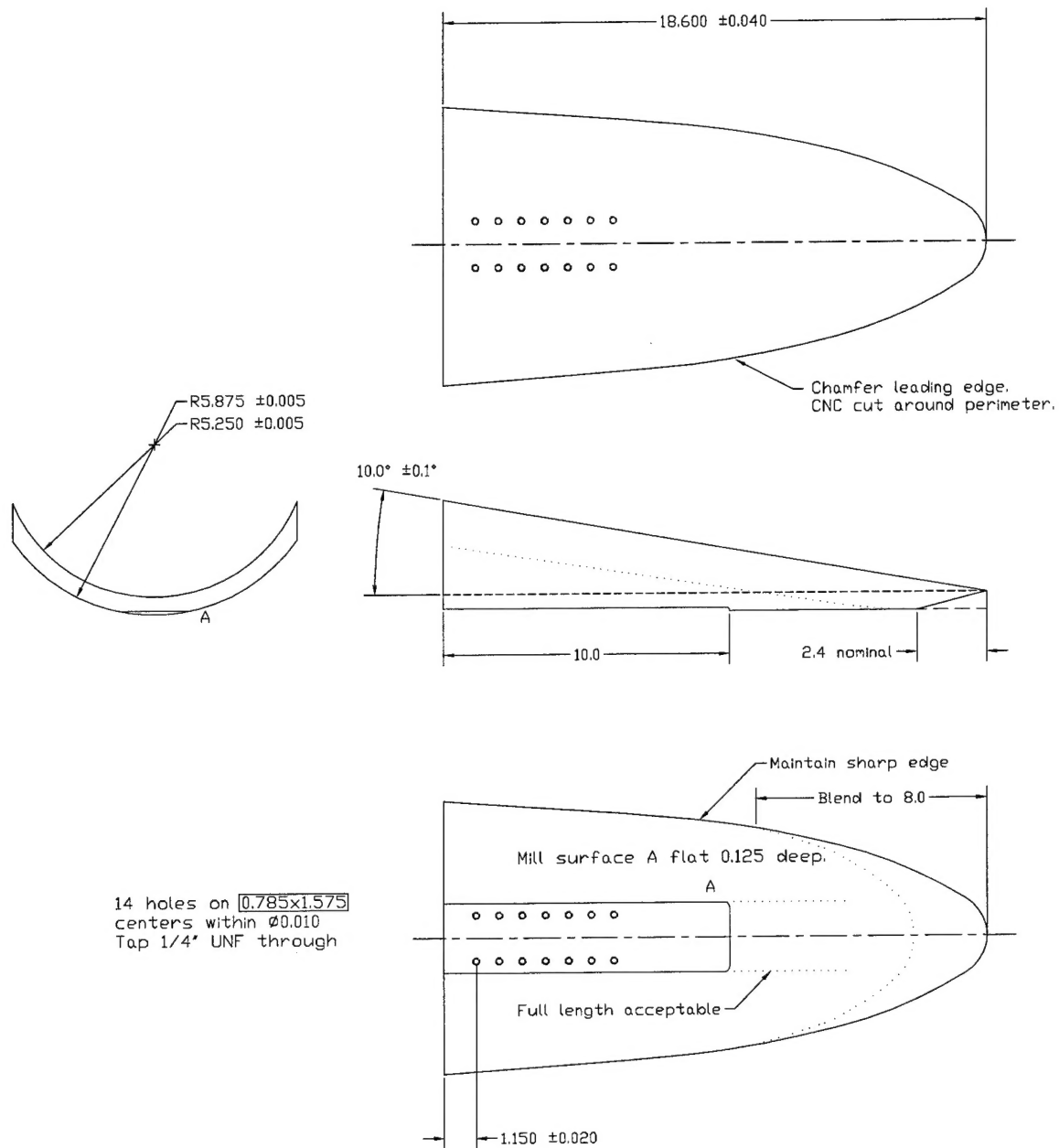


Figure F.3: Shock generator technical details.